A fundamental approach of the wetting at Zn/Al2O3 interface: the effect of a Cr buffer

Maya Messaykeh

▶ To cite this version:

Maya Messaykeh. A fundamental approach of the wetting at Zn/Al2O3 interface: the effect of a Cr buffer. Condensed Matter [cond-mat]. Sorbonne Université, 2018. English. NNT: 2018SORUS478. tel-02924972

HAL Id: tel-02924972

https://theses.hal.science/tel-02924972

Submitted on 28 Aug 2020

THÈSE DE DOCTORAT
DE SORBONNE UNIVERSITÉ
CAMPUS PIERRE ET MARIE CURIE

Spécialité : Physique
Ecole Doctorale de Physique et Chimie des Matériaux

réalisée au sein de
l'Institut des NanoSciences de Paris

Presentée par

MESSAYKEH Maya

pour obtenir le grade de :
DOCTEUR DE SORBONNE UNIVERSITÉ

Sujet de la thèse :

A fundamental approach of the wetting at Zn/Al_2O_3 interface: the effect of a Cr buffer

Soutenue le 09 Novembre 2018 devant le jury composé de:

M^{me}. SOLAL Francine	Professeur (IPR, Rennes)	Rapporteur
M^{me} GRENET Geneviève	Directeur de Recherche (STMS/INL, Lyon)	Rapporteur
M. ETCHEBERRY Arnaud	Directeur de Recherche (ILV, Versailles)	Examinateur
M. HUMBLOT Vincent	Chargé de Recherche (LRS, Paris)	Examinateur
M. KOLTSOV Alexey	Ingénieur (ArcelorMittal, Maizières-Lès-Metz)	Co-encadrant de thèse
M. LAZZARI Rémi	Directeur de Recherches (INSP, Paris)	Directeur de thèse

September 21, 2018

CONTENTS

Contents

Introduction

INTRODUCTION

The industrial context

Recent trends in steel used in the automotive industry towards improved safety, enhanced formability and reduced weight for lower CO_2 emission at an affordable manufacturing cost led to a major interest in the so-called Advanced High Strength Steel (AHSS). This new generation of materials consists of highly alloyed steel grades, where next to silicon and manganese, aluminum, is one of the most used alloying light elements. Not only does it contribute to improve the elasticity but it provides as well better stiffness performance thanks to its low density (figure 1). However, these alloyed steel grades challenge established fabrication processes of steel sheets at several levels. In particular, the historical protection against corrosion by galvanization faces serious issues in the presence of the alloying elements .

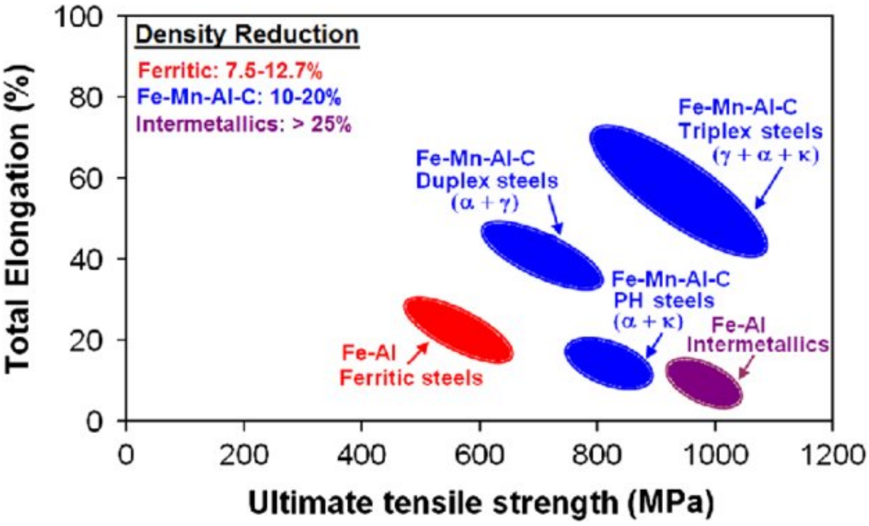

Figure 1: Strength-elongation plot of some low-density steels. Density reductions in these steels are also indicated [Rana et al., 2014].

In fact, continuous hot-dip galvanization (figure 2) is the historical technique for protecting steel sheets by immersion of the strip in a bath of molten zinc at a temperature of ~ 730 K to reach, after quenching and skin pass processes, a continuous coating of micrometric thickness. At contact with atmosphere, zinc being less anodic than iron, it corrodes preferentially at a low rate and provides a cathodic sacrificial protection allowing a longer and predictable lifetime of the products. However, problems occur at the previous step of the process where cold-rolled strips are recrystallized by annealing at $\sim$ 1070 K in order to remove remaining stresses and metal texture induced by the rolling process. Despite the reducing atmosphere of the annealing furnace (N_2+5%H_2; dew point below $-40°$ C) used to prevent oxidation of iron according to thermodynamics, electropositive alloying elements such as Al, Mn, Si are prone to external oxidation; the resulting oxide films extensively cover surfaces and dramatically impede the adhesion and wetting of the anticorrosive zinc protection [Drillet et al., 2004, Ollivier-Leduc et al., 2010, Giorgi et al., 2012]. This oxidation-induced segregation results in a switch from a Zn-Fe alloyed metallic interface to a non-reactive weak one between zinc and wide band gap oxides such as alumina. Different strategies are developed by the steel industry to overcome this issue: (i) to modify and control upstream the morphology and the surface coverage of the oxide by switching from external to more internal oxidation of the alloying element and (ii) to optimize the conditions of galvanization to control adhesion at zinc/oxide interface [Cavallotti, 2014a]. But these approaches face the bottleneck of thermodynamics boundaries and industrial constraints. Recently, Arcelor-Mittal steel company developed a breakthrough innovation by opening a galvanization factory based on jet vapor deposition of zinc (https://belgium.arcelormittal.com/fr/environnement-de-travail/jet-vapor-deposition/). By taking advantage of its low vapor pressure, a zinc coating is deposited in vacuum on a continuously passing strip that was previously annealed. Prior to metal evaporation, buffer layers, based mainly on transition metals, are deposited to improve zinc adhesion on the existing surface oxides. The questions risen by these adhesion layers go well-beyond the galvanization process and concern all industrial fields related to coating and film technologies, among which packaging, microelectronics or glass industry.

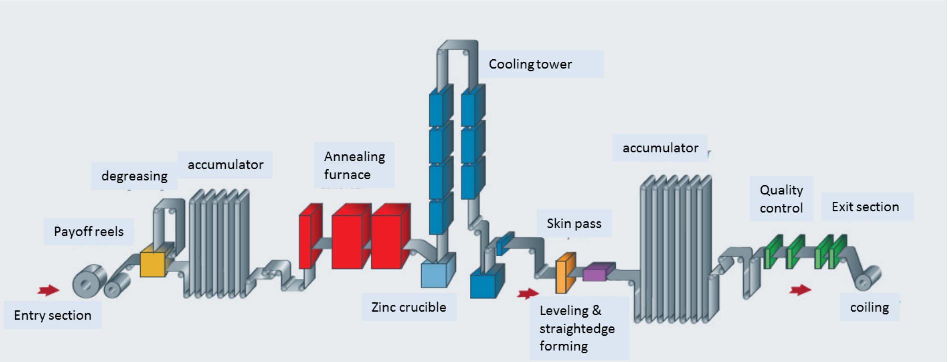

Figure 2: Scheme of the industrial process of hot-dip galvanization of steel sheets [Cavallotti, 2014a].

The studied interface: $Zn/Cr/Al_2O_3(0001)$

In this context, this thesis aims at understanding, at a fundamental level through a surface science approach, the actual impact of this buffer layer on the adhesion of zinc. The complexity of the oxide-covered alloyed-steel surface being out of grasp at a detailed level, this study requires beforehand the definition of a representative model system.

For steel or more model Fe-Al polycristalline alloys with a high content of aluminum, previous studies [Cavallotti, 2014a] concluded that the annealing in industrial conditions at low dew point (lower than $-40°$C) results in the formation of a continuous polycristalline alumina layer with a thickness of 60-80 Å and an atomic structure close to the metastable

$\gamma-$alumina. As a reminder, the high temperature and most stable polymorph of alumina is the corundum α-phase. Although the exact bulk crystallographic structure of γ-alumina is still debated [Krokidis et al., 2001,Paglia et al., 2005,Sun et al., 2006,Digne et al., 2004,Digne et al., 2006], the study of R. Cavallotti [Cavallotti, 2014a] has demonstrated, that, despite their structural differences, the surfaces of α and γ phases have very similar electrostatic characteristics. Therefore, as the polar or non-polar character of the surface drives to a large extend the reactivity of the surface with its environment, it has been decided to consider α-Al_2O_3 single crystal as a representative substrate for this study, in particular the most-stable (0001) basal plane. On a practical point view, it has also to be reminded that large γ-alumina single crystal are not available at the opposite to α-phase. However, a comparison to $\gamma-$alumina film grown on a FeAl alloy will be performed in the X-ray absorption part of the present work.

Previous theoretical and experimental works [Cavallotti, 2014a,Cavallotti et al., 2014,Cavallotti et al., 2016,Le et al., 2017b] highlighted the poor adhesion at Zn/α-Al_2O_3(0001) interface. On the one hand, an excess of surface charge provided by a polar termination or by hydroxylation can considerably reinforce the zinc adsorption energy and allows to switch from a interfacial to a cohesion cleavage [Le et al., 2017b]. Nevertheless, the interaction of zinc with hydroxyl groups was found to be thermally activated. On the other hand, *ab initio* studies [Le et al., 2016,Le et al., 2017a] reported on the positive influence of metallic buffers on the adhesion characteristics at the weakly interacting Zn/Al_2O_3 interface. Among transition metals from the middle and the end of the 3d series, Ti and Cr particularly had the most pronounced impact driven by both strong interfacial metal-oxygen (M-O) and metal-zinc (M-Zn) bonds. It was also demonstrated theoretically that buffer oxidation MO_x, whatever the stoichiometry ($x = 1, 3/2, 2$), has a clear detrimental effect on zinc adhesion. But this conclusion is less underlined with multi-components buffer including several metals [Le et al., 2017a] ; they are expected to be more operative in industrial conditions.

In the light of those results, the present study focused on the experimental investigation of the model system Zn/Cr/α-Al_2O_3(0001). It was split in into two parts, one dealing with the Cr/Al_2O_3 interface and one with the Zn/Cr/Al_2O_3 interface (buffer effect). The former is a necessary prerequisite in the understanding of the latter. For Cr/Al_2O_3, a main concern was the hydroxylation state of the alumina surface. An expected reaction between residual hydroxyl groups and Cr adatoms would considerably affect both the chemistry and morphology of supported particles as previously seen for other metal/oxide systems [Libuda et al., 1997, Chambers et al., 2002, Lazzari and Jupille, 2002, Lazzari and Jupille, 2005]. Regarding the buffer effect, the influence of the chromium chemical state, wetting behavior and epitaxy on adhesion, chemistry and wetting of zinc were thoroughly studied. The key parameters of the study were mainly the chromium buffer thickness and its oxidation state.

Outline of the thesis

The manuscript is divided into five chapters in addition to the present introduction and a general conclusion with some perspectives.

The first chapter introduces the experimental set-up and techniques that were combined during the course of this study: X-ray Photoemission Spectroscopy (XPS) for chemical identification and film thickness quantification, Surface Differential Reflectivity Spectroscopy (SDRS) for morphology and growth characterization, Electron Diffraction (LEED/RHEED) for crystallographic analysis, Extended X-ray Absorption Fine Structure (EXAFS) for the determination of the Cr local environment, and Temperature Programmed Desorption (TPD) for giving an insight on the thermal stability of the films. Beyond the experimental aspects and the description of these techniques, some specific points regarding their data analysis (XPS, EXAFS) are introduced as well in this chapter.

In the second chapter, a detailed state of the art is given. An exhaustive, however made brief, overview of the literature tackles the questions of α-$Al_2O_3(0001)$ surface, its reconstructions, thermodynamic stability and hydroxylation state. It is then followed by a review of metal/alumina interfaces with a focus on the chemical states of the metals, their adsorption sites, the epitaxy of the grown films, and their adhesion and wetting behaviors. This chapter constitutes a basis to which we will refer to interpret and discuss the results for Zn/Cr on alumina.

The SDRS being not a common technique for wetting and growth mode characterization at the nanoscale, the third chapter is dedicated to the underlying theory with an emphasis on the special cases of Zn and Cr. After an introduction on the Fresnel coefficients of thin films in the framework of the excess fields and interfacial susceptibilities, the dielectric calculation of the polarizability tensor of truncated spheres and spheroids is explained. Follows the description of particle polarization in terms of eigenmodes of charge vibration which will help in understanding the role of signal integration to distinguish growth phases. The dielectric functions of Cr and Zn are the introduced and compared to the more common metals of plasmonics. They are used to simulate the expected optical response as a function of particle aspect ratio and to demonstrate, despite interband transition, the sensitivity of the SDRS technique to wetting. Afterwards, the polarization modes of the Cr and Zn particles are investigated in an attempt to grasp the involvement of interband transitions. Finally, the chapter ends with the question of the optical response of stack of layers. The screening induced by a continuous film on a particle is handled through an new analytic model at the dipolar level, for an isolated dipole and a lattice of dipoles.

Results on Cr/Al_2O_3 interface are presented and discussed in the fourth chapter. The questions of interfacial chemistry, adsorption site and growth mode of chromium are tackled. Cr 2p, Al 2s and O 1s core-level photoemission peaks are scrutinized to determine chemical states; they give some hints on a possible reaction between the metal adatoms and the residual hydroxyl groups adsorbed at the alumina surface. By comparing EXAFS measurements at the Cr K-edge and *ab initio* calculations of various Cr/Al_2O_3 interface configurations, the local environment of the metal at the interface is found to be oxygen-rich with a Cr-O distance and a coordination number in agreement with a reaction of hydroxyl groups and an oxidation state close to 3+. Dielectric simulations of SDRS results point at the growth of flat metallic particles that percolate quickly. Finally, a non-epitaxial growth is found by RHEED and assigned to the interface chemical reaction.

The above described goal of the study is developed in the fifth and last chapter, where the effect of the chromium buffer on the chemistry, growth and thermal stability of zinc deposits on α-Al_2O_3 surface is explored. Photoemission yields a dramatic and non-linear increase of the room-temperature sticking coefficient of zinc with chromium coverage and typical fingerprints of metallic zinc. SDRS is used to point at clear correlation between Cr and Zn deposit morphology. Finally, the analysis of TPD experiments focuses on the impact of chromium and its chemical state on the desorption energy of zinc.

Beyond a summary of the achieved results, the conclusion points at open questions and tries to draw some perspectives.

CHAPTER 1

EXPERIMENTAL TECHNIQUES AND SETUPS

This chapter is aimed at giving an overview of the experimental setup (section 1.1), the surface/film preparation (section 1.2) and the techniques combined in this thesis to tackle the question of wetting of $Al_2O_3(0001)$ surfaces by chromium and zinc deposits. The key points for our study of the surface science classical techniques, namely photoemission (XPS: X-ray photoemission, section 1.3), electron diffractions (LEED: Low-Energy Electron Diffraction section 1.4.1, RHEED: Reflection High Energy Electron Diffraction section 1.4.2) and desorption (TPD: Temperature Programmed Desorption Spectroscopy section 1.5) will be reminded. Experimental determination of the Cr absorption site was done using X-ray absorption at synchrotron SOLEIL; its principle will be detailed in section 1.6. While technical details about the less-common Surface Differential Reflectivity Spectroscopy (SDRS, section 1.7) are presented at the end of this chapter, its interest in wetting study at the nanoscale and its theoretical analysis are postponed to chapter 3.

1.1 The ultra-high vacuum setup at INSP

Experiments were performed in an ultra-high vacuum setup composed of two stainless steel chambers (preparation and analysis) equipped with various surface science facilities including XPS (X-ray Photoelectron Spectroscopy), LEED (Low Energy Electron Diffraction), TPD (Temperature Desorption Spectroscopy) and SDRS (Surface Differential Reflectivity Spectroscopy). RHEED (Reflection High Energy Electron Diffraction) measurements have been performed in an other vacuum chamber having the same overall structure. The pumping system is composed of two ionic pumps (MECA 2000, 400 l/s) associated with Ti sublimators, in addition to two turbomolecular pumps (PFEIFFER, 200 l/s) backed by two rotary pumps. After baking out the system at ~ 410 K for two to three days and degassing all the heating elements, base pressures of 2×10^{-10} mbar and 5×10^{-11} mbar are obtained in the preparation and analysis chambers, respectively. Pressures are measured by Bayard-Alpert gauges. Figure 1.1 illustrates the setup used at INSP (Institut des NanoSciences de Paris) in the frame of this PhD thesis. Its main elements are:

- The load-lock system pumped by the preparation turbomolecular pump through a bypass allows a fast introduction of the samples, and their exposure to high gas pressures, notably water vapor ($p \simeq 1$ mbar) for their hydroxylation, without ruining the vacuum

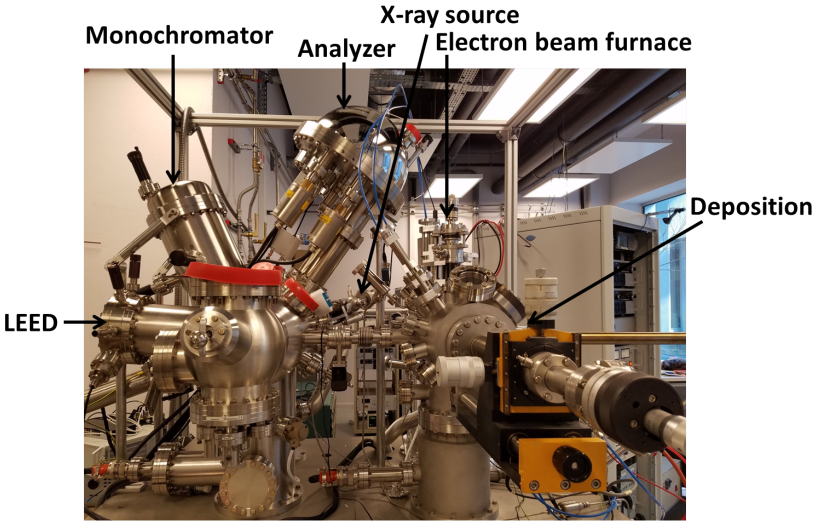

Figure 1.1: A photo of the UHV setup featuring the preparation (right) and analysis (left) chambers with all the elements in addition to the monochromated source (not used in this work).

conditions in the chambers. The water vapor is obtained by performing several cycles of freeze/pump on deionized water in an ancillary gas pipe system.

- The preparation chamber in which the substrates are annealed and the deposition of Zn and Cr took place contains:
    - ▶ A home-made electron bombardment furnace used for the annealing at temperatures up to 1800 K measured with a pyrometer.
    - ▶ In front of the heating position, a gas doser made of a bundle of Ni tubes (aspect ratio¿40) to increase the local partial pressure on the surface once set a distance of ~ 1 mm of the substrate [Campbell and Valone, 1985].
    - ▶ An ion gun for sputtering the surface (not used in this study).
    - ▶ A manipulator able to resistively heat the sample up to $\sim$ 1100 K for sample annealing and thermal desorption measurements.
    - ▶ A quadrupole mass spectrometer (QMS 200 from PFEIFFER) for thermal desorption measurements.
    - ▶ A low-temperature effusion cell for zinc evaporation controlled by a PID (Proportional Integral and Derivative) temperature regulator.
    - ▶ An electron bombardment cell (EFM3 from OMICRON) for chromium evaporation.
    - ▶ The SDRS optical benches which are mounted on two silica windows of the chamber (see section 1.15).
    - ▶ A quartz microbalance that can be set at the the sample position to estimate evaporation rates.

- The analysis chamber in which XPS and LEED measurements are done contains:
    - ▶ A dual Al/Mg non-monochromated X-ray source (XR50 from SPECS).

  - ▶ A hemispherical energy analyzer (PHOIBOS 110 from SPECS) equipped with a 1D delay-line detector.
  - ▶ A low energy electron diffractometer with four retarding grids and an electron gun (ErLEED from SPECS).

- A set of gas pipes connected to the chamber via leak valves which allows the exposure of the sample to oxygen and water vapor at a controlled pressure. High purity research grade gases were used during this work.

  The analysis chamber was renovated at the end of the thesis and is now equipped with an X-ray monochromator, a new manipulator and is shielded by μ-metal.

1.2 Substrate preparation and metal deposition

1.2.1 Alumina preparation

The control of the substrate surface preparation and its reproducibility is crucial in any surface science study. Ion bombardment should be prohibited since it is knwon to lead to poorly crystallized and non-stoichiometric surfaces even high-temperature treatment [French and Somorjai, 1970, Gautier et al., 1991b, Gautier et al., 1994]. As the alumina surface can not be easily obtained by cleavage, high temperatures annealings at $\sim 1200 - 1400$ K under oxygen atmosphere are needed in order to remove carbon contamination and heal polishing damages. For that reason, an oxygen doser was designed, allowing a directional oxygen flux and a local partial pressure (estimated in the range of 10^{-5} mbar [Campbell and Valone, 1985]), to clean the surface at reduced temperature and time, and most importantly without strongly degrading the residual vacuum in the chamber during the process.
One-side epipolished $(9 \times 9 \times 0.5)$ mm^3 α-Al_2O_3 (0001) single crystals (provided by MaTecK GmbH [Mateck,]) were firmly fixed via welded tantalum clips on molybdenum plates previously cleaned with *aqua regia*. They are then heated by electron bombardment of the backplate at $\sim 1200 - 1400$ K (temperature measured with a pyrometer of emissivity previously set by comparison to a thermocouple reference spot welded on the plate) for 10 minutes at a chamber partial pressure of oxygen of $\simeq 6 \times 10^{-7}$ mbar (but the estimated sample local pressure is about ten times higher). On the other hand, an annealing under vacuum at a temperature higher than 1600 K results in the reconstruction $(\sqrt{31} \times \sqrt{31})\pm 9^\circ$ of the alumina surface as initially reported by French and Somorjai [French and Somorjai, 1970, Renaud et al., 1994, Renaud, 1998] which corresponds to the loss of the last two oxygen planes of the corundum structures. In our study, reconstructed surfaces were used as model systems for dehydroxylated surfaces. During such high temperature annealing under UHV, the pressure rose up to the low $\times 10^{-8}$ mbar before going back quickly in the low $\times 10^{-9}$ mbar at the end of the treatment.
The carbon contamination level of all samples was systematically checked through the C 1s core level intensity that was lower than the detection threshold (about 0.01 of a monolayer). However, calcium segregation coming from bulk impurities up was observed in photoemission. As previously observed by surface X-ray diffraction [Guénard et al., 1998], calcium hampers neither the crystalline quality of the surface nor the (1×1) reconstruction (Figure 1.2). More-

over, no evolution of Ca chemical state was ever observed upon Cr deposition. No other contaminants were found on the annealed surfaces at the sensitivity of photoemission.

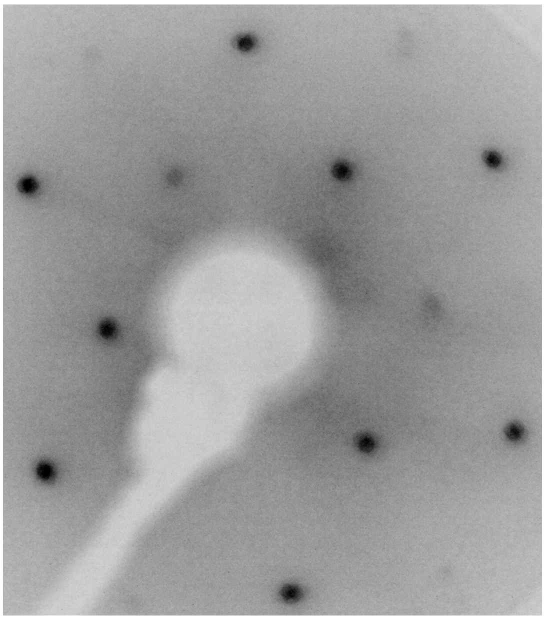

Figure 1.2: Sharp (1 × 1) LEED pattern at a beam energy of $E = 107$ eV obtained after sample preparation.

1.2.2 Metal evaporation

Films of Cr and Zn of different thicknesses were thermally evaporated on the substrate at 300 K. Cr was evaporated from a metallic rod heated by electron bombardment in a EFM3 Focus OMICRON evaporation cell at a rate of ~ 1 Å.min^{-1} or ~ 0.5 Å.min^{-1} depending on the final sought thickness (4-16 Å or a fraction of Å, respectively). The ion flux monitor of the e-beam cell allows a good reproducibility of the evaporation rate. On top of Cr deposit, Zn was evaporated at a rate of ~ 1 Å.min^{-1} from a low-temperature effusion cell (MBE-Komponent GmBh) which crucible is thermally regulated at a temperature between 493 and 513 K via a PID temperature regulator. Actually, the final thicknesses reported in this manuscript are calculated based on the ratio of core-level areas in the photoemission spectrum as explained in section 1.3.7. Both evaporators were thoroughly out-gazed so that growth took place at a pressure of $\sim 8\times10^{-10}$ mbar.

1.3 X-ray photoemission spectroscopy (XPS)

The history of XPS goes back to the discovery of the photoelectric effect observed by Heinrich Hertz in 1887, yet only explained in 1905 by Albert Einstein [Einstein, 1965]. It was the starting point of the development of a highly useful analytical tool by the group of Siegbahn later in the 1960s [Siegbahn, 1970]. The XPS technique, surface sensitive, expands to provide a rich panoply of information on the nature of chemical species in the sample under study, on their chemical states, on band-structure in addition to information such as the quantities of materials and the thicknesses of deposits. In the following subsections, the principle of this technique, the various features of an XPS spectrum and the information that can be extracted will be detailed with some emphasis of relevant points relative to insulators.

1.3.1 Photoemission principle

The XPS technique, together with Ultraviolet Photoelectron Spectroscopy (UPS), relies on the photoelectric effect in which photons of known energy $\hbar\omega$ impinge on a sample, expelling photoelectrons out of the sample from initial states with binding energies E_B (in reference to the Fermi level). Their kinetic energy E_K is given by:

$$E_K = \hbar\omega - E_B - \phi, \tag{1.1}$$

where ϕ=E_{vacuum}-E_{Fermi} is the work function of the material [Hoffman, 2013]. Knowing ϕ_A the analyzer work function, the photoelectron kinetic energy measured by the analyzer gives access to E_B through:

$$E_K = \hbar\omega - E_B - \phi - (\phi_A - \phi) = \hbar\omega - E_B - \phi_A. \tag{1.2}$$

The energy of the incident beam, ranging from 100 eV to 10 keV in XPS and from 10 to 50 eV in UPS is the key difference between the two techniques [Oura et al., 2013]. As a consequence, the penetration depth of photons in XPS ($\sim$ 20 nm - several µm) is larger than in UPS ($\sim 20-50$ nm) [Henke et al., 1993]. In addition, the photoionization cross section decays with photon energy [Yeh and Lindau, 1985]. Owing to these differences, XPS is conventionally used to probe deep core levels while UPS is rather used for studying valence states. However, this subdivision is only a matter of convention all the more that some radiation sources such as synchrotrons can cover a continuum of excitation energies from the soft ultra-violet to the hard X-ray [Oura et al., 2013].

Figure.1.3 illustrates the process of photoemission with a schematic spectrum and the corresponding probed density of states [Fadley and Shirley, 1970]. This diagram, shows that the XPS spectrum is a fingerprint of occupied states in a material. However, in addition to elastic photoelectron peaks, there is a continuous background composed of the inelastically ejected electrons (secondary electrons), Auger transitions, satellite peaks and plasmon losses (on the lower binding energy side of each peak) (see figure 1.4). These features will be detailed in the section 1.3.5.

1.3.2 Electron detection

The emitted photoelectrons are usually detected in energy by an electrostatic analyzer, such as the hemispherical analyzer we used. Electrons are first focused and decelerated/accelerated by a lens system before going through an energy filter. Depending on the choice of entrance slits and focusing conditions of the lenses, either angular acceptance or resolution is favored playing therefore on the analyzed area, angular resolution and intensity. The energy filter is composed of two hemispheres biased at the so-called pass energy which selects the electrons that will go through the analyzer and get detected. Pass energy affects the resolution and intensity. The former is given by the instrument related FWHM of the transmitted line:

$$\delta E_{an} = E_p\left(\frac{\omega}{2R_0} + \frac{\alpha^2}{4}\right), \tag{1.3}$$

where ω is the exit slit width, R_0 the mean radius of the two hemispheres, α the entrance aperture half-angle, and E_p the pass energy.

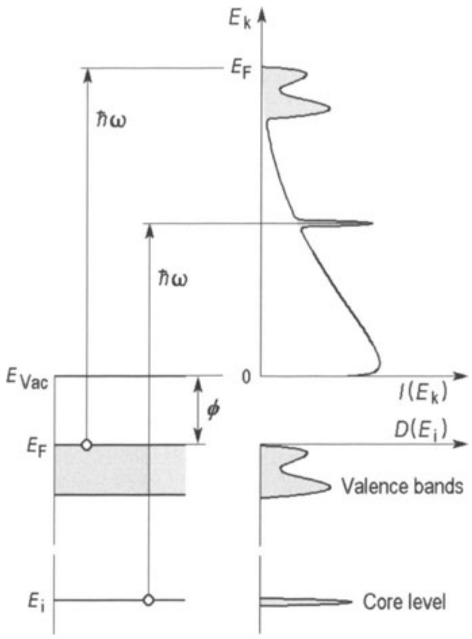

Figure 1.3: Schematic diagram of the photoemission process. The correspondence between the density of occupied states D(E_i) in the solid and the angle-integrated photoemission spectrum I(E_k) is shown. (After [Oura et al., 2013]).

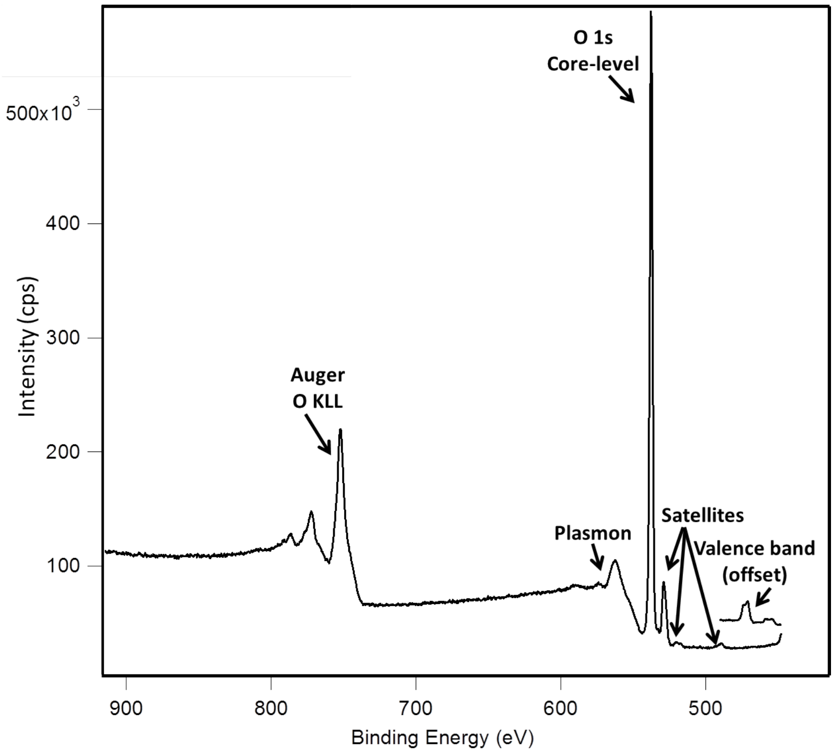

Figure 1.4: Part of an XPS spectrum for an alumina substrate excited with a Mg source. Different features appear: core-level peak, Auger peak, plasmon, satellites and valence band. Note the very weak intensity of the valence band features shifted in binding energy and intensity axes.

1.3.3 Surface Sensitivity

Because of the relatively strong interaction of the photoelectron with matter, there is a high probability of inelastic scattering events (plasmon excitations, excitation of electrons in valence band, ionization of core levels). Additionally, multiple elastic scattering events extend the distance travelled by electrons increasing by that the probability of inelastic processes. As a consequence, although the penetration depth of X-ray photons into a solid is of the order of the µm, the surface sensitivity of XPS stems from the fact that the mean free path of the emitted photoelectrons in the considered range of kinetic energies (5-2000 eV) is limited to ∼ 10 nm [Tanuma et al., 1991a] (see figure 1.5). Accordingly, the probability for a photoelectron to be detected depends on the depth of the emitter z from the surface and on the inelastic mean free path λ through the Beer-Lambert relation:

$$P \propto e^{-z/\lambda}. \tag{1.4}$$

λ represents the average distance that an electron can propagate in matter without undergoing inelastic scattering. The intensity of the signal coming from a small region of thickness dz is therefore proportional to:

$$dI \propto e^{-z/\lambda} n_s A dz \tag{1.5}$$

where A is the anlyzed surface and n_s the atomic density of emitters. For a deposit of thickness t, the total intensity is therefore obtained by integrating between 0 (surface plane) and t equation 1.5 which results in [Lüth, 2001]:

$$I \propto I_0(1 - e^{-t/\lambda}). \tag{1.6}$$

While this is the case for normal emission, for a take-off angle θ between the surface normal and the analyzer direction, the mean free path should be decreased by a factor of $\cos\theta$. Hence, collecting the photoelectrons at a grazing angle enhances the surface sensitivity of XPS [Oura et al., 2013]. This was particularly applied in the framework of this thesis to enhance the signal coming from the residual surface hydroxyl groups (see section 2.1.4). The inelastic mean free path follows a "universal" curve with a minimum in the range of 50-100 eV of electron kinetic energy. Actual values are tabulated or can be estimated depending on the material under study [Tanuma et al., 1988,Tanuma et al., 1991a,Tanuma et al., 1991b,Tanuma et al., 1993, Tanuma et al., 1994, Tanuma et al., 1997, Tanuma et al., 2003, Tanuma et al., 2005, Shinotsuka et al., 2015].

1.3.4 Charge effects

Charging effects are a problem encountered in all techniques probing insulating samples with charged particles. In XPS, for electrically insulating or poorly-conductive materials, the ejected photoelectrons not being compensated by electrons from the ground cause charges to accumulate at the surface until the potential is stabilized by the cascade of secondary hot electrons. As a consequence, the kinetic energy of the leaving photoelectrons is decreased by an electrostatic effect leading to an apparent binding energy shift or a distortion of the peaks. In order to eliminate these effects, several solutions can be adopted, such as the metalization of the sample or the use of a low energy electron flood gun (also referred to as charge neutralizer) to compensate for the positive charge. However, in the case of alumina studied herein, no such technique was adopted. Since the problem of charge effects occurred only mainly in the determination of chemical shift from the absolute peak positions, relative peak positions or Auger parameter helped surmounting this obstacle (see section 1.3.5.1). However, the internal calibration (relative shifts) is valid under the lack of differential charging with kinetic energy.

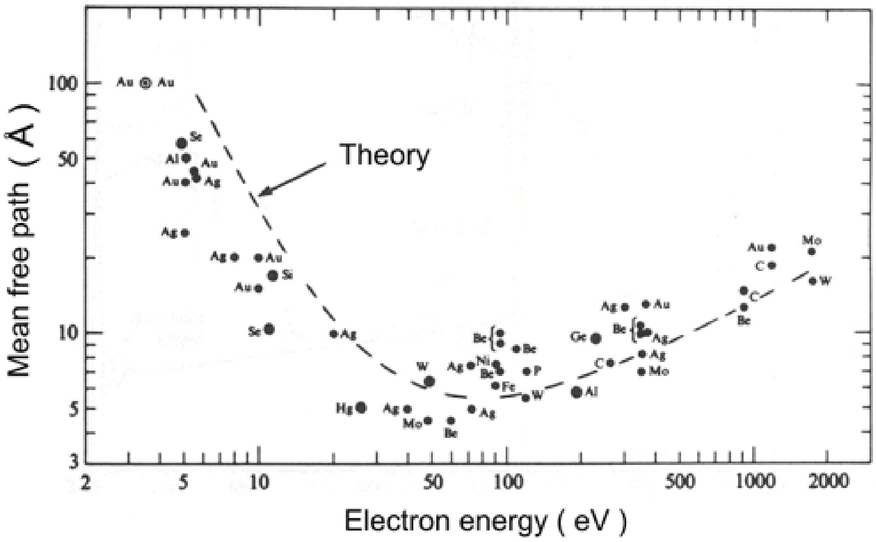

Figure 1.5: Universal plot of photoelectron inelastic mean free path for different elements [Lüth, 2001]

1.3.5 Spectral features

1.3.5.1 Core levels

The elastic photoelectrons come from the inner shells of the atoms or the valence band of the material. Their notation is given by the principal quantum number of the corresponding electron shell, followed by the angular momentum number attributed to the orbitals (s, p, d, f...) and a subscript which denotes the total angular momentum due to the coupling of the angular and spin momenta. For example, a photoelectron denoted $3p_{3/2}$ is an electron coming from the M shell with an angular momentum equal to 2 and a spin down.

Core levels give rise to the most intense and sharpest peaks in a XPS spectrum and their location in binding energy is an intrinsic characteristic of atomic species. Thanks to this elemental specificity, by comparing the peak energies to tabulated values [Naumkin et al., 2012], one can trace back to the chemical composition of the surface. This is exactly why XPS is also known as the Electron Spectroscopy for Chemical Analysis (ESCA).

Additionally, despite the fact that core electrons do not take part in chemical bonds, they do provide an information on the chemical state of the considered species through the analysis of binding energy shifts. Their origin is the change of the electronic density in the atom, thus of the screening of the Coulomb attraction by the nuclei, due to the charge transfer of electrons involved in a chemical bond. It follows that the photoelectron peak shifts to higher binding energies when the atom gets more cationic while it shifts to lower energies when the atom gets more anionic. For transition metals, the chemical shift is up to several eV between the metal and its oxide. In this study, the analysis of the energy shift helped us to identify the chemical state of chromium deposits. As underlined in section 1.3.4, a relative analysis of peak positions was used to overcome the influence of charge effects. In fact, the position of the Cr 2p peak was referenced to the Al 2s peak of the same run before and after oxidation. In the case illustrated in figure 1.6, the apparent chemical shift of 9.2 eV obtained from the difference between absolute positions of Cr 2p peak is obviously impacted by charge effects, while the calculation based on relative positions gives a result of 3.3 eV closer to the chemical shift expected from the literature [Biesinger et al., 2004,Salvi et al., 1995,Sainio et al., 2005,Naumkin et al., 2012].

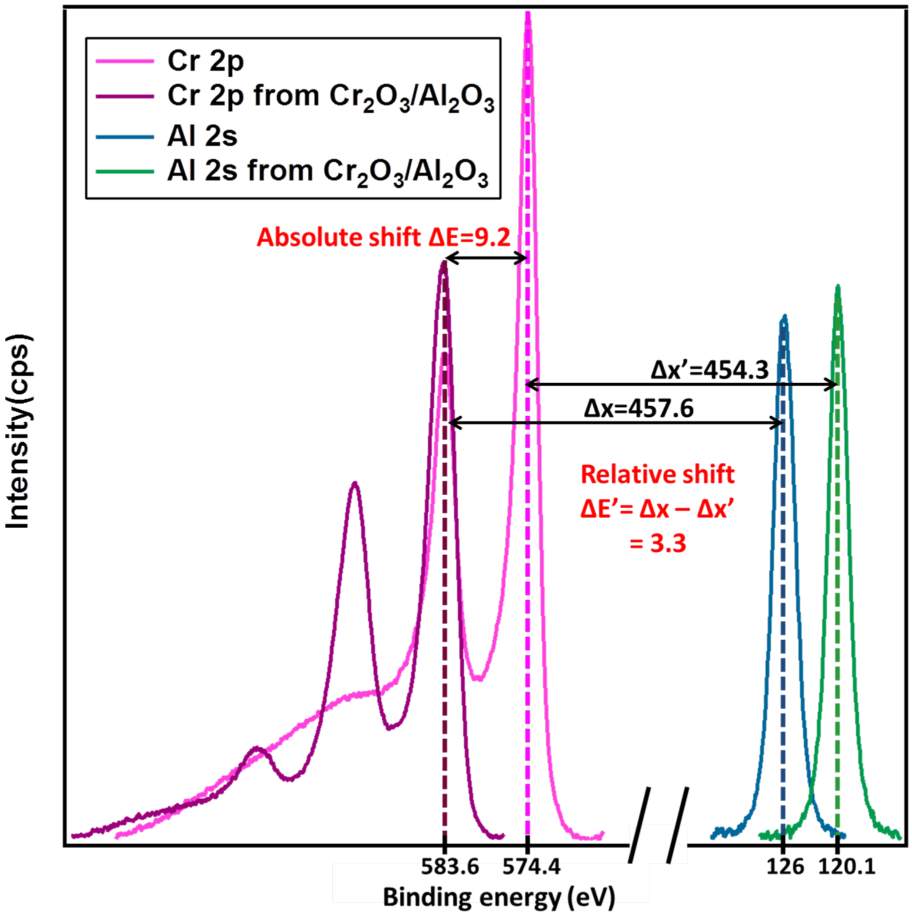

Figure 1.6: Charge effects and binding energies: for a 14.5 Å thick chromium deposit on alumina, the chemical shift between metallic and on-purpose oxidized films is calculated using Al 2s line as a reference to compensate from charge effects.

Another possible way to probe the chemical state is the spin-orbit splitting which changes according to the chemical environment of the atoms (9.3 and 9.7 eV for metallic and oxidized chromium). This splitting is a ground state effect that occurs due to the coupling between the electron spin momentum and its angular momentum when this latter is different from zero. Thus, electrons ejected from core levels with symmetries (p, d, f. . .) give rise to doublet peaks representing doublet core states characterized by j = | L+S |, which defines the state multiplicity, namely 2j+1. The relative area of these doublet pairs are given by $(2(l-\frac{1}{2})+1)/(2(l+\frac{1}{2})+1)$. The ratio is equal to $\frac{1}{2}$, $\frac{2}{3}$, $\frac{3}{4}$ for p, d and f orbitals respectively.

The method of Auger parameter to determine the chemical state of an element and which is free of charge effect will be detailed in section 1.3.5.3.

1.3.5.2 Secondary electrons and background

Secondary electrons are simply excited electrons that underwent inelastic scatterings but still had sufficient energy to overcome the material work function and get detected by the analyzer. These electrons give rise to a continuous background in the XPS spectrum that needs to be accounted for in the quantification and data analysis. Numerous background functionals are encountered in the literature: linear, Shirley and the universal cross-section Tougaard backgrounds. The Shirley background [Shirley, 1972] at a given binding energy (as used in our data fitting) is proportional to the integral of the elastic signal of higher kinetic energy. It is determined iteratively to reach given values well below and well after the considered peak [Briggs and Seah, 1983].

1.3.5.3 Auger peaks

The Auger peaks are broad signatures that extend on a rather large region in binding energy. Unlike the photoluminescence deexcitation process in which after the emission of a core electron, a less tightly-bounded electron fills the core hole by emitting a photon, the Auger process involves the transfer of the deexcited electron energy to another one (*i.e.* the so-called Auger electron) that will be ejected. Figure 1.7 illustrates the difference between the two processes.

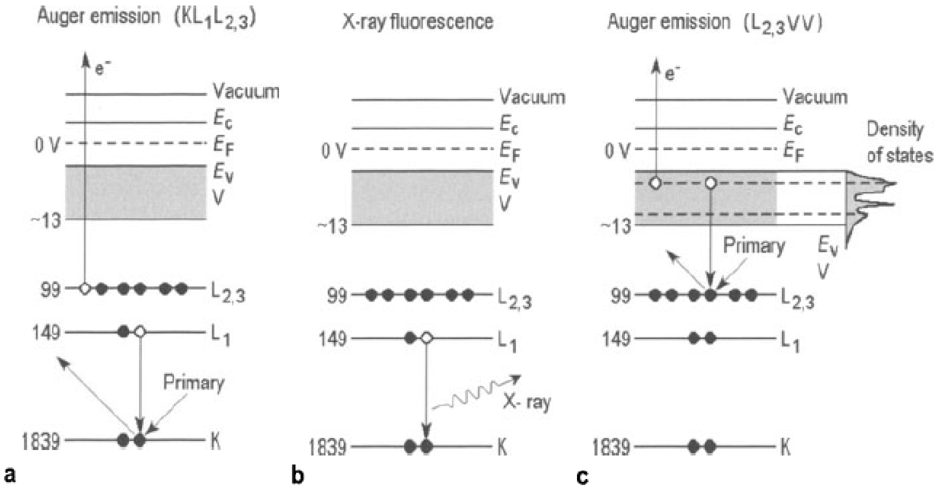

Figure 1.7: Schematic diagrams illustrating the two competing paths for deexcitation process after the emission of a core electron from the K level (the so-called primary electron in the figure): a) KLL Auger emission and b) X-ray fluorescence. c) Schematic diagram for $L_{2,3}VV$ Auger transition which involves two valence electrons (the deexcited one and the Auger electron). (After [Chang, 1971]).

An Auger transition is labeled XYZ, where X designates the inital state from which the photoelectron is ejected, Y the initial state of the transition and Z the state from which the Auger electron was ejected. X, Y and Z letters stand for the shells involved in the process (table 1.1) in the order of occurrence. A suffix may be added to indicate the sub-shell while a letter V denotes a valence electron. When two levels are not resolved experimentally, most commonly with a spin-orbit splitting, a comma is added between the considered subscripts [Vij, 2006]. For instance, the levels $2p_{1/2}$ and $2p_{3/2}$ are denoted L_2 and L_3. Finally, if a hole is filled with an electron from the same shell, the transition is known as a Coster-Kronig one. Table 1.1 summarizes the state notations in the case of photoelectrons and Auger electrons.

The excess of energy remaining after the transition of an electron from the state Y to fill the hole in state X is given to the electron in state Z which is detected by the analyzer with a kinetic energy:

$$E_{K,Auger} = E_{B,X} - E_{B,Y} - E_{B,Z} - \phi_A. \tag{1.7}$$

n	l	j	Spectroscopic state	X-ray suffix	X-ray state
1	0	1/2	1s	1	K
2	0	1/2	2s	1	L_1
2	1	1/2	$2p_{1/2}$	2	L_2
2	1	3/2	$2p_{3/2}$	3	L_3
3	0	1/2	3s	1	M_1
3	1	1/2	$3p_{1/2}$	2	M_2
3	1	3/2	$3p_{3/2}$	3	M_3
3	2	3/2	$3d_{3/2}$	4	M_4
3	2	5/2	$3d_{5/2}$	5	M_5

Table 1.1: Spectroscopic notations

The kinetic energy of an Auger electron is independent from the photon energy, thus from the type of excitation responsible for the creation of the hole in state X. Like photoemission lines, Auger peaks are characteristic of the nature of surface species and their chemical state. It is important to add that the Auger electrons are very sensitive to the oxidation state not only through the energy position but also through the peak profiles. This is particularly true for zinc [Schön, 1973a, Kowalczyk et al., 1973a, Ley et al., 1973, Yin et al., 1974, Fox et al., 1977, Antonides et al., 1977a, Antonides et al., 1977b, Cavallotti, 2014b] (see figure 2.22).

The so-called Auger parameter α which is given by the sum of the considered Auger electron kinetic energy and the binding energy of the photoelectron ejected from state X brings information about the chemical state of an element while being independent from charge effects which cancel out in the sum [Chang, 1971, Oura et al., 2013, Wagner, 1979]. α is roughly given by the double of the extra-atomic relaxation energy of the considered core levels and is therefore quite sensitive to the chemical environment. In the present study, this method was systematically used to verify the chemical state of zinc atoms through the most intense Zn $2p_{3/2}$ peaks for the photoelectron and Zn $L_3M_{4,5}M_{4,5}$ for the Auger transition:

$$\alpha = E_K(\mathrm{Zn}L_3M_{4,5}M_{4,5}) + E_B(\mathrm{Zn}2p_{3/2}). \tag{1.8}$$

The value of α for metallic zinc is typically 2013.9 eV and 2009.8 eV for zinc oxyde [Naumkin et al., 2012].

1.3.5.4 Plasmon Losses

A plasmon loss occurs following the interaction between photoelectrons and collective oscillations of electrons in the bulk. The corresponding loss takes place at an energy $\hbar\omega_b$ where ω_b is the bulk plasmon frequency. Subsequent plasmon losses may also happen resulting in a series of peaks equally seperated by $\hbar\omega_b$ with a decreasing intensity. The excitation of surface plasmon at $\hbar\omega_b/\sqrt{2}$ or localized ones in nanoparticles are possible but can be more difficult to see [O'Connor et al., 2013].

1.3.5.5 Shake-up and shake-off satellites

The photoemission process can leave the atom in an excited final state under two possible forms:

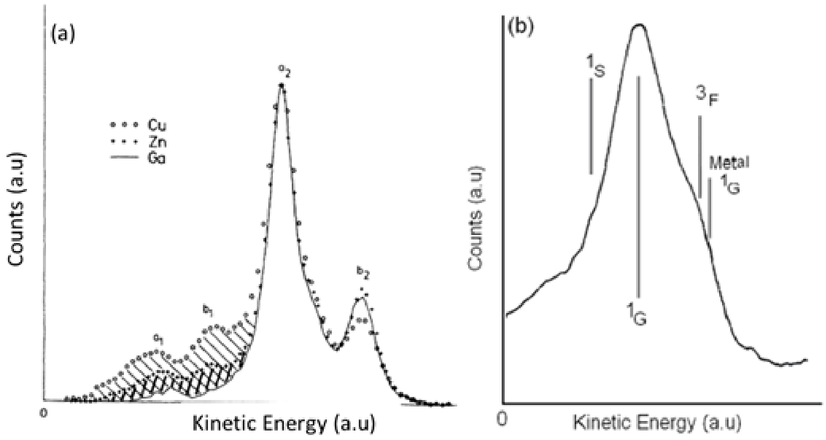

Figure 1.8: Zn $L_3M_{45}M_{45}$ peak shape for metallic zinc (a) (after [Antonides et al., 1977b]) compared to that for ZnO (b)(after [Fox et al., 1977]).

- an electron is in an excited bound state,
- an electron is emitted into the continuum of unbound states above the vacuum level.

Such phenomena leave less energy for the emitted photoelectron which results in the appearance of satellites with lower kinetic energy. The features at hand are referred to as shake-off satellites (excitation to the continuum) and shake-up satellites (excitation to a bound state). In fact, the core ionization is often accompanied by a relaxation of valence electrons to compensate for the positive core hole. On its way out, the departing photoelectron can lose kinetic energy to these relaxing electrons, forcing the system into an excited state (the so-called shake-up process). If some cases, this excitation may result in the ejection of outer-shell electrons from the atom, which is known as the shake-off process [Persson et al., 2001].

1.3.6 Data fitting

The section above tackled the various features in a XPS spectrum. These different contributions make the fitting of core levels not a simple task. Plasmon losses, shake-up and shake-off features, and background should be properly implemented in the fitting process in order to obtain satisfying results. However, one main additional complexity is related to the core level lineshape itself. This is principally linked to the broadening of the peak induced by different effects:

- the X-ray excitation profile,
- the core-hole lifetime and thermal effects,
- surface potential inhomogeneities and surface charging,
- the electron analyzer resolution.

To describe them, a Voigt lineshape defined as the convolution of a Lorentzian $L(E)$ and Gaussian $G(E)$ is often assumed:

$$V(E) = A \int_{-\infty}^{+\infty} L(E')G(E-E')dE', \tag{1.9}$$

where:

$$G(E) = \sqrt{\frac{\ln 2}{\pi}} \frac{1}{\gamma_G} \exp\left[-\frac{E^2 \ln 2}{\gamma_G^2}\right]; \quad L(E) = \frac{1}{\pi\omega_L} \frac{\gamma_L}{(E - E_0)^2 + \gamma_L}. \tag{1.10}$$

$2\gamma_G$ and $2\gamma_L$ are the Full-Widths at Half-Maximum (FWHMs) of the Gaussian and Lorentzian components, E_0 the peak position and A the peak area. The lorentzian contribution accounts for the core-hole lifetime and for the X-ray emission (0.7 eV and 0.85 eV for Mg Kα and Al Kα respectively see section 1.3.8) while the remaining sources of broadening are included in the gaussian profile.

It is worth adding that if the material under investigation is a metal, a large number of excitations from the valence band to the conduction band are possible. In addition to the collective oscillations of the electronic gas (*i.e.* plasmon) already mentioned which appear as intrinsic sidebands, another possible event is the creation of an electron-hole pair, the probability of which obeys an inverse power law of their energy, introducing an asymmetry in the lineshape towards high binding energies [Hüfner, 1995, Hoffman, 2013]. These excitations have been accounted for in the so-called Doniach-Sunjic lineshape [Doniach and Sunjic, 1970]:

$$DS(E, \alpha) = A \frac{\cos\left[\pi\frac{\alpha}{2} + (1 - \alpha)\arctan\left(\frac{E - E_0}{\gamma_{ds}}\right)\right]}{\left[(E - E_0)^2 + \gamma_{ds}^2\right]^{\frac{1-\alpha}{2}}}, \tag{1.11}$$

where α is an asymmetry parameter and γ_{ds} is related to the FWHM. $\alpha = 1$ corresponds to a Lorentzian profile. Of course, a convolution with a Gaussian is necessary to account for the instrumental broadening.

During this thesis, photoemission spectra were fitted through the Levenberg-Marquadt χ^2 minimization with Voigt and Doniach-Sunjic profiles, for oxide and metallic core levels respectively, superimposed to a Shirley background. The Lorentzian FWHM was fixed to 0.7 eV for Mg Kα and 0.85 eV for Al K$alpha$. The area ratio for doublet peaks was slightly varied around the theoretical value given by $(2(l - \frac{1}{2}) + 1)/(2(l + \frac{1}{2}) + 1)$ [CasaXPS,].

1.3.7 Quantification

One of the major advantages of XPS as mentioned before is the ease with which quantitative data can be routinely obtained. Indeed, the analysis of the area under the core level peaks allows an estimation of surface coverage, atomic density and film thickness. For a semi-infinite substrate, the integrated intensity I_s of the signal coming from one of its components is given by:

$$I_s = C\sigma_s T(E_K) n_s \lambda_{ss} \cos\theta, \tag{1.12}$$

with:

- σ_s : the photoionization cross section of the considered core level [Yeh and Lindau, 1985],
- $T(E_K)$: the analyzer transmission function at kinetic energy E_K which is proportional to $1/\sqrt{E_K}$ for a perfect hemispherical analyzer [Ruffieux et al., 2000],
- n_s : the density of atoms,
- λ_{ss} : the inelastic mean free path in the substrate for a photoelectron of energy E_K,

- θ : the emission angle .

C is a prefactor independent of the kinetic energy and linked to the geometry of electron collection [Briggs and Seah, 1983]. To circumvent the difficult measurement of absolute intensity from a reference, one looks only at ratio of areas. For a deposit on a substrate, the strategy of analysis at hand depends on the film geometry and implies the choice of a calculation model to describe the morphology. In the presence of a continuous overlayer of thickness t, on one hand, the substrate intensity I_s (equation 1.12) is damped by a factor $\mathrm{e}^{-t/\lambda_{sa}\cos\theta}$, where λ_{sa} is the inelastic mean free path of substrate photoelectron in the layer. On the other hand, the signal from the film amounts to:

$$I_a = C\sigma_a T(E_a) n_a \lambda_{aa} \cos\theta (1 - e^{-t/\lambda_{aa}\cos\theta}) \tag{1.13}$$

where parameters have meanings similar to the substrate case. Therefore, the ratio

$$\frac{I_s}{I_a} = \frac{n_s}{n_a}\frac{T_s}{T_a}\frac{\sigma_s}{\sigma_a}\frac{\lambda_{ss}}{\lambda_{aa}}\frac{e^{-t/\lambda_{sa}\cos\theta}}{1 - e^{-t/\lambda_{aa}\cos\theta}}, \tag{1.14}$$

can be used to deduced t by dichotomy from the knowledge of all the other parameters. The values of λ were obtained herein from the predictive formula of Tanuma, Powell and Penn [Tanuma et al., 1988, Tanuma et al., 1991a, Tanuma et al., 1991b, Tanuma et al., 1993,Tanuma et al., 1994,Tanuma et al., 1997,Tanuma et al., 2003,Tanuma et al., 2005,Shinotsuka et al., 2015] as implemented in the QUASES-IMFP-TPP2M software [Tougaard,].

In the frame of this study, despite the Volmer-Weber 3D growth, the thickness of Zn and Cr deposits were systematically quantified by using the continuous layer model for two main reasons (i) the lack of knowledge of the actual surface covered by nanoparticles and (ii) the growth of particles with very large aspect ratio as revealed by SDRS. It is vital to note that an additional damping factor of the signal coming from the substrate through the intermediate layer of chromium is added in equation 1.14 for the determination of Zn thickness. Table 1.2 sums up the parameters used in this work to quantify Cr, Zn, Ca, C with respect to Al substrate signal.

Core level	Cross-section (a.u)		Transmission function	Mean free path (Å)				Atomic density (mol.cm^{-3})
	Mg K$_\alpha$	Al K$_\alpha$		Mg K$_\alpha$		Al K$_\alpha$		
				λ_{sa}	λ_{aa}	λ_{sa}	λ_{aa}	
Al 2s	0.015	0.01	7.6	22.5		26.1		0.0775
Cr 2p	0.254	0.1577	9.94	18.2	12.3	21.1	15.4	0.1375
Zn 2p	0.6057	0.3907	12.1	19	6.3	-	-	0.1092
Ca 2p	0.1132	0.068	8.6	38.2	31.8	44.4	38.1	0.1162
C 1s	0.022	0.013	8.3	29.6	26.2	-	-	0.1625

Table 1.2: Parameters used in photoemission quantification (equation 1.14) for Zn, Cr, Ca, C on alumina. λ_{xy} stands for the mean free path at a kinetic energy corresponding to the core-level binding and excitation energies for an electron coming from an element x in a material y. s corresponds to substrate and a to adsorbate. Data are extracted from references [Yeh and Lindau, 1985, Tougaard,]. The atomic densities correspond to the bulk compounds. Transmission function values are given by the supplier of the analyzer.

1.3.8 Experimental details

The XPS setup mounted on the analysis chamber includes (i) a Mg/Al twin anode X-ray source (XR 50) and (ii) a hemispherical electron energy analyzer (PHOIBOS 100) from SPECS. Detection is performed via a delay line detector with 124 channels. The X-rays are produced in the source by bombarding the anode, cooled with water, with high energy electrons (up to 300/400W for Mg/Al respectively at 10 keV). At the exit of the source a thin aluminum foil is placed to protect the sample from stray electrons, contamination and heat coming from the anode. For both target materials Mg and Al, the spectrum is dominated by the unresolved doublet $K_{\alpha 1,2}$ centered at 1486.7 eV and 1253.7 eV for Al and Mg respectively resulting from the $2p_{1/2} \rightarrow 1s$ and $2p_{3/2} \rightarrow 1s$ transition. However, this main emission line is accompanied by (i) satellite peaks coming from lower transition orders and (ii) by the Bremsstrahlung emission produced by electrons decelarating in the target. Table 1.3 gathers the relative intensities of satellite peaks and their position in energy compared to the main ones [Wagner, 1979]. These effects distort the spectra and limit the resolution to 0.7 eV for Mg and 0.85 eV for Al anodes [Hoffman, 2013]. In our study, Mg K_α was systematically used to avoid the overlap between Zn LMM Auger peak and the Cr 2p photoelectron peak.

	$\alpha_{1,2}$	α_3	α_4	α_5	α_6	β
Mg displacement(eV)	0	8.4	10.2	17.5	20	48.5
Mg relative height	100	8	4.1	0.55	0.45	0.5
Al displacement(eV)	0	9.8	11.8	20.1	23.4	69.7
Al relative height	100	6.4	3.2	0.4	0.3	0.55

Table 1.3: Satellite peaks for Al and Mg X-ray sources.

1.4 Electron Diffractions

1.4.1 Low Energy Electron Diffraction (LEED)

LEED is a diffraction technique used to determine the surface crystallographic structure, more precisely in our case to check the reconstruction of alumina surfaces, using a collimated low kinetic energy electron beam (30-200 eV). In this typical energy range, the electrons wavelength given by De Broglie relation $\lambda(\text{Å})= \sqrt{\frac{150}{E(eV)}} \simeq 1-2$ Å) is of the order of the interatomic distances in a solid, satisfying thereby the atomic diffraction conditions. Furthermore, another interest for this technique stems from its surface sensitivity. Since the mean free path of electrons turns out to be minimal at the energy range used for the incident beam (a few atomic layers), most elastic collisions take place in the outermost layers of the sample. Therefore, the probed reciprocal space is made-out of rods normal to the surface, the positions of which are given by the surface reciprocal lattice. Due to multiple scattering effects, the diffracted beam intensity is strongly dependent on the energy.

Experimentally, the electrons extracted from a tungsten cathode filament impinge on the surface at normal incidence and the diffracted beams are collected in the backward direction. The directions of diffraction are given by the intersection of the Ewald sphere and of the surface rods. Before colliding with a fluorescent screen, the backscattered electrons pass through a series of grids. A first grounded grid seperates the space above the sample from the retarded field. It is followed by two inner grids (known as suppressor) polarized to a potential close to that of the cathode with a retarding voltage adjusted for the best spot-to-background contrast. These grids are used to reject the inelastically scattered electrons. After a fourth grounded grid, the elastic electrons previously retarded are re-accelerated to a few keV to cause flurorescence on the screen biased to +5 kV where the diffraction pattern is obtained. Figure.1.9-a illustrates the LEED apparatus [Oura et al., 2013].

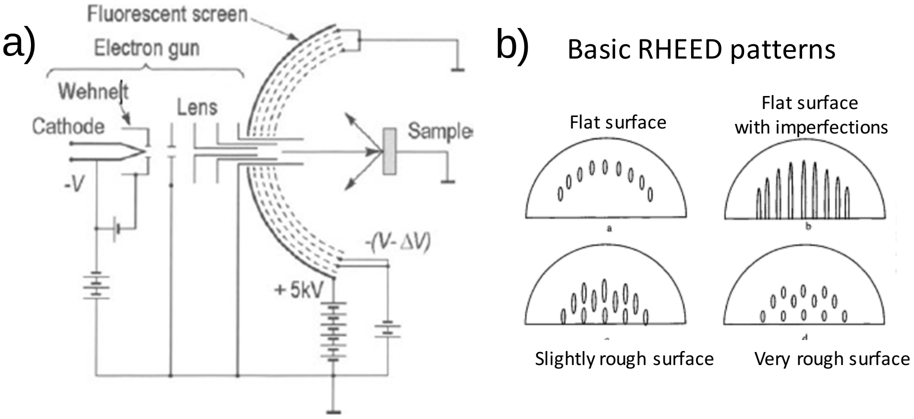

Figure 1.9: a) Scheme of the LEED apparatus with all the elements mentioned in the text. After [Oura et al., 2013]. b) Basic diffraction patterns obtained in RHEED for different surface topographies.

1.4.2 Reflection High Energy Electron Diffraction (RHEED)

Reflection High Energy Electron Diffraction (RHEED) [Ibach, 2006] is a technique often used in the field of thin film growth to monitor the evolution of roughness and strain. It involves electrons that impinge on the surface at grazing incidence (a few degrees) with a kinetic energy from a few to 30 keV which corresponds to a wavelength much smaller than in LEED. The corresponding Ewald sphere is therefore so large that it can be assimilated to its tangent plane; it can intersect (or not) with the diffraction rods characteristic of the surface. Due to higher kinetic energy, electron trajectories are less perturbed and sensitive to the environment. Transmitted diffraction through surface roughness give rise to spotty patterns (see figure 1.9-b). But small diffraction angles require large distance between the sample and the fluorescent screen. Depending on the roughness, the pattern can switch from spotty bulk-like diffraction in transmission to rod-like on a very flat surface. Strain in the growing film can be obtained from the distance between scattering rods.

1.5 Temperature Programmed Desorption (TPD)

Temperature programmed desosorption (or Thermal Desorption Spectroscopy) is a technique in which samples are annealed in an attempt to determine the desorption activation energies of adsorbed species; these latter correspond in a first approximation to the heats of adsorption since this adsorption process frequently does not involve an activation energy [Ibach, 2006].

1.5.1 Experimental setup

Figure 1.10 illustrates the used setup for a TPD experiment. In the UHV chamber, the sample faces a retractable quadrupolar mass spectrometer (QMG 220 from PFEIFFER) enclosed in a differentially pumped quartz tube whose aperture diameter is smaller than the crystal surface. This hole is brought close to the surface (at $\sim$ 1 mm) to avoid the species desorbing from the sample holder and surroundings. The spectrometer is composed of (i) a filament emitting electrons which ionize the desorbing molecules or atoms by bombardment, (ii) a mass analyzer which selects the ions based on the mass over charge ratio by electrostatic deflection, and (iii) a channeltron detector to amplify the signal. It allows measuring partial pressures down to 10^{-14} mbar. The sample holder allows annealing the sample at temperatures up to $\sim$ 1000 K using an heated filament. The temperature is measured by a K-type thermocouple welded on the manipulator in the vicinity of the sample. The temperature is linearly increased using a PID regulator as $T = T_0 + \alpha t$, where α is the heating rate in the range of the K.s^{-1}. As suggested by Redhead [Redhead, 1962], this linearity allows the determination of activation energies, hence the name Temperature Programmed Desorption commonly given to this technique.

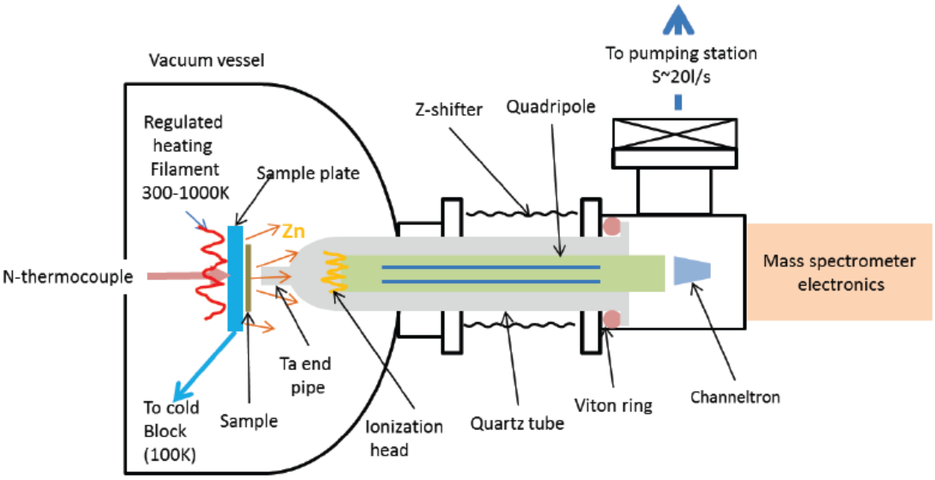

Figure 1.10: Scheme of the TPD apparatus.

1.5.2 Theory

For a given element, the desorption rate per surface unit is given by [Redhead, 1962, King, 1975, Ibach, 2006]:

$$r_d = -\frac{d\Theta}{dt} = \frac{V}{AKT_g}\left(\frac{dP}{dt} + \frac{S}{V}P\right), \tag{1.15}$$

where A is the analyzed surface, Θ is the coverage (proportional to the number of atoms per cm^2), P is the increase in pressure in the quartz tube beyond the residual partial pressure, V the tube volume, S its pumping speed and T_g the gas temperature. If the pumping speed to volume ratio is large and the heating rate α is low, then $dP/dt \ll (S/V)P$ and the desorption rate becomes proportional to the pressure increase P which scales with the detected ion current.

Complex desorption traces consisting of multiple peaks and shoulders were traditionally interpreted in terms of a set of physically and chemically distinct bounded species (example: molecular γ-nitrogen and atomic β-nitrogen on tungsten [Ehrlich, 1961]) each having a different desorption activation energy [Ehrlich, 1961, Redhead, 1962]. Additionally, these multiple peaks were attributed to species desorbing from different crystal planes in the case of polycrystals. However, it was shown for homogeneous single crystals that these complex traces could arise from repulsive lateral interactions between adsorbed species where the entire adsorbed layer is homogeneous at all coverages [King, 1975]. The desorption traces are often analyzed based on the Polanyi-Wigner model based on a quasi-equilibrium between adsorption and desorption. It gives the desorption rate [King, 1975, Ibach, 2006] as function of coverage Θ:

$$r_d = -\frac{d\Theta}{dt} = \nu(\Theta)\Theta^{n(\Theta)} \exp\left[-\frac{E_a(\Theta)}{k_B T}\right], \tag{1.16}$$

with $n(\theta)$ is the desorption order, $\nu(\Theta)$ a rate constant, $E_a(\Theta)$ the desorption activation energy, and k_B the Boltzmann constant. Zero desorption order occurs in the case of autocatalytic reaction like desorption of water from ice, while order one corresponds to direct desorption and order two is often assigned to desorption processes that require the recombination of two adsorbates. More complex situations with fractional order are encountered in the case of desorption from nanoparticles.

1.5.3 Data analysis

Interpretation of TPD is a complex task since the involved parameters (e.g. activation energy, frequency factor and desorption order) depend on the coverage. To overcome this issue, different strategies were developped [Redhead, 1962, King, 1975, Schroeder and Gottfried, 2002]:

- Redhead's desorption peak temperature method,
- heating rate variation method,
- leading edge analysis,
- Arrhenius plot as a function of the order (plots of $\ln\left(\frac{\tilde{r}_{des}}{\tilde{\theta}^n}\right)$ vs 1/T),
- fractional desorption spectroscopy,
- Monte Carlo simulations.

One of the simplest approches is the Redhead method [Redhead, 1962] which relates the activation energy for a first order desorption to the temperature T_{max} at which occurs the desorption peak:

$$E_a = RT_{max}\left[\ln\left(\frac{\nu T_{max}}{\alpha}\right) - \ln\left(\frac{E_a}{RT_{max}}\right)\right], \tag{1.17}$$

where $\ln\left(\frac{E_a}{RT_{max}}\right)$ is small relative to the first term in brackets and estimated to 3.46. The error introduced through this estimate is less then 1.5% for $10^8 < \nu/\alpha < 10^{13}$ K^{-1}. In addition, since this method is employed to extract the activation energy from a single desorption spectrum, it requires to use an approximate value of the order of $\nu = 10^{13}$ s^{-1}. Relying on an approximate value of ν, on $n = 1$ and on the independence of the activation parameters on converage, this approach holds some ambiguities that demand further analysis of the desorption trace lineshape [King, 1975]. The more elaborate leading edge analysis was preferred in our case for the analysis of Zn desorption. It will be detailed later (section 5.3.1).

1.6 Extended X-ray Absorption Fine Structure (EXAFS)

X-ray absorption fine structure is a technique used to determine the local environement around an element absorbing high-energy photons. It is conveniently divided into the XAFS range which extends about 50 eV above an absorption edge, and the near edge structure known as XANES. In an X-ray absorption spectrum, a series of oscillations in the measured absorption coefficient are seen above the absorption edge. These oscillations are the result of the constructive and destructive interferences between the outgoing part of the photoelectron wavefunction and the part of it backscattered by neighboring atoms (see figure 1.11). Due to the electron mean free path which is larger below 50 eV of kinetic energy and minimal in the range between 50 and 100 eV for most materials (see figure 1.5), the EXAFS signal in the absorption spectrum is dominated by short range single scattering events about 50 eV above the absorption edge [O'Connor et al., 2013]. Therefore, EXAFS can be seen as an interferogram of the spatial distribution of the nearest neighbors, and can be analyzed to provide information about bond lengths, bond angles, number and types of neighboring atoms and degree of order. EXAFS typically gives very accurate interatomic distances in particular to the nearest neighbors with ± 0.02 Å accuracy. However the determination of the coordination number is more difficult but can be improved through comparison to a standard compound with a well known structure [O'Connor et al., 2013].

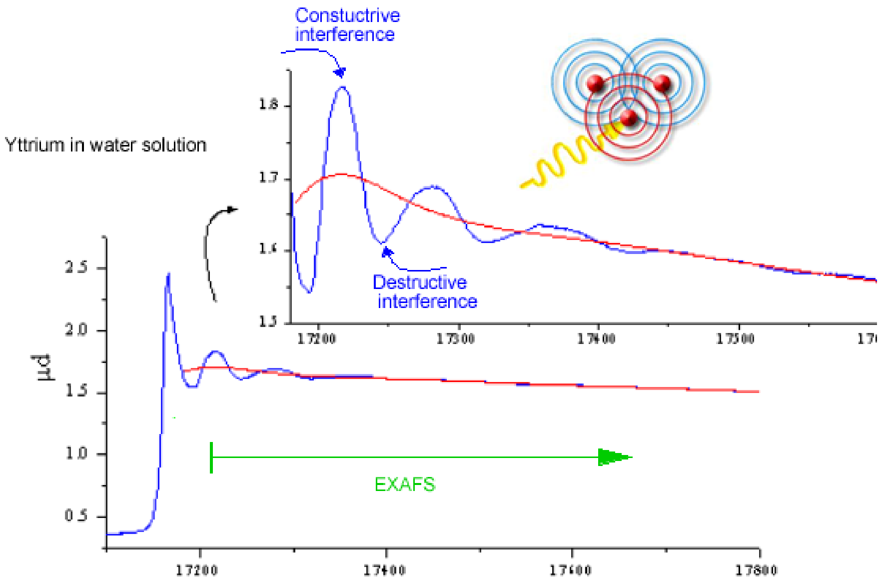

Figure 1.11: A X-ray absorption spectrum with an illustration of the process responsible for the EXAFS signal. The circles in red represent the outgoing part of the photoelectron wavefunction emerging from the absorber while the blue ones represent the backscattered part by the neighboring atoms. The red plain line stands for the smooth absorption background and would correspond to the signal of an isolated atom.

1.6.1 Theoretical background and analysis

Since the scattered electron waves undergo phase shifts at the absorber and the scatterer atom, much of the EXAFS analysis consists in the determination of the phase and the amplitude functions of the involved scattering processes. This can be achieved by dedicated analysis softwares based on multiple scattering calculations [Rehr et al., 2009]. After substraction of the isolated atom absorption coefficient often achieved by a smooth curve fitting (figure 1.11, red curve), the absorption data in energy are thus converted to the Fourier k-space. The oscillations $\chi(k)$ are then fitted by a sum of sinusoidal contributions from many shells [Stern, 1974] where all the atoms in the considered i-th shell are assumed to be identical and located at the same R_i distance from the absorber:

$$\chi(k) = \sum_i \frac{N_i A_i(k)}{k R_i^2} \exp\left(\frac{-2R_i}{\lambda}\right) \exp\left(-2\sigma_i^2 k^2\right) \sin[2kR_i + \phi_i(k)]. \tag{1.18}$$

N_i is the number of atoms in the i-th shell, A_i the scattering amplitude function, k the photo-electron wave vector, λ the magnitude of the electron mean free path, ϕ_i the phase function, and σ_i the Debye-Waller factor which accounts for the thermal and structural disorder. Due to attenuation by the Debye-Waller factor and the mean free path, the inital signal is often k-weighted, generally by k^3, to compensate for the oscillation damping prior to the background subtraction. Without special analysis, the direct back-Fourier transform can yield a radial distribution function $\chi(R)$ with peaks which are directly indicative of the involved interatomic distances [O'Connor et al., 2013] (see model in figure.1.12).

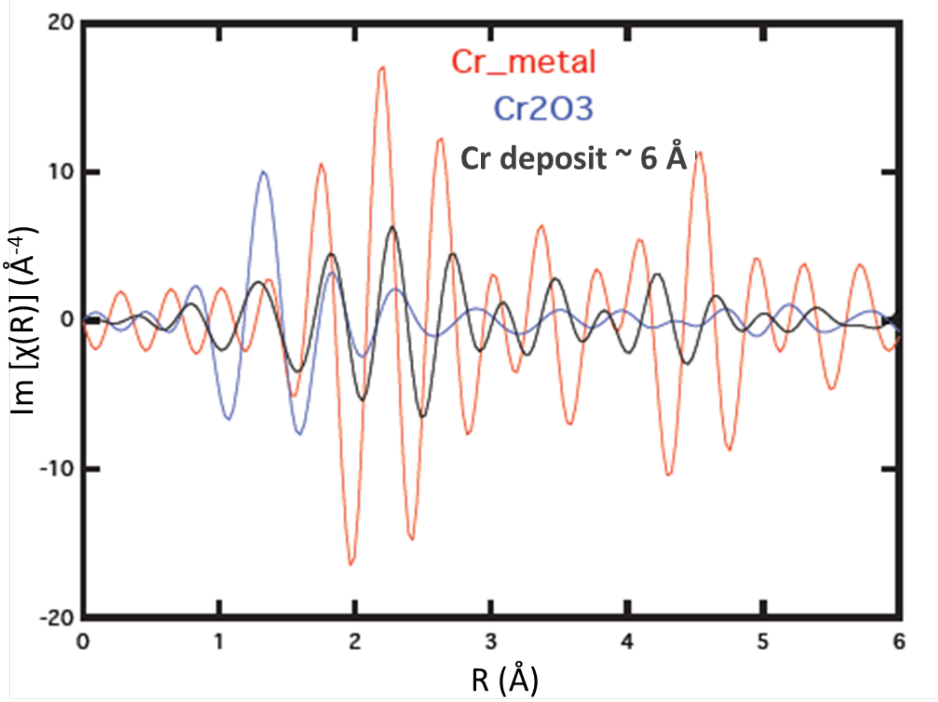

Figure 1.12: EXAFS signal recorded on a Cr deposit of a thickness ∼ 6 Å on alumina compared to measurements of metallic chromium and of Cr_2O_3. The comparison favors an oxidized environment.

1.6.2 Experimental Details

Conceptually, the experiment is simple and consists in measuring the absorption coefficient of the sample in the X-ray regime by tuning the photon energy from the absorption edge of interest to approximately 1 keV above the edge. EXAFS is almost totally a synchrotron based technique to achieve a reasonable signal/noise ratio. Only a few laboratory systems were developed [Udagawa, 1996] that are generally restricted to samples with a high concentration of the absorbant element [O'Connor et al., 2013]. In the frame of this thesis, EXAFS experiments were performed to study the adsorption site of Cr on alumina at the LUCIA beamline of the synchrotron SOLEIL (St Aubin, France). LUCIA is dedicated to the Micro-Fluorescence and the X-ray Absorption Spectroscopy techniques in the energy range 0.8-8 keV. It allows to perform XAS experiments at the K-edge for elements going from sodium to iron included, at L edge for elements between nickel and gadolinium, and at M-edge for rare earth elements and actinides [Flank et al., 2006]. The beam obtained from an undulator HU52 "Apple II" type source is focused and filtered (to remove high order harmonics) as it passes through spherical and planar mirrors respectively. A double crystal monochromator is then used to select a given energy; the beam is finally refocused on the sample using reflection mirrors until a spot of $2.5 \times 2.5\,\mu\text{m}^2$ is obtained in focused experiments. Spectra have been recorded herein in the total electron yield mode by measuring the sample current which is proportional to the absorption coefficient. At the beamline, an UHV setup with a preparation and an analysis chamber is available for surface science experiments (see figure. 1.13). The sample preparation and deposition methods are identical to those used in our laboratory. Auger spectroscopy on a Concentric Mirror Analyzer (CMA) and LEED were used to monitor the state of the substrate after high temperature preparation.

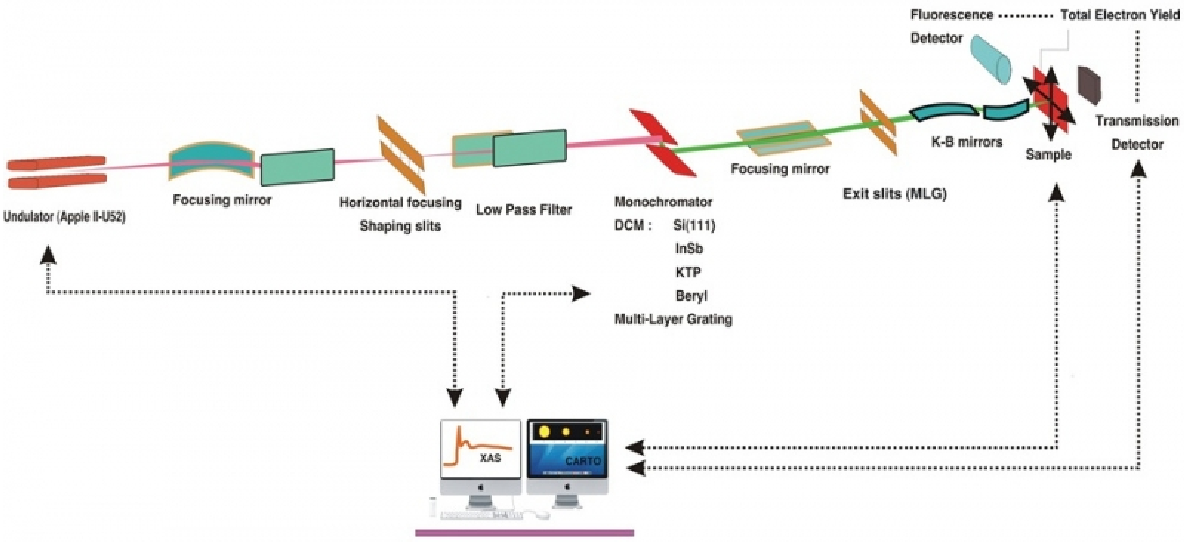

Figure 1.13: The LUCIA beamline with all the components that yield the incident beam into the chamber and the scattered signal to the detectors [https://www.synchrotron-soleil.fr/fr/lignes-de-lumiere/lucia].

1.7 Surface Differential Reflectivity Specroscopy (SDRS)

1.7.1 Principle

Surface Differential Reflectivity Spectroscopy (SDRS) is a non-destructive technique based on the use of UV-visible light to probe growth and morphology of supported metallic nanoparticles. The signal at hand is given by the relative variation of the sample reflectivity during growth:

$$\frac{\Delta R}{R}(\omega, t) = \frac{R(\omega, t) - R(\omega, 0)}{R(\omega, 0)}, \tag{1.19}$$

where $\omega/2\pi$ is the photon frequency, $R(\omega, 0)$ the reflection coefficients of the bare substrate and $R(\omega, t)$ of that covered by a deposit of thickness t. The normalization to the bare substrate signal is used to cancel experimentally, for each value of ω, the unknown response of the optical bench *i.e.* the lamp emission, the transmission of the optics, the monochromator transfer function and the detector response. However, it is of paramount importance to have a stable optical bench all along the measurements to assume these quantities as constants. SDRS proved to be a powerful and sensitive technique to probe *in situ* and in real time the growth of supported metallic nanoparticles (or any adsorbate like organic molecules). SDRS probes the variations of the dielectric behavior of the growing interface. In the case of a metal deposit on an oxide substrate, a sensitivity down to a fraction of a monolayer is easily achieved due to the high contrast between the dielectric constants of the two media and the low absolute reflection coefficient especially in p-polarization near the Brewster angle of the substrate (figure 1.14). It might be worth to remind that p-polarization corresponds to an electric field in the plane of incidence and s-polarization normal to it. During the growth of metallic nanoparticles, the incident light excites collective oscillations of the electronic gas, the so-called localized surface plasmon. Theses oscillations are damped by the imaginary part of the dielectric constant leading to light absorption, which profile depends on the particle shapes, more specifically on their aspect ratios, from where stems the possibility to probe indirectly the wetting at nanoscale. A more theoretical and detailed description of the optical response of supported particles will be given in chapter 3.

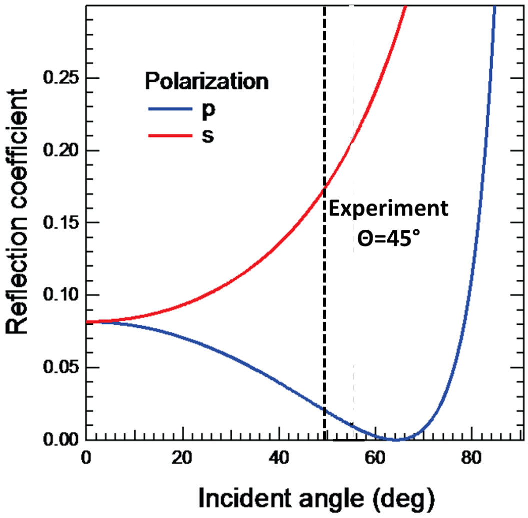

Figure 1.14: Calculated reflection coefficient of alumina in s and p polarization as a function of the incident angle. The angle of incidence imposed by the chamber geometry in our experiments is 45° and is indicated by the dashed line.

1.7.2 Experimental setup

SDRS experiments have been carried out in the preparation chamber during metal deposition process. The used setup (figure 1.15) was specially designed to record simultaneously the s and p polarization states. The source is a deuterium-halogen lamp which covers the UV-near infrared range. The light it emits is guided into a Y-shaped optical fiber. The beam in the first branch, diaphragmed and collected at the entrance of a three-channel spectrometer (from AVANTES company), is used to correct the two other channels for the lamp drift. The beam in the other branch of the fiber is focused on the sample through a transparent silica window. The light reflected on the sample at an angle of $\theta_0 = 45°$ passes through a fused silica condenser and a barium borate Wollaston prism which splits it at an angle of 25° for $\lambda = 600$ nm into two beams corresponding to s and p polarizations. This splitting angle is constant over the considered spectral range, but increases up to 45° below $\lambda \sim 300$ nm which leads to a loss of UV intensity. While s-polarized light allows to probe excitations only parallel to the substrate, the electric field in p-polarization probes both directions through its parallel and perpendicular components. The two resulting beams are then collected by lenses and guided into optical fibers to the free entrances of the spectrometer [Lazzari et al., 2014a] (see figure. 1.15). All optical fibers in the setup are made out of solarized silica in order to keep the UV transmittance. The spectrometer consists in three fixed identical dispersing grating benches with CCD Si-array detectors. The detector response and the optical bench transmission limit the accessible spectral range from 200 to about 900 nm (*i.e.* 1.4-6.2 eV in energy). Because of this wide wavelength bandwidth, high-order diffraction peaks on a given detector pixel are suppressed by the mean of a wedge coating on the detector. The spectral resolution is limited to 5 nm by the entrance slit and the grating groove density. A wavelength-pixel calibration of the spectrometer was performed at the factory and verified using deuterium sharp lines. UV signal is enhanced by the use of Czerny-Turner optical benches through grating blazing, internal lens condenser and special UV coatings.

Despite the low reflectivity of the alumina substrate, the typical integration time is in the range of 10 ms thanks to the high sensitivity of CCD Si detectors. In the case of slow evaporation rate (~ 1 Å.min^{-1}), this allows averaging over hundreds of spectra and acquiring a dozen of actual spectra per minute to follow in real time the growth process. A smoothing over a moving window of 5 pixels over the 1700 active pixels helps enhancing further the statistics without loosing the intrinsic resolution. An overall signal stability of $\Delta R/R \simeq 2 \times 10^{-3}$ is achieved in the wavelength range 300-900 nm after a sufficient thermalization/stabilization time. Bare spectra are corrected from dark signal, source drift and normalized over a reference spectra averaged over one ten of acquisitions before the beginning of evaporation in order to get the actual differential data. All spectra presented in this thesis are normalized to the reflectivity of the bare alumina when successive Cr and Zn depositions are performed.

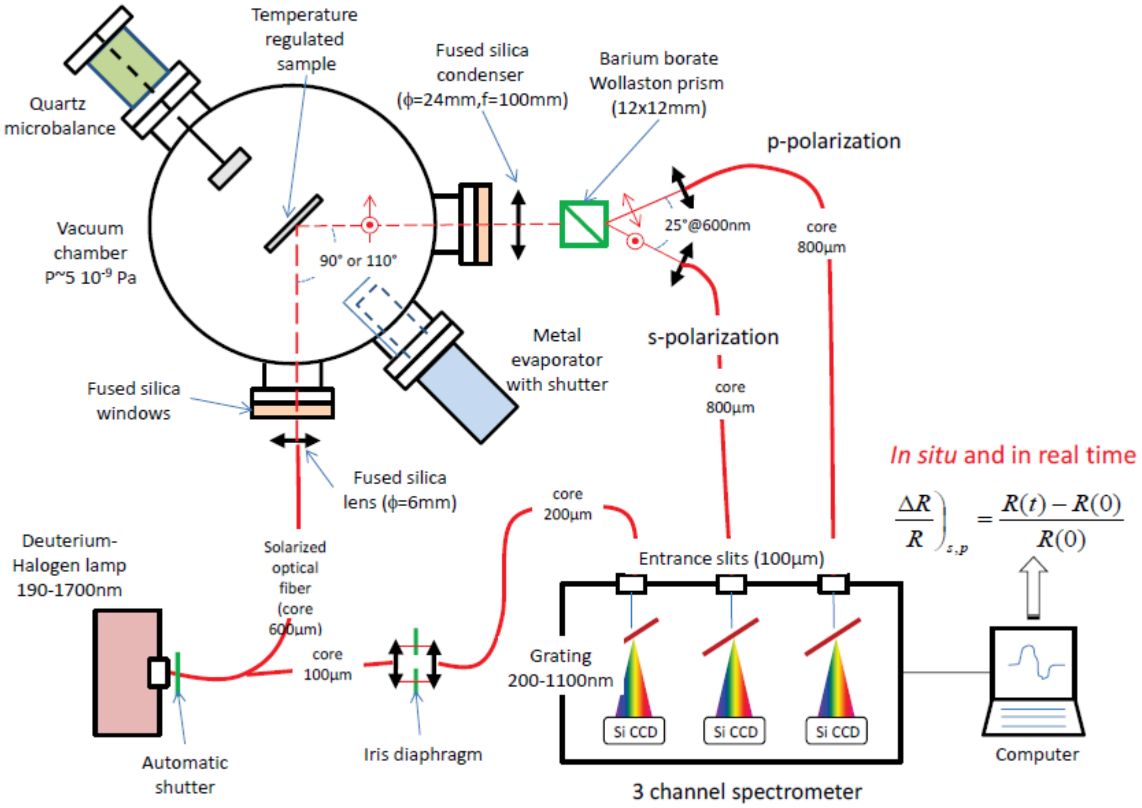

Figure 1.15: Used SDRS setup. The solid red lines represent the optical fibers, while the dashed red lines stand for the light path under vacuum. All optical elements are made of silica to allow a better transmission of UV. After [Lazzari et al., 2014a].

CHAPTER 2

ALUMINA AND ITS INTERFACES WITH METALS: A STATE OF THE ART

The aim of this chapter is to give a brief overview of the literature knowledge on the α-$Al_2O_3(0001)$ surface (section 2.1.2), its reconstructions (section 2.1.3), its thermodynamic stability, its hydroxylation state (section 2.1.4) and its interface with metals (section 2.2). Basics concepts about wetting and adhesion (section 2.2.4.1) will also be reminded. The emphasis will be put on surface science literature.

2.1 Alumina properties: from bulk to surfaces

2.1.1 Bulk alumina polymorphs

Alumina is a material with a large band gap of 8.8 eV as experimentally determined [French, 1990] which results from the weak orbitals overlap and high ionicity of the bonds. Various polymorphs of alumina have been reported ($\alpha, \gamma, \delta, \theta, \kappa, \eta$ and amorphous). They all consist in an oxygen sub-lattice in which the Al cations occupy tetrahedral and/or octahedral distorted sites. The type of oxygen stacking and the differences in occupation probability of these vacancy sites determine the crystal structure. The most common polymorphs and their characteristics are gathered in table 2.1; some of the atomic structures are represented in figure 2.1. Depending on the stacking sequence, three groups of alumina can be distinguished:

- ABAB…stacking: the oxygen sub-lattice has a hexagonal compact (hcp) structure; α-alumina, which is the topic of this thesis, is the most representative of this group;
- ABCABC …stacking: the oxygen sub-lattice has a face centered cubic structure (fcc); γ-alumina is among those;
- Disordered stacking: the oxygen sub-lattice has neither a hcp nor a fcc structure (ex: β-alumina).

The distance between oxygen atoms within the packed hexagonal planes is in the range of 2.75 Å for all the compounds. The distance between O planes is around 2.2 Å while the Al-O distance is distributed between 1.65 and 2 Å.

Alumina phase	Crystal system	Space group	Lattice parameters	Oxygen sublattice	Occupied anionic sites
α-Al_2O_3	Trigonal	$R\bar{3}c$	a = 4.759 Å, c = 12.991 Å	hcp	Octa (100 %)
κ-Al_2O_3	Orthorhombic	$Pna2_1$	a = 4.84 Å, b = 8.33 Å c = 8.95 Å	hcp	Octa (75 %)/Tetra (25 %)
γ-Al_2O_3	Cubic	$Fd\bar{3}m$	a = 7.93 Å	fcc	Octa (63 %)/Tetra (37 %)
θ-Al_2O_3	Monoclinic	C12/m1	a = 5.64 Å, b = 2.92 Å c = 11.83 Å, β = 104°	fcc	Octa/Tetra
δ-Al_2O_3	Tetragonal	-	a = 7.96 Å, c = 11.70 Å	fcc	Octa/Tetra
β-Al_2O_3	Hexagonal	-	a = 5.60 Å, c = 22.5 Å	fcc	Octa/Tetra
α-Al_2O_3	-	-	-	Random	Tetra

Table 2.1: Crystal structures of the most important alumina polymorphs. 'Octa' and 'Tetra' stand for octahedral and tetrahedral sites, respectively.

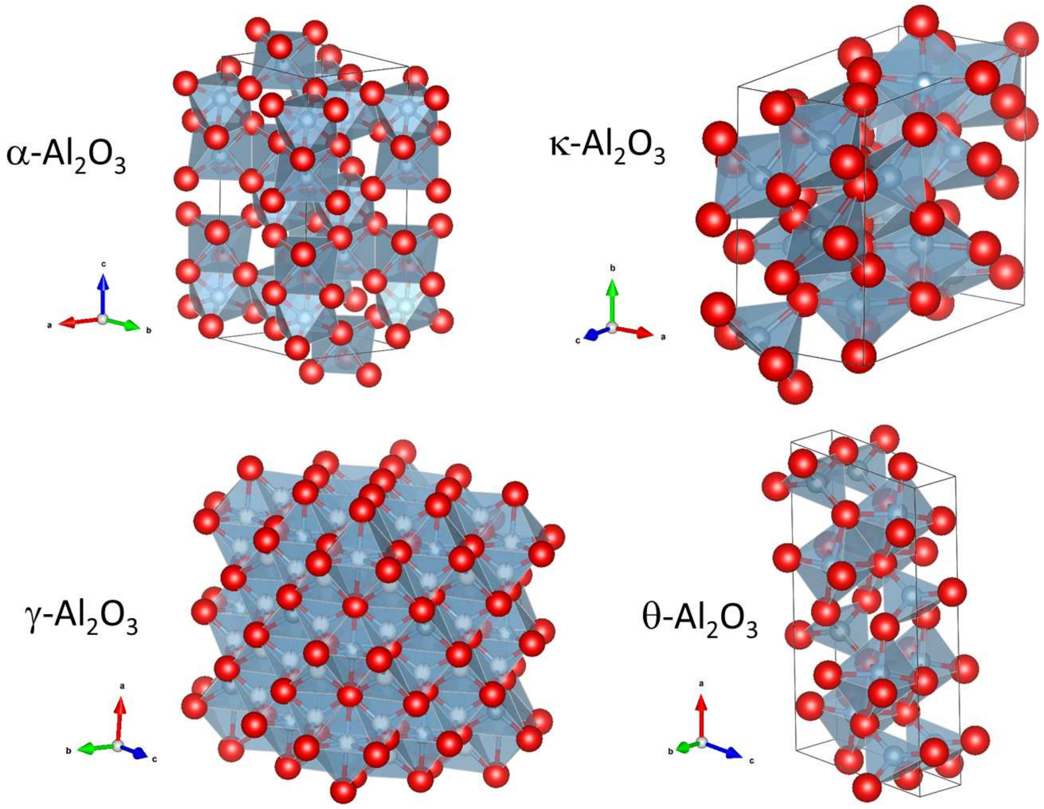

Figure 2.1: Ball models of a few bulk alumina atomic structures showing the coordination polyhedra around cations. Red spheres stand for oxygen anions and blue ones for aluminum cations. Al cations are either surrounded by a distorted octahedron or by a tetrahedron made out of O nearest neighbors. Partial occupancy of sites is not uncommon.

The relative stability of the alumina polymorphs and their transformation sequence is complex and differs upon the precursor nature and the thermal treatment followed [Levin and Brandon, 1998]. Being the most thermodynamically stable phase and available as large single crystals, α-Al_2O_3, known as corundum, is a prototype used for understanding metal oxides. Although being rhombohedral, α-Al_2O_3 (figure 2.2-a) is often described in a hexagonal unit cell ($a = 4.761$ Å, $c = 12.997$ Å, $\alpha = \beta = 90°$, $\gamma = 120°$) containing 18 planes of pure Al or O that stack along the [0001] direction with the sequence O-Al-Al where the distance between Al-Al bilayer planes is 0.485 Å. The distance between successive O planes in the hcp stacking is $c/6 = 2.16$ Å. In this structure, Al atoms occupy only distorted octahedral sites with two Al-O bond lengths (1.86 and 1.96 Å, figure 2.1-a). γ-Al_2O_3 has a defect spinel structure with Al ions distributed between octahedral and tetrahedral sites. θ-Al_2O_3 alumina is closely related to γ-Al_2O_3. Through a slight change of the arrangement of the Al ions in the interstices, the lattice becomes monoclinic instead of cubic. The local geometry of the ion configuration (bond lengths and angles) is the same of that of γ-Al_2O_3. The last alumina to mention is amorphous aluminum oxide a-Al_2O_3. Even if it lacks long-range order, it has a significant short-range order like in glass; it can be described as clusters of oxygen with aluminum in tetrahedral vacancies.

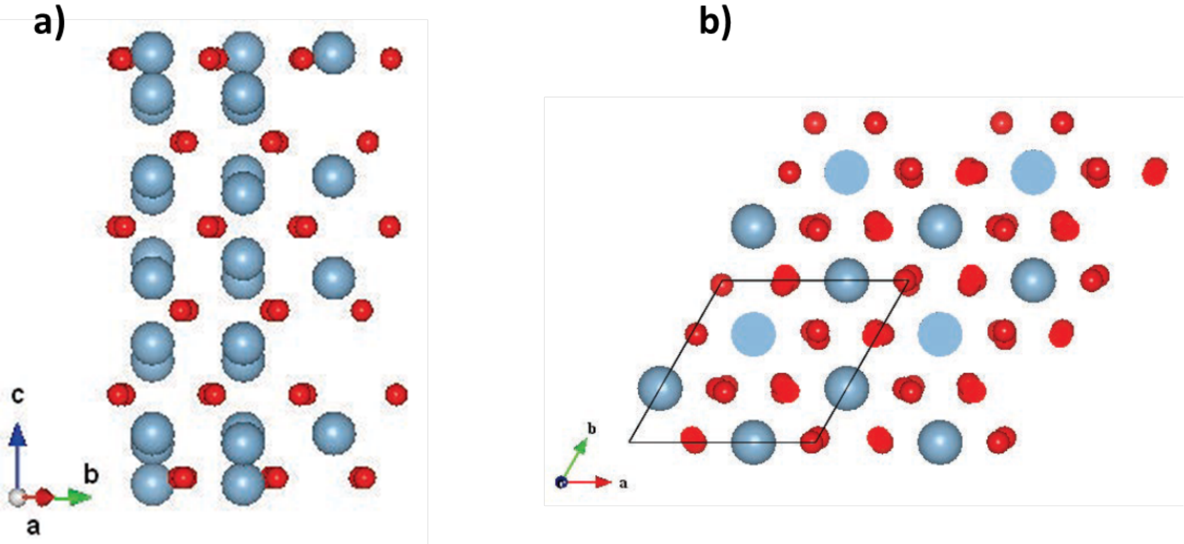

Figure 2.2: Corundum structure of α-Al_2O_3 (aluminum cations are in blue, oxygen anions in red): a) illustration of atoms stacking along the [0001] axis, b) a view of the basal plane (0001); darker colors represent the topmost atoms.

2.1.2 α-Al_2O_3(0001)-(1 × 1) surface

From a surface science point of view, only the various surfaces of the thermodynamically stable α-Al_2O_3 polymorph have been studied in the literature due to the availability of large and good quality single crystals. Studies have been reviewed in references [Renaud, 1998, Kelber, 2007, Woodruff, 2013]. The discussion will be restricted herein to the most stable (0001) orientation. Its (1 × 1) termination was the subject of many experimental [French and Somorjai, 1970, Ahn and Rabalais, 1997, Toofan and Watson, 1998, Suzuki et al., 1999, Soares et al., 2002, Cuccureddu et al., 2010] and theoretical [Causa et al., 1989, Manassidis et al., 1993, Puchin et al., 1997, Wang et al., 2000] studies. One main complexity about the structure of the surface is the possibility of different ideal plane terminations. Due to the stacking sequence along the [0001] direction of the corundum structure, three bulk terminations can be obtained: (i) with a single Al plane (Al/O/Al/…sequence), (ii) with a single O layer (O/Al/Al/…sequence) and (ii) with a Al bilayer (Al/Al/O/…sequence) (see figure 2.3). Through simple electrostatic arguments, only termination (i) with only one Al plane is self-compensated on chemical and polarity points of view [Goniakowski et al., 2007] (*i.e.* without a dipolar moment perpendicular to the surface that increases dramatically the surface energy).

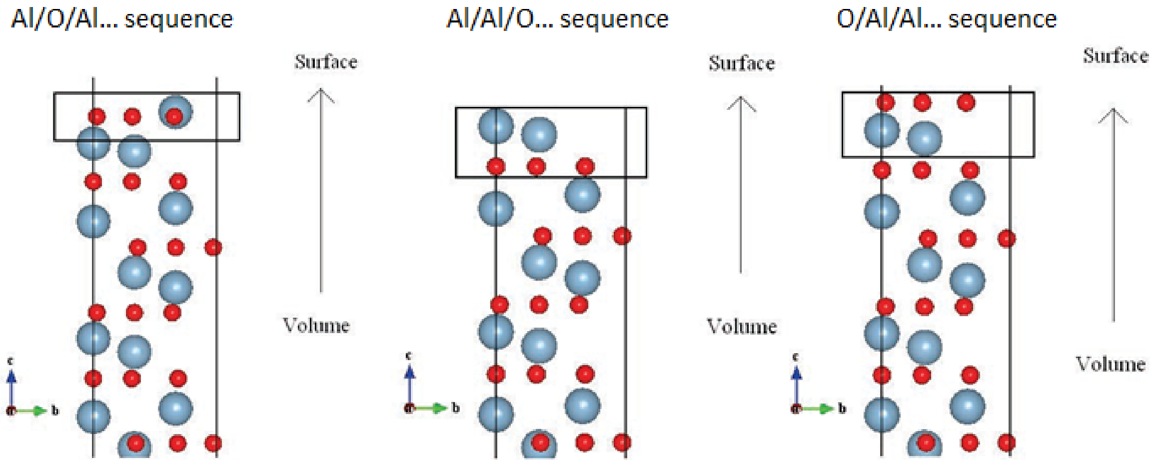

Figure 2.3: Bulk $Al_2O_3(0001)$ terminations: single Al, bilayer Al and O termination from left to right. Red balls stand for oxygen and blue ones for aluminum. After [Cavallotti, 2014a].

Theoretical and experimental studies agree that the (1×1) (0001) surface in oxygen-lean conditions (UHV) is Al terminated with a strong inward relaxation followed by sizable ones in the next planes. Experimentally observed contractions by surface x-ray diffraction and inelastic ion scattering range from 51% [Guénard et al., 1998] to 63 % [Ahn and Rabalais, 1997, Soares et al., 2002], whereas density functional theory based on pseudopotentials predicts a relaxation of $\sim$ 85 % [Manassidis et al., 1993, Wang et al., 2000, Di Felice and Northrup, 1999] and Hartree-Fock calculations give 48 % of the bulk value [Causa et al., 1989, Puchin et al., 1997]. The disagreement on the numerical value between 0 K calculations and room temperature experiments may be explained by the existence of large anharmonic vibrations of the top layer aluminum atoms [Harrison et al., 1999], or by the presence of a static disorder as pointed out by Gloege *et al.* in the case of α-Cr_2O_3 [Gloege et al., 1999]. In addition to these suggestions given for single-species terminations, actual surface termination can potentially be phase-separated, but this possibility was precluded for α-Al_2O_3 since single Al-layer surface has the lowest surface energy over the full range of chemical potentials [Batyrev et al., 1999, Di Felice and Northrup, 1999, Tepesch and Quong, 2000, Wang et al., 2000]. At last, partial hydroxylation may also be at the origin of the numerical discrepancy between calculated and measured relaxations [Ahn and Rabalais, 1997, Wang et al., 2000].

The phase diagram shown in figure 2.4 features the Gibbs free surface energy of all possible terminations of alumina relative to oxygen chemical potential in realistic environmental conditions at 0 K and 1000 K [Wang et al., 2000]. It shows that, for systems containing only aluminum and oxygen, the Al-O_3Al-R corresponding to a single Al atom termination is the

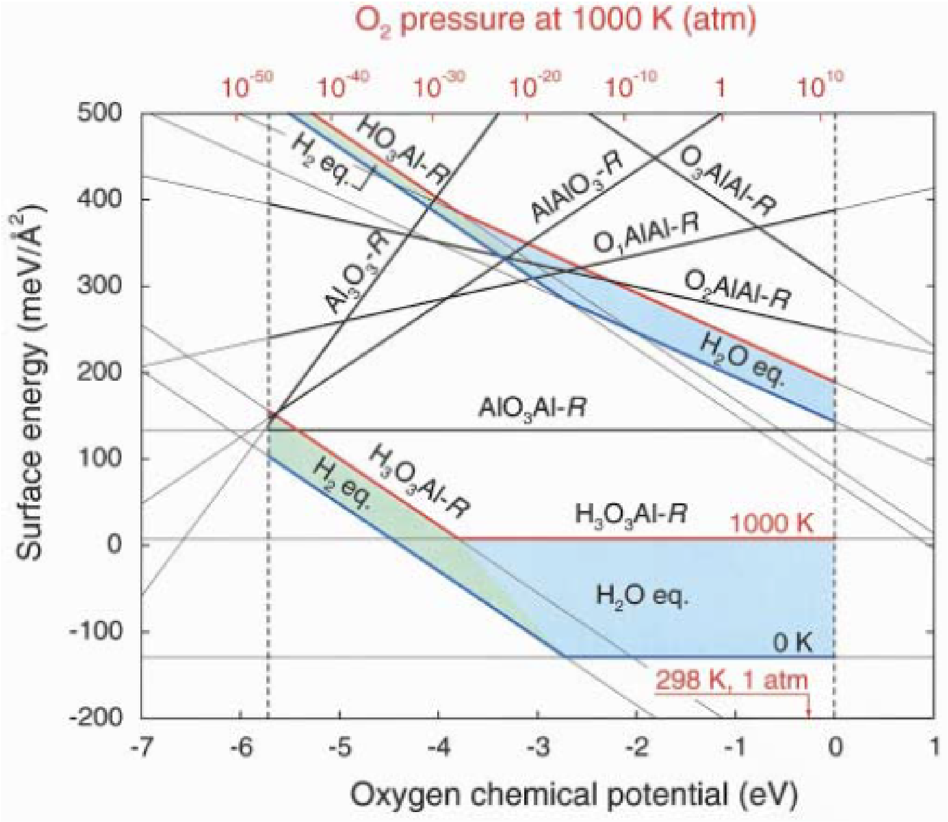

Figure 2.4: Surface energies of different $Al_2O_3(0001)$ surface terminations. The dashed vertical lines indicates the allowed range of the oxygen chemical potential μ_O for bulk stability. Values in red indicate actual examples of temperature and pressure. The green and blue regions indicate the range where hydrogen on the surface is in equilibrium with H_2 and H_2O, respectively, from 0 K up to 1000 K and 1 atm pressure (red lines). After [Wang et al., 2000].

most stable structure across the entire range of oxygen chemical potentials. This stability was explained by an inward relaxation of surface aluminum atoms until they become practically coplanar with the oxygen layer, and a rehybridization to a sp^2 orbital configuration stabilized by autocompensation and bonding considerations. Moreover, changing the position of the topmost Al atoms from their bulk position was seen to dramatically increase the surface energy. In addition, stoichiometric oxygen-terminated alumina with the highest surface dipole was found to be the most unfavorable, while considering one or two oxygen vacancies (O_2AlAl-R and O_1AlAl-R, respectively) led to lower free energies (see figure 2.5). At 1000 K, under the most oxygen-deficient conditions, the metal terminated surface (with two topmost Al layer $AlAlO_3$-R) is revealed to be the lowest energy termination, in perfect agreement with the alumina reconstruction when annealed under UHV at temperatures above 1250 K (see section 2.1.3). At last, it was interestingly demonstrated that adding one hydrogen per unit cell to the oxygen-terminated surface brought a decrease in surface energy and in work function, while the saturation of all surface oxygens resulted in the H_3O_3AlAl-R termination (conf B in figure 2.6), the most stable among all the examined surfaces. Finally, it was surprisingly found that when a hydrogen atom occupies site 1 (figure 2.5) the calculated contraction between the first Al and O layers is ~ 69 % in very good agreement with the experimental value found by Ahn and Rabalais [Ahn and Rabalais, 1997] (configuration A in figure 2.6).

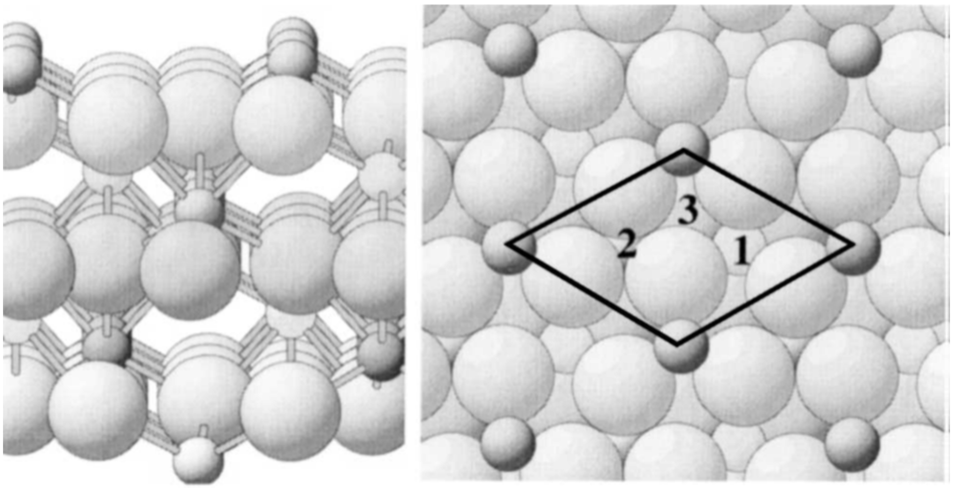

Figure 2.5: Side and top view of the AlO_3Al-R surface of α-Al_2O_3, in which 1, 2, and 3 indicate three sites which could be occupied by the topmost Al instead of the bulk site. The large circles denote O atoms and the small circles denote Al atoms. After [Wang et al., 2000].

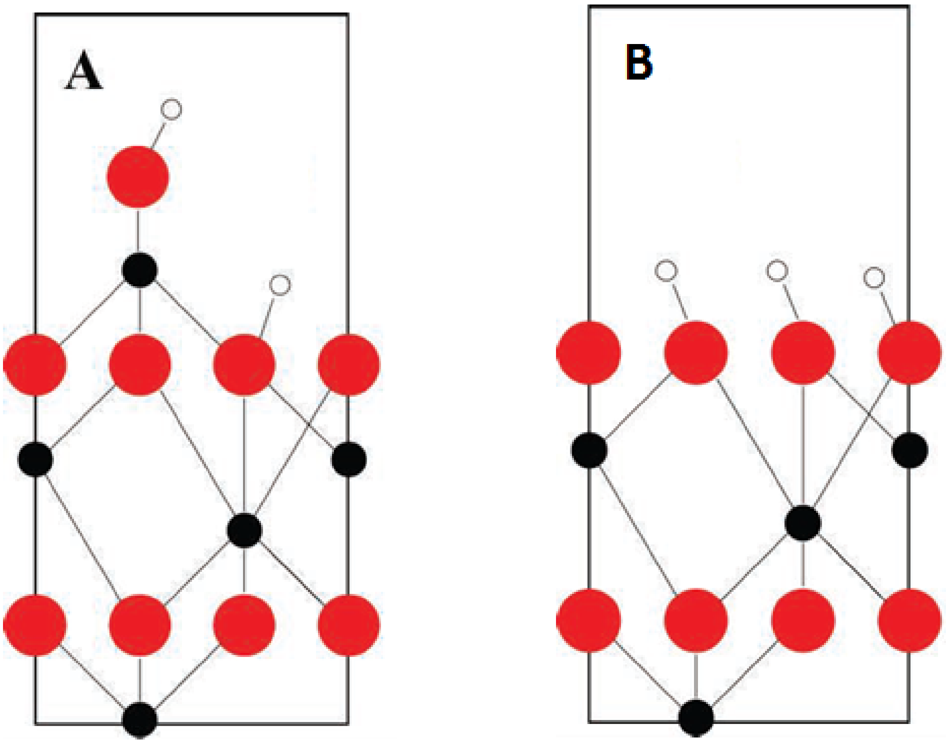

Figure 2.6: Schematic configurations of fully hydroxylated Al (A) and 3O (B) -terminated alumina surfaces (H_2OAlO_3Al-R and H_3O_3AlAl-R respectively) . Red, black and white represent O, Al and H atoms respectively. After [Cavallotti, 2014a].

2.1.3 α-Al_2O_3(0001) surface reconstruction

The (0001) surface of α-Al_2O_3 undergoes a change of surface structure under heat treatment in vacuum. It exhibits a (1 × 1) bulk-like structure up to ∼ 1500 K under oxygen, then rearranges when heated UHV to give rise to a series of O-deficient reconstructions [French and Somorjai, 1970, Gautier et al., 1991b, Gautier et al., 1994, Renaud, 1998]:

$$(1\times 1)\underset{1473\ K}{\longrightarrow}(\sqrt{3}\times\sqrt{3})R30^\circ\longrightarrow(2\sqrt{3}\times 2\sqrt{3})R30^\circ$$
$$\underset{1573\ K}{\longrightarrow}(3\sqrt{3}\times 3\sqrt{3})R30^\circ\underset{1673\ K}{\longrightarrow}(\sqrt{31}\times\sqrt{31})R\pm 9^\circ$$

The so-called Wood notation used above expresses the ratio of lattice parameters and the rotation angle between the reconstructed and (1×1) surface unit cell. Figure 2.7 displays the LEED patterns obtained for a (1×1) and a $(\sqrt{31}\times\sqrt{31})R\pm 9^\circ$ surfaces.

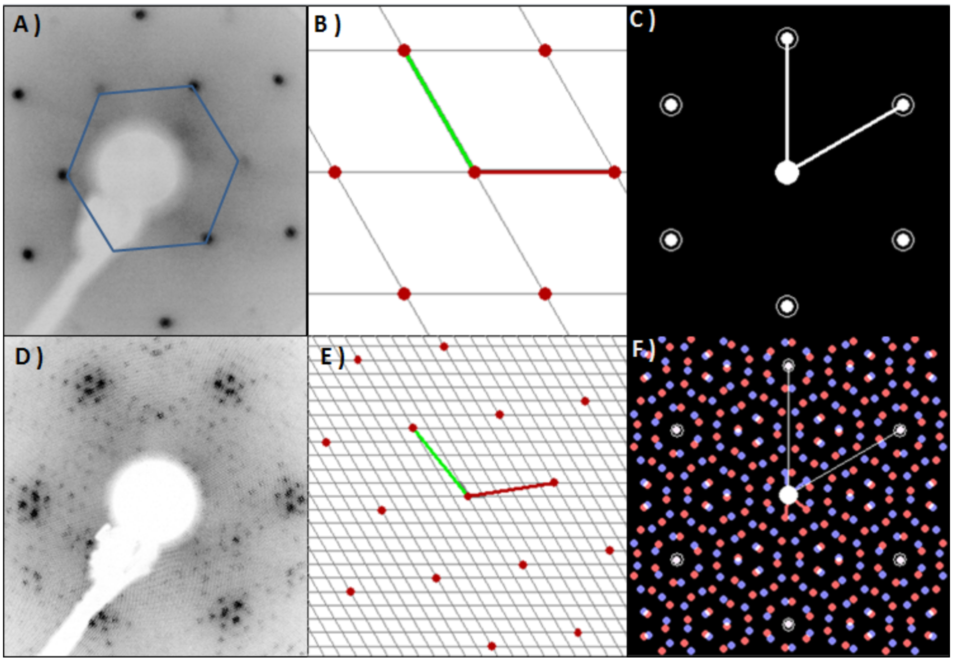

Figure 2.7: LEED patterns obtained in this study for (A) (1×1) and (D) $(\sqrt{31}\times\sqrt{31})R\pm 9^\circ$ surfaces compared to the corresponding simulated diffraction patterns in the direct (B), (E), and reciprocal (C), (F) spaces respectively.

In fact, the atomic and electronic structures of the high-temperature reconstructions puzzled the researchers who investigated them using various experimental surface science techniques and calculation models. French *et al.* concluded from early LEED studies [French and Somorjai, 1970] that a cubic arrangement of Al atoms is formed at the surface, and interpreted the LEED pattern as the result of lattice site coincidence between the rearranged surface and the hexagonal bulk. This interpretation was rejected by Renaud *et al.* [Renaud et al., 1994] who demonstrated based on a very elaborate GIXD (Grazing Incidence X-ray Diffraction) study the presence of two aluminum planes, commensurate with the substrate, with a hexagonal symmetry. They additionally interpreted the reconstruction as a tiling of Al domains separated by domain walls with perfect hexagonal order at the center and disorder at the boundaries which was confirmed by energy-minimization simulations [Vilfan et al., 1997]. The work of Gautier *et al.* [Gautier et al., 1994] (LEED and GIXS) and that of Barth and Reichling [Barth and Reichling, 2001] in which atomically resolved dynamic scanning force microscopy images were obtained, came in good agreement with the proposed hexagonal arrangement and order/disorder domains (see figure 2.8). Barth and Reichling further pointed out the formation of well ordered defects reproducing the rhomboidal structure of the reconstructed surface after their samples were exposed to residual gas at $\sim 5\times 10^{-6}$ mbar, which potentially represented, as they proposed, small $Al(OH)_3$ crystallites (see figure 2.9).

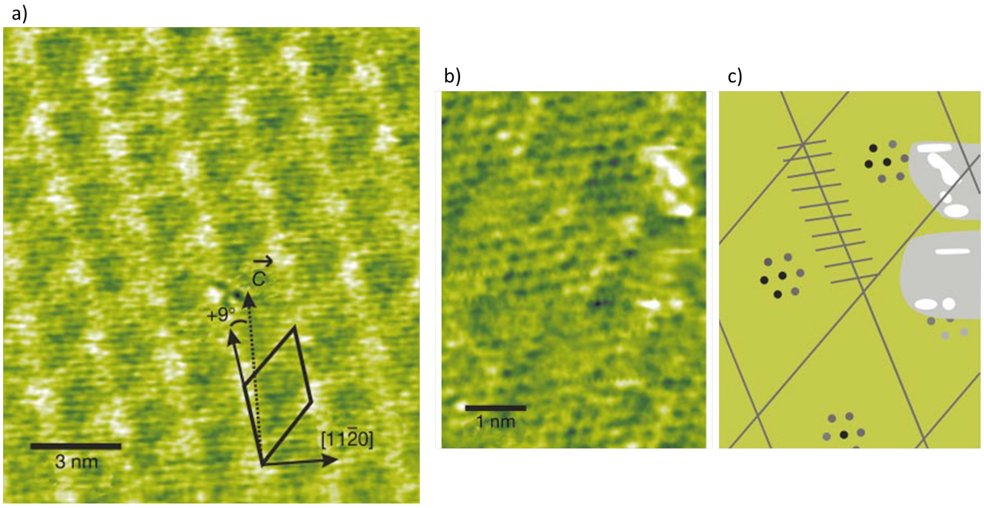

Figure 2.8: a) Structure of the α-$Al_2O_3(0001)$ surface in its $(\sqrt{31} \times \sqrt{31})R \pm 9^\circ$ reconstruction, as imaged by dynamic scanning force microscopy. The reconstruction appears in form of a rhombic grid of protrusions with the highest elevations at the crossing points. The rhombi directly represent the unit cell of the reconstructed surface and are tilted by 9° with respect to the a-axis of the alumina crystal. Stripes in the [11$\bar{2}$0] direction represent rows of aluminum atoms. b) Section of the surface in a) with higher magnification and c) the corresponding schematic representation. Hexagonal order and surface disorder are visible in the center and at the periphery of the rhombi respectively. The grey lines in c) represent the ten atomic rows of intersection between two rhombis. After [Barth and Reichling, 2001].

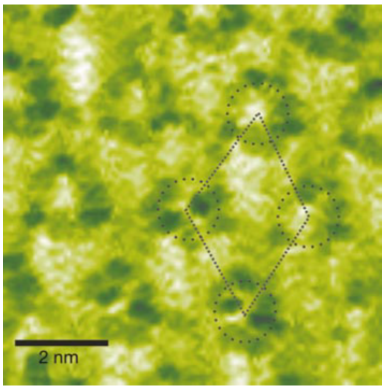

Figure 2.9: The reconstructed α-$Al_2O_3(0001)$ surface after exposure to water and hydrogen originating from the residual gas of the chamber. A substructure in form of rings centered at the points of highest elevation and largest disorder of the reconstructed surface, are formed by up to 8 clusters, representing the hydroxide crystallites (probably $Al(OH)_3$) reproducing the rhomboidal structure of the reconstructed surface. The inversion of contrast compared to figure 2.8 is presumably due to the difference in interaction between the tip and Al_2O_3 and that between the tip and OH clusters. After [Barth and Reichling, 2001].

Concerning the electronic structure, XPS investigation of the valence band, XAS (X-ray Absorption Spectroscopy) at the O_K edge, EELS (Electron Energy Loss Spectroscopy) and self-consistent tight-binding calculations [Gautier et al., 1991b, Gautier et al., 1994] indicate an increase of the covalency, and decrease of the band-gap at the $(\sqrt{31} \times \sqrt{31})R \pm 9^\circ$ α-alumina surface (see figure 2.10). This reconstruction was seen to affect the size of copper clusters evaporated on alumina via EXAFS study of bond length and coordination number [Gota et al., 1995, Gota et al., 1996] where smaller sizes were exhibited on the primitive (1×1) lattice compared to the $(\sqrt{31} \times \sqrt{31})R \pm 9^\circ$ α-alumina.

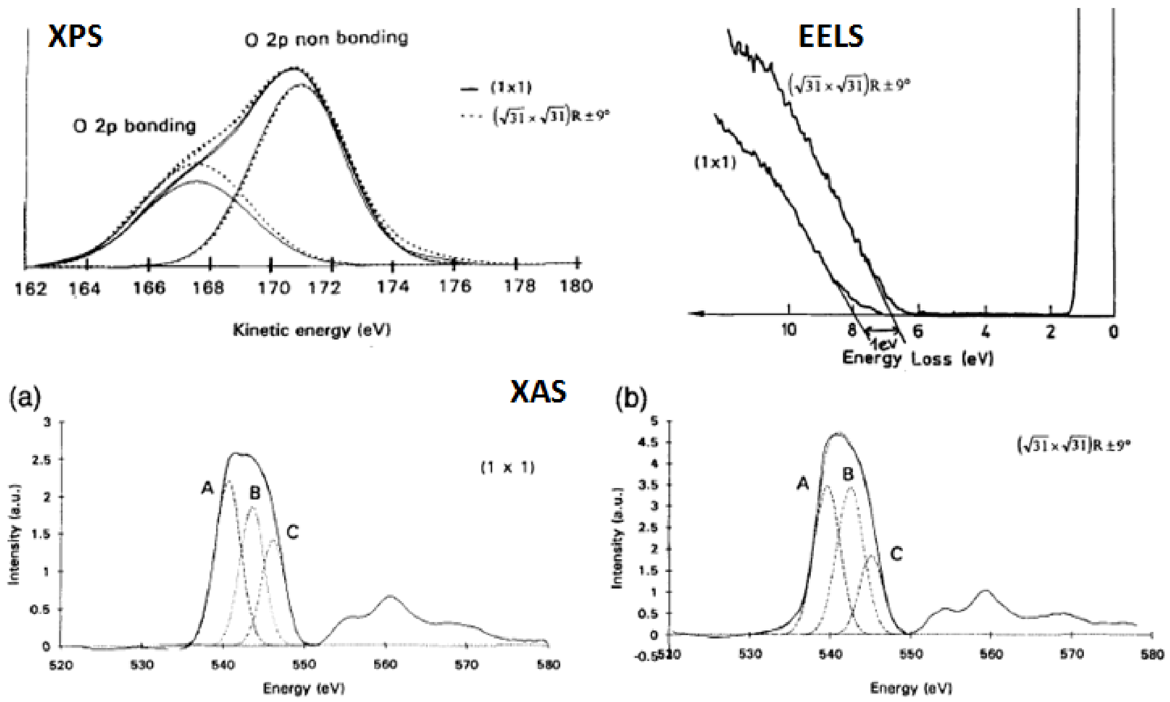

Figure 2.10: Proof of the increase of covalency character in bonding at the reconstructed $(\sqrt{31}\times\sqrt{31})R\pm 9°$ α-alumina surface by: i) XPS: the valence band DOS decomposition shows the intensification of the O 2p bonding orbitals relative to the non-bonding ones on the reconstructed surface, proving more important rehybridization between O 2p and Al 2p, Al 3s orbitals, hence a more pronounced covalent character compared to (1×1) surface. ii) EELS: Band gap width estimated by extrapolating the segment of maximum negative slope to the background level, narrower on the reconstructed surface. iii) XAS at the O K edge (total electron yield). A, B and C correspond to O 2p-Al 3s, O 2p-Al 3p, and O 2p-Al 3d hybridizations. Significant changes in the hybridizations are observed in the O 2p occupied states (valence band) and as well empty states, which indicates a change in the covalency of the Al_2O_3 surface with the reconstruction. After [Gautier et al., 1994].

2.1.4 Surface hydroxylation

The presence of hydroxyl groups at the surface of α-Al_2O_3 constituted a center of interest of many theoretical and experimental studies [Coustet and Jupille, 1997, Nygren et al., 1997, Hass et al., 1998, Di Felice and Northrup, 1999, Eng et al., 2000, Nelson et al., 1998, Elam et al., 1998, Liu et al., 1998, Łodziana et al., 2003] as they drive to a great extend the chemical reactivity of the surface.

The coordinatively unsaturated surface Al ions provide strong Lewis acid sites (electron-acceptor) for H_2O dissociative adsorption. Hydroxyl groups were first experimentally detected on clean α-Al_2O_3(0001) surfaces (i) by Coustet *et al.* through HREELS (High Resolution Energy Electron Loss Spectroscopy) OH vibrational (at 3720 cm^{-1}) and shifted XPS O 1s (1.6±0.2 eV) fingerprints [Coustet and Jupille, 1997] (see figure 2.11), and (ii) by Ahn *et al.* via TOF-SARS (Time-Of-Flight and Recoiling Spectrometry) [Ahn and Rabalais, 1997], (iii) then indirectly evidenced by thermal desorption [Nelson et al., 1998, Elam et al., 1998].

In the work of Ahn and Rabalais, the lack of hydrogen features in the crystal azimuthal angle scan suggested that H atoms reside in sites above the plane of the first-surface layer where they are not shadowed by other atoms. The water dissociation process was eluci-

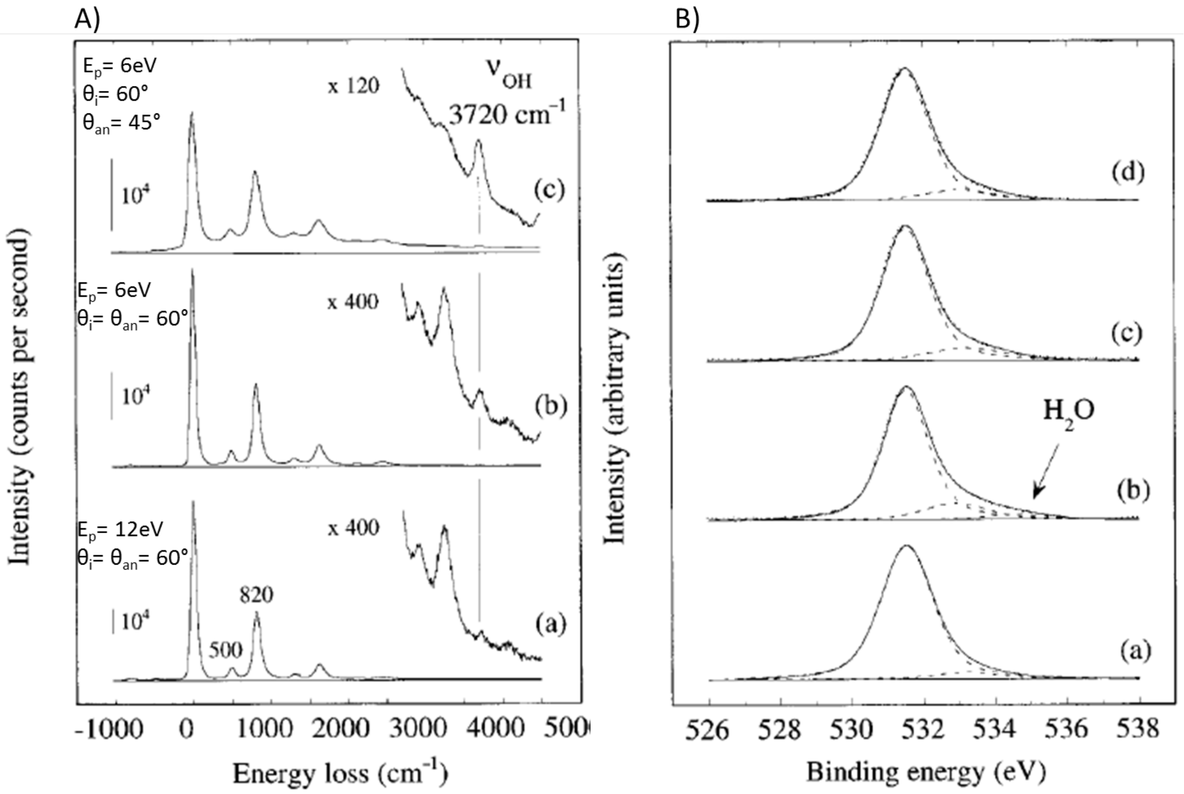

Figure 2.11: Fingerprints of OH groups using a) HREELS and b) XPS on a hydroxylated α-$Al_2O_3(0001)$ surface after an exposure to 0.6 Pa.s of H_2O at 110 K. a) Resonant scattering of the OH stretching mode. b) XPS spectra on a) clean surface; b)c)d) after an exposure to 0.6 Pa.s of H_2O at 110 K. Spectra were recorded at intermadiate temperatures $110 < T(b) < T(c) < T(d) = 300$ K. Two features shifted with respect to bulk at 1.6 ± 0.2 eV and 2.9 ± 0.2 eV, corresponding to OH and molecular H_2O appear after the exposure to water. The latter disappears at temperatures lower than 300 K while the former is always present even on clean surface not exposed to water (a). After [Coustet and Jupille, 1997].

dated in [Elam et al., 1998] where a kinetic model was proposed to explain the evolution of hydroxyl coverage with respect to water pressure and exposure. Additionally, *ab initio* molecular dynamics simulations [Hass et al., 1998] which showed that an optimized geometry of the 1-4 dissociative state (shown in figure 2.12) dominated the dissociation of preadsorbed water molecules. Further observations at high water coverage revealed rapid dissociation and collective effects resulting in water-catalysed dissociation through synchronous proton transfer between a weakly physisorbed H_2O molecule and neighboring hydrogen bond [Hass et al., 1998].

In our study, hydroxylation was performed through exposure of a vacuum annealed surface to a high partial pressure of water (20 mbar). According to [Elam et al., 1998], the temperature, time and pressure values we employed lead to a saturated surface with a hydroxyl coverage $\Theta_{OH} \approx 0.5 \times 10^{15}$ OH groups.cm^{-2}. OH coverage was found to slightly increase with H_2O pressure up to 1.3 mbar then levels off and becomes independent of the pressure. A close correspondance between the OH coverage at saturation and the aluminum atomic concentration at the topmost layers (0.51×10^{15} atoms.cm^{-2}) combined with the dissociative

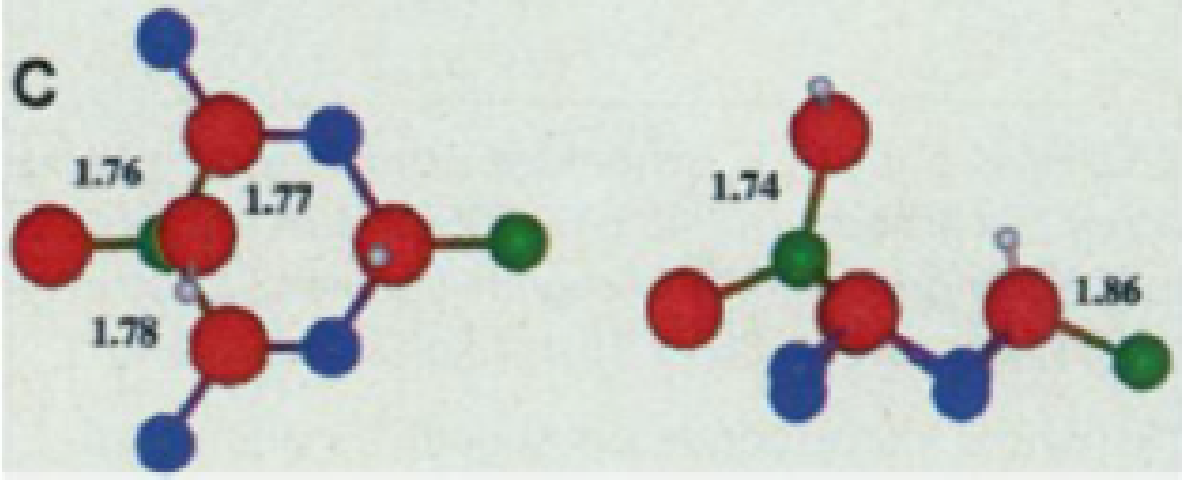

Figure 2.12: Top view (left) and side view (right) of the optimized geometry of 1-4 dissociated H_2O on α-Al_2O_3(0001). In red, blue, green and grey are oxygen, interior Al, top-layer Al, and hydrogen atoms. Bond lengths are expressed in angstroms. The adsorption pulls the Al surface atom that is bound to water oxygen away from the relaxed surface, by 15% of the bulk interlayer spacing. After [Hass et al., 1998].

nature of H_2O adsorption (meaning that one OH group and one H atom binds to one top-layer Al and one O atom from the second layer, respectively) implies that only 50% of the possible adsorption sites are occupied at 300 K [Elam et al., 1998]. The final product after full hydroxylation of the α-Al_2O_3 (1×1) surface from a structural point of view was seen as a gibbssite-like surface structure where Al ions reside approximately in the same plane and have distorted octahedral coordination with a double layer of close-packed OH ions [Eng et al., 2000]. According to first principles investigation, a stable $OH_{||}^{\perp}$(0001)-(1×1) H-terminated surface with 1/3 in-plane and 2/3 out-of-plane OH dimers composition can be formed by dissociative adsorption of H_2O on $Al_{1/3}$(0001) (single Al-terminated surface) surface [Di Felice and Northrup, 1999].

At the opposite, the complete removal of hydroxyl groups upon vacuum annealing remains controversial. It was observed at 700 K, 770 K, and 1000 K in the following works, respectively [Elam et al., 1998, Nelson et al., 1998, Fu et al., 2006, Coustet and Jupille, 1997]. Moreover, density functional calculations showed that, at atmospheric pressure, the surface dehydroxylation starts at around 700 K and a surface free of hydroxyls is obtained at ~ 900 K, while α-Al_2O_3 dehydroxylatation should start at 350 K in UHV [Łodziana et al., 2003]. These theoretical results contradict the presence of hydroxyl groups on the surface even after annealing at 1373 K claimed by Ahn et Rabalais [Ahn and Rabalais, 1997]. Likewise, an additional component in the O 1s core level peak shifted by $\sim 1.6 \pm 0.1$ eV was observed after annealing at the same temperature in UHV, and was attributed to residual surface hydroxyl groups in one case [Lazzari and Jupille, 2002, Lazzari and Jupille, 2005] and to a possible surface relaxation effect in the other [Fu et al., 2006]. The same chemical shift was observed after water adsorption and assigned to hydroxyl groups [Coustet and Jupille, 1997, Liu et al., 1998, Niu et al., 2000, Kelber et al., 2000, Chambers et al., 2002, Lazzari and Jupille, 2002, Lazzari and Jupille, 2005]. It is worth noting that two components shifted by +2 eV and +1.7 eV were detected by Liu *et al.* and were assigned to OH groups adsorbed at defect sites and at terrace sites below a water vapor pressure threshold of 1 torr and above it respectively [Liu et al., 1998]. It was equally shown by Cappus *et al.* that OH formation occurs at both defect and surface sites on Cr_2O_3 while it does exclusively on defect sites for NiO(100) and rather on regular surface sites for NiO(111) [Cappus et al., 1993]. It might be interesting to note that by annealing the surface, hydroxyl groups desorb recombinatively [Nelson et al., 1998].

OH groups were additionally found to be present at the $(\sqrt{31}\times\sqrt{31})R\pm 9^\circ$ reconstructed alumina surface by Dynamic Atomic Force Microscopy [Barth and Reichling, 2001]. Furthermore, the fit of the O 1s XPS peak on alumina surfaces that were recontructed at 1623 K featured an additional component shifted by $\sim 1.3\ eV$ to the higher binding energies. Its assignment to residual surface hydroxyl groups is still open to discussion. Yang *et al.* suggested through the analysis of the zeta potential vs pH curves that OH groups exist on reconstructed surfaces of alumina but are of an altered nature [Yang et al., 2010].

Finally, hydroxyl groups were seen to react with adsorbed metals affecting by that their growth and their chemical state (see section 2.2) [Libuda et al., 1997, Niu et al., 2000, Pang et al., 2000, Kelber et al., 2000, Chambers et al., 2002, Lazzari and Jupille, 2002, Lazzari and Jupille, 2005, Cavallotti et al., 2014, Cavallotti et al., 2016, Le et al., 2017b]

2.2 Metals on alumina: a review

A considerable interest was devoted to the study of metal layers on oxide substrates, either in the context of catalytic activity of metal clusters [Campbell, 1997, Henry, 1998] or, as done in this thesis, in the fields of wetting and adhesion tackled in the context of thin films, soldering or welding. The underlying questions of structure, physics and chemistry of metal/oxide contact are countless. Therefore, this paragraph reviews only the problems risen by metals on α-alumina surfaces. The purpose is to cover the large span of questions tackled in the literature in order to understand the growth of our Cr and Zn deposits from the submonolayer regime to thick films.

2.2.1 Chemical states

The interfacial chemistry between the deposited metal and the oxide substrate beneath is quite important to explore since it has a substantial influence on wetting, adhesion and structural properties. Depending on the electronegativity of the metal, an initial formation of an oxidized metal species in the submonolayer range followed by the growth of metallic clusters at higher coverages is generally seen. In the case of stoichiometric α-alumina surfaces, this was proven to be true for cobalt [Chambers et al., 2002], rhodium [Libuda et al., 1997], titanium [Scheu et al., 1996, Bernath et al., 1998, Lazzari and Jupille, 2002, Lazzari and Jupille, 2005], aluminum [Lazzari and Jupille, 2002, Lazzari and Jupille, 2005] but unlikely for silver [Campbell, 1997, Lazzari and Jupille, 2012] while copper [Scheu et al., 1996, Kelber et al., 2000, Niu et al., 2000, Gota et al., 1995, Gota et al., 1996, Gautier et al., 1991b, Gautier et al., 1992] is borderline. The role of hydroxyl groups was put forward in this context.

In contradiction to [Scheu et al., 1996, Kelber et al., 2000, Niu et al., 2000], the absence of Cu-O bonds was evidenced in EXAFS and XANES studies [Gota et al., 1995, Gota et al., 1996]. The XANES spectra for 0.3 and 0.6 monolayer (ML) of Cu deposited onto a stoichiometric α-$Al_2O_3(0001)$ exhibiting a (1×1) LEED pattern closely resembled that of metallic copper (see figure 2.13). Even when comparing Cu deposit on reduced (by ion bombardment) and oxidized (ion bombardment followed by annealing under oxygen) alumina, no signature of possible Cu-O bonds was detected (figure 2.14).

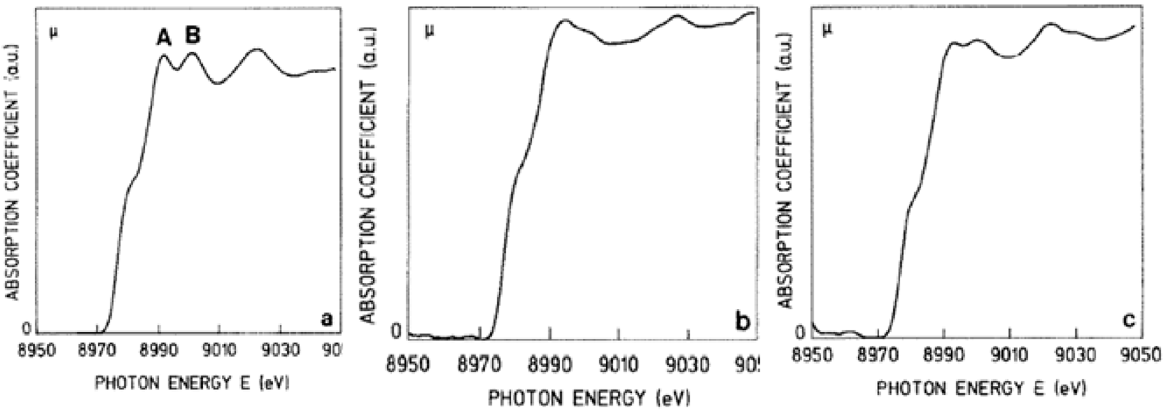

Figure 2.13: Cu K adsorption edge (XANES spectrum) obtained for a) metallic copper (total electron yield detection), b) 0.3 ML of copper on stoichiometric α-Al_2O_3 (0001) (Cu Kα fluorescence yield detection), c) 0.60 ML of copper on stoichiometric α-Al_2O_3 (0001) (total electron yield detection). After [Gautier et al., 1991a].

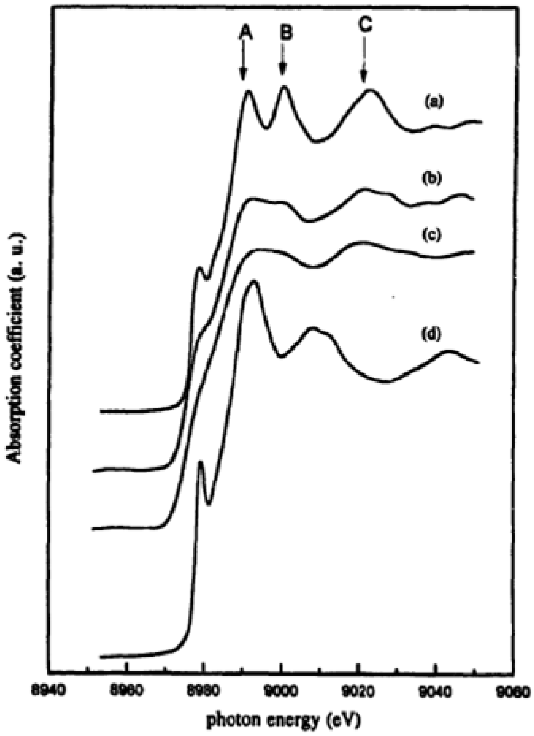

Figure 2.14: Comparison between the normalised Cu K edge absorption spectra (XANES region) of a) a metallic copper foil, b) 0.8 ML of copper deposited on a reduced $Al_2O_3(0001)$ surface, c) 0.80 ML of copper deposited on an oxidized $Al_2O_3(0001)$ surface and d) Cu_2O. After [Gota et al., 1996].

However, in two of their previous publications, Gautier *et al.* [Gautier et al., 1991a, Gautier et al., 1992] stated that an evolution of the Auger parameter, calculated from the Cu $L_{23}M_{45}M_{45}$ Auger and Cu $2p_{3/2}$ core level peaks, showed a continuous increase from Cu(I) to Cu(0). A metallic parameter was obtained for an equivalent thickness of 2 and 0.5 ML on the (1×1) and $(\sqrt{31} \times \sqrt{31})R \pm 9°$ surfaces respectively (see figure 2.15). This could be explained by the fact that, in the initial stages of growth, copper tends to oxidize and metallic clusters start to form at a certain thickness threshold. However, the results in these works were interpreted by a final state effect due to the difference in the cluster size, with a larger size on reduced (*i.e.* reconstructed) alumina in consistency with the metallic state of Cu revealed by XANES and EXAFS in the same study.

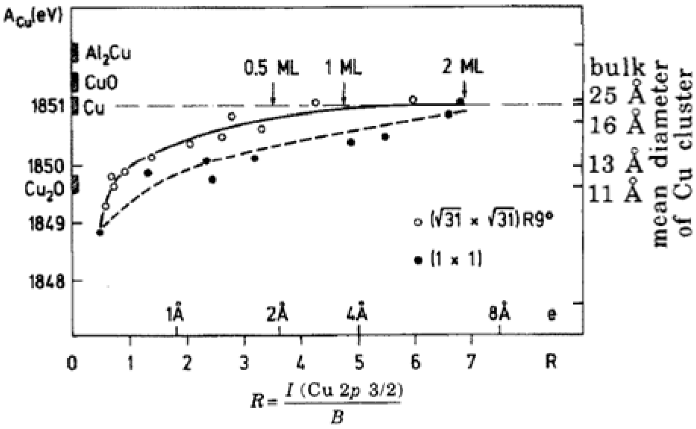

Figure 2.15: Evolution of the Cu Auger parameter A_{Cu} as a function of the number of copper atoms at the surface, monitored by the ratio of the intensity of the photoelectron line Cu $2p_{3/2}$ to the background level (B). The equivalent thicknesses deposited on the quartz microbalance are indicated. After [Gautier et al., 1991a, Gautier et al., 1992].

On the other hand, the works of Kelber and Niu [Kelber et al., 2000, Niu et al., 2000] agreed upon the formation of initially oxidized copper Cu(I) up to ∼ 0.35 ML when deposited on hydroxylated sapphire as demonstrated by XPS (see figure 2.16) and first-principles calculations. An older ELNES (Energy-Loss Near Edge Structure) investigation of Cu and Ti

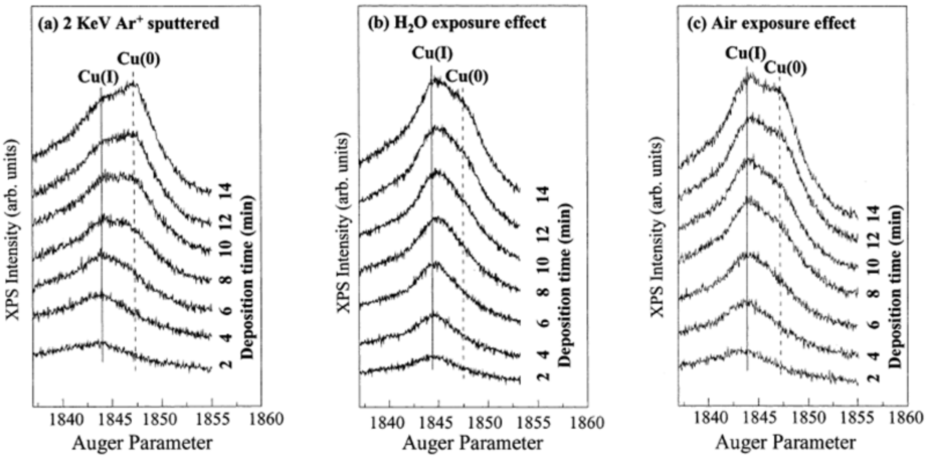

Figure 2.16: Cu(LMM) evolution during Cu deposition with a deposition rate of 0.03 ML Cu.min^{-1} on a) a dehydroxylated by 2 keV Ar^{+} sputtering for 30 min; b) dehydroxylated then exposed to 2 torr water vapor; c) dehydroxylated then exposed to air. Increase of surface hydroxylation promotes Cu(I) formation. After [Niu et al., 2000].

growth on (0001) α-Al_2O_3 at the O-K, Al-$L_{2,3}$, Cu-$M_{2,3}$ and Ti-$L_{2,3}$ edges indicated likewise the presence of Cu(I) and an unprecised oxidation state of titanium at the interface, but related these observations to a bonding between the metals and the oxygen sublattice of alumina without altering the aluminum coordination [Scheu et al., 1996]. Based on the finding of Ahn and Rabalais [Ahn and Rabalais, 1997] concerning the lack of a (1×1) alumina surface free of hydroxyl groups even by annealing at 1400 K, residual hydroxyl groups should be considered as potential nucleation sites for metals [Ertl and Freund, 1999, Libuda et al., 1997, Heemeier et al., 2000, Bogicevic and Jennison, 1999], and could explain the oxidation of the latter at the submonolayer range. It is worth noting that, according to Kelber *et al.* [Kelber et al., 2000], 0.47 ML of initial surface OH and ∼0.35 ML of Cu(I) adlayers were found, both calculated relatively to oxygen. The closeness of those values supports the interaction between the metal and the OH groups.

The situation for the reactivity of transition metals on alumina is clearer. Moving to Rh on hydroxylated Al_2O_3 films grown on NiAl(110) [Libuda et al., 1997], the fits of Al 2p, O ls and Rh 3d core levels point to a direct chemical interaction between the metal deposit and the surface hydroxyl groups. Consumption of the hydroxyl groups was directly monitored via the disappearance of characteristic features in the photoelectron spectra (figure 2.17).

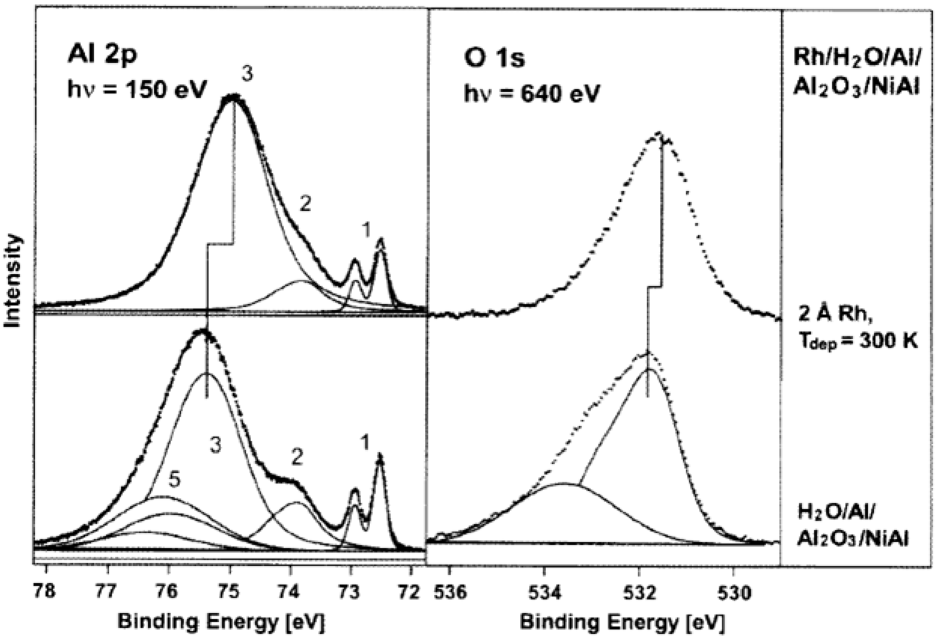

Figure 2.17: A1 2p and O ls photoelectron spectra ($\theta = 0°$) for the modified alumina film before and after deposition of 2 Å Rh (for simplicity, only the sums of the spin orbit split peaks are shown for components 1-3). After [Libuda et al., 1997].

Moreover, the comparison of the grazing-emission O 1s photoemission peak before and after a deposit of 0.8 ML of Co on a fully hydroxylated (1×1) α-$Al_2O_3(0001)$ shows a clear reduction in the intensity of the OH component corresponding to the removal of ∼ 0.4 ML of OH [Chambers et al., 2002]. In parallel, a spectral evidence for the oxidation of cobalt to a Co^{2+} state was given through the analysis of the Co 2p peak after a deposition of 0.3 and 0.8 ML (see figure 2.18). However, the superposition of Co 2p with the Co $L_2M_{23}M_{45}$ complicated the quantitative separation of the Co(0) and Co(II) contributions. It was additionally observed that the Co(0) peak at both coverages is much broader than that measured for metallic bulk Co suggesting inequivalent bonding positions for the former. DFT calculations performed in the frame of the same study implied the requirement of adjacent surface OH and a metal atom that can overcome the relevant barrier of the redox reaction. It equally proposed that Co(II) are generated directly upon impact on top of the O-site and react near

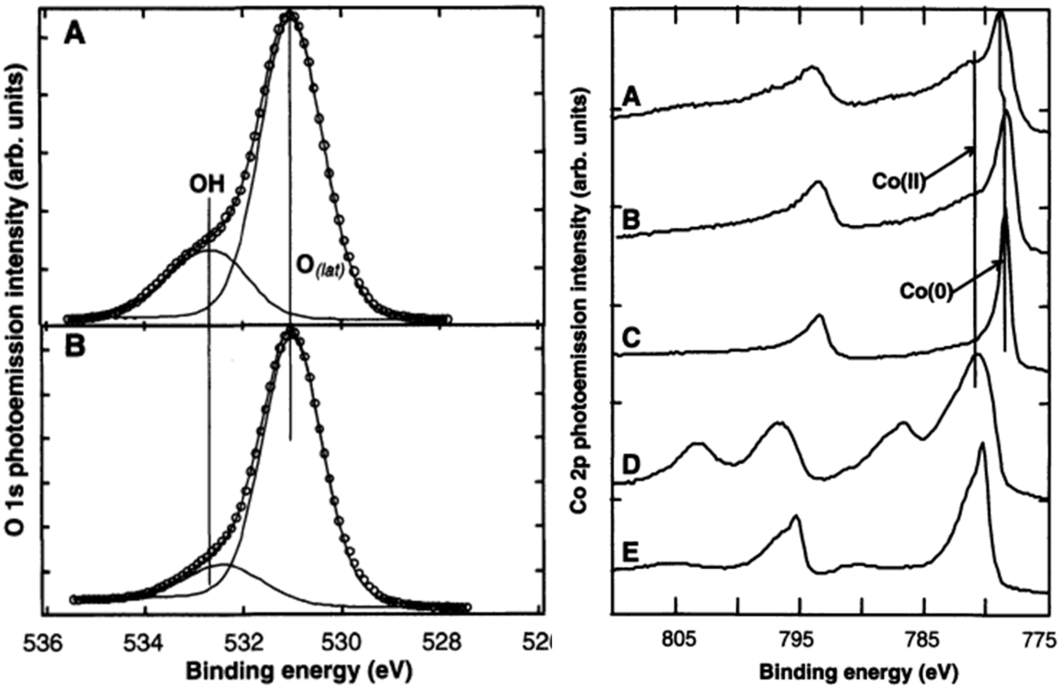

Figure 2.18: Left panel: O 1s core level spectrum measured at a 10° take-off angle for α-Al_2O_3(0001) a) after oxygen plasma cleaning and b) after $\sim$ 0.8 ML Co deposition. Right panel: Co 2p core level spectrum measured at a 10° take-off angle for a) 0.3 ML (A), and b) 0.8 ML Co on α-Al_2O_3(0001). Reference spectra of c) thin film of Co/Si(001), d) of CoO/MgO(001) and e) of γ-Co_2O_3/MgO(001) are also shown. The comparison shows that the Co adlayer contains a mixture of Co(0) and Co(II). After [Chambers et al., 2002].

the O-bridge (see figure 2.19). Co(II) then locally pins metallic Co atoms that missed the bridge site and didn't undergo an oxidation. This explains the experimental observation of limited oxide metal formation followed by metal clustering at 0.8 ML.

Similarly, oxidized titanium was detected at the Ti/α-Al_2O_3(0001) interface prepared by molecular beam epitaxy at low temperatures. The comparison of the energy-loss structure near Ti-$L_{2,3}$, Al-$L_{2,3}$, and O-K edges between the interface and the two surrounding bulk materials [Scheu et al., 1996] indicated bonding between titanium and oxygen with a possible Ti^{4+} state (not determined), while aluminum atoms did not participate in the interfacial bonding. The interfacial thickness was calculated and found equal to 0.5±0.1 nm which corresponds to $\sim$ 2.2 ML of Ti atoms with a coordination or oxidation state different from the bulk [Scheu et al., 1996].

In [Lazzari and Jupille, 2002, Lazzari and Jupille, 2005], the oxidation of titanium deposited on (1×1) Al_2O_3(0001) surface via metal-oxygen bonding was disregarded and was rather explained as the result of a reaction with residual hydroxyl groups. Indeed, the Ti-induced -2.8 eV shift observed on the Ti 2p XPS peak in this work would correspond to $\sim$ 0.5 electron charge transfer per atom. Since the charge of the surface oxygen is predicted to be hardly perturbed by the metal adlayer in the frame of a dominant convalency of Ti-alumina bond at the submonolayer range, 0.5 is a strong value hardly acceptable. Thus, the occurrence of Ti-alumina bonds to explain the O 1s shift can be rejected. Other possible origins of the O 1s and Ti 2p peak shifts were excluded after neat examination, bracing by that the Ti-OH reaction

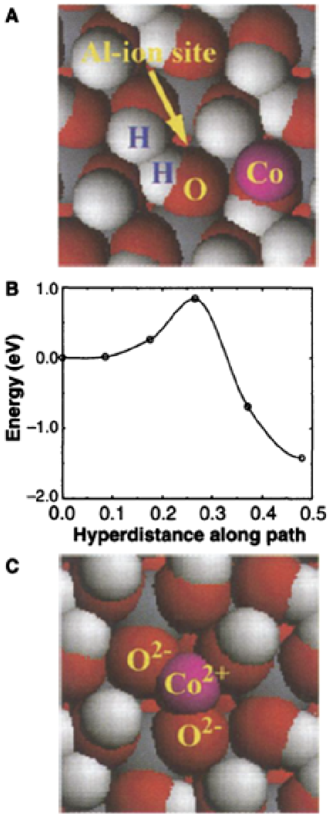

Figure 2.19: The preferred initial state geometry for the OH terminated surface in the presence of isolated Co adatoms. a) The computed activation barrier for the reaction between Co adatoms and OH groups : $2OH^- + Co^0 \rightarrow Co^{2+}2O^{2-} + H_2$; b) The zero is set to the initial state energy. The calculated barrier height is ∼0.85 eV, occurring when the Co is near the O-O bridge site. c) The final state of Co adatoms geometry after the reaction. Note that grey is Al, red is O, pink is Co and white is H. After [Chambers et al., 2002].

hypothesis. Moreover, two successive oxidation states occurred during the growth of Ti, Ti^{2+} (up to 0.3 Å) and Ti^{4+} (starting at 0.7 Å), it is only above 2 Å that metallic titanium starts to get clearly identifiable. The presence of two oxidation states reconciles the inability to determine one oxidation state of Ti in [Scheu et al., 1996]. The occurrence of under-stoichiometric Ti oxides was equally suggested as the reason of discrepancy found between OH coverage (0.9×10^{15} OH groups.cm^{-2}) and oxidized Ti (1.7×10^{15} atoms.cm^{-2}) [Lazzari and Jupille, 2005] (see figure 2.20).

Aluminum grown on alumina was likewise found to oxidize at the interface after reaction with hydroxyl groups giving rise to an AlO_x component which does not differ much from the alumina substrate [Lazzari and Jupille, 2005], in agreement with the prediction that ionic Al-O bonds dominate the Al/Al_2O_3 interface [Batyrev and Kleinman, 2001].

Zinc requires condensation at low temperatures (100 K) to achieve a sizable sticking coefficient which is zero at room-temperature [Cavallotti, 2014a, Le et al., 2017b]. Regarding the interaction of zinc with hydroxyl groups, both experimental and computational results [Le et al., 2017b] showed that an activated reaction of Zn with the OH-covered surface, followed by hydrogen desorption, produces dispersed interfacial moieties involving both oxidized Zn species and under-coordinated oxygen ions that lead to a significant improvement of adsorption/adhesion characteristics of the following atoms in the film. The key role of interfacial under-coordinated anions, remnants of the hydroxylation layer, in adhesion improvement was highlighted. In fact, TPD experiments showed, for Zn/OH-covered (1 × 1) alumina, an enhancement of desorption of H_2 at temperatures lower than that of Zn peak (figure 2.21-b), in line with the appearance of a kink at the onset of the Zn TPD spectra surface between 400

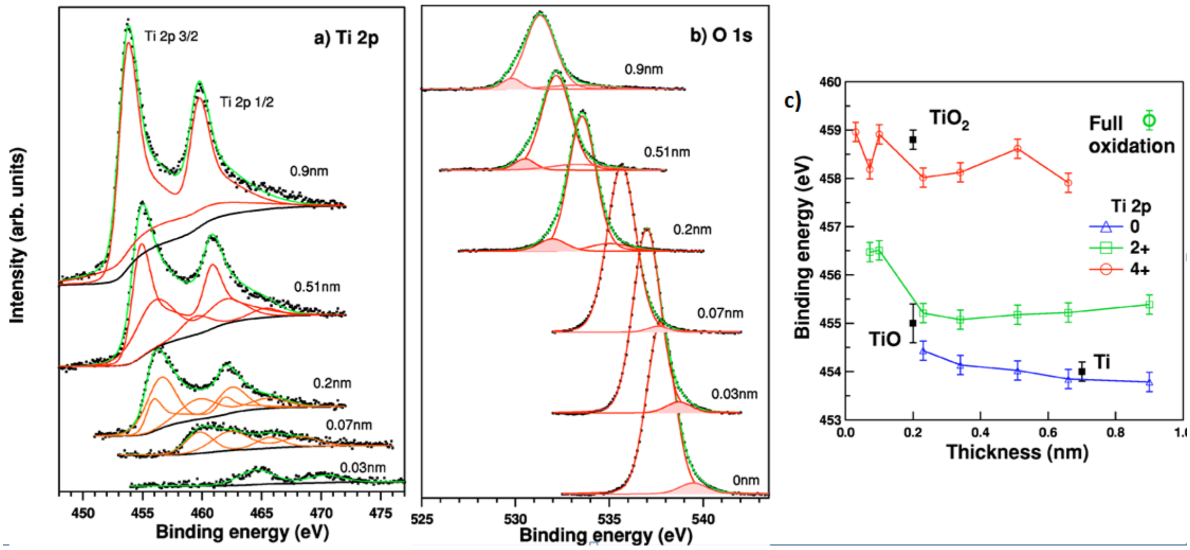

Figure 2.20: XPS spectra recorded during the deposition of Ti on α-Al_2O_3(0001) at room temperature: a) Ti 2p and b) O 1s core levels and the associated peak decomposition, with an emphasis on the early stage of the growth. The equivalent titanium thickness is given in the figure. c) Binding energy of the various components of the Ti 2p core level (labeled Ti^0, Ti^{2+}, Ti^{4+}). Absolute values of the binding energy have been determined by taking the alumina core levels as references. The bar indicates the tabulated values of binding energy for various titanium oxidation states (taken from [Wagner, 1979]). The circles correspond to the measured value after a full oxidation of the deposition under an oxygen partial pressure at high temperature ($T = 800$ K). After [Lazzari and Jupille, 2005].

and 450 K (indicated with an arrow in figure 2.21-c). Together, these observations, absent on reconstructed surfaces, referred to as OH-free surfaces (figure 2.21-a), suggested an oxidation of Zn via a complex OH-Zn reaction [Le et al., 2017b]. This assumption was substantiated by the oxidized zinc component emerging after annealing at ~ 425 K in the Zn $L_3M_{45}M_{45}$ Auger transition and peaking at 505 K contrary to a metallic state of zinc persistent upon annealing on OH-free surfaces (see figure 2.22). Furthermore, the quantification of oxidized zinc from photoemission yielded 5×10^{14} atoms.cm^{-2} which corresponds to one Zn per Al_2O_3 surface unit cell, or to one Zn^{2+} every two OH groups. Therefore, the oxidation of zinc is limited by the OH coverage and involves all surface hydroxyl groups [Le et al., 2017b]. Consistently, numerical simulations showed, after testing the adsorption energy of zinc on hydroxylated Al-terminated surfaces in different configurations (shown in figure 2.23), that the (Al)OH$Zn_{0.5}$ configuration (A_4 in figure 2.23) is the most stable under poor hydrogen conditions (see phase diagram-d in figure 2.37). It results when zinc replaces two protons per unit cell according to the following equation: $2H^+ + Zn \rightarrow Zn^{2+} + H_2$ [Le et al., 2017b, Cavallotti, 2014a].

2.2.2 Metal adsorption sites

While no experimental determination do exist on the absorption sites of metals on α-Al_2O_3(0001), theoretical works are quite numerous. A dependence on the alumina surface termination, metal coverage, and other properties of adatoms (size, charge distribution and ionicity, mechanical stiffness...) will be pointed out in the following discussion.

Let's start by defining the three main adsorption sites that were considered in these theo-

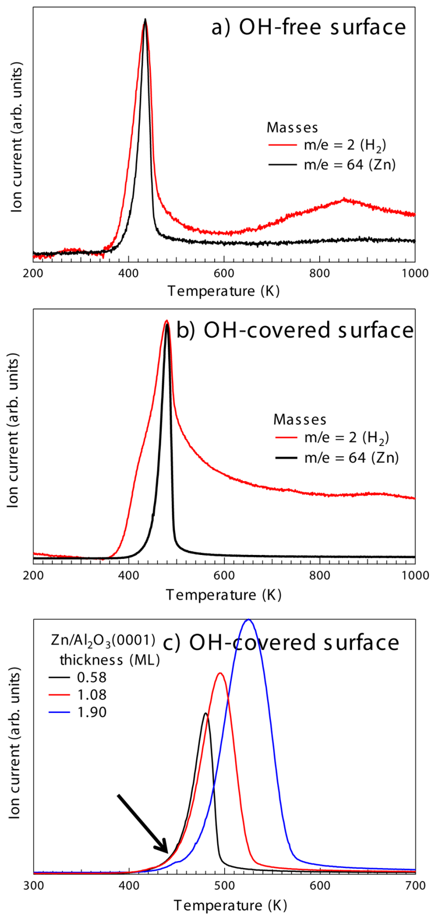

Figure 2.21: H_2 and Zn thermal desorption spectra from a) Zn/OH-free (0.9 ML thick Zn film) and b) Zn/OH-covered (0.4 ML thick Zn film) alumina surfaces. c) Zinc TPD spectra from Zn/OH-covered alumina for three different coverages; note the reproducible kink shown by an arrow for the highest coverage. The heating rate is 0.5 $K.s^{-1}$. After [Cavallotti, 2014a, Le et al., 2017b].

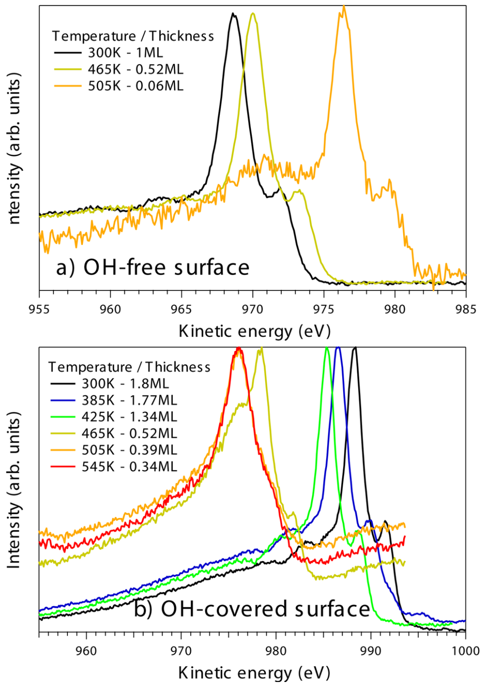

Figure 2.22: Zn $L_3M_{45}M_{45}$ Auger spectra: a) 1.0 ML thick Zn film on OH-free alumina surface annealed at increasing temperatures. Zinc remains metallic even at 505 K; b) 1.8 ML thick Zn film on OH-covered alumina surface; note the change of line shape from metallic Zn (300 to 425 K) to oxidized Zn (505 and 545 K) via a metal/oxide mixture (465 K). Spectra have been normalized to the maximum of intensity and not corrected from charge effects due to the insulating character of the alumina substrate. After [Cavallotti, 2014a, Le et al., 2017b].

retical studies as shown clearly in figure 2.24:

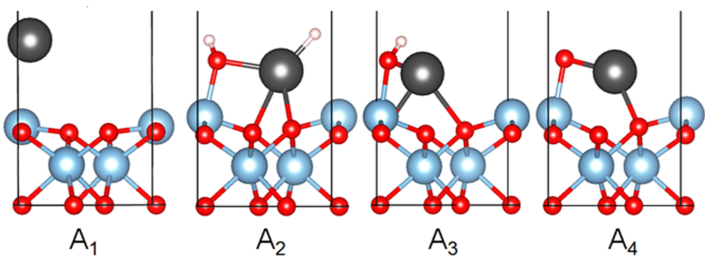

Figure 2.23: Adsorption configurations of Zn adatoms on a dry (A_1) and a hydroxylated (A_2-A_4) Al_2O_3 (0001)-(1×1) surface under various environment conditions. Red, blue, white, and gray balls stand for oxygen, aluminum, hydrogen, and zinc atoms, respectively. After [Cavallotti, 2014a, Le et al., 2017b].

1. O-top: metals adsorb above the topmost oxygen atoms.
2. Al-top: this could be the topmost Al ion in an Al-terminated surface, or so-called Al hollow which corresponds to Al atoms from deeper layers (Al_3 and Al_2 in inset of figure 2.26-c). In their work, Zhukovskii *et al.* represented these sites as centers of equilateral O triangles E_1 (closest) and E_2 (remoted) for O and Al-terminated surfaces respectively (see figure 2.25).
3. H: Hollow sites as described by Zhukovskii *et al.* [Zhukovskii et al., 2002] are present over non-equilateral O triangles (hollow site triangles) which lie over the subsurface oxygen atoms characterized by the absence of an Al^{3+} ion below (see figure 2.25).

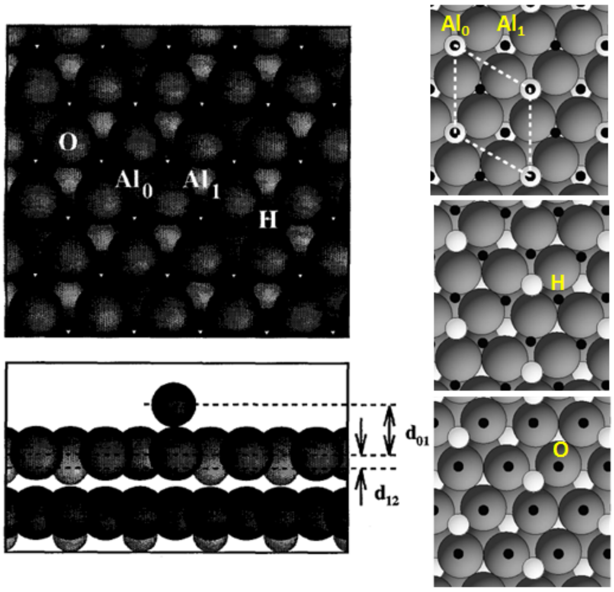

Figure 2.24: Top and side views of the alumina surface with indication of potential adsorption sites. Al ions are drawn smaller than O ones. The right panels show a clearer representation of these sites taken from [Siegel et al., 2002] with grey: O, white: Al, black: adatoms. After [Bogicevic and Jennison, 1999].

The discussion of theoretical findings on preferential adsorption sites of various metals will be split according to the metal coverage (1/3 ML and 1 ML).

2.2.2.0.1 1/3 ML coverage At 1/3 ML coverage, almost all calculations agreed upon a preferential adsorption of metal on the Al-top site attracted by the O^{2-} ions. This corresponds to the prolongation of the corundum lattice.

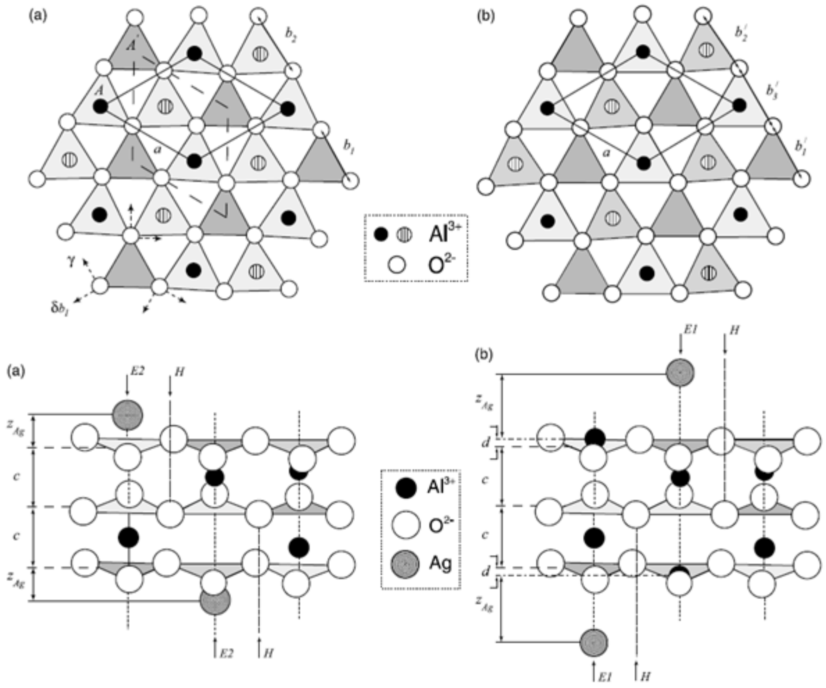

Figure 2.25: (upper panel) Top view oxygen planes of the alumina substrate before a) and after b) optimization including the 2D rhombic unit cell and neighboring Al planes (above: black, and below: striped circles). Optimization is obtained by synchronous transformation of triangles by rotation of δ and extension δb_i. The larger the triangle, the lighter its shading is. White is for hollow site triangle. (bottom panel) Side views of the alumina slabs where silver atoms at 1/3 ML coverage are distributed regularly on the aluminum C_{3v} axes above and below a) O-terminated, and b) Al-terminated substrates, respectively. The interlayer structure of the interface is defined by the parameters c, d and z_{Ag}. Note that a top view of the internal O plane corresponds to that shown in the upper panel a) while both outermost planes are in-plane reconstructed (upper panel b). After [Zhukovskii et al., 2002].

This was true for cobalt according to what was mentioned in section 2.2.1 where Co ions generated at the O-O bridge site after a redox reaction with OH settle in the surface Al hollow sites adjacent to the final state O^{2-} ions (figure 2.19 [Chambers et al., 2002]). Dispersion-corrected DFT calculations showed likewise a well-pronounced preference of the hollow Al_3 site for adsorption of isolated Ag adatoms, based on a calculated Ag-O distance $d_{Ag-O} = 2.59$ Å which corresponds to the prolongation of the corundum lattice [Lazzari et al., 2016] (figure 2.26-b). This site remained even for multilayer coverage ($d_{Ag-O} = 2.67$ Å) (figure 2.26-c). These results were consistent with experimental measurement of the nearest neighbor distance using grazing EXAFS at 60° which revealed the presence of an additional component (undetected at normal incidence) best accounted for by an Ag-O bond with $d_{Ag-O} = 2.65$ Å (figure 2.26-a). A preference of E_1 site (Al-hollow) was also found for Ag by Verdozzi *et al.* [Verdozzi et al., 1999].

In their paper [Bogicevic and Jennison, 1999], Bogicevic and Jennison presented the results of their DFT calculations performed on a series of metals (Li, K, Y, Nb, Ru, Pd, Pt, Cu, Ag, Au and Al) atop 5 Å of Al_2O_3 films deposited on Al(111) substrates. Once again, metals were generally seen to bind preferentially in the three-fold hollow (Al_0) site (shown in figure 2.24) attracted by the O^{2-} ions. This was true for all metals under review at a 1/3 ML coverage

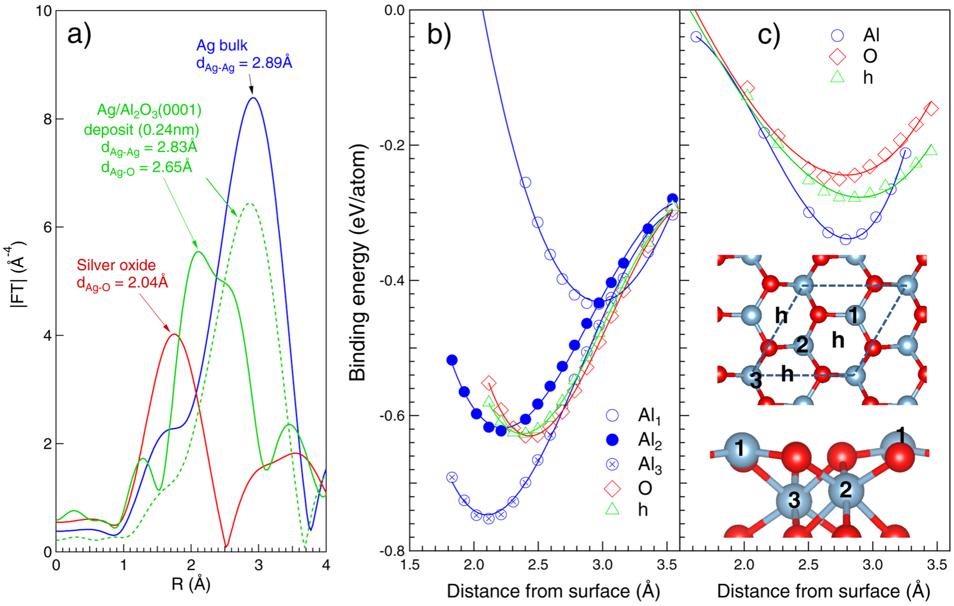

Figure 2.26: EXAFS analysis and first-principles results on Ag/α-Al$_2$O$_3$ (0001): a) Magnitude of the Fourier transform of the fine structure function corresponding to a 2.4 Å thick deposit of Ag/Al$_2$O$_3$(0001) (green curves). At normal incidence (dotted green line), a unique component is evidenced which corresponds to the Ag-Ag distance. At grazing incidence (green line), an extra component appears which is assigned to the Ag-O distance. The analysis of silver oxide (red line) and bulk silver (blue line) are shown for comparison. b) Binding energies of isolated atoms of Ag on α-Al$_2$O$_3$(0001) as a function of Ag-oxide distance for different sites of the alumina surface as defined in the insets shown in c. c) Average binding energy (per interfacial Ag) of a multilayer Ag deposit at different lattice registry with the substrate. The insets show a representation of the α-Al$_2$O$_3$ (0001) surface (top: top view; bottom: side view). The various Al atoms (1,2,3; blue balls) and hollow (h) sites are explicitly indicated; O atoms are represented by red balls. After [Lazzari et al., 2016].

with an increasing binding energy to the left of the periodic table (see table 2.27). The first trend is explained by a decrease in ion size, reducing the anion-oxide distance, strenghtening consequently the bond. The second trend is ascribed to the increasing metal ionicity as one moves to the left which leads to stronger bonds despite the length of these latter as for Ru-Nb-Y.

On another hand, while all the previously discussed studies agreed upon a preference of Al-top sites, some studies resulted in a different adsorption position of some metals at 1/3 ML coverage. In fact, Verdozzi *et al.* and Gomes *et al.* found that O-top site was favored for Pt [Verdozzi et al., 1999] and Pd [Gomes et al., 2002] adsorption and this was explained by the adatom large size preventing it from sinking deeply into the Al-hollow sites.
Moreover, in *ab initio* simulations of atomic and electronic structure of Ag on Al- and O-terminated alumina performed by Zhukovskii *et al.*, a slight preference of H position prevails on both surface terminations (figure 2.28) (binding energy of 5.7 eV (0.54) on H sites compared to 5.1 (0.48) atop E$_2$ sites at the O-terminated surface (Al-terminated)). One can note that the adsorption site preferences are qualitatively the same on both terminations. However, they differ substantially in terms of binding type, where a significant charge transfer indicates strong interfacial ion bonding on the O termination due to polarity effect, promoted by a noticeable contribution of subsurface O^{2-} ions in the interfacial bonding (see figure 2.29),

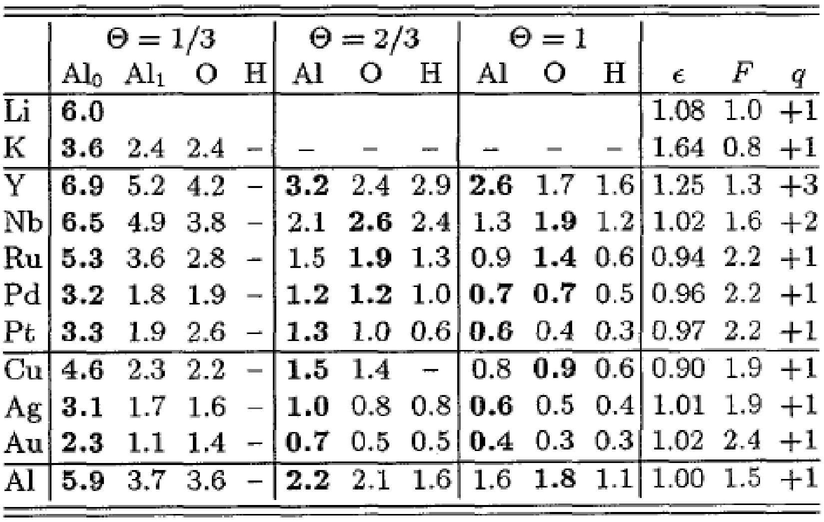

	$\Theta = 1/3$				$\Theta = 2/3$			$\Theta = 1$					
	Al_0	Al_1	O	H	Al	O	H	Al	O	H	ϵ	F	q
Li	**6.0**										1.08	1.0	+1
K	**3.6**	2.4	2.4	–	–	–	–	–	–	–	1.64	0.8	+1
Y	**6.9**	5.2	4.2	–	**3.2**	2.4	2.9	**2.6**	1.7	1.6	1.25	1.3	+3
Nb	**6.5**	4.9	3.8	–	2.1	**2.6**	2.4	1.3	**1.9**	1.2	1.02	1.6	+2
Ru	**5.3**	3.6	2.8	–	1.5	**1.9**	1.3	0.9	**1.4**	0.6	0.94	2.2	+1
Pd	**3.2**	1.8	1.9	–	**1.2**	**1.2**	1.0	**0.7**	**0.7**	0.5	0.96	2.2	+1
Pt	**3.3**	1.9	2.6	–	**1.3**	1.0	0.6	**0.6**	0.4	0.3	0.97	2.2	+1
Cu	**4.6**	2.3	2.2	–	**1.5**	1.4	–	0.8	**0.9**	0.6	0.90	1.9	+1
Ag	**3.1**	1.7	1.6	–	**1.0**	0.8	0.8	**0.6**	0.5	0.4	1.01	1.9	+1
Au	**2.3**	1.1	1.4	–	**0.7**	0.5	0.5	**0.4**	0.3	0.3	1.02	2.4	+1
Al	**5.9**	3.7	3.6	–	**2.2**	2.1	1.6	1.6	**1.8**	1.1	1.00	1.5	+1

Figure 2.27: Table of calculated adsorption energies (eV) in LDA for various metals at different adsorption sites and coverages. Preferred sites are highlighted and unstable adsorptions are indicated by a dash. The metallic radius ϵ normalized to Al (1.43 Å), the Pauling electronegativity factor (F) and the calculated ionic charge (q) at 1/3 ML coverage are given to conclude on the binding trend along the studied series. After [Bogicevic and Jennison, 1999].

compared to a physisorption limited to electronic charge polarization in the vicinity of Ag nuclei on Al terminated surface.

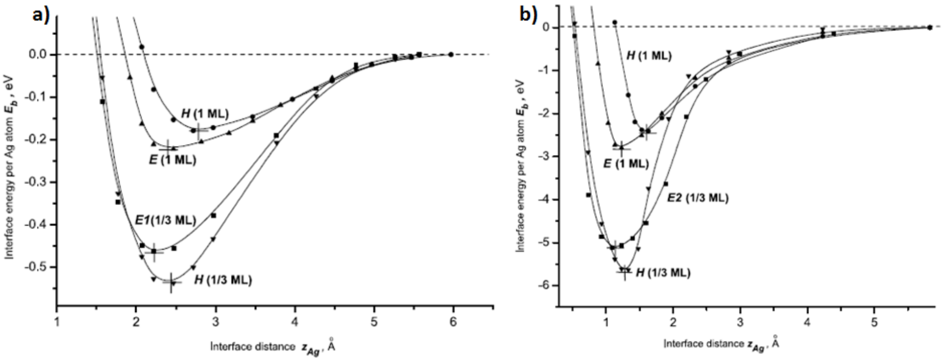

Figure 2.28: Interface energies calculated as a function of the interface distance z_{Ag} for the two adsorption sites E and H at 1/3 and 1 ML silver coverage on Al a) and O b) -terminated surfaces. After [Zhukovskii et al., 2002].

2.2.2.0.2 Monolayer coverage At a monolayer coverage, Al and O-top could serve as adsorption sites. Indeed, the preference of one over the other can be explained by the stiffness of the pure metals as stated in [Bogicevic and Jennison, 1999]. As a matter of fact, Al-top adsorption promotes buckling inside the metal film due to a lack of aluminum ions underneath. In particular, for hard metals, this buckling requires more energy, which is why they prefer to bind at the O sites without buckling. However, this interpretation does not apply to Y (adsorbing at the Al-top site with an energy of 2.6 eV) presenting a large strain at $\theta > 1/3$ ML, and could be explained by the formation of an incommensurate overlayer or a lattice rotation

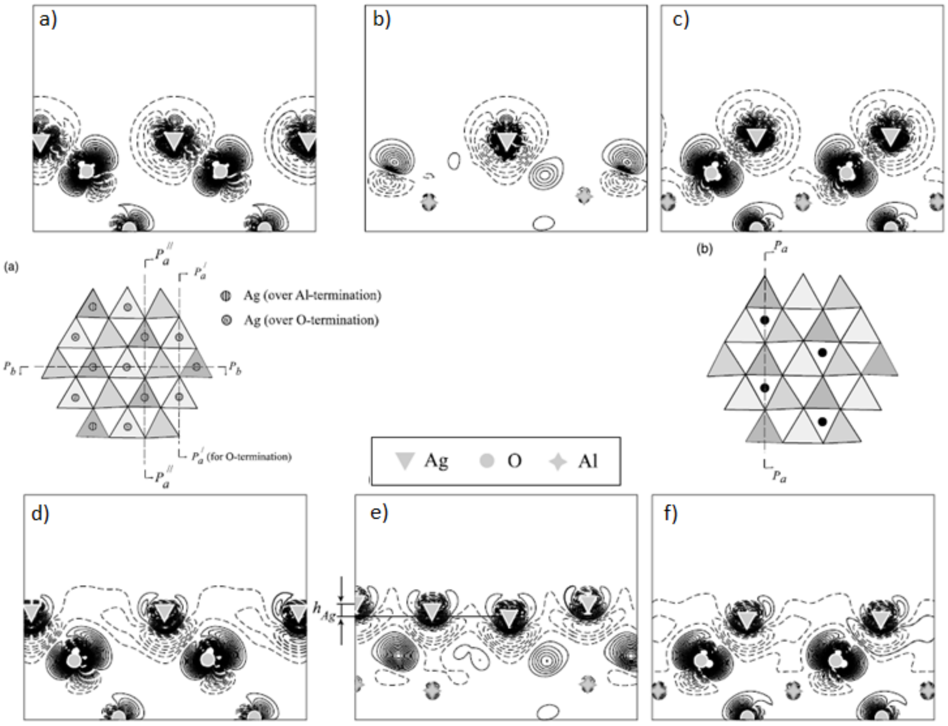

Figure 2.29: 2D Charge redistribution curves. Grey symbols indicate the atoms at the cross-section. a)b) two cross-sections for 1/3 ML of a Ag(111) plane over E_2 sites along P'_a-P'_a and P_b-P_b directions; c) section for 1/3 ML of a Ag(111) plane over H sites along the P_a-P_a direction; d)e) two cross-sections for Ag(111) monolayers over all the equilateral oxygen triangles, along P'_a-P'_a and P_b-P_b directions (inset); f) section for the distorted Ag(111) monolayer over all versatile oxygen triangles along the P_a-P_a direction. The full and dashed curves correspond to positive and negative difference electron densities, respectively. e) shows a step in the buckled Ag(111) monolayer of height h_{Ag}. The directions are represented in the insets a and b. After [Zhukovskii et al., 2002].

affecting the surface registry [Bogicevic and Jennison, 1999].
In addition, in the phase diagrams for Ag/Al_2O_3 and Al/Al_2O_3 interfaces calculated by Zhang and Smith [Zhang and Smith, 2000a], one can clearly see (figure 2.30) that on the stoichiometric (single Al) termination, Ag atoms prefer to adsorb on top of hollow sites while Al atoms bind at the topmost Al sites. Whereas, for oxygen-terminated surfaces, the Al-top site is preferred for adsorption of both Ag and Al atoms. In this case, the authors suggested that an important rumpling of the metal occurs, in agreement with the results of Zhukovski *et al.* [Zhukovskii et al., 2002] for silver and Verdozzi *et al.* for silver and platinum [Verdozzi et al., 1999] where stepped overlayers were evidenced.

In fact, for monolayers and thicker films, Zhukovskii *et al.* [Zhukovskii et al., 2002] underlined the structural restrictions brought by H sites to the silver film (*i.e.* silver network distortion induced by subsurface O^{2-}-like distribution). Consequently, a monolayer of Ag buckles in order to preserve the same interatomic distance as in bulk silver. The charge redistribution within this layer contributes to making the Al-hollow the preferential adsorption sites of the adatoms in agreement with the lower interface energy at E sites for 1 ML (figure 2.28).
Finally, the results of Cavallotti *et al.* [Cavallotti et al., 2016] are of particular interest for this work. The adhesion strength estimated from separation energies yielded a preference of O-top, and Al-top sites for Zn at the Al and O-terminated surface respectively. When a

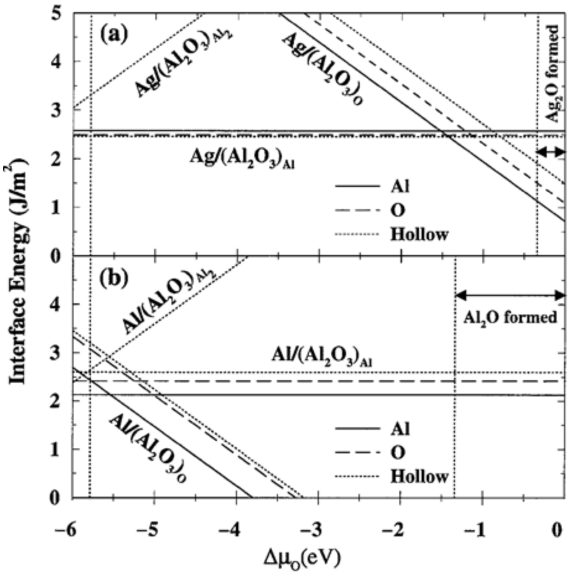

Figure 2.30: Interfacial energies versus $\Delta\mu_O$ (difference between oxygen chemical potential in the material and its value for ambient gas). Interfaces are defined in the text. The three metal site locations are indicated by solid, dashed, and dotted curves. Vertical dotted lines are located at oxygen chemical potential values for which bulk oxides could form as indicated. After [Zhang and Smith, 2000a].

buffer of Cr is included, Cr preferentially occupies Al-top sites at the Cr/Al-terminated Al_2O_3 and hollow sites of the zinc surface at the Zn/Cr interface. In a previous work, Cavallotti *et al.* [Cavallotti et al., 2014] stated that the particularly weak Zn adhesion is associated with the asymmetric 2-fold bridge adsorption geometry whereas a 3-fold symmetric adsorption site leads to a stronger adhesion of Cu and Ag on the Al termination.

It is important to note at the end that atomic relaxations were taken into account in the frame of the above-mentioned works since these relaxations bring a difference to the interfacial bonding. Indeed, this effect was made clear by Siegel *et al.* [Siegel et al., 2002] who compared the adhesion energy of Al atoms on Al_2O_3 in both relaxed and unrelaxed cases. They found that interfacial geometry optimization results in substantial atomic displacements leading to metal atoms assuming positions normally occupied by Al^{3+} ions in bulk, whereas they would bind above O sites out of the relaxation approach.

2.2.3 Epitaxy

The relative orientation of the crystallographic structures of metallic deposits and of alumina, the so-called epitaxy, is of great relevance, since it is known to play an important role on growth and wetting behaviors. Most of the studies of the literature concluded at an epitaxial growth of the metal on alumina for face-centered cubic (fcc) and hexagonal compact (hcp) structures, as shown in the case of cobalt (hcp), palladium (fcc), copper (fcc), titanium (hcp) and aluminum (fcc) [Dehm et al., 1997, Dehm et al., 1998, Suzuki et al., 1999, Chambers et al., 2002, Søndergård et al., 2003, Lazzari and Jupille, 2005, Lazzari et al., 2016]. Due to obvious symmetry reasons, the epitaxial plane is (0001) for hcp and (111) for fcc. For transition metals, the atomic structure of the first layer is ill-defined, probably because of the reaction with hydroxyl groups.

A RHEED investigation [Chambers et al., 2002] in real time during the growth of Co on a fully hydroxylated α-Al_2O_3(0001) surface along the $\langle 1\bar{1}00 \rangle$ direction (see figure 2.31) showed that a highly disordered interfacial layer is followed by the growth of a (0001)-oriented Co film. The spacing between streaks appearing in the RHEED pattern increased until ~ 5 ML, reflecting a decreasing in-plane lattice parameter until a full relaxation at 5 ML due to the large mismatch with the substrate (+5 %). These neat streaks suggested a layer-by-layer growth starting after 5 MLs leading to a flat Co film, a finding which was further confirmed by tapping AFM (Atomic Force Microscopy); images showed a complete coverage of the alumina surface with no height variation across the film nor 3D islands even at step edges (normally acting as nucleation sites) (figure 2.32). The unexpected full coverage of the surface was assigned to the reaction with hydroxyl groups evidenced by XPS.

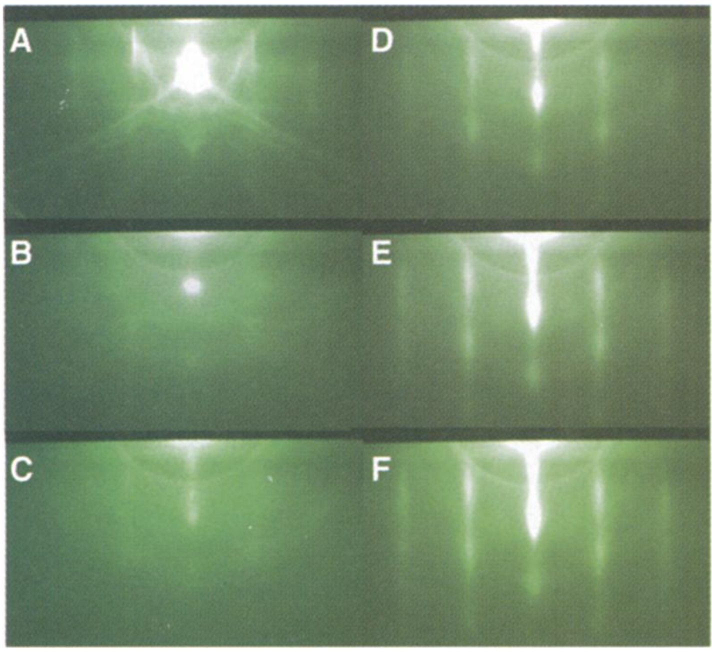

Figure 2.31: RHEED patterns in the $\langle 1\bar{1}00\rangle$ zone axis of a) a clean α-$Al_2O_3(0001)$ and as a function of Co coverage b) 2 c) 4 d) 6 e) 8 and f) 10 MLs. A quasi-epitaxial structure is achieved despite the +5 % lattice mismatch between the metal and the substrate. After [Chambers et al., 2002].

RHEED was also used to characterize the growth of Cu on α-alumina at 473 K [Dehm et al., 1998]. Initial diffraction rings were observed until 10 nm followed by the apparition of streaks along the $\langle 10\bar{1}0\rangle$ azimuth of Al_2O_3, indicating a polycrystalline nucleation pursued by the growth of a single crystalline Cu film along the $\left\langle 1\bar{1}0\right\rangle$ Cu azimuth. TEM (Transmission Electron Microscopy) and HRTEM (High-Resolution Transmission electron Microscopy) correlate well with the RHEED observation by revealing homogeneous Cu film with 2 µm grains exhibiting an epitaxial $(111)_{\mathrm{Cu}}\left\langle 1\bar{1}0\right\rangle_{\mathrm{Cu}} \parallel (0001)_{\mathrm{Al_2O_3}}\langle 10\bar{1}0\rangle_{\mathrm{Al_2O_3}}$ orientation relationship.

In the same study [Dehm et al., 1998], the growth of a Cu/Ti bilayer was investigated. The results reported for 500 nm of Cu grown on 100 Å of Ti suggested epitaxial growth of Ti from the beginning along the $\langle 2\bar{1}\bar{1}0\rangle$ azimuth. RHEED streaks started to develop for Ti at 3 Å with an increasing intensity up to 20 Å possibly indicating a layer-by-layer growth. The observation of streaks continued as the deposition switched from Ti to Cu with the alignment of the $\left\langle 1\bar{1}0\right\rangle_{\mathrm{Cu}}$ azimuth and a weak broadening at the transition. This result interestingly points at an epitaxial layer-by-layer growth of Cu on Ti/Al_2O_3 in contrast with its growth on bare alumina characterized by an initial polycrystalline island mode before epitaxial alignment. This puts forward the influence of Ti on the growth behavior of copper. Photodiffraction

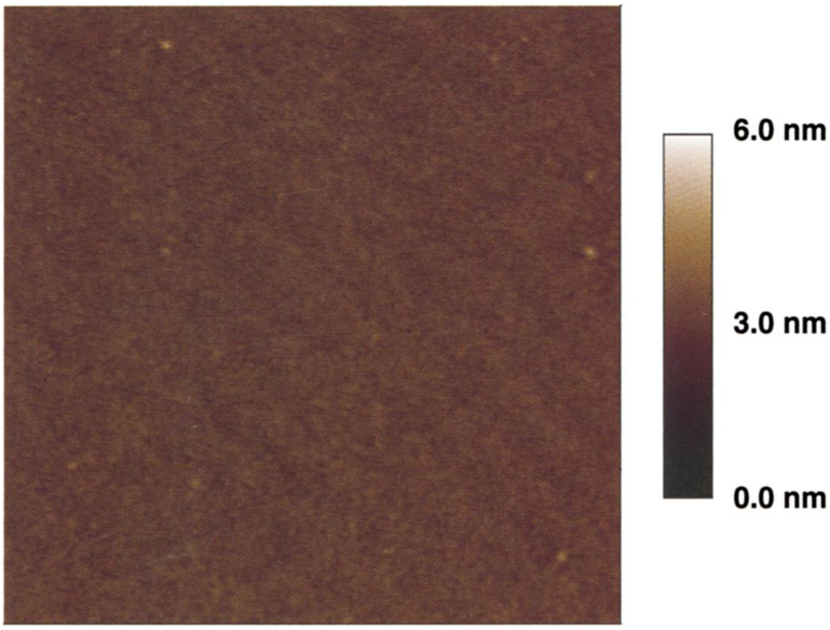

Figure 2.32: A (1×1) µm AFM image after deposition of 10 MLs of Co on hydroxylated $Al_2O_3(0001)$ at 300 K. After [Chambers et al., 2002].

analysis, consistent with the RHEED and TEM observations, revealed the same epitaxial plane by comparing the variation of the Ti 2p and O 1s XPS peak areas with the collection angle [Lazzari and Jupille, 2005]. The same analysis of the Al 2s peak area helped unveiling an ordered fcc arrangement of Al in the $\langle 111 \rangle$ direction with two twin domains ABC and ACB. Additionally, RHEED and CAICISS (Co-Axial Impact Collision Ion Scattering Spectroscopy [Suzuki et al., 1999]) showed, that after the deposition of 40 ML of Ti on α-Al_2O_3, an α-Ti film is formed following the $(0001)\,\langle 1\bar{1}00 \rangle_{\alpha-\mathrm{Ti}} \parallel (0001)\,\langle 2\bar{1}10 \rangle_{\mathrm{Al_2O_3}}$ epitaxial orientation relationship. In the initial stage of growth, Ti was found to follow the periodicity of Al_2O_3 and to form a pseudomorphic layer. From the critical angle measurements of CAICISS α scans (where α is the incidence angle), it was suggested that Ti adatoms are located on top of 3^{rd} and 4^{th} layer Al atoms.

In their work, Sondergaard *et al.* [Søndergård et al., 2003] demonstrated that the effect of a titanium buffer on the crystallinity and growth of silver depends of the thickness of the former. This was linked to the elastic relaxations within the Ti film. In fact, in a first step, the study started with an investigation of Ti growth alone on alumina. Figure 2.33 shows how Ti starts to grow with a lattice parameter close to that of alumina substrate with broad rods indicating a low degree of order. Upon an increase of coverage, an intensification of the diffraction pattern is observed with the coexistence of two lattice parameters, l_1 intense at low thickness and l_2 which dominates after a few nms of deposition. By carefully evaluating the position of the rods with respect to the surface lattice, the Ti film was found to surprisingly contract (2%) to the lattice parameter l_1 then relax to l_2 (6.3% larger than the substrate) close to the bulk value of titanium.

In a second step, the crystallinity of silver films on bare and titanium covered alumina were compared for different buffer layer thicknesses. Figure 2.34 sums up the results. On bare alumina, a ring structure evidences a poly-crystalline 3D growth without any epitaxial relation (a), while in the presence of a Ti buffer (c), silver grows with a sixfold symmetry pattern char-

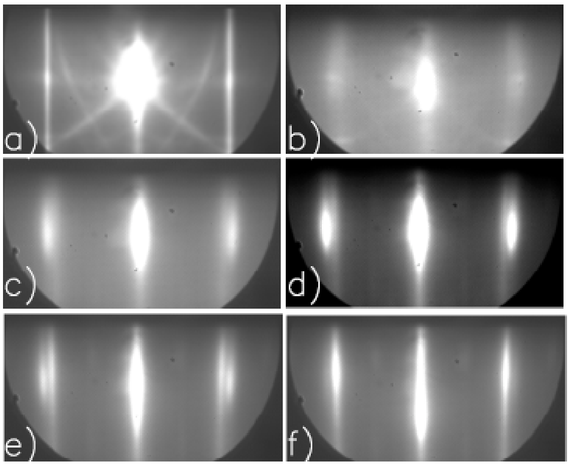

Figure 2.33: RHEED patterns of Ti growth on $Al_2O_3(0001)$ along the $\langle 10\bar{1}0 \rangle$ axis. a) Bare substrate, b) with 6 Å, c) 18 Å, d) 39 Å, e) 47 Å, f) 60 Å of Ti. After [Søndergård et al., 2003].

acteristic of Ag(111). For low Ti coverages, where l_1 and l_2 distances coexist, silver exhibits a complex 3D texture (b) compared to a good epitaxial growth and 2D morphology at higher coverages where only l_2 spacing is present.

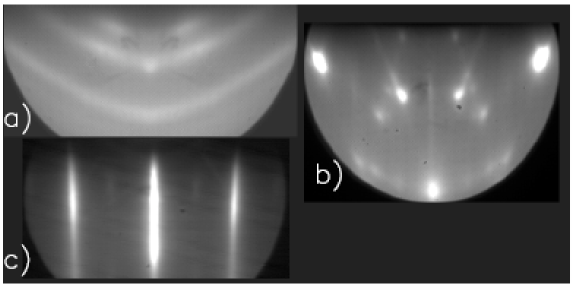

Figure 2.34: RHEED patterns of a 20 Å thick silver film desposited on a) bare alumina, or an a b) 40 Å and c) 60 Å of Ti film on $Al_2O_3(0001)$. After [Søndergård et al., 2003].

2.2.4 Adhesion and wetting of metals on alumina

Wetting during the growth of a metal on an oxide is the propensity of the metal to spread on the substrate [Campbell, 1997, Henry, 1998]. It involves a complex interplay between thermodynamic aspects of adhesion and kinetic parameters of growth which are the flux of incoming atoms and the temperature of the substrate in the case of evaporation. Controlling wetting is of paramount importance at such interfaces in many technological areas (glass industry, packaging, microelectronics etc...) since metal/oxide adhesion is generally weak due to the disymmetry of atomic bonds between the two partners [Campbell, 1997, Henry, 1998]. Beyond kinetic, one lever to tune wetting and adhesion is through the substrate chemical state or through, the so-called buffer layers.

2.2.4.1 Theoretical aspects of adhesion at metal/alumina interfaces

Metal/oxide adhesion is driven by short-range (*i.e.* ionocovalent bonding) and long-range (*i.e.* image [Stoneham and Tasker, 1985] and Van der Waals [Naidich, 1981]) contributions, so that the energy of adhesion is often decomposed as follows:

$$W_A = W_{bonding} + W_{image} + W_{vdW}. \tag{2.1}$$

The first term of the right side of equation 2.1 determines the strength of local chemical bonds formed at the interface including M-O and M-M bonds [Campbell, 1997]. In the case of alumina, a first molecular orbital picture of these interactions was given by Johnson and Pepper [Johnson and Pepper, 1982] to emphasize the decreasing covalent character of M-O bonds across the series of transition metals. The filling of the anti-bonding M-O molecular orbitals resulting from the interaction between the metal d-orbitals and the oxygen p-orbitals destabilize progressively the M-O bond by moving in the periodic table from early to late transition and noble metals because of the increasing d-band occupancy [Chatain et al., 1988, Alemany et al., 1993, Goniakowski, 1999]. An ionic character of the bonding, *i.e.* a charge transfer, was equally noticed in atomistic caclulations for M-O bonds in the case of isolated adatoms [Verdozzi et al., 1999], early transition [Zhang and Smith, 2000b] and sp [Siegel et al., 2002] metals.

However, in the case of noble metals, the contribution of short-range forces is marginal and adhesion is rather dominated by long-range (van der Waals and image) interactions [Jupille and Lazzari, 2006]. In the frame of the dielectric continuum model developed by Barrera *et al.* [Barrera and Duke, 1976], the adhesion energy was evaluated on the basis of van de Waals interactions alone. This model, although it overestimates the adhesion energy by neglecting contributions from short-range forces in the case of chemically active metals, has shown good agreement with values deduced for metals on alumina, glass and silica [Jupille and Lazzari, 2006]. More interestingly, this model revealed two main trends: the increase of adhesion with metal plasmon energy (*i.e.* density of conduction electrons) (see figure 2.35), and its decrease with increasing oxide band gap [Didier and Jupille, 1994, Didier and Jupille, 1996, Jupille and Lazzari, 2006], which is consistent with the observation of stronger adhesion of Ag particles on ZnO than that on Al_2O_3 [Lazzari and Jupille, 2005]. To this contribution, the image-charge concept should be added as its is quite significant in the case of two medias with a big mismatch in dielectric constants. In fact, the presence of a spatial boundary dividing two regions of different dielectric constants affects the polarization energy and thus the interfacial energy. This change of polarization energy is accounted for by including the interaction with an image charge which is the mirror of the actual charge with respect to the boundary. In the case of non reactive metals, like noble ones, this image term is believed to provide a significant part of adhesion [Stoneham and Tasker, 1985]. While contribution of charge transfer and image forces are well-accounted for in *ab initio* simulations [Goniakowski, 1999], the Van der Waals contribution is often set aside.

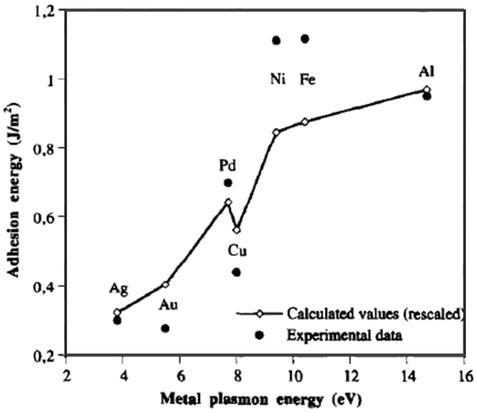

Figure 2.35: Trend of work of adhesion calculated in the frame of the dielectric continuum model rescaled by a factor 0.5 (empty circles) and those deduced from contact angle measurements by the sessile drop method for different metals on alumina [Chatain et al., 1988] (filled circles). After [Jupille and Lazzari, 2006].

Anyway, as a rule of thumb, metals poorly adhere to oxide surfaces leading to three-dimensional growth (see section 2.2.4.2). The confrontation of this problem led to several strategies to strengthen the metal/oxide bonds either through the hydroxylation of the surface [Kelber et al., 2000, Chambers et al., 2002, Cavallotti et al., 2014, Cavallotti et al., 2016, Le et al., 2017b] or by adding an intermediate metallic buffer at the interface [Dehm et al., 1998, Lazzari and Jupille, 2005, Jupille and Lazzari, 2006, Le et al., 2016].

In a screening of the interaction between transition metal adatoms and alumina, *ab initio* calculations showed a dependency on the polar (O-termination)/non-polar (Al-termination) character of the surface termination and on its hydroxylation state [Cavallotti et al., 2016]. A much stronger adhesion was obtained on polar terminated surfaces, a finding explained by the polarity healing mechanism provided by the electronic density of the metal [Goniakowski et al., 2007]. Indeed, calculated adsorption energies of 0.57 and 5.73 eV per Zn atom on Al-terminated and 3O-terminated alumina surfaces respectively testify for a strong interaction between zinc and the anionic polar termination compared to a weak one on the Al termination giving place to poorly bound metallic aggregates [Cavallotti, 2014a]. This was proved to be true for all transition metals, where the polarity of the (3O) termination provokes large charge transfer and ionization of the metals leading to a strong adsorption compared to a weak one on Al-terminated surfaces (see figure 2.36). However, according to the surface stability phase diagram, the experimental conditions of surface preparation in UHV falls in the Al-terminated stability range [Cavallotti, 2014a, Cavallotti et al., 2014] (see figure 2.4), therefore preventing to benefit from this increase of adhesion provided by polarity healing. Annealing of formed interface, provided that atom mobility is sufficient and ignoring dewetting or desorption, could be a way to reach this more stable polar termination/metal interface.

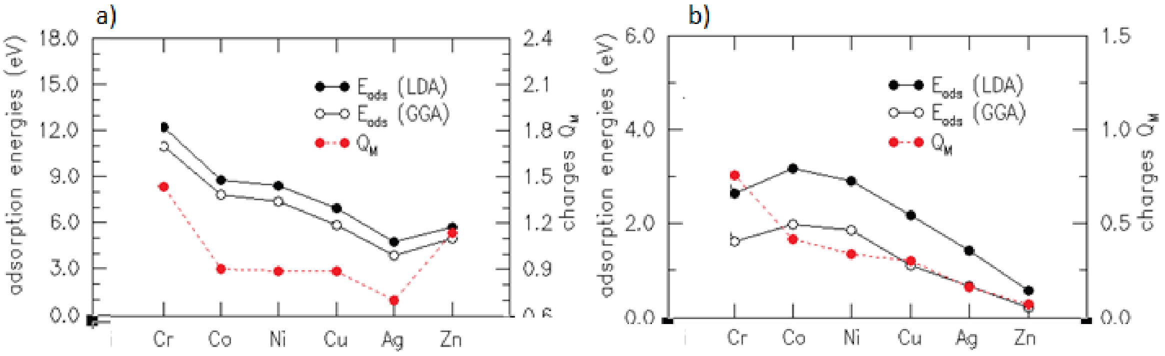

Figure 2.36: Calculated adsorption energies (in LDA and GGA approximations) and the charge of transition metal adatoms on a) the polar 3O and b) stoichiometric Al surface terminations. After [Cavallotti, 2014a].

In a second step, in an investigation of metal interaction on hydroxylated surfaces, metal-hydrogen exchange was shown to efficiently stabilize the otherwise weakly bound metal adatoms at the neutral Al-terminated surface [Cavallotti et al., 2014]. In particular, a noticeable improvement was found for zinc and was principally assigned to its low cohesive energy (1.9 eV) [Cavallotti et al., 2016, Cavallotti, 2014a]. Proceeding in the same way with other transition metals, the thermodynamic stability diagrams displayed in figure 2.37 present the most stable metal-alumina configurations for selected metals as a function of oxygen and hydrogen potentials. Regardless of the precise thermodynamic conditions and hydroxylation state of the alumina, simulations revealed that, among the transition metals, chromium has a particularly strong interaction due to its small electronegativity and atomic radius. This suggested that the addition of a middle transition metal buffer (Cr or Co) could substantially enhance the metal(Zn)/alumina interaction. With the help of Density Functionnal Theory calculations, by investigating the seperation energies at the buffer/alumina and buffer/metal adatoms interfaces, chromium was proved to be the best candidate to improve the adhesion of zinc due to the strong metal-oxide and metal-metal bonds that it forms at the first and second interface respectively [Le et al., 2016]. Indeed, to be effective, the buffer should display an enhancement of adhesion at both interfaces. However, it should be noted that buffer oxidation tends to reduce the number of metal/buffer strong bonds, hence the buffer favorable effect on adhesion.

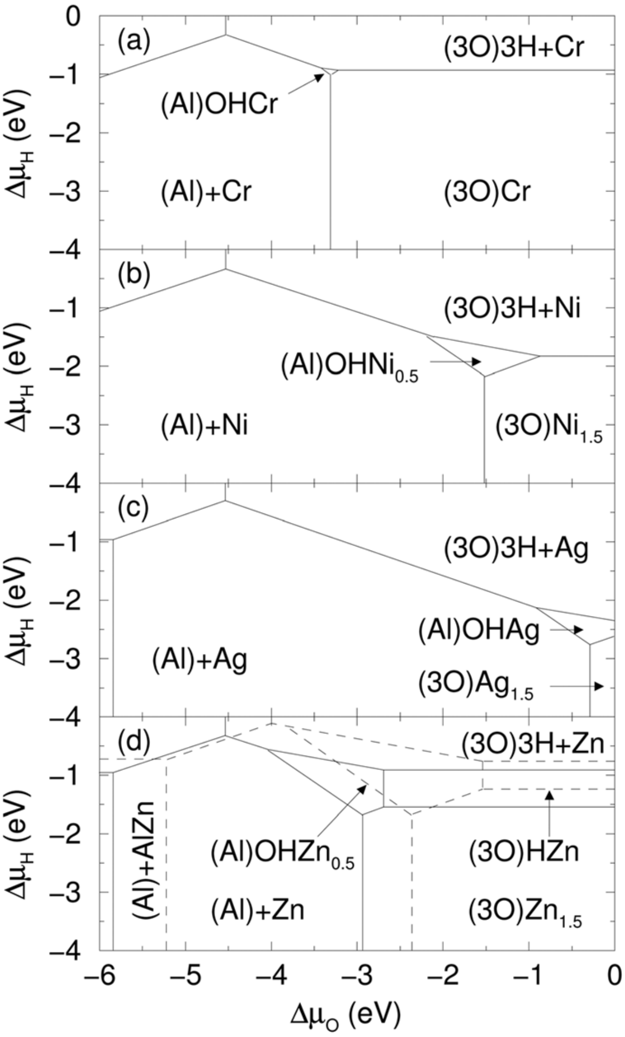

Figure 2.37: Diagrams of the most stable surface configurations of metal covered $Al_2O_3(0001)$ terminations as a function of oxygen and hydrogen chemical potentials $\Delta\mu_O$ and $\Delta\mu_H$. Solid and dashed lines represent LDA and GGA results, respectively. After [Cavallotti et al., 2016].

Experimentally, the interfacial chemistry generally involving a reaction with residual hydroxyl groups was shown to promote a rather laminar growth in the metal layer, in particular in the case of Co [Kelber et al., 2000, Chambers et al., 2002]. The dispersed character of the oxidized moities was shown to be fundamental in anchoring metallic atoms [Le et al., 2017b]. But the ability of this layer to really tune the adhesion of all metallic films was questioned experimentally [Lazzari and Jupille, 2005] and theoretically [Cavallotti et al., 2016, Le et al., 2017b]. The growth of three-dimensional islands found by SDRS [Lazzari and Jupille, 2005], although quite flat, on this oxidized intermediate layer, demonstrates that thermodynamic trends of wetting may be not reversed but that the oxidized layer could favor an earlier percolation.

2.2.4.2 Thermodynamic aspects of wetting and film growth

Subsequent to a weak adhesion energy, oxide surfaces are poorly wetted by metals. Indeed, on wide band gap oxides, metals adatoms show a tendency to cluster in 3D particles. Depending on adhesion W_{adh} and metal γ_A surface energies, three growth modes of a film on a substrate are usually distinguished according to the Bauer criterion [Bauer, 1958]: (i) the Frank-van der Merwe layer-by-layer growth mode ($W_{adh} > 2\gamma_A$), (ii) the Stranski-Krastanov one characterized by the formation of a continuous layer followed by the emergence of 3D clusters ($W_{adh} \sim 2\gamma_A$), and (iii) the Volmer-Weber one corresponding to the formation of 3D clusters from the beginning ($W_{adh} < 2\gamma_A$) (see figure 2.38). In the case of 3D particles, the equilibrium shape is governed by the relative surface energies. If the latter are isotropic as in the case of a molten metal in the sessile drop experiments, the droplet adopts a truncated sphere shape characterized by its contact angle θ_c related to the adhesion energy through the Young-Dupr formula:

Figure 2.38: Film growth modes according to the criterion of adhesion/surface energies. The Frank van der Merwe mode corresponds to a layer-by-layer growth, the Stranski-Krastanov mode to growth of a continuous layer followed by 3D clusters and the Vomer-Weber mode is characteristic of 3D island growth.

$$W_{adh} = \gamma_A + \gamma_B - \gamma_{A/B} = \gamma_A(1 + \cos\theta_c) \tag{2.2}$$

γ_A, γ_B and $\gamma_{A/B}$ are the surface energies of the metal A, and of the substrate B and the interface energy $\gamma_{A/B}$. $\theta_c < 90°$ ($\theta_c > 90°$) is usually assigned to situations of good (bad, respectively) wetting. In the solid state, the surface energy anisotropy leads to the so-called Wulff-Kaischew shape [Campbell, 1997, Henry, 1998]. Table 2.2 gives some typical values of W_{adh}, surface and interface energies in addition to the contact angle calculated for various transition metals on alumina taken from [Campbell, 1997]).

This assumed 3D growth was reconsidered by Markov and Kaischew [Markov and Kishishev, 1976] who showed the influence of kinetic factors on the growth of thin films, in particular the notion of supersaturation p/p_0 that plays a role on the free enthalpy released during the condensation of metallic vapor on the substrate surface $\Delta G/kT = \ln(p/p_0)$. p/p_0 is the ratio between the pressure of the condensing element and its equilibrium vapor pressure. It was shown that ΔG shifts the Bauer criterion and that three-dimensional nucleation is energetically favored if:

$$\gamma_B < \gamma_A + \gamma_{A/B} + \frac{kT}{\mathcal{A}} \ln\left(\frac{p}{p_0}\right) \tag{2.3}$$

Metal (M)	W$_{adh}(J/m^2)$	$\gamma_{Al_2O_3}(J/m^2)$	$\gamma_M(J/m^2)$	$\gamma_{M/Al_2O_3}(J/m^2)$	θ_c(deg)
Ti	2.03	0.65-0.925	1.7	0.32-0.595	78
Co	1.14	0.65-0.925	1.87	1.38	113
Cu	0.49	0.65-0.925	1.25-1.32	1.41-1.755	127-129
Cr	2.00	1.92	2.07	2.01	88
Zn	0.65	1.92	0.53	1.82	132
Ag	0.323	0.65-0.925	0.814-0.926	1.141-1.528	120-130

Table 2.2: Experimental values are given for Ti, Cu, and Co taken from [Campbell, 1997], while those for Zn and Cr were theoretically determined in [Le et al., 2017a]. Ag is introduced for comparison between transition and noble metals. The experimental values are measured for liquid metals, assuming that solid metals have a similar interface energy with oxide surfaces and a surface energy larger by a factor of ∼7%.

with $\mathcal{A}$ the surface of the substrate occupied by one metallic atom and T the substrate temperature. This condition implies that three-dimensional nucleation is favored at supersaturations lower than a precise critical value and 2D nucleation takes place at higher values. Although thermodynamic data lack precision for the vapor pressure at low temperatures [Brandes and Brook, 1983], the estimated supersaturations for Al and Ti are higher than 50 which implies a 2D growth on alumina, while Ag forms 3D islands even when accounting for this effect [Lazzari, 2000]

2.2.4.3 Growth mode and wetting of metals on alumina: thermodynamic versus kinetics

To supplement the information given in sections 2.2.1,2.2.3, this paragraph will give a brief overview of the surface science studies on the wetting, growth and morphology of various metals deposited on α-Al_2O_3(0001) using different approaches and techniques.

The wetting of (1×1) and $(\sqrt{31}\times\sqrt{31})R\pm9^\circ$ alumina surfaces by palladium and copper was studied using NC-AFM (Non-Contact Atomic Force Microscopy) in [Pang et al., 2000]. For palladium, 3D islands are observed on both surfaces with a step-dominated growth contrary to the breath figure growth proposed by Gautier *et al.* for copper [Gautier-Soyer et al., 1996]. It was additionally evidenced that copper adopts most probably a Volmer-Weber growth mode on the reconstructed surface without ruling out the possibility of a 2D followed by 3D Stranski-Krastanov mode because of the lack of information at coverages lower than 0.3 ML where the 2D-to-3D transition usually occurs [Xu et al., 1997, Lai et al., 1998]. In the work of Kelber *et al.* [Kelber et al., 2000], a sharp change in the slope of the Cu 2p/O 1s XPS intensity ratio plot versus the Cu deposition time at 0.35 ML was interpreted as the sign of the 1st layer completion indicating a layer-by-layer growth promoted by the presence of hydroxyl groups. While the effect of hydroxylation on reconstructed surfaces is unclear, the possibility of a copper continuous layer formation on the (1×1) surface as suggested by Kelber is not to be excluded, in particular because copper islands were not resolved on the (1×1) Al_2O_3(0001) at 0.3, 1 and 1.4 ML [Pang et al., 2000]. These results contradict the results of XANES and EXAFS showing a marked metallic character of Cu and the absence of Cu-O bonds independently of the oxidation state and crystallinity of the α-Al_2O_3 substrate [Gota et al., 1995]. This result was used as a principal argument to support a Volmer-Weber growth sustained by earlier photoemission studies of Cu growth on Al_2O_3 [Di Castro et al., 1985, Di Castro and Polzonetti, 1987]. In another experimental approach using RHEED and TEM to study the growth of Cu/α-Al_2O_3 and Cu/Ti/α-Al_2O_3 [Dehm et al., 1998], results rather showed the presence of a few pores at the Cu/Al_2O_3 interface suggesting the initial growth of Cu clusters in agreement with the proposed Volmer-Weber mode by [Pang et al., 2000]. In contrast, Cu was seen to grow continuously on Ti covered alumina ($\sim$ 100 Å) through a two-dimensional layer-by-layer mechanism [Pashley, 1985].

Concerning titanium or cobalt, RHEED streaks [Chambers et al., 2002, Suzuki et al., 1999,Søndergård et al., 2003,Søndergård et al., 2004] and TEM images favor a 2D growth from the beginning which might be surprising according to the Bauer criterion [Bauer, 1958] predicting a rather 3D mode. But in the frame of the Markov and Kaischew approach [Markov and Kishishev, 1976, Markov and Kaischew, 1976], the supersaturation of the vapor phase might accelerate the transition from a 3D to a 2D behavior through an earlier percolation [Dehm et al., 1998].

The wetting of α-Al_2O_3(0001) by titanium, aluminum, silver, and zinc was also studied by SDRS (Surface Differential Reflectivity Spectroscopy), a powerful tool allowing to follow *in situ* and in real time the growth of particles during deposition [Simonsen et al., 2000, Lazzari et al., 2001, Lazzari and Jupille, 2011]. Despite a very high bulk plasma frequency for Al and Ti and the presence of interband transitions that broaden peaks in the case of Ti, plasmon resonances occur in the UV-visible range from the very beginning of deposition at low coverages, indicating the formation of 3D clusters [Lazzari and Jupille, 2005]. The experimental SDRS spectra compared favorably with dielectric simulations with truncated spheroidal shape of aspect ratio (diameter/heigth) ranging between 4 and 8, which is compatible with the 2D growth trend suggested by RHEED strikes previously discussed. However, this 2D growth is a 3D one in nature and arises from the high density of 3D clusters, subsequent to a high nucleation rate and limited mobility, merging into a continuous layer as the coverage increases. A strong dependence of growth and wetting on temperature was additionally revealed, where truncated spheroids with aspect ratios of 7.5 and 4.2 were assigned to Al particles grown on alumina at 200 K and 600 K respectively [Lazzari and Jupille, 2005]. Concerning silver, it was proved that it poorly wets the surface of bare alumina; appropriate dielectric fits with the truncated sphere model led to particles with a low aspect ratio (1.8) and a high contact angle (130°) [Lazzari and Jupille, 2005]. It was additionally demonstrated that a significant improvement of the wetting is achieved via the predeposition of a thin titanium film (≥ 6 Å) provided that it is metallic. Indeed, the oxidation of titanium prior to silver deposition resulted in a poor wetting resembling that on bare alumina. Moreover, it was found that 0.05 nm of Ti did not affect much the wetting behavior of Ag in contrast with a 0.9 nm film, which is interestingly consistent with an oxidized state of Ti at low coverages caused by the reaction with surface hydroxyl groups [Lazzari and Jupille, 2005]. It might be worth to add that the exposure of the Ag/Ti/Al_2O_3 system to oxygen, in this same work, resulted in silver dewetting as a consequence of titanium oxidation.

Moving to zinc, the wetting behavior was tested both on (1×1) and $(\sqrt{31} \times \sqrt{31})R \pm 9^\circ$ alumina surfaces before and after hydroxylation [Cavallotti et al., 2014]; this work was performed in the frame of R. Cavallotti thesis to which our results will be compared. It is important to keep in mind that the above-mentioned deposits were made at 100 K since the sticking coefficient of zinc on bare alumina is negligible at room temperature [Rodriguez et al., 1996, Cavallotti et al., 2014]. SDRS spectra for zinc on all four surfaces presented an asymmetry to the low photon energy side characteristic of interband transitions [Lazzari et al., 2014a]. The plasmon resonance was centered around 3.6 eV all along the deposition (see figure 2.39). The dielectric simulations using a hemispheroidal model resulted in calculated aspect ratios of 2.8 and 3.4 for Zn particles on (1×1) dry and hydroxylated surfaces respectively at a thickness of 7.5 Å. This corresponds to a mean contact angle close of 65° and an adhesion energy of $W_{adh} = \gamma_{Zn}(1 + \cos\theta) = 1.1$ J.m^{-2} based on a surface energy of zinc $\gamma_{Zn} \approx 0.8$ J.m^{-2} [Falke et al., 1977]. However, this value is an upper limit since the aspect ratio was calculated for particles during the coalescence stage probably in non-equilibrium conditions (temperature of 100 K). In addition, the curves of integrated differential reflectivity signal versus deposition time revealed a slow take off in particular in the case of the dry reconstructed alumina surface (see figure 2.40). This is coherent with a low sticking coefficient of zinc on alumina. Up to 5 mins of deposition time, the origin for the absence of optical signal was verified by XPS, (0.5 Å despite a deposition rate of 1.6 Å/min). The normalization of integrated signals to thickness allow to distinguish clearly the three phases of nucleation, growth and coalescence of zinc particles (see figure 2.41).

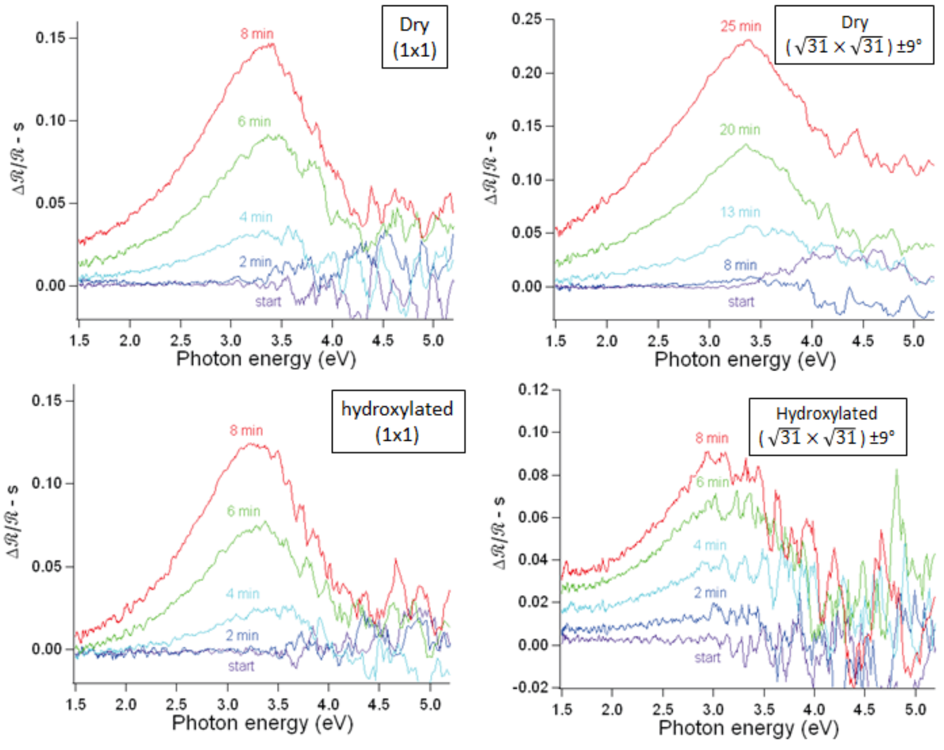

Figure 2.39: Evolution of SDRS spectra recorded in polarization s during the deposition of zinc on dry and hydroxylated (1×1) and $(\sqrt{31} \times \sqrt{31})$R±9° surfaces during 8 and 25 mins, respectively. After [Cavallotti, 2014a].

2.3 Conclusion

This chapter reviewed the question of termination of $Al_2O_3(0001)$ in relation with its ability to hydroxylate and its interaction with metals. The growth of metals on alumina seems to proceed throught 3D particles (Volmer-Weber growth mode). Transition (Co, Ti) and sp-

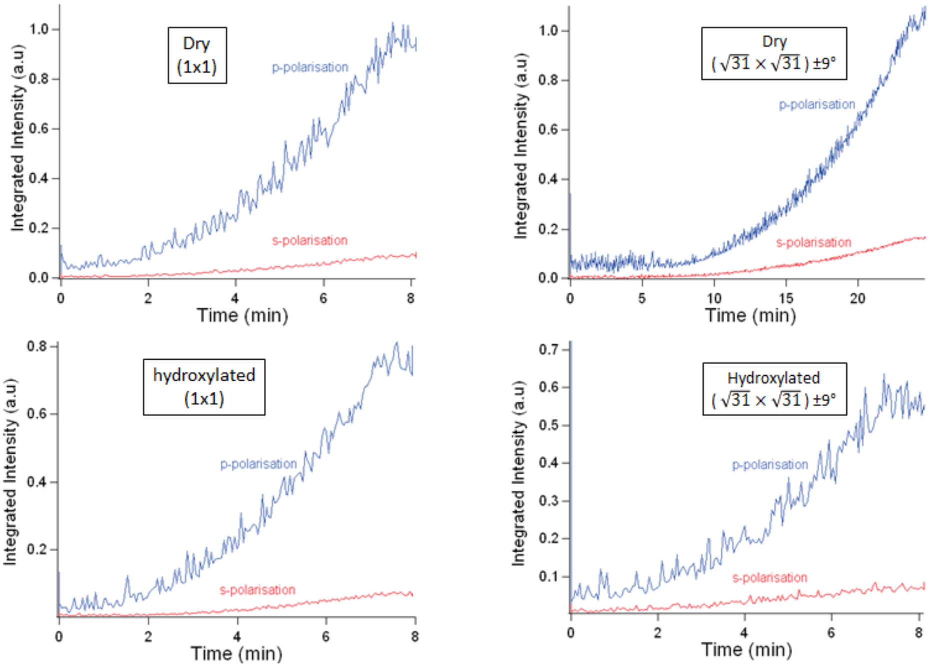

Figure 2.40: The evolution of integrated SDRS signal versus time of deposition of zinc on dry and hydroxylated (1×1) and ($\sqrt{31}\times\sqrt{31}$)R±9° surfaces during 8 and 25 mins respectively. After [Cavallotti, 2014a].

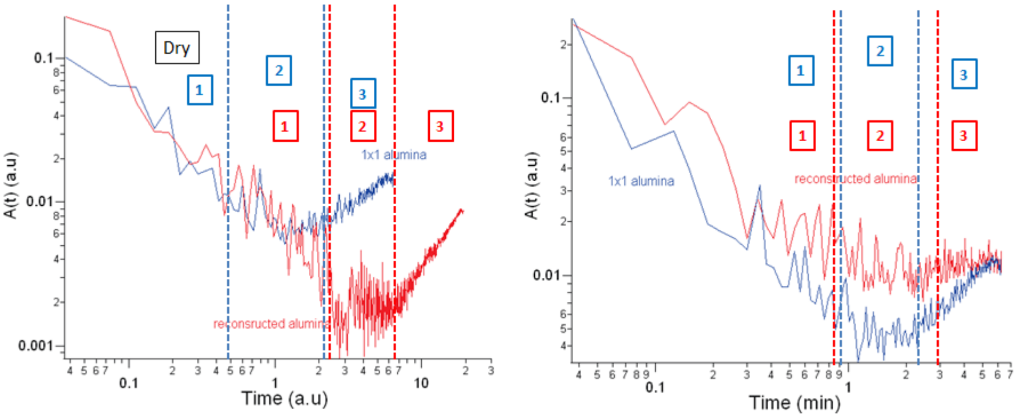

Figure 2.41: Integrated intensity divided by deposition time versus deposition time of zinc on dry and hydroxylated (1×1) and ($\sqrt{31} \times \sqrt{31}$)R±9° surfaces, featuring the three regions corresponding to 1: nucleation, 2: growth, 3: coalescence. After [Cavallotti, 2014a].

metals (Al) are found to initially react with hydroxyl groups leading to an oxidized layer of atomic thickness. In the case of the noble metal like Ag, no reaction occours while for Zn it is thermally activated and for Cu the situation is not so clear-cut. The three dimensional growth on top of this oxidized layer questions the ability of OH to really improve the adhesion, since kinetic effects due to supersaturation can be sizable in the case of transition metals with low vapor pressure leading to an earlier percolation and a metastable film [Campbell, 1997,Lazzari and Jupille, 2005,Jupille and Lazzari, 2006]. Finally, in this context, the SDRS technique due to its sensitivity to particle aspect ratio has proven to be an efficient and relevant tool to study wetting at the nanoscale at metal/alumina interface.

CHAPTER 3

OPTICAL PROPERTIES OF SUPPORTED NANOPARTICLES: THE CASE OF CHROMIUM AND ZINC

This chapter is aimed at giving an overview of the dielectric modeling of the optical response of thin films made of nanoparticles. It will serve as a basis of the SDRS analysis of growth mode of Cr and Zn performed in the next chapters. After an introduction on the Fresnel coefficients in the framework of excess fields and interfacial susceptibilities (section 3.2), the calculation of the truncated sphere/spheroid polarizability tensor which drives the optical film response will be reminded (section 3.3.1). The way the particle polarizes will be then described in terms of eigenmodes of charge vibration (section 3.3.2) that will help to understand the direct inversion of differential reflectivity spectra (section 3.3.3) and the link to the growth mode (section 3.3.3). The specificity of interband transitions in the dielectric functions of Cr and Zn compared to the more classical metal of plasmonics (Ag, Au) will then be highlighted (section 3.4). These dielectric functions will then be used in simulations to stress on the sensitivity of SDRS to particle aspect ratio and therefore wetting (section 3.5). Section 3.6 will focus on the complexity of the polarization modes in Zn and Cr particles due to interband transitions. At last, the question of film stacking will be tackled, in particular for a particle supported on film (section 3.7). A study of the screening induced by a continuous film will be developed at dipolar order both for an isolated dipole and a lattice of dipoles. The case of Cr/alumina and alumina/Cr will be used as examples.

3.1 Plasmonics of supported particles: interest in the field of wetting and layer growth

Light is a non-destructive probe that can be operated at any temperature, either in vacuum or in gaseous and liquid environments. More specifically, the capability of UV-visible wavelengths to characterize via plasmon excitations sub-wavelength metallic objects (the so-called localized surface plasmons) [Bohren and Huffman, 1983, Kreibig and Vollmer, 1995, Noguez, 2007, Rycenga et al., 2011] has boosted the development of nanoplasmonics. Plasmon polaritons of free-standing spheres or spheroids can be determined in the framework of the Mie theory with the extraordinary achievement that exact solutions exist even for the scattering of a plane wave in the retarded limit [Mie, 1908, Bohren and Huffman, 1983, Kreibig and Vollmer, 1995]. In the classical example of a sphere of radius R in an homogeneous medium, the so-called extinction coefficient σ_{ext} (ratio between the incident power and the transmitted one) is the sum of scattering σ_{scat} and absorption σ_{abs}. Since Rayleigh scattering scales as $\sigma_{scat} \propto (R/\lambda)^4$ and absorption as $\sigma_{abs} \propto R/\lambda$ at optical wavelength λ, plasmonics of nanoobjects is mainly driven by light absorption. In the nano-sized regime, σ_{abs} is tremendously sensitivity to the particle shape [Bohren and Huffman, 1983, Kreibig and Vollmer, 1995, Noguez, 2007, Rycenga et al., 2011]. For instance, upon flattening a sphere to a spheroid, the degeneracy of the dipole plasmon resonance of the sphere is lifted leading to two dipolar modes along the large and small axis. Depending on the metal, their splitting in energy and relative intensities due to the so-called depolarization field is extremely sensitive to the particle aspect ratio. This is at the heart of the ability of plasmonics to derive wetting trend as employed in this work. However, when particles are synthetized through the Volmer-Weber growth process on a substrate, the plasmonic response of the object is dramatically impacted by the break in symmetry of the particle environment [Román-Velázquez et al., 2000, Nordlander and Prodan, 2004, Knight et al., 2009, Lermé et al., 2013] and by the truncated shape due to wetting [Simonsen et al., 2000, Lazzari et al., 2001, Lazzari et al., 2002, Albella et al., 2011]. Even for a supported nanosphere, a rich set of plasmon resonances can be promoted by approaching the object from the substrate due to an increasing role of the image field [Beitia et al., 1999, Román-Velázquez et al., 2000, Lermé et al., 2013]. The dipole excited by the incident light induces an image dipole which perturbs the local field seen by the particle which in turns excites a quadrupole which is mirrored in the substrate and so on.... The phenomenon can be viewed as a cascade of multipole excitations or an hybridization phenomenon between the eigenmodes of polarization of the particle and of its mirror image [Nordlander and Prodan, 2004, Aubry et al., 2011, Lermé et al., 2013]. Resonance lineshapes and frequencies are quite sensitive to (i) the particle-substrate distance and image strength [Beitia et al., 1999, Pinchuk et al., 2004, Dmitriev et al., 2008, Mock et al., 2008, Vernon et al., 2010, Chen et al., 2011], with a strong field enhancement within the gap [Aubry et al., 2011, Letnes et al., 2011, Lermé et al., 2013] for nanosphere, (ii) substrate dielectric properties [Hilger et al., 2001, Knight et al., 2009] which drives not only the image field but also the interfacial damping of the excitation [Kreibig, 2008], (iii) the substrate/particle wetting and interface truncation [Simonsen et al., 2000, Lazzari et al., 2001, Lazzari et al., 2002, Lazzari et al., 2003a, Albella et al., 2011] and (iv) the electromagnetic coupling between objects [Swanglap et al., 2011]. Modelings of those phenomena have been performed using various frameworks [Zhao et al., 2008, Myroshnychenko et al., 2008] with spherical shapes [Beitia et al., 1999, Román-Velázquez et al., 2000, Nordlander and Prodan, 2004, Letnes et al., 2011, Lermé et al., 2013] or more realistic profiles [Lazzari et al., 2001, Lazzari et al., 2002, Noguez, 2007, Vernon et al., 2010] showing the richness of the polarization modes.

The earlier models developed in the literature, such as effective medium theory [Maxwell Garnett, 1904, Bruggeman, 1935] or Yamaguchi model [Yamaguchi et al., 1973, Yamaguchi et al., 1974] failed to described quantitatively the optical response of supported particles. Indeed, the effective medium theory, *i.e.* Maxwell-Garnett or Bruggeman models, assumes that the particles are embedded in a homogeneous medium with an effective uniform dielectric constant derived from object polarizability [Kreibig and Vollmer, 1995], but disregards the 2D geometry of the layer and treats rather poorly the interaction with the substrate. This is better handled by the Yamaguchi model [Yamaguchi et al., 1973, Yamaguchi et al., 1974] which replaces particles with spheroids of which field-induced dipoles interact with mirror-image dipoles in the substrate and with neighbors. This approach takes into account the contribution of all the local fields of neighbors and images, but does neither consider the exact shape of particles nor the multipolar coupling with the substrate. These limitations prompted Bedeaux and Vlieger [Bedeaux and Vlieger, 2001, Bedeaux and Vlieger, 1973, Bedeaux and Vlieger, 1974, Vlieger and Bedeaux, 1980, Bedeaux and Vlieger, 1983, Haarmans and Bedeaux, 1993, Haarmans and Bedeaux, 1995, Simonsen et al., 2000, Lazzari et al., 2001] to tackle the exact calculation of the polarizability of supported truncated spheres or spheroids (section 3.3) forming a thin granular film based on the concepts of excess fields and surface susceptibilities (section 3.2). Both the existence of a wetting angle and the local field felt by the object are perfectly described. The interest of such a modeling that will be detailed hereafter has been highlighted over the years both on optical and growth point of view:

- the physics of the multipolar excitation modes in Ag/Al_2O_3 [Lazzari et al., 2002, Lazzari et al., 2003b, Lazzari et al., 2014a];
- a quantitative comparison to small-angle X-ray scattering during Ag/MgO growth [Lazzari et al., 2009] with a good agreement on particle aspect ratio, the key parameter in wetting;
- the trends of wetting of various metals (Ti, Ag, Al, Zn) on alumina [Lazzari and Jupille, 2001, Lazzari and Jupille, 2005, Le et al., 2017b];
- the derivation of the morphology of a layer to discuss nucleation, growth and coalescence processes [Lazzari and Jupille, 2011, Lazzari and Jupille, 2012].

3.2 Fresnel coefficients of thin films in the framework of excess fields and interfacial susceptibilities

To model the optical response of nanoparticle films, Bedeaux and Vlieger [Bedeaux and Vlieger, 2001] developed a general formalism to treat the optical response of perturbed zone at the interface between two homogeneous media of dielectric functions ϵ_1 (vacuum in general) and ϵ_2 (substrate). The main assumption is that the characteristics sizes involved in this zone (thickness of the layer, in-plane correlation length, particle diameter and spacing, etc.. . .) are much smaller than the optical wavelength λ (figure 3.1-a). The boundary conditions between the bulk electromagnetic fields extrapolated to a fictitious dividing surface in the perturbed zone are obtained as integral of excess fields along the direction perpendicular to the surface. Excess fields are the difference between the actual field and the one in the homogenous medium extrapolated to the surface *i.e.* $\mathbf{E}_{exc}(\mathbf{r}) = \mathbf{E}(\mathbf{r}) - \mathbf{E}_1(\mathbf{r})H(-z) - \mathbf{E}_1(\mathbf{r})H(z)$ where $H(z)$ is the Heaviside function. Based on the assumption of smallness of lengths compared to λ, these unknown integrals are linked to the bulk field extrapolated to the dividing surface through coefficients called surface susceptibilities. These frequency-dependent complex coefficients $\gamma(\omega), \beta(\omega)$ characterize the way the interface can be polarized along the direction parallel (γ) and perpendicular (β) to the interface. In fact, these susceptibilities have the meaning of optical thicknesses and are given by:

$$\gamma = \int_{-\infty}^{+\infty} \left[\epsilon(z) - \epsilon_1 H(-z) - \epsilon_2 H(z)\right] dz,$$

$$\beta = \int_{-\infty}^{+\infty} \left[\frac{1}{\epsilon(z)} - \frac{H(-z)}{\epsilon_1} - \frac{H(z)}{\epsilon_2}\right] dz, \tag{3.1}$$

if the perturbed zone is only characterized by a profile of dielectric function $\epsilon(z)$ that depends only on the perpendicular coordinate z. For a continuous thin film of thickness t and isotropic

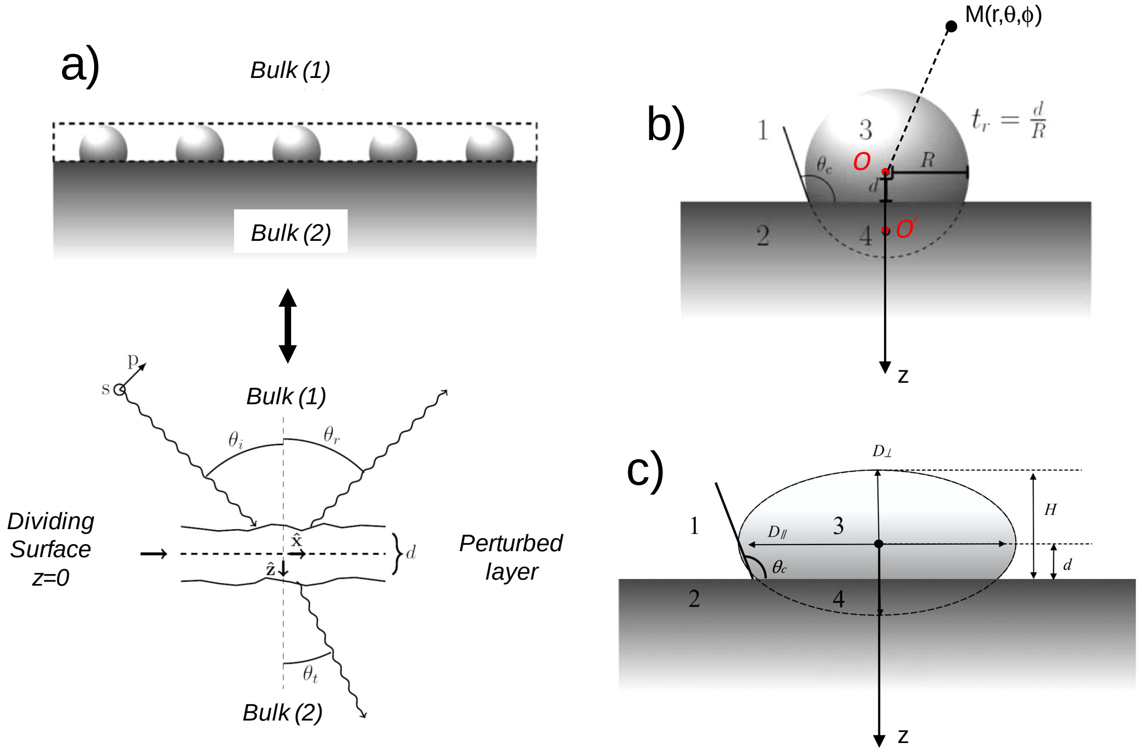

Figure 3.1: a) Illustration of the perturbed zone considered in the excess field theory to account for a particle layer. A boundary region of thickness d separates two bulk media characterized by their dielectric function ϵ_1, ϵ_2 or corresponding refractive indexes n_1, n_2 . Inside this boundary region, the $z = 0$ plane defines the arbitrary reference or dividing surface. Incident radiation is coming from the bulk in the negative z region at an angle θ_0, causing a reflected beam θ_r and a transmitted beam θ_t in the far field. The two eigen-states of linear polarization named p and s are shown. b) Truncated sphere of radius R, truncation $t_r = d/R$, height $H = (1 + t_r)R$, contact angle $\theta_c = \arccos(-t_r)$ and aspect ratio $Ar_r = 2R/H = 2/(1 + t_r)$. The direct O and image O' points used in the potential expansion are shown in red. c) Truncated oblate spheroid of parallel diameter $D_\| = 2R_\|$, perpendicular diameter $D_\perp = 2R_\perp$, truncation $t_r = d/R_\perp$ and aspect ratio $A_r = D_\|/H = 2R_\|/R_\perp(1 + t_r)$.

local dielectric constant $\epsilon(\omega)$, the surface susceptibilities are simply given by:

$$\gamma(\omega) = t[\epsilon(\omega) - \epsilon_1] \quad \text{and} \quad \beta(\omega) = t\left[\frac{1}{\epsilon_1} - \frac{1}{\epsilon(\omega)}\right], \tag{3.2}$$

i.e. the product of the thickness and of the dielectric function $\epsilon(\omega)$ or the loss function $1/\epsilon(\omega)$ of the film. The Bedeaux-Vlieger formalism can be seen as a generalization to any profile of dielectric function of the so-called thin plate model [McIntyre and Aspnes, 1971]. Two other coefficients $\delta(\omega), \tau(\omega)$ of second order in t/λ should be introduced due to the arbitrary choice of the dividing surface. The reason lies in the fact that the excess densities are coupled to the fields at their original positions rather than those at the dividing surface. This non-locality results from the translation of the density of polarization through the perturbed layer. Although included in the numerical simulations of this thesis for completness, $\delta(\omega), \tau(\omega)$ show little influence on the optical spectra of metallic islands which response is dominated by optical absorption described by $\gamma(\omega), \beta(\omega)$ [Lazzari et al., 2014b]. Knowing the boundary conditions for the bulk extrapolated fields as a function of the surface susceptibilities, it is then possible to obtain from the Maxwell equations all the Fresnel coefficients in amplitude [Bedeaux and Vlieger, 1973, Bedeaux and Vlieger, 2001, Haarmans and Bedeaux, 1995] (reflection, transmission, absorption, ellipsometric coefficient). The reflections coefficients in s- and p-polarizations are given by:

$$\begin{aligned} r_s &= \frac{n_1 \cos\theta_0 - n_2 \cos\theta_t + i(\omega/c)\gamma}{n_1 \cos\theta_0 + n_2 \cos\theta_t - i(\omega/c)\gamma} \\ r_p &= \frac{(n_2\cos\theta_0 - n_1\cos\theta_t)[1-(\omega/2c)^2\epsilon_1\gamma\beta\sin^2\theta_0] - i(\omega/c)\gamma\cos\theta_0\cos\theta_t + i(\omega/c)n_1 n_2\epsilon_1\beta\sin^2\theta_0}{(n_2\cos\theta_0 + n_1\cos\theta_t)[1-(\omega/2c)^2\epsilon_1\gamma\beta\sin^2\theta_0] - i(\omega/c)\gamma\cos\theta_0\cos\theta_t - i(\omega/c)n_1 n_2\epsilon_1\beta\sin^2\theta_0}, \end{aligned} \tag{3.3}$$

where θ_0 is the incident angle, θ_t is the complex transmitted angle given by the Snell-Descartes law: $n_1 \sin(\theta_0) = n_2 \sin(\theta_t)$, $n_1 = \sqrt{\epsilon_1}$ is the index of refraction of the incoming medium, $n_2 = \sqrt{\epsilon_2}$ of the substrate and $\omega/c = 2\pi/\lambda$ (c speed of light in vaccuum). As a reminder, s-polarization corresponds to an electric field perpendicular to the plane of incidence and parallel to the surface. In p-polarized light, the electric field located in the plane of incidence can be decomposed into components parallel and perpendicular to the surface. Equations similar to 3.3 including second order terms can be found in references [Bedeaux and Vlieger, 2001, Haarmans and Bedeaux, 1995]. The reflection coefficients in energy are given by $R_s = |r_s|^2$ and $R_p = |r_p|^2$ [Jackson, 1975]. If there is no perturbed interfacial zone *i.e.* $\gamma = \beta = 0$, one recovers the classical expression of the Fresnel coefficients of a semi-infinite substrate. In the case of differential reflectivity, the formula can be greatly simplified in the limit of very large wavelength *i.e.* $2\pi/\lambda|\gamma|, 2\pi/\lambda|\beta| \ll 1$ for a non-absorbing substrate as in the case of alumina:

$$\begin{aligned} \frac{\Delta R_s}{R_s} &= \frac{8\pi}{\lambda}\frac{n_1\cos\theta_0}{\epsilon_2 - \epsilon_1}\mathrm{Im}\left[\gamma\right] \\ \frac{\Delta R_p}{R_p} &= \frac{8\pi}{\lambda}\frac{n_1\cos\theta_0}{(\epsilon_2-\epsilon_1)(\epsilon_2\cos^2\theta_0 - \epsilon_1\sin^2\theta_0)}\left[(\epsilon_2 - \epsilon_1\sin^2\theta_0)\mathrm{Im}(\gamma) - \epsilon_2^2\epsilon_1\sin^2\theta_0\mathrm{Im}(\beta)\right] \end{aligned} \tag{3.4}$$

Equations 3.4 call for a few comments. The $\Delta R/R$ signal is proportional to the absorption in the layer, either only along the parallel direction in s-polarization ($\mathrm{Im}\,[\gamma]$-term for $\Delta R_s/R_s$), or along both directions in p-polarization ($\mathrm{Im}\,[\gamma]/\mathrm{Im}\,[\beta]$-terms for $\Delta R_p/R_p$). Since γ, β are directly proportional to the thickness of the perturbed layer (see equation 3.1), the measured SDRS signal should increase linearly with the amount of matter. In passing, the long-wavelength approximation behind equations 3.4 might fail in the case where the plasmonic resonance scales up the susceptibilities to values higher than the film thickness [Lazzari et al., 2014b] (see below). Anyway, despite the simplicity of equations 3.3, all simulations of Fresnel coefficients used in this thesis are based on expressions involving all surface susceptibilities $\gamma(\omega), \beta(\omega), \delta(\omega), \tau(\omega)$.

To go further on, it is mandatory to be able to link the susceptibilities to the geometry and the nature of the perturbed layer. For a continuous film, the expression fo the surface susceptibilities (equation 3.2) are trivial. For a layer made out of nanoparticles of sizes much smaller than the wavelength, it is possible to demonstrate that γ, β are linked to their surface density ρ and to the two components of the average tensor of polarizability of the object, parallel $\langle\alpha_{\parallel}(\omega)\rangle$ and perpendicular $\langle\alpha_{\perp}(\omega)\rangle$ to the surface *i.e.*:

$$\gamma(\omega) = \rho\left\langle\alpha_{\parallel}(\omega)\right\rangle \quad \text{and} \quad \beta(\omega) = \rho\left\langle\alpha_{\perp}(\omega)\right\rangle. \tag{3.5}$$

$\alpha(\omega)$ links the induced dipole in each particle to the exciting electric field of the incident light which polarizes the particles at the frequency ω. The resulting oscillating dipole is damped by the imaginary part of the dielectric constant which generates optical absorptions dependent on frequency. The polarizability should be averaged over size/shape and spatial distribution. Since $\alpha(\omega)$ is proportional to the particle volume, the corresponding $\gamma(\omega), \beta(\omega)$ terms are proportional to the average film thickness $t = \rho \langle V \rangle$.

3.3 The optical response of supported particles

3.3.1 Truncated sphere and spheroidal models: the polarizability tensor

The key point is to calculate accurately the polarizability tensor of a supported particle of a given shape in the quasi-static approximation *i.e.* by neglecting retardation effects and by assuming that the object is embedded in an homogeneous field oscillating at frequency ω. The choice of the particle geometry plays a pivotal role in the calculation as well as the account of the break of symmetry induced by the substrate, namely the image effect. In the historical models of Yamaguchi [Yamaguchi et al., 1973, Yamaguchi et al., 1974], the particle is replaced by a full spheroid the polarizability of which is known analytically in an homogeneous medium [Bohren and Huffman, 1983, Kreibig and Vollmer, 1995, Jackson, 1975]. The equivalent point dipole is then corrected from the interaction with its the image dipole leading to a renormalized expression of the polarizabilities; this case will be fully rederived in section 3.7 using Fourier transform of the Laplace equation instead of the dipole potential before a generalization to multilayers. But the weakness of such an approach is the lack of account of the cascade of polarization induced by the substrate. Indeed, the image dipole creates a non-constant field around the spheroid that gives rise to a quadrupole. The mirror of this latter in the substrate creates a quadrupolar field that excites an octopole and so on. Even if the Yamaguchi model grasps the main physics of image effect, by truncating the expansion of the potential to the dipole term, the way the particle is polarized is poorly described on a quantitative point of view. Moreover, on a physical point of view, the equilibrium shape of a supported particle involves a truncation of the Wulff shape by the substrate due to the interface energy. A first description is given by the truncated sphere which corresponds to the equilibrium shape of a material of isotropic surface energy. More flexibility to describe out-of-equilibrium situations is given by the truncated spheroidal shape which covers a larger range of aspect ratios.

Therefore, to obtain the polarizabilities in the case of a truncated sphere or spheroid (oblate and prolate) [Wind et al., 1987b, Wind et al., 1987a, Simonsen et al., 2000, Lazzari et al., 2001, Bedeaux and Vlieger, 2001] (figure 3.1-b,c), the Laplace equation $\nabla^2\Psi(\mathbf{r}) = 0$ for the electrostatic potential $\Psi(\mathbf{r})$ is solved exactly by accounting for the continuity of the potential and of the normal derivative of the displacement field at all interfaces. The potential is expanded over a multipolar basis in spherical (r, θ, ϕ) or spheroidal coordinates centered on the object and its image point to take into account naturally the boundary conditions on the flat surface of the substrate (image effect; see figure 3.1-b). The basis elements are products of a spherical/spheroidal harmonics Y_{lm} and of a radial function. For instance, in vacuum for a truncated sphere, the potential reads:

$$\Psi_1(\mathbf{r}) = \Psi_0(\mathbf{r}) + \sum_{l,m}^{l\neq 0} A_{lm} Y_{lm}(\theta, \phi) r^{-l-1} + \sum_{l,m}^{l\neq 0} A^r_{lm} Y_{lm}(\theta^r, \phi^r) \rho^{-l-1} \tag{3.6}$$

with (r, θ, ϕ) and (ρ, θ^r, ϕ^r) are the spherical coordinates from the direct and image points and

$\Psi_0(\mathbf{r})$ the potential for a homogeneous constant electric field. The reflected expansion coefficients A^r_{lm} are related to the direct ones by image effect: $A^r_{lm} = \frac{\epsilon_2-\epsilon_1}{\epsilon_2-\epsilon_1}A_{lm}$. The polarizabilities are given by the dipolar term *i.e.* $\alpha_\parallel \propto A_{l=1,m=\pm1}$ and $\alpha_\perp \propto A_{10}$. Boundary conditions on the surface of the particle are accounted for in a weak way by projecting them on a given spherical or spheroidal harmonics. By stopping the projection up to an oder M, this yields two linear systems of equations $\mathcal{M}_m A_{lm} = \mathcal{E}_m; m = 0, \pm1$ for the unknown multipolar coefficients of the potential expansion A_{lm}. Each of system of equation corresponds to the two components of the electric field, parallel $m = \pm1$ and perpendicular $m = 0$ to the surface. The right hand side of the system of equation comes from the two components of the excitating electric field. The elements of the matrix system depend on the dielectric functions of the various media (particle $\epsilon_{3,4}$, substrate ϵ_2, vacuum ϵ_1; figure 3.1-b,c) and on the particle shape through complex integrals (see references [Wind et al., 1987b, Wind et al., 1987a, Simonsen et al., 2000, Lazzari et al., 2001, Bedeaux and Vlieger, 2001] for details). Once filled up to a multipolar order M, the linear system of equations is solved numerically for each frequency and the polarizability is then obtained as the first term in the multipolar expansion. The convergence as a function of M depends on the particle truncation parameter, the importance of the image effect and the precision of the numerical integrals [Simonsen et al., 2000]. In general, a value of $M = 24$ (as used herein) turns out to be enough to reach a satisfactory precision in the case of alumina.

In the case of particle collection (figure 3.1-a), the polarizability is then corrected from the electrostatic effect of the neighbors to the dipolar or quadrupolar order which proved sufficient for a coverage lower than 50% [Lazzari et al., 2002]. Anyway, while higher orders are needed above this value, on an experimental point of view, morphology escapes the simple models of tuncated sphere/spheroid as the film starts percolating. Considering the interparticle coupling to dipolar order results mainly in a shift of the resonance to the red (blue, respectively) for the parallel (perpendicular, respectively) components of the polarizability without a noticeable change of the integrated intensity [Yamaguchi et al., 1973, Yamaguchi et al., 1974, Lazzari et al., 2003b]. Numerically, particles are usually arranged on a regular lattice (hexagonal, herein) since the difference between random and regular lattices turned out to be minor [Lazzari, 2000]. In order to get a rather good simulated fits of the experimental spectra, one should account for the inhomogeneous broadening which is inherent to the shape an size distributions. To avoid actual average and to allow tractable fits, it was chosen to fold the polarizabilities expression of the monodisperse case with gaussians as follows [Lazzari and Jupille, 2011]:

$$\langle \alpha_{\parallel,\perp}(\omega) \rangle = \frac{1}{\sigma_{\parallel,\perp}\sqrt{2\pi}} \int_{\omega_1}^{\omega_2} d\omega' \alpha_{\parallel,\perp}(\omega') \exp\left[-\frac{(\omega-\omega')^2}{2\sigma^2_{\parallel,\perp}} \right] \tag{3.7}$$

where ω_1 and ω_2 delimit the accessible spectral range, and $\sigma_{\parallel,\perp} \ll \omega_2 - \omega_1$ is an *ad hoc* gaussian width [Lazzari et al., 2014b, Lazzari and Jupille, 2011]. This convolution technique allows to reproduce satisfactorily the experimental spectra as it keeps constant the integrated oscillators strengths of polarization modes [Lazzari and Jupille, 2011] (see below). But it assumes a constant broadening whatever the modes which may be true if modes of dipolar character dominate the spectrum. The obtained morphology with such fits corresponds to the average particles on an optical point of view.

All this optical formalism was implemented in the *GranFilm* software developed by R. Lazzari and I. Simonsen [Granfilm, , Lazzari and Simonsen, 2002]. *GranFilm* includes the geometries of continuous film, rough film, truncated sphere/spheroid (oblate or prolate) layer.

3.3.2 Eigenmodes of polarization

In the artificial limit of zero damping, the matrix writing $\mathcal{M}_m A_{lm} = 0$ of the solution of the Laplace equation for the multipolar coffecicients A_{lm} in the case of a truncated sphere/spheroid allows to define the eigenmodes of polarization as the zero of the determinant of the real part of the matrix. The eigenvectors correspond to charge oscillation patterns that do not need an external field to be present. The mapping of the potential allows to locate the corresponding polarization charges. Compared to a full sphere or spheroid in vacuum, the break of symmetry due to the truncation and to the interaction with the substrate gives rise to the birth of a set of eigenmodes the energies and oscillator strengths of which depend on the dielectric function of the media and on the truncation. Their existence allows to derive, through an expansion to first order of the matrix system around each modes [Román-Velázquez et al., 2000, Lazzari et al., 2002, Lazzari et al., 2014b], a spectral representation of the polarizabilities of Kramers-Heisenberg type in terms of damped oscillators:

$$\alpha(\omega) \cong \alpha_{bk}(\omega) + \sum_i \frac{F_i \Gamma_i \sqrt{4\omega_i^2 - \Gamma_i^2}}{\omega_i^2 - \omega^2 - i\omega\Gamma_i}. \tag{3.8}$$

ω_i is the oscillator frequency, Γ_i is the broadening related to the damping, F_i is the oscillator integrated force and $\alpha_{bk}(\omega)$ is a non resonant term that accounts in particular for bulk absorption. F_i is proportional to the particle volume V, and when normalized it, it is together with ω_i mainly driven by the particle aspect ratio A_r [Lazzari et al., 2014b] [1]. The flatter the particle the higher F_i. As a result of dipolar electrostatic interactions between particles [Lazzari et al., 2002, Bedeaux and Vlieger, 2001, Lazzari et al., 2014b] (as demonstrated by replacing the bare polarizability with an oscillator in equation 3.76), the polarization modes are shifted in frequency according to:

$$\omega_i(\rho) = \omega_i(\rho = 0) \pm S\sqrt{\rho} F_i, \tag{3.9}$$

with the particle density ρ and the oscillator strength of the considered mode F_i. $S > 0$ is a constant prefactor related to the dielectric function, the ± sign is related to the parallel (+) and perpenicular (-) modes, and $\omega_i(\rho = 0)$ is the mode frequency of the isolated particle which is a function of the particle shape and therefore of F_i/V [Lazzari et al., 2014b].

For a substrate with a nearly constant real dielectric function, it turns out that, depending on the aspect ratio and truncation, the modes will appear at given values of the real part of the particle dielectric function. For truncated particle, a limited number of modes shape the experimental spectra (figure 3.2). Finally, when full absorption is taken into account, mode broadening and mixing blur the landscape (see section 3.6 for Cr and Zn).

3.3.3 Treatments of differential reflectivity spectra: inversion, signal integration and f-sum rule

As shown by the long-wavelength expression of the differential reflectivity for a non-absorbing substrate (equation 3.4), $\mathrm{Im}[\gamma(\omega)]$ and $\mathrm{Im}[\beta(\omega)]$ can be easily obtained from a simultaneous measurement of SDRS signals in s- and p-polarization. This is provided by the setup used in the present thesis. Nevertheless, a more elaborate and general inversion algorithm of SDRS, that goes beyond the $2\pi/\lambda|\gamma|, 2\pi/\lambda|\beta| \ll 1$ and non-absorbing substrate approximations, has been developed to deconvolute the film optical signature from that of the substrate and to

---

[1] For supported particle, A_r is defined as the ratio between the in-plane diameter and the height of the particle. The higher A_r the better the wetting.

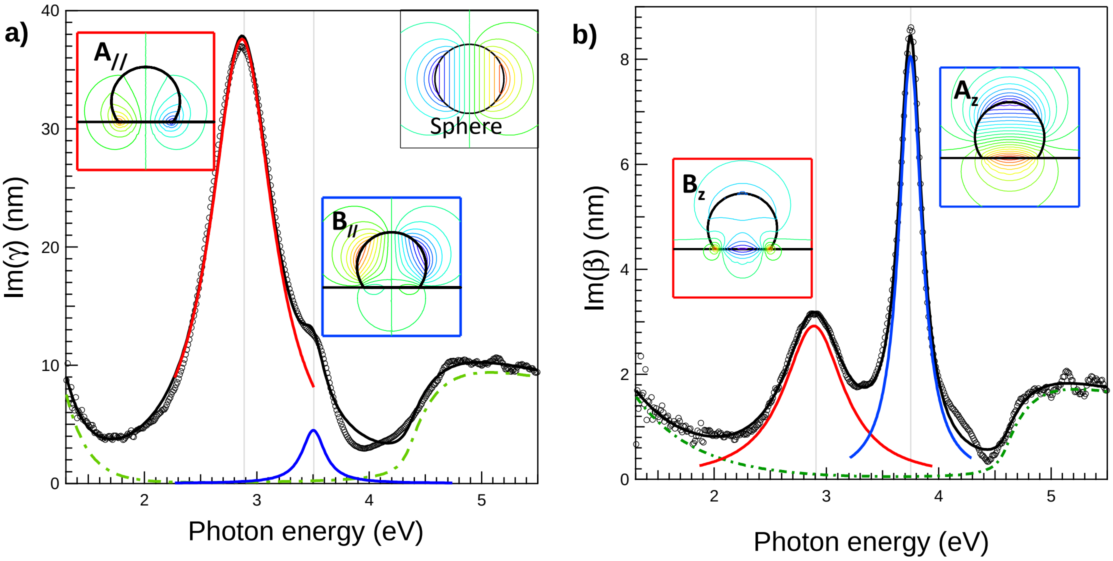

Figure 3.2: Decomposition of the experimental surface susceptibilities $\gamma(\omega), \beta(\omega)$ of Ag/Al$_2$O$_3$ nanoparticles with four oscillators (red and blue lines; equation 3.8) plus a interband transition background term (green line). The corresponding undamped modes $A_{\|}, B_{\|} A_{\perp}, B_{\perp}$ are mapped through potential lines. From reference [Lazzari et al., 2014a].

separate the parallel $\gamma(\omega)$ and perpendicular $\beta(\omega)$ film contributions which are intertwinned in p-polarization. The method is based on a numerical inversion of equations 3.3 that links the reflection coefficients and the susceptibilities under the constraints of Kramers-Kronig relation between real and imaginary parts of the complex causal quantities $\gamma(\omega), \beta(\omega)$:

$$\operatorname{Re}[\gamma;\beta(\omega)] = \frac{2}{\pi}\mathcal{P}\int_0^{\infty} d\omega' \frac{\operatorname{Im}[\gamma;\beta(\omega')]}{\omega'^2-\omega^2} \tag{3.10}$$

The limited spectral range in the Kramers-Kronig transform is partially compensated by the residual obtained through a basic fit with a spheroid in interaction with the substrate [Lazzari et al., 2014b, Lazzari et al., 2014a].

Beyond the analysis of the spectral lineshape (see section 3.5 for Cr/Al$_2$O$_3$ and Zn/Al$_2$O$_3$ examples), SDRS signal integration may provide direct hints about the growth process and particle wetting without complex fitting. From the differential reflectivity formula in the long-wavelength approximation (equation 3.4) for non-absorbing substrate and from the spectral representation of the polarizability (equation 3.8), it appears that the integrated signal:

$$\mathcal{A}_s(t) = \frac{1}{t}\int_0^{\infty} \frac{1}{\omega}\frac{\Delta R_s}{R_s}(\omega) d\omega \propto \frac{1}{t}\sum_i \rho(t)\left\langle F_{i,\|}(t)\right\rangle = \sum_i \frac{\left\langle F_{i,\|}(t)\right\rangle}{\left\langle V(t)\right\rangle} \tag{3.11}$$

is proportional to the sum of the integral of damped oscillators *i.e.* their oscillator strenghts. $t = \rho(t)\langle V(t)\rangle$ corresponds to the average film thickness or to the evaporation time if the sticking coefficient is equal to one; $\rho(t)$ and $\langle V(t)\rangle$ are the particle density and its average volume. Since $\langle F_i(t)\rangle / \langle V(t)\rangle$ scales only with the average aspect ratio $\langle A_r\rangle$ [Lazzari et al., 2014b, Cavallotti, 2014a] [2], the evolution of $\mathcal{A}_s(t)$ informs directly about changes in aspect ratio. The

---

[2] To first order, particle-particle interaction only shift peaks and does not modify oscillator strengths.

case of p-polarization (equation 3.4) is less clear since it involves the subtraction of $\mathrm{Im}[\gamma(\omega)]$ and $\mathrm{Im}[\beta(\omega)]$ terms. The main restriction of this analysis is the limited spectral $[\omega_1, \omega_2]$ range available in the experiments; if a mode peaks outside $[\omega_1, \omega_2]$, the integration is biased. This analysis of $\mathcal{A}_s(t)$, applied in this work to the growth of Cr and Zn on alumina, put forward the steps of the Volmer-Weber growth process: nucleation, growth, coalescence/percolation. During nucleation, particle density increases; it then stays constant at nearly constant particle shape (and aspect ratio A_r) if equilibrium is reached during the growth phase; finally particles flatten and their aspect ratio increases during coalescence/percolation.
To show that the present approach is not restricted to a given metal or substrate but is really representative of the Volmer-Weber growth process, figure 3.3 compares the evolution of $\mathcal{A}_s(t), \mathcal{A}_p(t)$ for various couples of metal/substrate. Although the dielectric behaviors of the involved metals may be drastically different (see section 3.4), the overall trend of $\mathcal{A}(t)$ is always the same, with a U-curve shape characteristic of nucleation, growth coalescence (see figure 3.3-c). The case of Ag/ZnO and Zn/Cr/Al_2O_3 in figure 3.3 are pathological at large thickness due to the formation of a continuous film and a poor integration of the resonant signal in the available spectral range. With such a comparison, one can even say the particle aspect ratio is much larger for Zn/Al_2O_3 (growth at 100 K out-of-equilibrium), Zn/Cr/Al_2O_3, Ag/ZnO than for Ag,Au/Al_2O_3. This integration approach demonstrates the interest of SDRS in pinpointing in real time the different regimes of growth that would turned out to be very difficult with microscopy techniques.

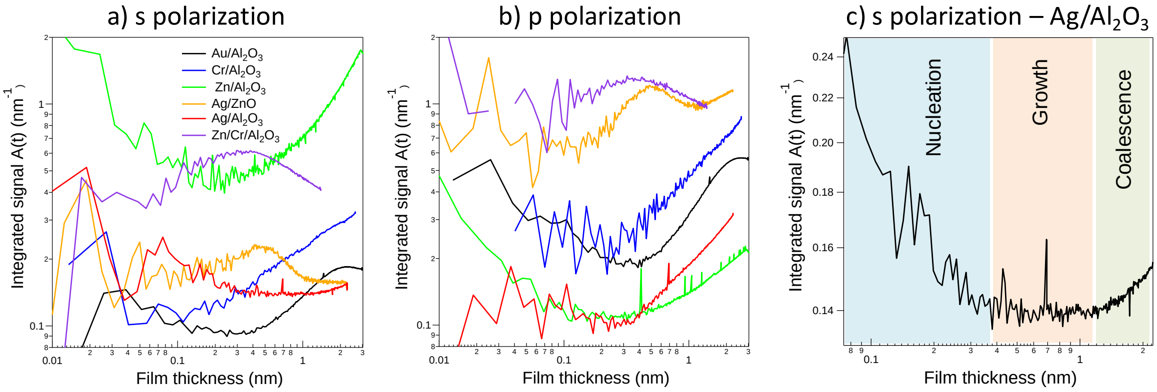

Figure 3.3: Integrated experimental differential reflectivity signal normalized to the thickness $\mathcal{A}(t)$ in a) s- and b) p-polarization for various metals on alumina and zinc oxide. For Zn/Cr/Al_2O_3, the intermediate Cr film has a thickness of 2.6 nm and the signal is normalized to Cr/Al_2O_3 reflectivity. All deposit are performed at room temperature except for Zn/Al_2O_3 performed at 100 K. c) Case of Ag/Al_2O_3 in s-polarization showing the different stages of nanoparticle growth.

Since interfacial susceptibilities are causal response functions, they should fulfill sum rules derived from the Kramers-Kronig link [Smith, 1985] between their real and imaginary parts (equation 3.10). At frequencies higher than any characteristic light absorption threshold, they are dominated by the inertial effects and not anymore by restoring or dissipative forces. Their asymptotic limits should therefore be given by:

$$\lim_{\omega \to +\infty} \mathrm{Re}[\gamma(\omega)] \simeq -t\frac{\omega_P^2(\gamma)}{\omega^2}, \quad \lim_{\omega \to +\infty} \mathrm{Re}[\beta(\omega)] \simeq -t\frac{\omega_P^2(\beta)}{\omega^2}, \tag{3.12}$$

where $\omega_P(\gamma), \omega_P(\beta)$ have the meaning of plasma frequencies related to the number of effective involved electrons [Smith, 1985] and t is the interface or film physical thickness. Within the reasonable assumption that $\mathrm{Im}[\gamma(\omega)]$ and $\mathrm{Im}[\beta(\omega)]$ falls off faster than ω^{-2} (which is the case for damped oscillator as in equation 3.8 or for any dielectric function), the high-frequency limit of the Kramers-Kronig relations:

$$\mathrm{Re}[\gamma(\omega)] = \frac{2}{\pi}\wp \int_0^{+\infty} d\omega' \frac{\omega' \mathrm{Im}[\gamma(\omega')]}{\omega'^2 - \omega^2}, \quad \mathrm{Re}[\gamma(\beta)] = \frac{2}{\pi}\wp \int_0^{+\infty} d\omega' \frac{\omega' \mathrm{Im}[\beta(\omega')]}{\omega'^2 - \omega^2} \tag{3.13}$$

lead to the so-called f-sum rules for the interfacial susceptibilities:

$$\omega_p^2(\gamma) = \frac{2}{\pi t}\int_0^{+\infty} \omega \mathrm{Im}[\gamma(\omega)] d\omega, \quad \omega_p^2(\beta) = \frac{2}{\pi t}\int_0^{+\infty} \omega \mathrm{Im}[\beta(\omega)] d\omega \tag{3.14}$$

When comparing to the continuous thin susceptibilities (equations 3.2), the above f-sum rules are a generalization of those well-known for the bulk dielectric $\epsilon(\omega)$ and loss $1/\epsilon(\omega)$ functions and provides a more proper interpretation of the direct integration of the SDRS signal.

3.4 Dielectric functions of the materials: Cr, Zn and Al_2O_3

Since the optical response of nanoparticles is driven by their dielectric behavior, it is logical to try to understand it in the bulk first. For a thin continuous film, the surface susceptibilities are even given directly by the dielectric function $\epsilon(\omega)$ and the loss function $1/\epsilon(\omega)$ for the directions parallel and perpendicular to the film. Cr and Zn, the two metals involved in this study, are compared in figure 3.4 to the well-known candidates of plasmonics, Au and Ag. $\epsilon(\omega)$ for Ag and Au were extracted from the compilation of Palik [Palik, 1985] the val-

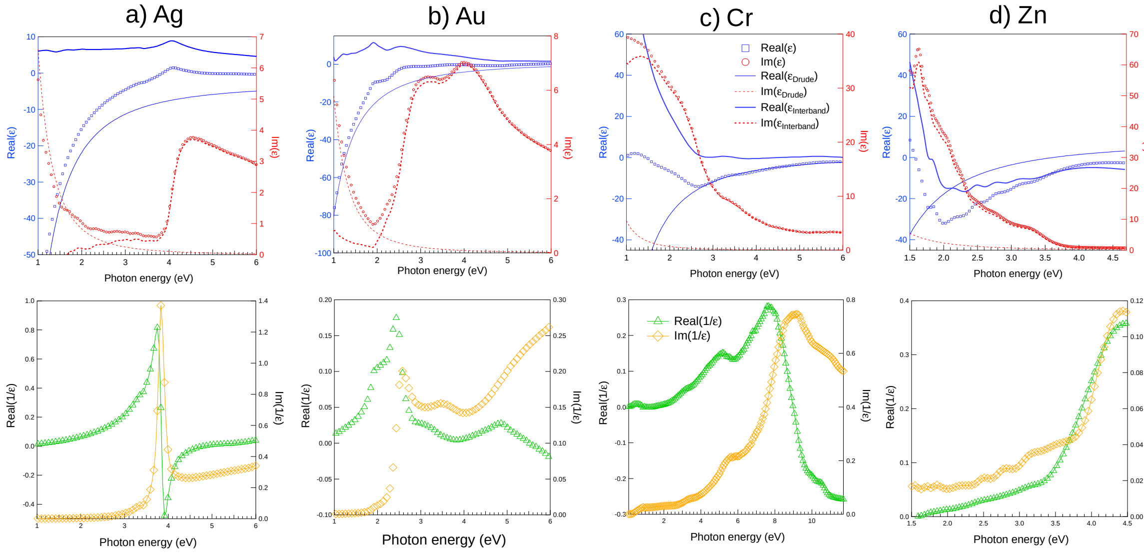

Figure 3.4: Dielectric functions $\epsilon(\omega)$ (top) and loss functions $1/\epsilon(\omega)$ (bottom) of various metals: a) Ag, b) Au, c) Cr, d) Zn. Real (respectively imaginary) parts are plotted on left (respectvely right) scales. $\epsilon(\omega)$ has been decomposed into Drude/interband (thin lines) and interband contributions (thick lines). Data have extracted from: Ag, Au [Palik, 1985, Johnson and Christy, 1972, Etchegoin et al., 2006], Cr [Bos and Lynch, 1970, Johnson and Christy, 1974, Palik, 1985, Rakić et al., 1998, Lovrinčić and Pucci, 2009], Zn [Mosteller Jr and Wooten, 1968, Rubloff, 1971, Weaver et al., 1972, Nash and Sambles, 1998].

ues of which compare well with other studies [Johnson and Christy, 1972, Stahrenberg et al., 2001]. For Zn, the most recent and exhaustive measurements of Nash and Sambles [Nash and Sambles, 1998] were preferred over the older ones on single crystals [Lenham and Treherne, 1964, Mosteller Jr and Wooten, 1968, Rubloff, 1971, Weaver et al., 1972] for the average over crystallographic orientations and for the lack of oxidation that is intrinsic to the performed measurements. Regarding Cr, $\epsilon(\omega)$ was extracted from references [Bos and Lynch, 1970, Rakić et al., 1998, Palik, 1985] instead of the work of Johson and Christy [Johnson and Christy, 1974] due to uncertainties on the grain/void structures in the used films.

In the plasmonic response of metals, a central issue is the mixing of free and bound electrons (or in other words, intraband and interband contributions) in resonant modes. In that sense, the four metals silver Ag($4\mathrm{d}^{10}5\mathrm{s}^1$), gold Au($5\mathrm{d}^{10}6\mathrm{s}^1$), chromium Cr($3\mathrm{d}^5 4s^1$) and zinc Zn($3\mathrm{d}^{10}4\mathrm{s}^1$) have similar s-shell filled with one electron but different filling for the d-shell. Added to a similar atomic density (Ag, Au: 0.058 atom.Å^{-3}, Cr: 0.081 atom.Å^{-3}, Zn: 0.066 atom.Å^{-3}), they should have a similar s-electron Drude behavior. Their dielectric constants were systematically decomposed into intraband and interband components in figure 3.4 as follows:

$$\epsilon(\omega) = \epsilon_p(\omega) + \epsilon_{ib}(\omega) = \epsilon_\infty - \frac{\omega_f^2}{\omega^2 - i\omega\Gamma_f} + \epsilon_{ib}(\omega). \tag{3.15}$$

The values of the plasma frequency $\hbar\omega_p = 9.17; 9.06; 10.75, 10.1$ eV and those of the damping factors $\hbar\Gamma_f = 0.021; 0.071; 0.047; 0.02$ eV, are extracted from the literature respectively for silver, gold [Johnson and Christy, 1972], chromium [Rakić et al., 1998], zinc [Mosteller Jr and Wooten, 1968]. These values were obtained by fitting the experimental data in the infrared region where the interband transitions are negligible for silver and gold [Johnson and Christy, 1972, Etchegoin et al., 2006], via the normal reflectance drop in the deep UV range for zinc [Mosteller Jr and Wooten, 1968] and through an accurate analysis from the infrared to the UV range of the dielectric function for Ag, Au and Cr [Rakić et al., 1998]. Despite similar Drude parameters, the four metals differ drastically on their interband transitions that progressively shift from 4 to 1.5 eV from Ag, Au, Cr and Zn. They are quite representative of different dielectric configurations of screening of s electrons by transitions involving d-ones. As a resonance in a particle will appear at a given value of $\mathrm{Re}[\epsilon(\omega)]$, plasmon absorption will be excited for silver nanoparticles in a energy range well below the interband transitions on the free electron contribution. For gold, they will be closer to interband transitions while for Zn and Cr, they are expected to happen on the tail of the interband transitions leading to a complex shape as explained afterwards. In particular, for Cr and Zn, since the link between $\mathrm{Re}[\epsilon(\omega)]$ and ω is non-bijective, a given resonant mode may appear at different energies.

As the optical measurements of this thesis were performed at room temperature, no variation of dielectric function had to be accounted compared to tabulated data [Lazzari and Jupille, 2011, Lazzari and Jupille, 2012]. However, in principle, the reduced lifetime of free electrons close to the Fermi surface due to surface/interface scattering induced by the confinement at the nanoscale (*i.e.* the size of particles < conduction electrons mean free-path) has to be taken into consideration through a modified relaxation time:

$$\Gamma_d = \Gamma_f + 2A\frac{v_f}{D}, \tag{3.16}$$

where v_f is the Fermi velocity of the metal ($\hbar v_f = 0.91; 0.90; 1.01; 0.97;$eV nm for Ag, Au, Cr, Zn), Γ_f the bulk relaxation constant, D the particles diameter and A a prefactor of the order of the unity [Kreibig and Vollmer, 1995,Kreibig and Fragstein, 1969,Kreibig, 1977]. Moreover, a reduced screening of s electrons by the more localized d-ones is to be expected when the surface/volume ratio increases in tiny particles; it is observed in silver below 1 nm in size and leads to a blue-shift with decreasing size [Liebsch, 1993]. However, since the observed resonances in Cr and Zn nanoparticles imply bound electrons that broadens the peaks (see below), one can expect a minor contribution of this effect which, anyway, was never documented for those metals.

Finally, the dielectric constant of the alumina substrate was taken from the Palik handbook [Palik, 1985] (inset of figure 3.5-a); it is nearly constant in the considered spectral range ($\epsilon(\omega) \simeq 3$) and without absorption because the large band gap of the material (≥ 9 eV). The calculated absolute reflection coefficients of Al_2O_3, Cr and Zn (figure 3.5) highlight the tremendous difference of optical properties between dielectrics and metals. Zinc is a better reflector than chromium and alumina is a good candidate for differential measurements as its absolute reflection is quite low thus enhancing relative signal. Due to a lower alumina reflectivity in p- than in s-polarization, SDRS signals should be always larger in p- than in s-polarization. In passing, all the optical data of this thesis have been referenced to alumina even in the case of several deposits.

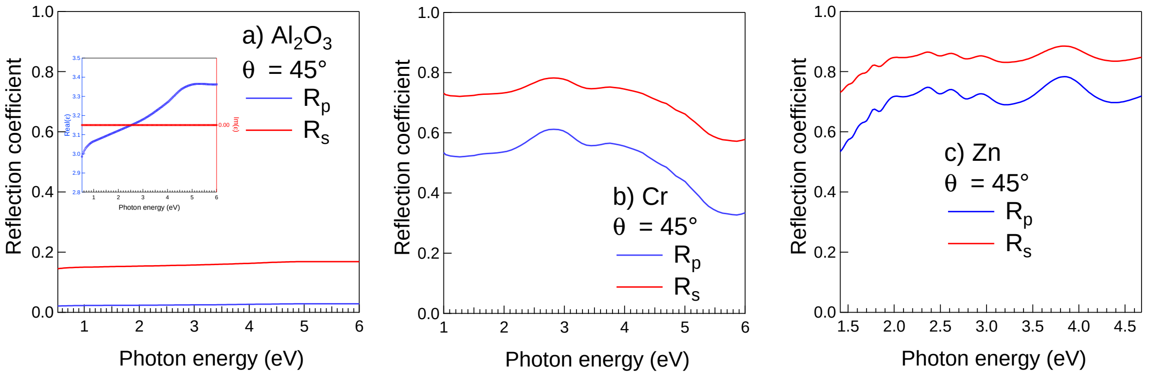

Figure 3.5: Calculated reflection coefficients in s- and p-polarization at $\theta_0 = 45°$ for semi-infinite substrate of a) Al_2O_3, b) Cr and c) Zn from the dielectric functions of figure 3.4. The inset of figure-a shows the dielectric function of alumina [Palik, 1985].

3.5 SDRS sensitivity to wetting of Zn and Cr on alumina

In the light of the complexity introduced by interband transitions in the dielectric functions of Cr and Zn compared to the well-knwon metals of plasmonics (Ag, Au), a strong damping of the plasmon resonances in nanoparticles is to be expected and may preclude any interest of optical measurements for the studies of wetting. To highlight the expected sensitivity to particle aspect ratio A_r (in-plane diameter D/height H), series of simulations of SDRS spectra have been performed at constant film thickness for Cr (figure 3.6) and Zn (figure 3.7) on alumina. Two shapes (top of figure 3.6) have been combined:

- an oblate hemispheroid ($R_\perp = H$) for aspect ratio $A_r = D_\parallel/H > 2$
- a truncated sphere for $A_r \leq 2$.

Of course, no particle-particle interactions have been accounted for since the coverage evolves with A_r at constant film thickness. The response of a continuous film (black line) has been added to figures for comparison. The conclusions from figures 3.6-3.7 are:

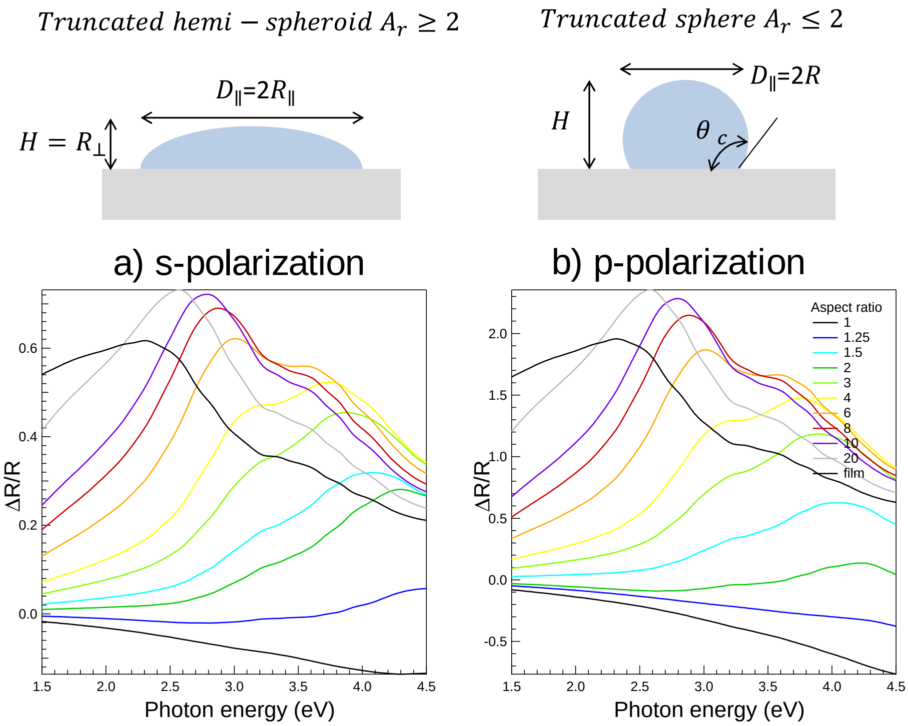

Figure 3.6: Simulated differential reflectivity spectra for Cr particles of different aspect ratios A_r on alumina in a) s- and b) p-polarization at $\theta_0 = 45°$. Particles are modeled by truncated hemispheroid or truncated sphere. The coverage was changed to keep constant the film thickness at 1.5 nm. $M = 24$ multipoles and bulk dielectric functions have been used.

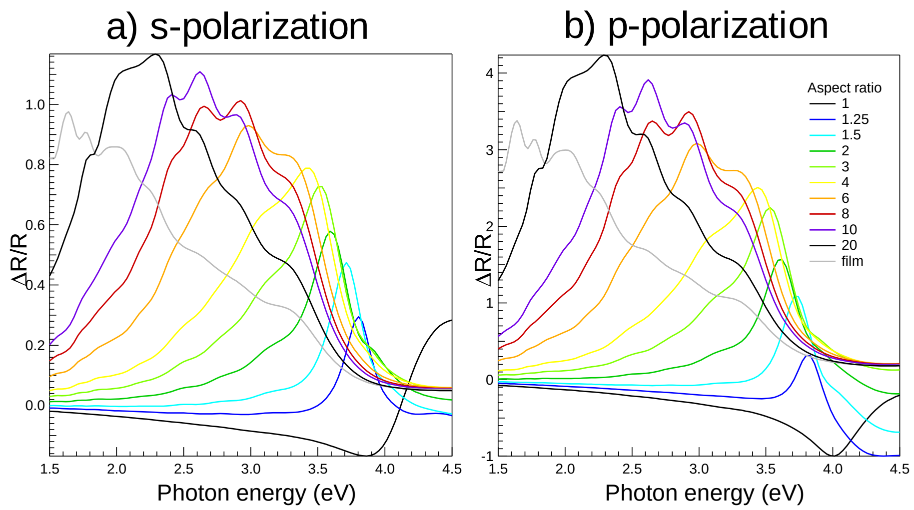

Figure 3.7: Same as figure 3.6 but for Zn.

- particle (Volmer-Weber) and Frank-van-der-Merwe (continuous film) growth modes have quite distinct optical signature;

- a resonance band both for Cr and Zn is clearly visible in the UV-visible domain accessible in measurements; it is quite sensitive to aspect ratio since poor wetting situation ($A_r > 2$) and flat particles are easily distinguished;
- measurements are poorly polarization-dependent, except on the intensity.

In a similar way to aspect ratio, the question of sensitivity to the surface covered by the particles $\Theta = \rho\pi R_{\parallel}^2$ (called coverage, afterwards) is of interest. It shows up through the electrostatic coupling between particles of density ρ. Figure 3.8 illustrates the role of particle-particle interaction at dipolar and quadrupolar order for a quite large coverage of $\Theta = 45$ % but below percolation threshold. For both metals, an enhancement of intensity at lower energy is present when switching on the interactions as expected from a global redhshift of peak centroid. But, owing to the inherent inhomogeneous broadening of experimental peaks, SDRS fits are expected to be poorly sensitivity to the coverage. In passing, even at a significant high coverage, the difference between dipolar and quadrupolar coupling is minor.

To prove that the positive differential reflectivity bump do correspond to an absorption as expected from expression 3.4, all the computed Fresnel coefficients (reflection R, transmission T and absorption $A = 1 - R - T$) have been plotted in figure 3.9 for a 1.5 nm thick nanoparticle film. The slight increase of reflection parallels a strong dip of transmission leading to an overall positive absorption.

3.6 Zinc and Chromium: plasmonics on interband transitions

To better understand experimental SDRS spectra and knowing the involvement of interband transitions, inversion of experimental data and dielectric simulations will be combined to grasp the way the Cr or Zn nanoparticles on alumina are polarized compared to noble metals.

3.6.1 Chromium

As shown in figure 3.10, the SDRS optical response of a chromium film on alumina, whatever the polarization, is dominated by a broad bump which maximum shifts from 3.7 to 2.7 eV. This band falls in the frequency range of interband transitions of Cr (figure 3.4-c). To clarify the reading of the optical anisotropy between the parallel and perpendicular directions, spectra have been inverted to obtain $\mathrm{Im}[\gamma(\omega)]$ and $\mathrm{Im}[\beta(\omega)]$ using the algorithm of references [Lazzari et al., 2014b, Lazzari et al., 2014a] (section 3.3.3). The resulting strong anisotropy of surface susceptibilities (figure 3.10-c,d) is a signature of the growth of flat objects. Notice that the absolute values of susceptibilities are much larger than the actual film thickness due to the resonant effect of the "plasmon" oscillations. As expected from equation 3.4, the dip in $(\Delta R/R)_p$ gives rise to a peak in $\mathrm{Im}[\beta(\omega)]$. Amazingly, this latter just increases in intensity with thickness while $\mathrm{Im}[\gamma(\omega)]$ involves a feature that starts around 3.7 eV and continuously increases in intensity at low photon energy.

The plasma frequencies $\omega_P(\gamma)$ obtained from sum rules (equation 3.14) applied to inverted experimental susceptibilities on the available spectral range are plotted in figure 3.11 and compared to values expected from tabulated bulk dielectric constants (figure 3.4 [Palik, 1985])

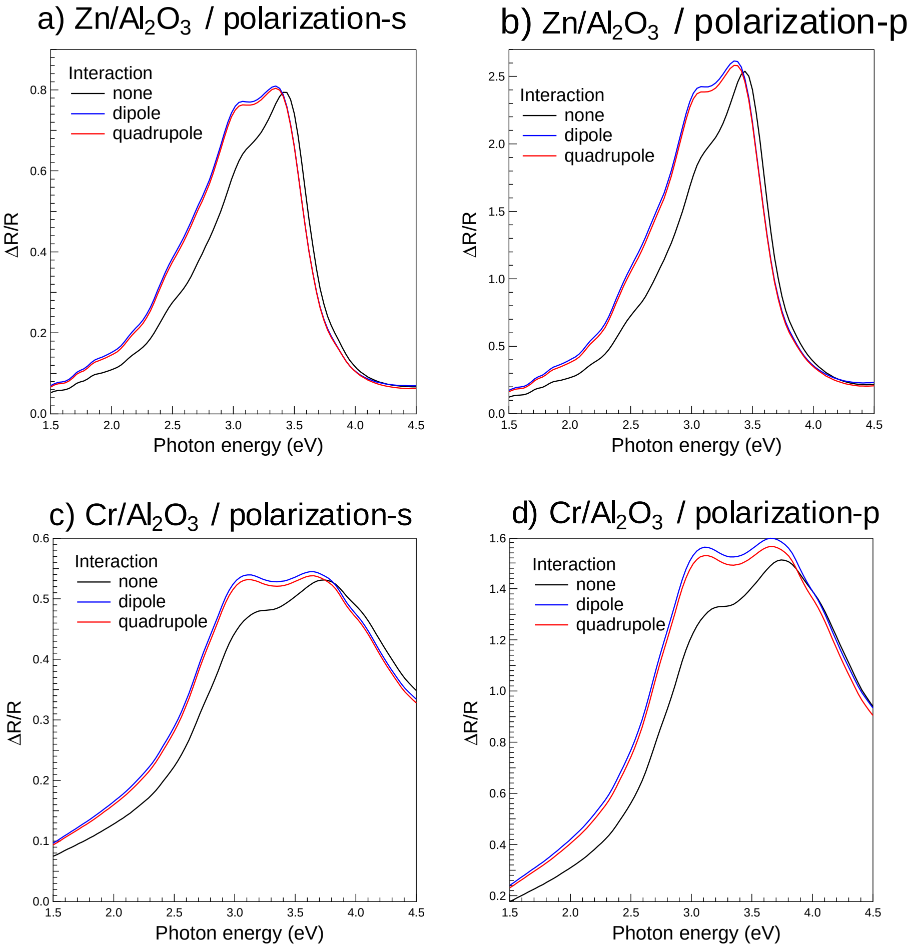

Figure 3.8: Effect of particle-particle interactions on simulated differential reflectivity spectra of Cr and Zn nanoparticles on alumina. Particles are modeled by hemispheroid of $R_{\|} = 10$ nm, $A_r = 4$ covering $\Theta = 45$ % of the substrate. Interaction are calculated on an hexagonal lattice of parameter $L = 28$ nm. The film thickness is $t = 1.5$ nm.

i.e. :

$$\omega^2_{P,bulk}(\gamma) = \frac{2}{\pi}\int_0^{+\infty} \omega \mathrm{Im}[\epsilon(\omega)]d\omega, \quad \omega^2_{P,bulk}(\beta) = \frac{2}{\pi}\int_0^{+\infty} \omega \mathrm{Im}[1/\epsilon(\omega)]d\omega. \tag{3.17}$$

$\omega_P(\gamma)$ tends to a constant value in the limit of the thickest films since the UV-visible spectral range encompasses most of the plasmon resonances of the nanoparticles after a progressive increase in lower thickness range. While $\omega_P(\gamma)$ increases with thickness, $\omega_P(\beta)$ is nearly constant pointing at different growth mechanisms along the parallel and perpendicular direction. Since the sum rules analysis also includes interband absorptions and substrate contributions, the agreement with the bulk behavior at large thickness validates *a posteriori* the inversion process [Lazzari et al., 2014a] which should fulfill electron conservation.

A raw comparison with simulations of figure 3.6 points at an initial Volmer-Weber growth of particles of aspect ratio larger than 3 up to to the formation of a nearly continuous film. More accurate fits will be presented in the next chapter. For the time being, a typical hemispheroidal shape of $A_r = 4$ will be used to better understand the observed experimental

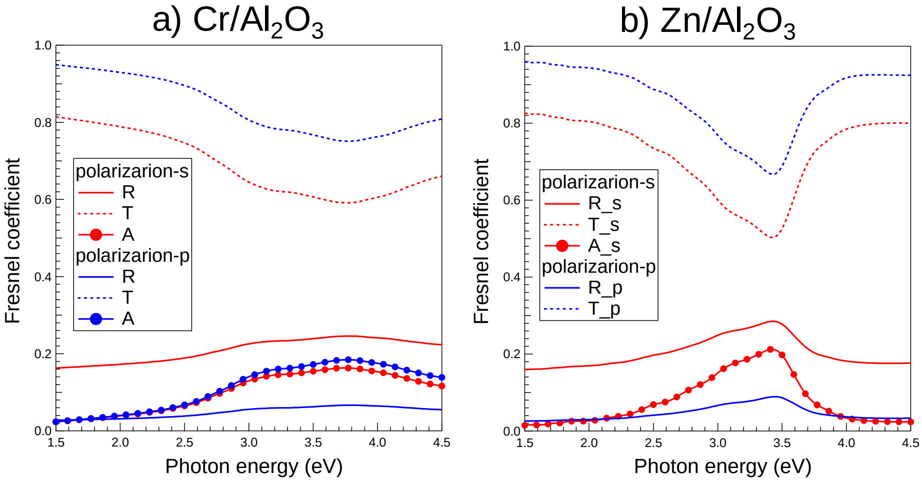

Figure 3.9: Calculated Fresnel coefficients (R=reflection, T=transmission, A=absorption) of a layer of nanoparticles of aspect ratio $A_r = 4$ (hemispheroid) in s- and p-polarization for a) Cr/Al_2O_3 and b) Zn/Al_2O_3. The coverage is $\Theta = 22.5$ % and $\theta_0 = 45°$.

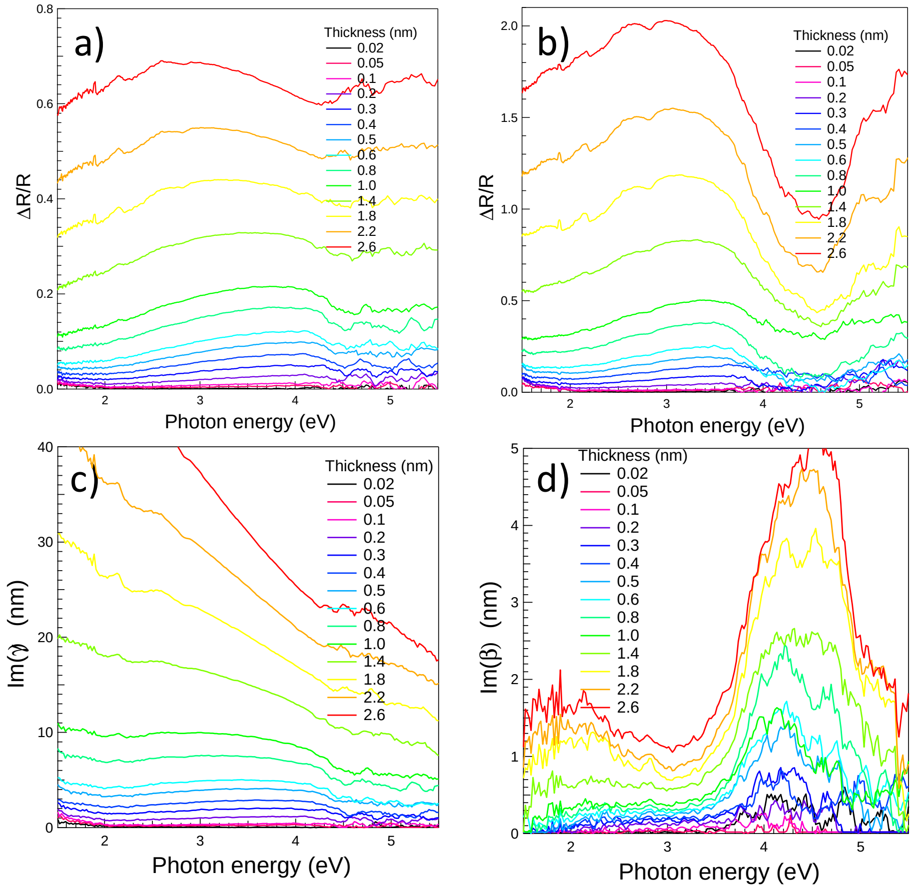

Figure 3.10: a)b) Differential reflectivity spectra collected during the room-temperature growth of Cr on $Al_2O_3(0001)$-(1×1) in a) s- and b) p-polarization. Thickness scale is calibrated on photoemission quantification. b)d) Imaginary parts of the experimental susceptibilities $\gamma(\omega), \beta(\omega)$ obtained from the inversion of the experimental data. Note the difference of scales on the two graphs.

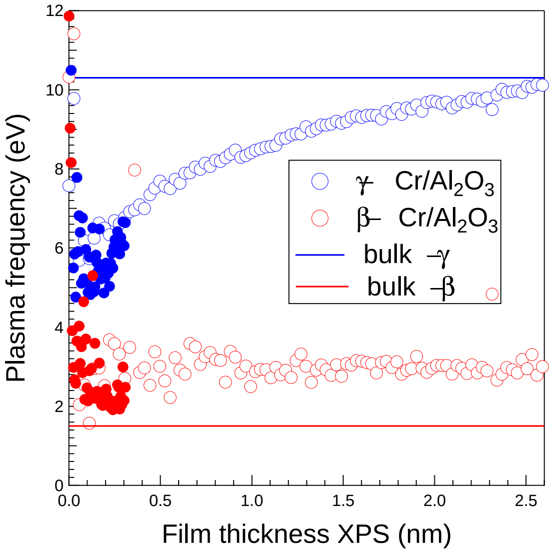

Figure 3.11: Plasma frequencies $\omega_P(\gamma), \omega_P(\beta)$ (points) obtained from f-sum rules (equations 3.14) applied to the growth of Cr film on Al$_2$O$_3$. They are compared to bulk values derived from the tabulated dielectric function (equations 3.17). Two data sets are compared (open and filled symbols).

features. Several simulations have been performed with fictitious dielectric functions for the metal (figures 3.12). When the imaginary part of the dielectric function of Cr is drastically reduced, the absorption coefficient becomes dominated by four modes along each direction, parallel (figure 3.12-a) and perpendicular (figure 3.12-b). The polarization charges of those modes excited in a metal without damping are mapped, through equipotential lines that surrounds charges, in figure 3.13. Through a comparison to the real part of the Cr dielectric function, these maps demonstrate that the modes go in pair, whatever the direction, due to the non-bijective dependence between ω and Re$[\epsilon(\omega)]$. Along the parallel direction, two main patterns of polarization are present: (i) the mode $A_{\parallel}$ around 2.5-3 eV displays charge localization at the apex of the particle while (ii) a dipole is present at the interface inside the particle for mode $C_{\parallel}$ at 1.8 and 4.3 eV. For Cr, only normal modes with ring shapes charges at the interface and a charge on top are present (modes $B_{\perp}, C_{\perp}$). Compared to previous findings for noble metals (Ag,Au/Al$_2$O$_3$) [Lazzari et al., 2002, Lazzari et al., 2014a] (see figure 3.2), the classical mode $A_{\perp}$ corresponding to a dipolar spreading of charge along the normal direction is absent. In a similar way, the mode $B_{\parallel}$ associated to a dipole parallel to the surface but shifted from the interface is not excited in Cr. The reason lies in different dielectric functions but also in the flattening of the object that mix $A_{\parallel}$ and $B_{\parallel}$ modes. Upon increasing damping *i.e.* the imaginary part of the dielectric function of the metal, peaks broaden and overlap. Mode mixing happens. In particular, modes below 2 eV are washed out by the sharp increase of Im$[\epsilon(\omega)]$ (figure 3.13). Simulations of figures 3.13 with only the Drude or interband components of $\epsilon(\omega)$ help to assign and interpret the surviving $A_{\parallel}, C_{\parallel}$ and $B_{\perp}, C_{\perp}$ modes above 2 eV. Modes $A_{\parallel}$ at 2.9 eV and $C_{\parallel}$ at 4.3 eV can be excited on the Drude component (figure 3.13-c, green line) but are strongly damped by interband transitions. On the other hand, the mode $A_{\parallel}$ at 2.4 eV is activated only on the real part of the dielectric function of interband transitions (red line in figure 3.12). As expected from the decay of $\epsilon_{interband}$ at large energy, perpendicular modes $C_{\perp}$ and $B_{\perp}$ at 3.9 and 4.4 eV are of Drude character.

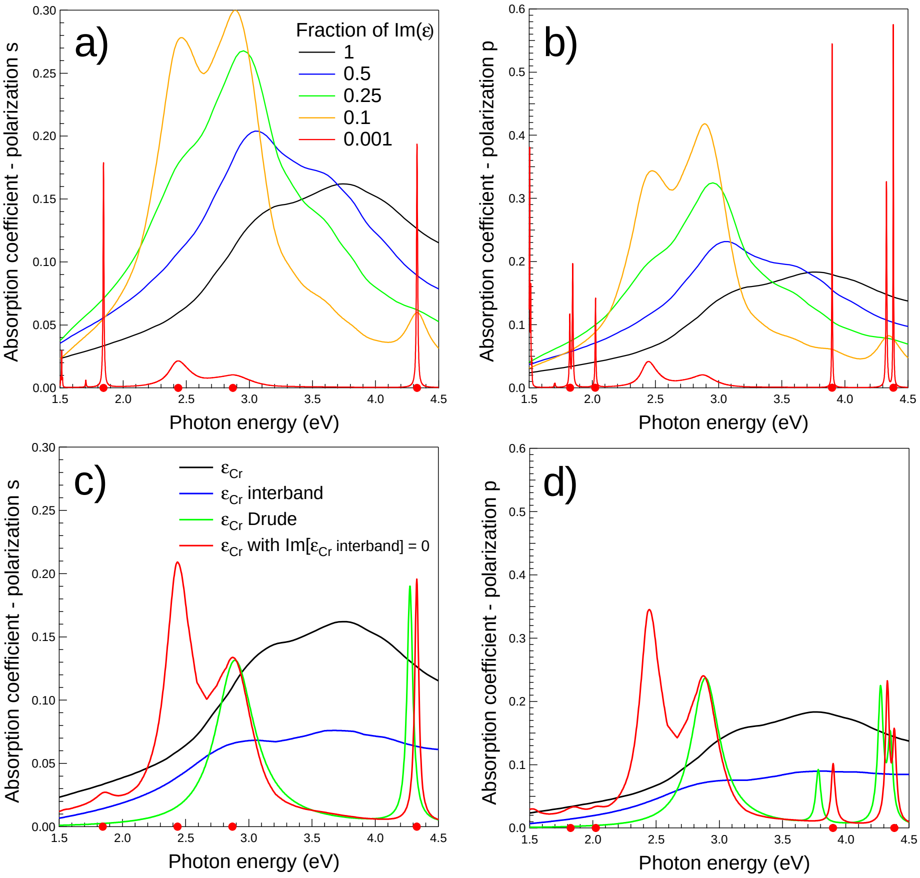

Figure 3.12: Calculated absorption coefficient in a)c) s- and b)d) p-polarization for a layer of hemispheroids of Cr/Al_2O_3 of aspect ratio $A_r = 4$ (coverage 25 %, film thickness 1.5 nm, incident angle $\theta_0 = 45°$) for different models of dielectric function for the metal. a)b) Only a given fraction of the imaginary part of the Cr bulk dielectric function is accounted for, c)d) $\epsilon_{metal}(\omega)$ only consists of the total, interband or Drude contributions or a fictitious $\epsilon(\omega)$ in which the imaginary part of the interband component has been canceled. The positions of the most intense resonant modes observed at small damping (red line in figures a,b) are pointed by red symbols; only the perpendicular active ones are shown in the p-polarization graph.

Since resonance frequencies are related to $\mathrm{Re}[\epsilon(\omega)]$ and damping to $\mathrm{Im}[\epsilon(\omega)]$, this distinction between Drude and interband reverts to distinguish in $\epsilon(\omega)$ ranges dominated by one or the other. This is quite artificial since mode mixing happens with the actual dielectric function. An other point of view is given by the plots of the imaginary part (and not the real as for the above modes) of the potential maps with a full account of damping. Those maps points at the region of enhanced absorption. As seen in figure 3.14, patterns similar to the eigenmodes are observed showing the robustness of the interpretation. Nevertheless, maps are distorted in p-polarization at $\theta_0 = 45°$; a better correspondance with previous finding is obtained at $\theta_0 = 90°$ with an excitation field only normal to the surface and not inclined at 45°.

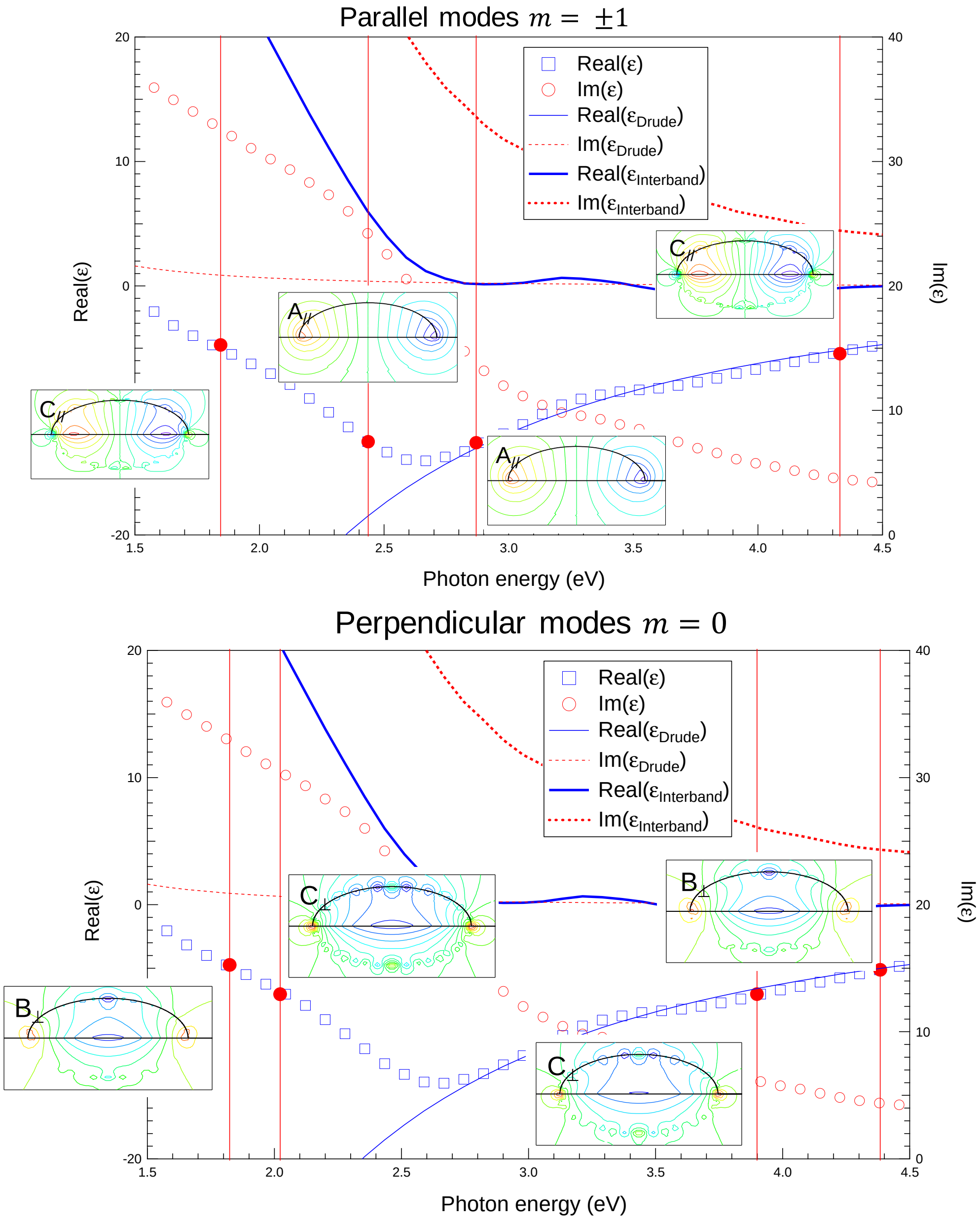

Figure 3.13: Maps of potential (real part) corresponding to the most intense undamped modes of polarization of figure 3.12 (red symbols). The equipotential lines surrounds the polarization charges. The black line stand for the contour of the particle. Energy positions (red verticals) are overlapped with the decomposition of the bulk dielectric function of Cr in Drude and interband contibutions. Note the symmetry plane perpendicular to the figure for parallel modes $m = \pm 1$ and the revolution axis normal to the substrate for the perpendicular ones $m = 0$. The labeling of modes follows findings of reference [Lazzari et al., 2014a].

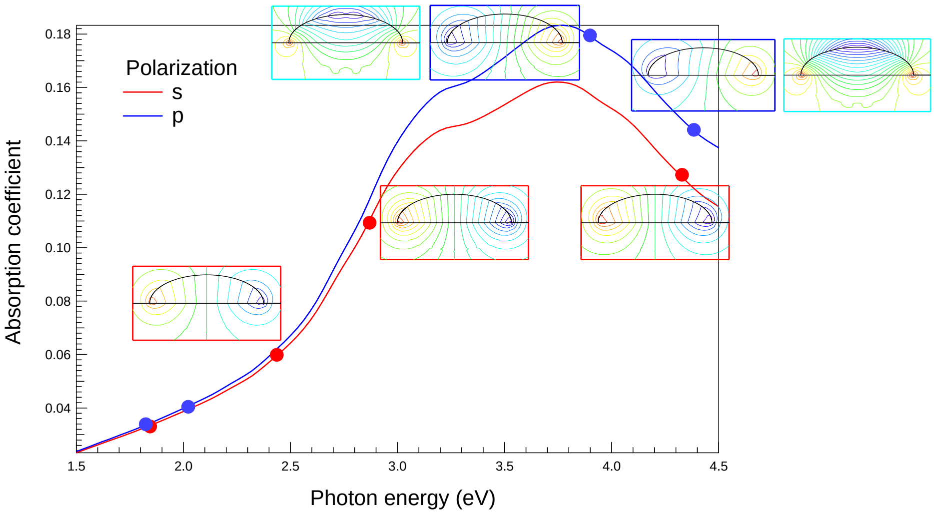

Figure 3.14: Maps of the imaginary component of the potential at energies corresponding to the eigenmodes of polarization pointed in figures 3.12-3.13. Maps calculated in s- or p-polarization at $\theta_0 = 45°$ are overlapped on the full absorption coefficients. Red (blue) boxes correspond to parallel (perpendicular) modes. Light blue boxes corresponds to a geometry where the electric field is normal to the surface ($\theta_0 = 90°$ in p-polarization).

3.6.2 Zinc

To see the parallel to Cr, exactly the same analysis with the same shape was performed with Zn (figures 3.15, 3.16, 3.13). When Im$[\epsilon_{Zn}(\omega)]$ is reduced, a similar set of eigenmodes of $A_{\parallel}, C_{\parallel}, B_{\perp}, C_{\perp}$ types can be excited in Zn nanoparticles (figures 3.15-a,b). As in the case of Cr, they go in pair due to the non-bijective relation between ω and Re$[\epsilon_{Zn}(\omega)]$ and those below 2 eV are broadened and killed by the increase of Im$[\epsilon_{Zn}(\omega)]$. But at the opposite to Cr, it appears from simulations of figure 3.15-c,d (red vs green lines), that the main bump around 3-3.5 eV is not excited on the Drude component of the dielectric function but on the tail of the interband transitions that induces an assymetric shape of the Fano type as observed in the case of Pd particles [Pakizeh et al., 2009]. Finally, as in the case of Cr, plots of the imaginary part of the potential at full damping and at eigenmodes energies (figure 3.17) do confirm the above interpretation in terms of polarization modes.

In conclusion, if for free electron metals like alkali or silver, the optically excited adsorption in nanoparticles are driven by the intraband transitions, those in chromium objects are strongly damped by the interband transitions. For Zn, they happen on a tail of interband transition. At the opposite to silver (figure 3.4), the U-shape variation of Re$[\epsilon(\omega)]$ for Cr and Zn gives rise to the excitation of the same mode at different energies. At last, it worth to stress that, while the nature of the observed modes of polarization is the same as they are intrinsic to the particle shape, their presence in an actual spectrum is strongly dependent on the structure of the dielectric function of the metal.

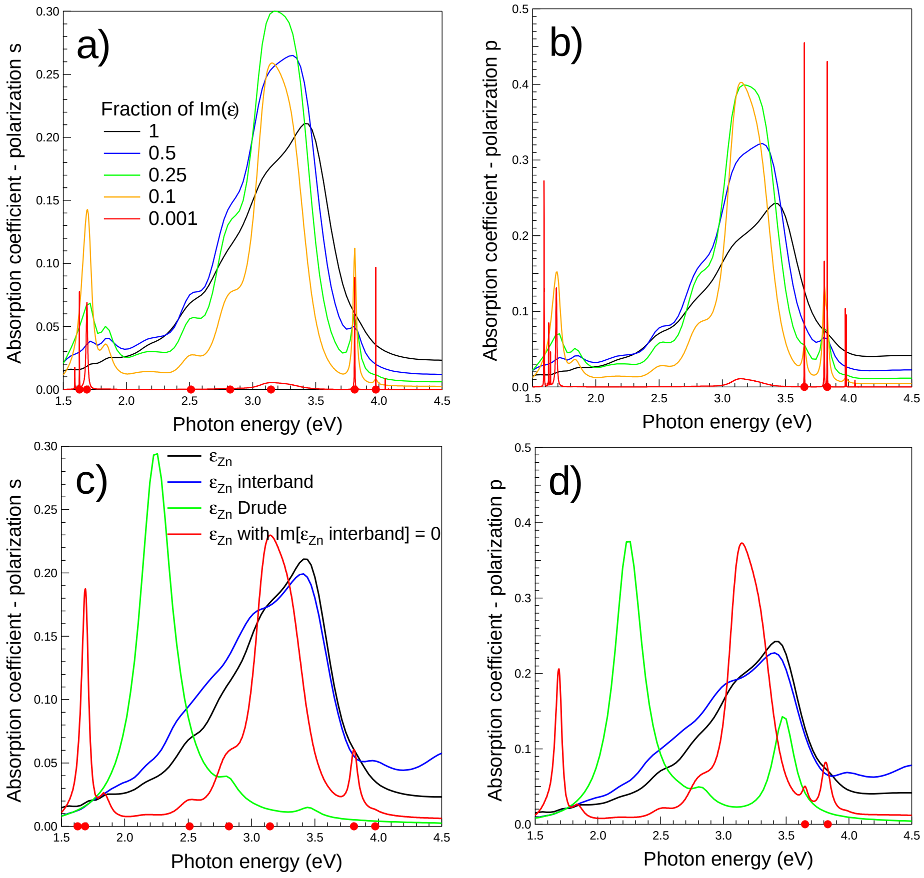

Figure 3.15: Same as figure 3.12 but for Zn.

3.7 The particle on a film: polarizability corrections

3.7.1 The question of layer stacking

In the framework of excess field theory, equations 3.1 show that the surface susceptibilities $\gamma(\omega), \beta(\omega)$ of a stack of films is nothing else than the sum of the susceptibilities of the individual components. Due to the arbitrary choice of the dividing surface, care should be taken when shifting the density of polarization in the calculation of the second order coefficients $\delta(\omega), \tau(\omega)$ of a stack (see reference [Haarmans and Bedeaux, 1995,Bedeaux and Vlieger, 2001] for details). Therefore, for a continous film of Zn of thickness t_{Zn} on a continuous film of Cr of thickness t_{Cr},

$$\begin{aligned}
\gamma(\omega) &= \gamma_{Cr}(\omega) + \gamma_{Zn}(\omega) = t_{Cr}\left[\epsilon_{Cr}(\omega) - \epsilon_1\right] + t_{Zn}\left[\epsilon_{Zn}(\omega) - \epsilon_1\right] \\
\beta(\omega) &= \beta_{Cr}(\omega) + \beta_{Zn}(\omega) = t_{Cr}\left[\frac{1}{\epsilon_1} - \frac{1}{\epsilon_{Cr}(\omega)}\right] + t_{Zn}\left[\frac{1}{\epsilon_1} - \frac{1}{\epsilon_{Zn}(\omega)}\right]. \qquad (3.18)
\end{aligned}$$

While $\gamma(\omega), \beta(\omega)$ have already been derived from particles of spherical/spheroidal shape on a substrate [Wind et al., 1987b, Wind et al., 1987a, Simonsen et al., 2000, Lazzari et al., 2001,Bedeaux and Vlieger, 2001] from the knowledge of the polarizability tensor (section 3.3.1), such a calculation has never been achieved for a particle on a continuous film. The aim of this section is, not to solve such a complex problem, but to explore the effect of screening of the electrostatic interaction due to the film on a substrate, a case that might be of interest in the

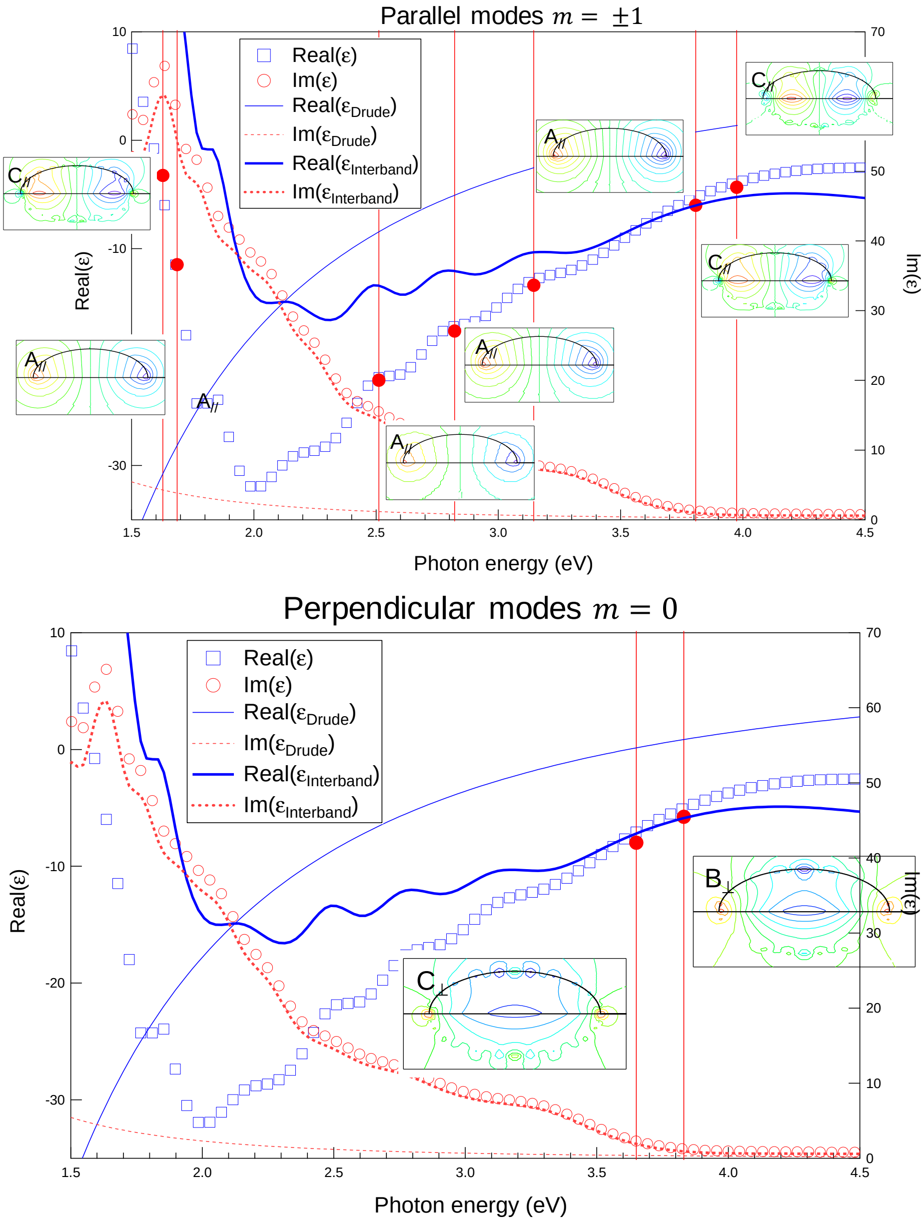

Figure 3.16: Same as figure 3.13 but for Zn.

present study of $Zn/Cr/Al_2O_3$. Although knwon to be approximate on a quantitative point of view for a particle on a semi-infite substrate [Yamaguchi et al., 1973, Yamaguchi et al., 1974], the corrections of polarizabilities will be derived only at the dipolar order to have a feeling of general trends. To do so, the Poisson equation will be solved in Fourier space by using the translation symmetry of the system. Isolated dipole and lattice of dipoles will be treated using the representative examples of a metallic layer on a dielectric substrate (Cr/Al_2O_3) or a dielectric layer on a metallic substrate (Al_2O_3/Cr). An effective dielectric function of thin film/substrate in terms of dipolar interaction will be derived. Upon a generalization to multipoles, such an approach could serve as a basis to tackle the case of an actual truncated sphere or spheroid, but this is is beyond the scope of this thesis

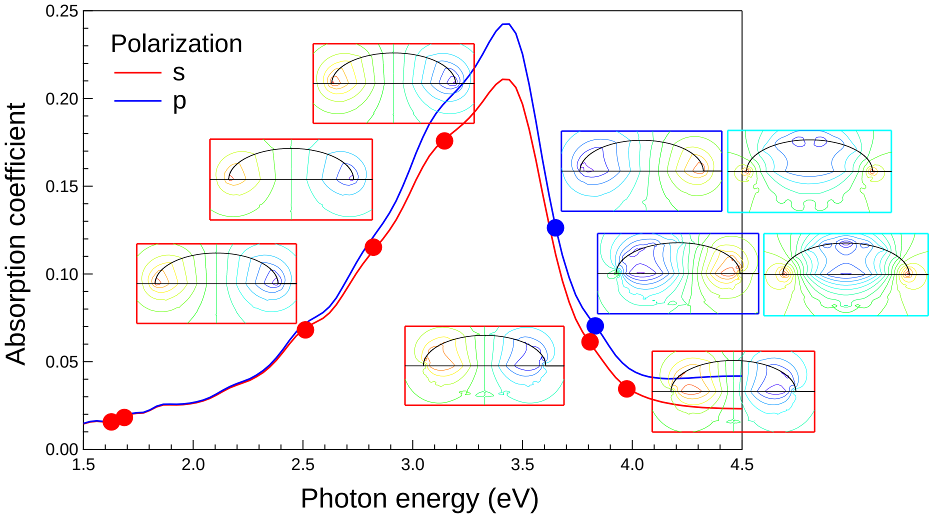

Figure 3.17: Same as figure 3.14 but for Zn.

3.7.2 Polarizable dipole in front a semi-infinite medium

The case has been derived by Yamaguchi *et al.* [Yamaguchi et al., 1973, Yamaguchi et al., 1974] using the dipole field and its image. The method used herein is based on Fourier transform parallel to the interface which is more suited when several interfaces are present.

3.7.2.1 Point charge in front of a surface

To setup the framework of calculations, let's consider the basic case of a point charge q in vacuum (dielectric function ϵ_1) in front of a semi-infinite medium (substrate) of dielectric function ϵ_2 (figure 3.18-a). The origin of the $z-$axis pointing towards the substrate is taken at the location of the charge which is put at a distance d from the surface. The electric potential $\Psi(\mathbf{r})$ it induces obeys to the Laplace equation:

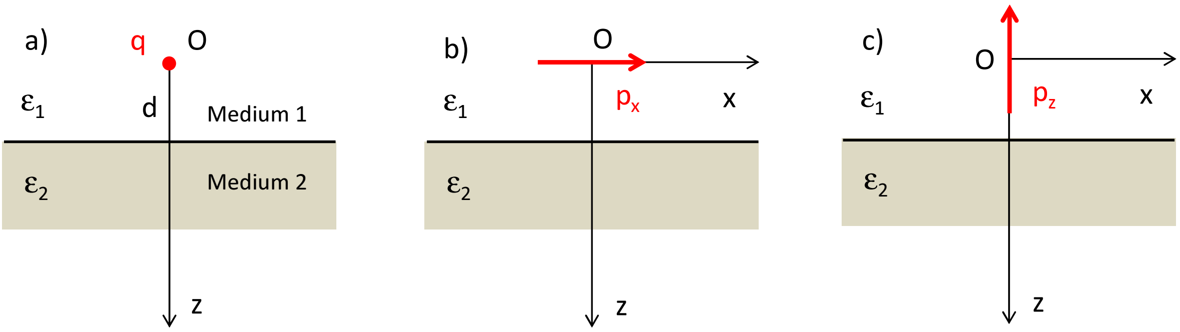

Figure 3.18: Drawing of the electrostatic problem: a) point charge and b) parallel or c) perpendicular dipole in front of a surface.

$$\Delta\Psi(\mathbf{r}) = -\frac{q}{\epsilon_1}\delta(\mathbf{r}), \tag{3.19}$$

which is much readily handled in Fourier space parallel to the surface. The transform and its reciprocal are defined by:

$$\begin{aligned}\widetilde{\Psi}(\mathbf{k}_\parallel, z) &= \int e^{i\mathbf{k}_\parallel\cdot\mathbf{r}_\parallel}\Psi(\mathbf{r}_\parallel, z)d^2\mathbf{r}_\parallel, \\ \Psi(\mathbf{r}_\parallel, z) &= \frac{1}{(2\pi)^2}\int e^{-i\mathbf{k}_\parallel\cdot\mathbf{r}_\parallel}\widetilde{\Psi}(\mathbf{k}_\parallel, z)d^2\mathbf{k}_\parallel.\end{aligned} \tag{3.20}$$

In Fourier space, equation 3.19 reads:

$$\left[\frac{\partial^2}{\partial z^2} - k_\parallel^2\right] = -\frac{q}{\epsilon_1}\delta(z). \tag{3.21}$$

Its general solution without right hand side is given by a weighted sum exponential functions:

$$\widetilde{\Psi}(\mathbf{k}_\parallel, z) = Ae^{k_\parallel z} + Be^{k_\parallel z}, \tag{3.22}$$

with constants $A(k_\parallel), B(k_\parallel)$ (their dependence on parameters will be dropped hereafter). A peculiar solution of the full equation comes readily from the Fourier transform along the interface normal:

$$\begin{aligned}\widetilde{\Psi}(\mathbf{k}_\parallel, \mathbf{k}_\perp) &= \int e^{ik_\perp z}\widetilde{\Psi}(\mathbf{k}_\parallel, z)dz \\ \widetilde{\Psi}(\mathbf{k}_\parallel, z) &= \frac{1}{2\pi}\int e^{-ik_\perp z}\widetilde{\Psi}(\mathbf{k}_\parallel, \mathbf{k}_\perp)dk_\perp.\end{aligned} \tag{3.23}$$

In this case, the Poisson equation $(k_\parallel^2 + k_\perp^2)\widetilde{\Psi}(\mathbf{k}_\parallel, \mathbf{k}_\perp) = q/\epsilon_1$ has a solution which is obtained from residue integration with a closing loop in the complex plane that depends on the sign of z to insure decays of the exponential term. For $z > 0$, the lower space is chosen:

$$\widetilde{\Psi}(\mathbf{k}_\parallel, z) = \frac{q}{2\pi\epsilon_1}\int\frac{e^{-ik_\perp . z}}{k_\parallel^2 + k_\perp^2}dk_\perp = -\frac{i}{q\epsilon_1}\text{Res}\left[-ik_\parallel, \frac{e^{-ik_\perp z}}{k_\parallel^2 + k_\perp^2}\right] = \frac{q}{2\epsilon_1}\frac{e^{-k_\parallel z}}{k_\parallel},$$

while for $z < 0$, it is the upper space:

$$\widetilde{\Psi}(\mathbf{k}_\parallel, z) = \frac{q}{2\pi\epsilon_1}\int\frac{e^{-ik_\perp . z}}{k_\parallel^2 + k_\perp^2}dk_\perp = +\frac{i}{q\epsilon_1}\text{Res}\left[ik_\parallel, \frac{e^{-ik_\perp z}}{k_\parallel^2 + k_\perp^2}\right] = \frac{q}{2\epsilon_1}\frac{e^{k_\parallel z}}{k_\parallel}.$$

Depending on medium, the total solution reduces to:

$$\begin{aligned}\widetilde{\Psi}_1(\mathbf{k}_\parallel, z) &= A_1 e^{k_\parallel z} + \frac{q}{2\epsilon_1}\frac{e^{-k_\parallel|z|}}{k_\parallel} \\ \widetilde{\Psi}_2(\mathbf{k}_\parallel, z) &= B_2 e^{-k_\parallel z} + \frac{q}{2\epsilon_1}\frac{e^{-k_\parallel|z|}}{k_\parallel},\end{aligned} \tag{3.24}$$

since $\Psi(\mathbf{r}_\parallel, z)$ should not diverge when $z \to \pm\infty$. The continuity of potential $\Psi_1(z = d) = \Psi_2(z = d)$ and of the normal derivative of the displacement field $\epsilon_1 (\partial\Psi_1/\partial z)(z = d) = \epsilon_2 (\partial\Psi_2/\partial z)(z = d)$ applied to the Fourier components of the potential leads to:

$$\begin{aligned}A_1 &= \frac{q}{2k_\parallel\epsilon_1}\frac{\epsilon_1 - \epsilon_2}{\epsilon_1 + \epsilon_2}e^{-2k_\parallel d} \\ B_2 &= A_1 e^{2k_\parallel d}.\end{aligned} \tag{3.25}$$

Therefore, the potential in the medium 1 where is located the charge is given by:

$$\widetilde{\Psi}_1(\mathbf{k}_\parallel, z) = \frac{q}{2k\epsilon_1}\left[\frac{\epsilon_1-\epsilon_2}{\epsilon_1+\epsilon_2}e^{-2k_\parallel d}e^{k_\parallel z} + e^{-k_\parallel |z|}\right]. \tag{3.26}$$

The first term corresponds to the image potential of an opposite point charge $-q\frac{\epsilon_2-\epsilon_1}{\epsilon_1+\epsilon_2}$ $(\epsilon_2 > \epsilon_1)$ located at a distance d in the substrate. The second one is due to the direct field due to the charge itself.

3.7.2.2 Point dipole in front of a surface and the correction of its polarizability

The potential Ψ_d due to a dipole (figure 3.18-b,c) corresponds to the limit of the sum of the potentials Ψ_q of two opposite charges infinitely close but carrying a charge q that diverges such that the product of q and their separation $2l$ is constant and equal to the dipole strength $p_l = \lim\limits_{\substack{l\to 0\\ q\to+\infty}} (2ql)$ along the l-direction:

$$\Psi_d = \lim_{\substack{l\to 0\\ q\to+\infty\\ ql\to p_l}} \left[\Psi_q(+q,l) + \Psi_q(-q,l)\right] = p_l\left[\frac{1}{q}\frac{\partial \Psi_q}{\partial l}\right] (l=0). \tag{3.27}$$

Since the approach of the previous section applied to a point charge shifted by $(\mathbf{r}_{\parallel,0}, z_0)$ gives:

$$\widetilde{\Psi}_1(\mathbf{k}_\parallel, z) = \frac{q}{2k\epsilon_1}\left[\frac{\epsilon_1-\epsilon_2}{\epsilon_1+\epsilon_2}e^{k_\parallel(z+z_0-2d)} + e^{-k_\parallel |z-z_0|}\right] e^{i\mathbf{k}_\parallel\cdot\mathbf{r}_{\parallel,0}}, \tag{3.28}$$

the Fourier components of the potential in medium 1 due to the image i of a dipole oriented along the $x-$ (figure 3.18-b) or $z-$ (figure 3.18-c) axis is given by:

$$\begin{aligned}
\widetilde{\Psi}^{x,i}_{1,d}(\mathbf{k}_\parallel, z) &= \frac{ik_x p_x}{2k_\parallel\epsilon_1}\frac{\epsilon_1-\epsilon_2}{\epsilon_1+\epsilon_2}e^{-2k_\parallel d}e^{k_\parallel z} && (3.29)\\
\widetilde{\Psi}^{z,i}_{1,d}(\mathbf{k}_\parallel, z) &= \frac{p_z}{2\epsilon_1}\frac{\epsilon_1-\epsilon_2}{\epsilon_1+\epsilon_2}e^{-2k_\parallel d}e^{k_\parallel z}. && (3.30)
\end{aligned}$$

Since $\mathbf{E}(\mathbf{r}) = -\nabla\Psi(\mathbf{r})$ translates in Fourier space as:

$$\begin{aligned}
\mathbf{E}_\parallel(\mathbf{r}) &= \frac{-1}{(2\pi)^2}\int e^{-i\mathbf{k}_\parallel\cdot\mathbf{r}_\parallel}(-i\mathbf{k}_\parallel)\widetilde{\Psi}(\mathbf{k}_\parallel, z)d^2\mathbf{k}_\parallel\\
E_z(\mathbf{r}) &= \frac{-1}{(2\pi)^2}\int e^{-i\mathbf{k}_\parallel\cdot\mathbf{r}_\parallel}\frac{\partial\widetilde{\Psi}}{\partial z}(\mathbf{k}_\parallel, z)d^2\mathbf{k}_\parallel, && (3.31)
\end{aligned}$$

the corresponding Fourier components of the dipole field in medium 1 are given from equations 3.30 by:

$$\begin{aligned}
\widetilde{\mathbf{E}}^{x,i}_{1,d,x}(\mathbf{k}_\parallel, z) &= -\frac{\mathbf{k}_\parallel k_x p_x}{2k_\parallel\epsilon_1}\frac{\epsilon_1-\epsilon_2}{\epsilon_1+\epsilon_2}e^{-2k_\parallel d}e^{k_\parallel z}\\
\widetilde{E}^{z,i}_{1,d,z}(\mathbf{k}_\parallel, z) &= \frac{p_z k_\parallel}{2\epsilon_1}\frac{\epsilon_1-\epsilon_2}{\epsilon_1+\epsilon_2}e^{-2k_\parallel d}e^{k_\parallel z}. && (3.32)
\end{aligned}$$

The actual image electric field felt by the dipole located at the origin of space is given by the integral of its $(z=0)$ Fourier components, namely:

$$\mathbf{E}^{x,i}_{1,d,x}(\mathbf{r}=0) = \frac{1}{(2\pi)^2}\int \widetilde{\mathbf{E}}^{x,i}_{1,d,x}(\mathbf{k}_\parallel, z=0)d^2\mathbf{k}_\parallel. \tag{3.33}$$

The corresponding dipole image field along the x-axis for a dipole parallel to the x-axis (figure 3.18-b) is given by:

$$E^{x,i}_{1,d,x}(\mathbf{r}=0) = -\frac{1}{(2\pi)^2}\frac{p_x}{2\epsilon_1}\frac{\epsilon_1-\epsilon_2}{\epsilon_1+\epsilon_2}\int \frac{k_x^2}{k_\parallel}e^{-2k_\parallel d}d^2\mathbf{k}_\parallel, \tag{3.34}$$

where the integral in polar coordinates amounts to:

$$I_x = \int_0^{2\pi} d\theta \int_0^\infty dk_\parallel k_\parallel^2 \cos^2\theta e^{-2k_\parallel d} = \frac{\pi}{4d^3}. \tag{3.35}$$

Finally, $E^{x,i}_{1,d,x}(\mathbf{r}=0) = -\mathcal{I}p_x$ where:

$$\mathcal{I} = \frac{1}{32\pi\epsilon_1}\frac{\epsilon_1-\epsilon_2}{\epsilon_1+\epsilon_2}\frac{1}{d^3}. \tag{3.36}$$

If the dipole corresponds to an entity with a polarizability α_x along the $x-$axis, the induced dipole p_x is due to the incident field $\mathbf{E}^{x,0}_1(\mathbf{r}=0)$ and to the induced image field $\mathbf{E}^{x,i}_{1,d,x}(\mathbf{r}=0)$:

$$p_x = \alpha_x[\mathbf{E}^{x,0}_1(\mathbf{r}=0) + \mathbf{E}^{x,i}_{1,d,x}(\mathbf{r}=0)]. \tag{3.37}$$

Once introduced the expression of the image dipole electric field equation 3.36, this gives a polarizability α_x^c corrected by the dipolar interaction with the image:

$$\alpha_x^c = \frac{\alpha_x}{1+\mathcal{I}\alpha_x}. \tag{3.38}$$

In the same spirit, the dipole image field along the z-axis for a dipole along the z-axis (figure 3.18-c) is given by:

$$E^{z,i}_{1,d,z}(\mathbf{r}=0) = \frac{-1}{(2\pi)^2}\frac{p_z}{2\epsilon_1}\frac{\epsilon_1-\epsilon_2}{\epsilon_1+\epsilon_2}\int k_\parallel e^{-2k_\parallel d}d^2\mathbf{k}_\parallel. \tag{3.39}$$

Since the previous integral:

$$I_z = \int_0^{2\pi} d\theta \int_0^\infty dk_\parallel k_\parallel^2 e^{-2k_\parallel d} = 2I_x \tag{3.40}$$

amount to 2 times the previous one I_x, the corresponding corrected polarizability along the z-axis reads:

$$\alpha_z^c = \frac{\alpha_z}{1+2\mathcal{I}\alpha_z}. \tag{3.41}$$

Equations 3.36,3.38,3.41 are not new. They do correspond to the classical polarizability renormalization [Yamaguchi et al., 1973, Yamaguchi et al., 1974, Bedeaux and Vlieger, 2001] due to the electrostatic interaction with a substrate found more classically by expanding the potential using the spherical symmetry of the point charge and using the image charge trick to take into account the boundary conditions on the flat surface. But the present approach, based on the invariance by translation, is much more adapted to case of multilayers on a substrate as it is shown hereafter.

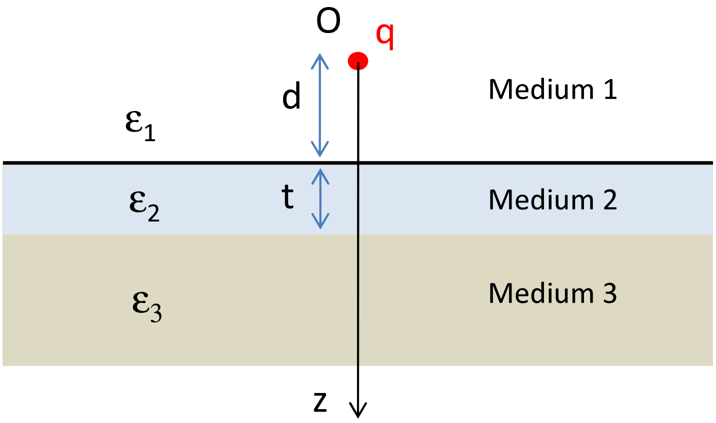

Figure 3.19: Drawing of the electrostatic problem: a point charge q is located a distance d from the surface of a film of thickness t and dielectric constant ϵ_2 deposited on a substrate of dielectric constant ϵ_3.

3.7.3 Polarizable dipole in front a layer on a semi-infinite substrate

3.7.3.1 Case of a point charge

The system at hand (figure 3.18) consists in a point charge q placed in vacuum (dielectric constant ϵ_1) at a distance $d+t$ from a substrate of dielectric function ϵ_3 covered by an homogeneous film of thickness t and dielectric function ϵ_2. In the same spirit as in section 3.7.2.1, the parallel Fourier components of the electrostatic potential in each medium are given by:

$$\begin{aligned}
\widetilde{\Psi}_1(\mathbf{k}_{\|}, z) &= A_1 e^{k_{\|} z} + \frac{q}{2\epsilon_1}\frac{e^{-k_{\|}|z|}}{k_{\|}} \\
\widetilde{\Psi}_2(\mathbf{k}_{\|}, z) &= A_2 e^{k_{\|} z} + B_2 e^{-k_{\|} z} + \frac{q}{2\epsilon_1}\frac{e^{-k_{\|} z}}{k_{\|}} \\
\widetilde{\Psi}_3(\mathbf{k}_{\|}, z) &= B_3 e^{-k_{\|} z} + \frac{q}{2\epsilon_1}\frac{e^{-k_{\|} z}}{k_{\|}}. \qquad (3.42)
\end{aligned}$$

They fullfill finiteness as $|z|$ tends to infinity and to the boundary conditions given by the continuity of the potential and the normal derivative of the displacement field on each interface, namely:

$$\begin{aligned}
\widetilde{\Psi}_1(\mathbf{k}_{\|}, d) &= \widetilde{\Psi}_2(\mathbf{k}_{\|}, d) \\
\widetilde{\Psi}_2(\mathbf{k}_{\|}, d+t) &= \widetilde{\Psi}_3(\mathbf{k}_{\|}, d+t) \\
\epsilon_1 \frac{\partial \widetilde{\Psi}_1}{\partial z}(\mathbf{k}_{\|}, d) &= \epsilon_2 \frac{\partial \widetilde{\Psi}_2}{\partial z}(\mathbf{k}_{\|}, d) \\
\epsilon_2 \frac{\partial \widetilde{\Psi}_1}{\partial z}(\mathbf{k}_{\|}, d+t) &= \epsilon_3 \frac{\partial \widetilde{\Psi}_2}{\partial z}(\mathbf{k}_{\|}, d+t). \qquad (3.43)
\end{aligned}$$

These conditions leads to a linear system of 4 equations with 4 unknowns:

$$\begin{aligned}
A_1 e^{2k_\| d} &= A_2 e^{2k_\| d} + B_2 \\
A_2 e^{2k_\| (d+t)} + B_2 &= B_3 \\
\epsilon_1 A_1 e^{2k_\| d} &= \epsilon_2 A_2 e^{2k_\| d} - \epsilon_2 B_2 + \frac{q}{2k_\| \epsilon_1}(\epsilon_1 - \epsilon_2) \\
\epsilon_2 A_2 e^{2k_\| (d+t)} - \epsilon_2 B_2 &= -\epsilon_3 B_3 + \frac{q}{2k_\| \epsilon_1}(\epsilon_2 - \epsilon_3),
\end{aligned} \tag{3.44}$$

of which the most important is the image term in medium 1, namely A_1. After straightforward algebra, it is given by:

$$A_1 = -\frac{q}{2k_\| \epsilon_1} e^{-2k_\| d} \frac{\mathcal{A}_{12} + \mathcal{A}_{23} e^{-2k_\| t}}{1 + \mathcal{A}_{23}\mathcal{A}_{12} e^{-2k_\| t}}, \tag{3.45}$$

where the shorthand notation is given by:

$$\mathcal{A}_{ij} = \frac{\epsilon_j - \epsilon_i}{\epsilon_i + \epsilon_j}. \tag{3.46}$$

A quick check shows that the limit cases of $[\epsilon_2 = \epsilon_3; t = 0]$ or $[t \to \infty]$ allows to recover the case of semi-infinite medium given by equation 3.25. The point charge in medium 1 feels an image potential due to the interaction with the film/substrate given by: $\widetilde{\Psi}_1^i(\mathbf{k}_\|, z) = A_1(\mathbf{k}_\|, \mathcal{A}_{12}, \mathcal{A}_{23}) e^{k_\| z}$.

3.7.3.2 Point dipole in front a layer and its polarizability correction

Using the definition of a point dipole as two infinitesimally close and opposite point charges (equation 3.27), the Fourier components of the potential of a dipole p_x or p_z aligned along the $x-$axis or $z-$axis are given by:

$$\begin{aligned}
\widetilde{\Psi}_{1,d}^{x,i}(\mathbf{k}_\|, z) &= i k_x p_x \frac{A_1}{q} e^{k_\| z} \\
\widetilde{\Psi}_{1,d}^{z,i}(\mathbf{k}_\|, z) &= k_\| p_z \frac{A_1}{q} e^{k_\| z}.
\end{aligned} \tag{3.47}$$

The related Fourier components of the image electric field along the direction of the dipole read:

$$\begin{aligned}
\widetilde{E}_{1,d,x}^{x,i}(\mathbf{k}_\|, z) &= i k_x^2 p_x \frac{A_1}{q} e^{k_\| z} \\
\widetilde{E}_{1,d,z}^{z,i}(\mathbf{k}_\|, z) &= -k_\| p_z \frac{A_1}{q} e^{k_\| z},
\end{aligned} \tag{3.48}$$

The previous equations give the actual image electric field calculated as the sum of the Fourier components:

$$\begin{aligned}
E_{1,d,x}^{x,i}(\mathbf{r} = \mathbf{0}) &= -\frac{p_x}{(2\pi)^2} \frac{1}{q} \int k_x^2 e^{k_\| z} A_1(k_\|) d^2\mathbf{k}_\| \\
E_{1,d,z}^{z,i}(\mathbf{r} = \mathbf{0}) &= -\frac{p_z}{(2\pi)^2} \frac{1}{q} \int k e^{k_\| z} A_1(k_\|) d^2\mathbf{k}_\|.
\end{aligned} \tag{3.49}$$

Using the expression equation 3.45 of $A_1(k_\parallel)$ in the case of a layer, those fields read:

$$\begin{aligned} E^{x,i}_{1,d,x}(\mathbf{r}=\mathbf{0}) &= \frac{1}{(2\pi)^2}\frac{p_x}{2\epsilon_1}I_x \\ E^{z,i}_{1,d,z}(\mathbf{r}=\mathbf{0}) &= \frac{1}{(2\pi)^2}\frac{p_z}{2\epsilon_1}I_z, \end{aligned} \tag{3.50}$$

where:

$$\begin{aligned} I_x &= \int \frac{k_x^2}{k_\parallel} e^{-2k_\parallel d}\frac{\mathcal{A}_{12}+\mathcal{A}_{23}e^{-2k_\parallel t}}{1+\mathcal{A}_{23}\mathcal{A}_{12}e^{-2k_\parallel t}} d^2\mathbf{k}_\parallel \\ &= \int_0^{2\pi}\cos^2\theta d\theta \int_0^\infty k_\parallel^2 e^{-2k_\parallel d}\frac{\mathcal{A}_{12}+\mathcal{A}_{23}e^{-2k_\parallel t}}{1+\mathcal{A}_{23}\mathcal{A}_{12}e^{-2k_\parallel t}} dk_\parallel = \pi I_k \qquad (3.51) \\ I_z &= 2\pi I_k. \qquad (3.52) \end{aligned}$$

In the same way as for a dipole in front of a surface, the polarizability of the entity corrected from the image dipole field is still given by equation 3.38, 3.41 but with:

$$\mathcal{I} = -\frac{1}{(2\pi)^2}\frac{1}{2\epsilon_1}\int_0^\infty k_\parallel^2 e^{-2k_\parallel d}\frac{\mathcal{A}_{12}+\mathcal{A}_{23}e^{-2k_\parallel t}}{1+\mathcal{A}_{23}\mathcal{A}_{12}e^{-2k_\parallel t}} dk_\parallel, \tag{3.53}$$

that can be expressed in adimensional units relative to the case of the uncovered substrate:

$$\begin{aligned} \mathcal{I} &= -\frac{\mathcal{A}_{13}}{32\pi\epsilon_1}\frac{1}{(d+t)^3}\mathcal{I}_s \\ \mathcal{I}_s &= \frac{1}{2}\left(1+\frac{t}{d}\right)^3\int_0^\infty \frac{u^2}{\mathcal{A}_{13}}\frac{\mathcal{A}_{12}+\mathcal{A}_{23}e^{-ut/d}}{1+\mathcal{A}_{23}\mathcal{A}_{12}e^{-ut/d}}e^{-u}du, \end{aligned} \tag{3.54}$$

or to the case of a semi-infinite layer:

$$\begin{aligned} \mathcal{I} &= -\frac{\mathcal{A}_{12}}{32\pi\epsilon_1}\frac{1}{d^3}\mathcal{I}_l \\ \mathcal{I}_l &= \frac{1}{2}\int_0^\infty \frac{u^2}{\mathcal{A}_{13}}\frac{\mathcal{A}_{12}+\mathcal{A}_{23}e^{-ut/d}}{1+\mathcal{A}_{23}\mathcal{A}_{12}e^{-ut/d}}e^{-u}du. \end{aligned} \tag{3.55}$$

The integral $\mathcal{I}_s$ that encompasses the role of the dipolar screening of the substrate by the overlayer has a complex expression as function of hypergeometric function and is better determined numerically. In parallel, $\mathcal{I}_l$ yields the weight of the image field in the layer.

3.7.3.3 Examples: metal on dielectric and vice-versa

To illustrate the effect of the influence of a layer on the screening of a dipole, the quantities $|\mathcal{I}_s|$ (equation 3.54) and $|\mathcal{I}_l|$ (equation 3.55) have been calculated for two different cases, namely Cr/Al_2O_3 and Al_2O_3/Cr, corresponding to two extreme cases of a high refractive index material on a dielectric substrate and vice-versa (figure 3.20). For completness, their dielectric constants extracted from the datbase of reference [Palik, 1985] are given in figure 3.21 as bold lines.

As expected for a metallic layer on a dielectric substrate, the screening is completely modified when growing a layer (figures 3.20-a). Only at very low $t/d \lesssim 0.02$ *i.e.* very low thickness

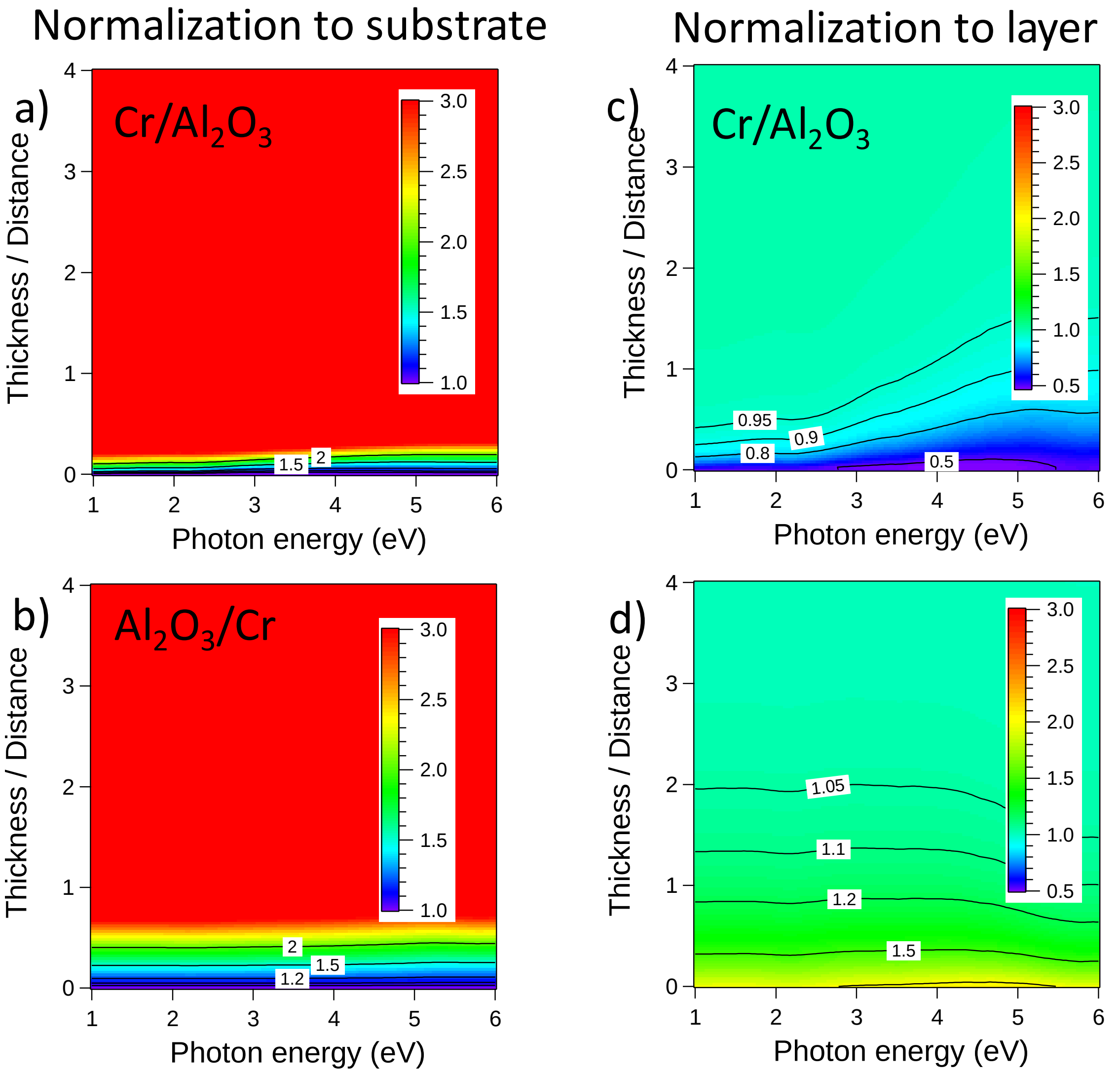

Figure 3.20: Effect of a layer on the screening of a dipole compared to a fictitious semi-infinite substrate corresponding to the actual substrate $|\mathcal{I}_s|$ (figure a,b) or the layer $|\mathcal{I}_l|$ (figures c,d) in the case of Cr/Al$_2$O$_3$ (figures a,c) and Al$_2$O$_3$/Cr (figures b,d).

or very large distance, the screening is driven by the substrate ($|\mathcal{I}_l| \simeq 1$). As soon as $t/d \gtrsim 0.5$, the image field develops in the metallic layer (figures 3.20-c). The behavior is similar for a dielectric layer on a metallic substrate (figures 3.20-b,d) but the boundaries are softer since the ratio of dielectric function is reversed. The dipole reflects only in the layer if $t/d \gtrsim 2$. These findings also holds true for the phases of the complex $\mathcal{I}_l, \mathcal{I}_s$ quantities that approaches zero as the modulus gets closer to one.

Regarding the screening by the complete system, an effective substrate dielectric function ϵ_e can be defined by equating the exact $\mathcal{I}$ terms equation 3.53 and that of a fictitious semi-infinite medium starting at distance d of the dipole. This gives:

$$\begin{aligned}
\frac{\epsilon_e - \epsilon_1}{\epsilon_e + \epsilon_1} &= \frac{1}{2}\int_0^\infty u^2 \frac{\mathcal{A}_{23} + \mathcal{A}_{12} e^{ut/d}}{\mathcal{A}_{23}\mathcal{A}_{12} + e^{ut/d}} e^{-u} du = \mathcal{I}_u \\
\epsilon_e &= \frac{1 + \mathcal{I}_u}{1 - \mathcal{I}_u}\epsilon_1. \qquad (3.56)
\end{aligned}$$

This effective dielectric function ϵ_e is plotted in figure 3.21 for Cr/Al_2O_3 or the inverse system Al_2O_3/Cr. While a progressive transition is observed for Cr/Al_2O_3, surprisingly the role of the alumina layer on chromium substrate is far from being negligible even for small t/d values; in other words, ϵ_e converges slowly towards ϵ_{Cr} with an amazing mix between real and imaginary parts of the metal dielectric function.

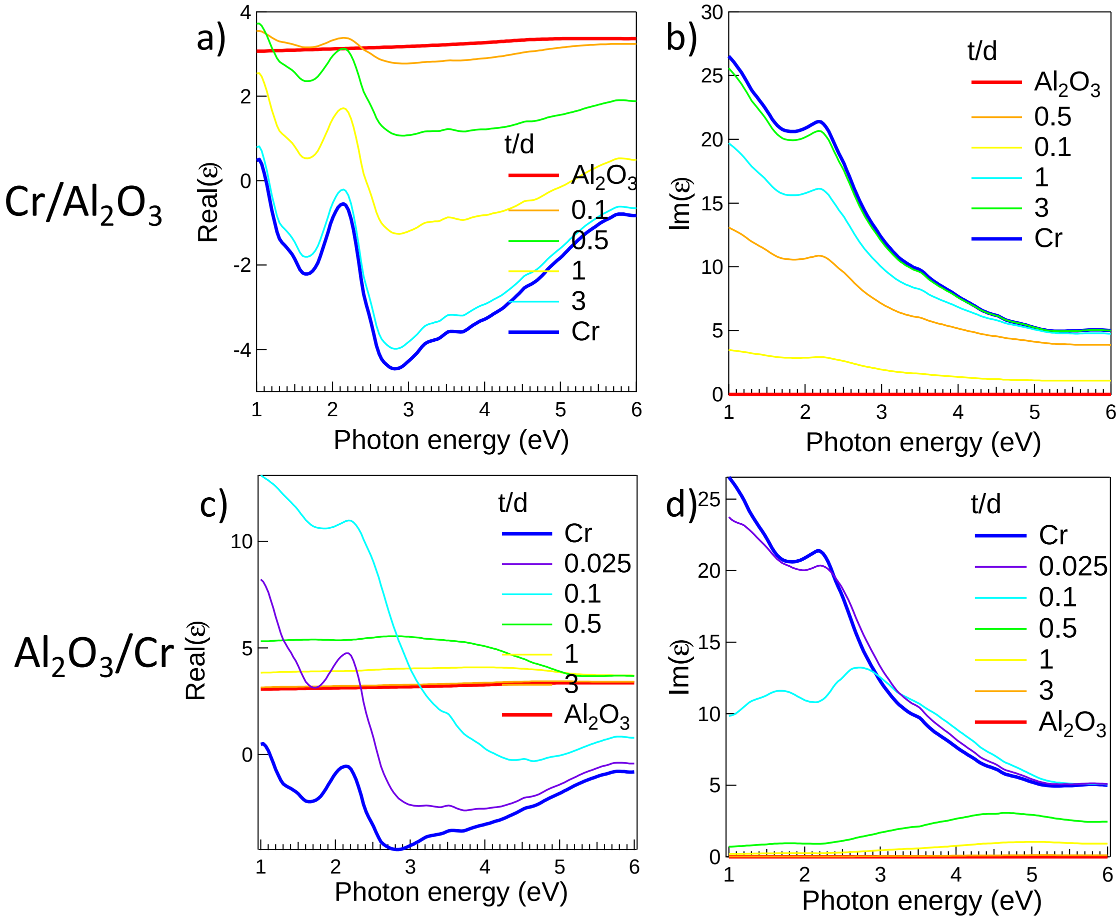

Figure 3.21: Effective dielectric function ϵ_e for a)b) Cr/Al_2O_3 or c)d) Al_2O_3/Cr layers as a function of t/d.

3.7.4 Dipole assembly

3.7.4.1 Semi-infinite substrate

As done previously section 3.7.2.2, let's consider the classical case of an assembly of dipoles (figure 3.22) in front of substrate of dielectric function ϵ_2. Each dipole and its image in the substrate will create a depolarization field at the origin which will modify the polarizability of the entity located there. To simplify the problem, all dipoles ($i = 1, \dots, \infty$) are assumed to be the same, p_x either along the x-axis or p_z parallel to the z-axis; they are located at position $\mathbf{R}_{\parallel,i}$ along the substrate but at the same height d from the substrate.

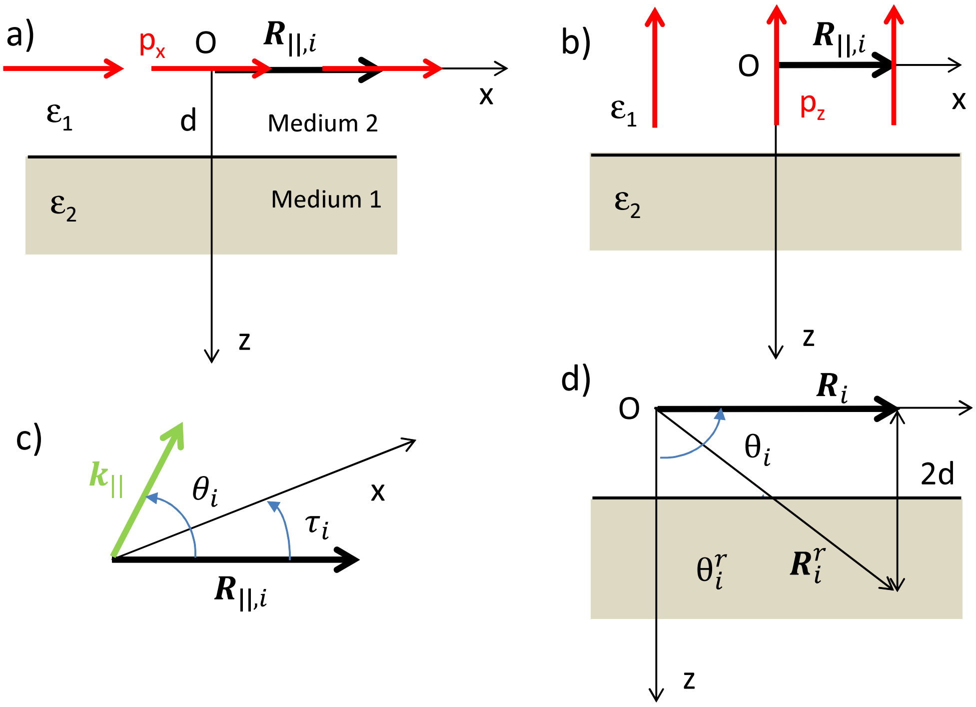

Figure 3.22: Assembly of dipole interactions in front of a surface: a) parallel and b) perpendicular dipoles located at $\mathbf{R}_{\parallel,i}$.

Using the additivity of potentials and the results obtained from a single dipole equations 3.32, the Fourier components of the electric field parallel (or perpendicular) to the surface produced by dipoles $p_{x,i}$ (or $p_{z,i}$) are given in medium 1 by:

$$\begin{aligned}
\widetilde{E}^x_{1,d,x}(\mathbf{k}_\parallel, z) &= -\frac{k_x^2 p_x}{2k_\parallel \epsilon_1}\left[\frac{\epsilon_1-\epsilon_2}{\epsilon_1+\epsilon_2} e^{-2k_\parallel d} e^{k_\parallel z} \sum_i e^{i\mathbf{k}_\parallel \cdot \mathbf{R}_{\parallel,i}} + e^{-k_\parallel |z|} \sum_i e^{i\mathbf{k}_\parallel \cdot \mathbf{R}_{\parallel,i}}\right] \\
\widetilde{E}^z_{1,d,z}(\mathbf{k}_\parallel, z) &= \frac{p_z k_\parallel}{2\epsilon_1}\left[-\frac{\epsilon_1-\epsilon_2}{\epsilon_1+\epsilon_2} e^{-2k_\parallel d} e^{k_\parallel z} \sum_i e^{i\mathbf{k}_\parallel \cdot \mathbf{R}_{\parallel,i}} + e^{-k_\parallel |z|} \sum_i e^{i\mathbf{k}_\parallel \cdot \mathbf{R}_{\parallel,i}}\right]. \qquad (3.57)
\end{aligned}$$

The phase term $e^{i\mathbf{k}_\parallel \cdot \mathbf{R}_{\parallel,i}}$ comes from the spatial shift along the parallel direction of the dipole in the Poisson equation (see equation 3.28). The first term in each equation corresponds to the sum over the image dipoles while the second one is due to the direct interaction. The minus sign in the second equation comes from the derivative versus z_0 in equation 3.28 and means that along the $z-$direction image and direct dipole fields add which is not the case along the parallel direction. To calculate the polarizability correction, the actual electric field at the origin along the direction of the dipole is obtained from the inverse Fourier transform:

$$\begin{aligned}
\mathbf{E}^x_{1,d,x}(\mathbf{r}=0) &= -\frac{1}{(2\pi)^2}\frac{p_x}{2\epsilon_1}\left[\frac{\epsilon_1-\epsilon_2}{\epsilon_1+\epsilon_2}\sum_i\int\frac{k_x^2}{k_\parallel}e^{-2k_\parallel d}e^{i\mathbf{k}_\parallel.\mathbf{R}_{\parallel,i}}d^2\mathbf{k}_\parallel+\sum_{i\neq 0}\int\frac{k_x^2}{k_\parallel}e^{i\mathbf{k}_\parallel.\mathbf{R}_{\parallel,i}}e^{-k_\parallel\eta}d^2\mathbf{k}_\parallel\right]\\
E^z_{1,d,z}(\mathbf{r}=0) &= \frac{1}{(2\pi)^2}\frac{p_z}{2\epsilon_1}\left[-\frac{\epsilon_1-\epsilon_2}{\epsilon_1+\epsilon_2}\sum_i\int k_\parallel e^{-2k_\parallel d}e^{i\mathbf{k}_\parallel.\mathbf{R}_{\parallel,i}}d^2\mathbf{k}_\parallel-\sum_{i\neq 0}\int k_\parallel e^{i\mathbf{k}_\parallel.\mathbf{R}_{\parallel,i}}e^{-k_\parallel\epsilon_z}d^2\mathbf{k}_\parallel\right]
\end{aligned} \tag{3.58}$$

The term $i=0$ is excluded from the sum in the direct interaction to avoid the self-interaction of the dipole with itself in the evaluation of the depolarization field. A factor $e^{-k_\parallel\eta}$ ($\eta>0$) has been added in the back Fourier transform of the direct field to insure convergence of the integrals; the limit $\eta=0$ corresponding to $z=0$ will be taken at the end. Two integrals evaluated at $\eta=0,2d$ comes into play:

$$\begin{aligned}
I_x(\eta,\mathbf{R}_{\parallel,i}) &= \int\frac{k_x^2}{k_\parallel}e^{-k_\parallel\eta}e^{i\mathbf{k}_\parallel.\mathbf{R}_{\parallel,i}}d^2\mathbf{k}_\parallel\\
I_z(\eta,\mathbf{R}_{\parallel,i}) &= \int k_\parallel e^{-k_\parallel\eta}e^{i\mathbf{k}_\parallel.\mathbf{R}_{\parallel,i}}d^2\mathbf{k}_\parallel.
\end{aligned} \tag{3.59}$$

They are more easily handled in polar coordinates defined from $\mathbf{R}_{\parallel,i}$ direction (see figure 3.22-c). The first one reads:

$$I_x(\eta,\mathbf{R}_{\parallel,i}) = \int_0^\infty k_\parallel^2 e^{-2k_\parallel\eta}dk_\parallel\int_{-\pi}^{\pi}\cos^2(\theta_i-\tau_i)e^{ik_\parallel R_{\parallel,i}\cos\theta_i}d\theta_i, \tag{3.60}$$

where $\theta_i(\tau_i)$ are the angles between $\mathbf{R}_{\parallel,i}$ and $\mathbf{k}_\parallel$ (or the $x-$axis, respectively) (see figure 3.22-c). Using $2\cos^2(\theta_i-\tau_i)=1+\cos(2\theta_i)\cos(2\tau_i)+\sin(2\theta_i)\sin(2\tau_i)$ and the Jacobi-Anger's expansion in terms of Bessel's functions $J_n(z)$:

$$e^{iz\cos\theta} = J_0(z)+2\sum_{i=0}^{\infty}i^nJ_n(z)\cos(n\theta), \tag{3.61}$$

the angular part of equation 3.60 reduces to:

$$\begin{aligned}
I_{x,\theta}\quad(\eta,\mathbf{R}_{\parallel,i}) &= \frac{1}{2}\int_{-\pi}^{\pi}\left[J_0(k_\parallel R_{\parallel,i})\right.\\
-\quad & \left.2\cos(2\tau_i)J_2(k_\parallel R_{\parallel,i})\cos^2(2\theta_i)\right]d\theta_i\\
= \quad & \pi J_0(k_\parallel R_{\parallel,i})-\pi\cos(2\tau_i)J_2(k_\parallel R_{\parallel,i})\\
= \quad & \pi J_0(k_\parallel R_{\parallel,i})+\pi J_2(k_\parallel R_{\parallel,i})-2\pi\cos^2(\tau_i)J_2(k_\parallel R_{\parallel,i}).
\end{aligned} \tag{3.62}$$

The previous expression can be further simplified by considering regular (square or hexagonal) or fully random lattice of dipoles. By symmetry in those cases, the sum of over i in equations 3.57 gives a $1/2$ average per dipole for the $\cos^2(\tau_i)$ term for all dipoles located at the same distance $R_{\parallel,i}$; in other words, the depolarisation field is by symmetry directed along the dipole axis. Therefore:

$$I_{x,\theta}(\eta,R_{\parallel,i}) = \pi J_0(k_\parallel R_{\parallel,i}), \tag{3.63}$$

and $I_x(\eta, \mathbf{R}_{\parallel,i})$ appears as an Hankel's transform

$$\begin{aligned} I_x(\eta, \mathbf{R}_{\parallel,i}) &= \pi \int_0^\infty k_\parallel^2 e^{-k_\parallel \eta} J_0(k_\parallel R_{\parallel,i}) dk_\parallel = \pi \frac{\partial^2}{\partial \eta^2} \left[\int_0^\infty e^{-k_\parallel \eta} J_0(k_\parallel R_{\parallel,i}) dk_\parallel \right]_\eta \\ &= \pi \frac{\partial^2}{\partial \eta^2} \left[\frac{1}{\sqrt{R_{\parallel,i}^2 + \eta^2}} \right] = -\pi \frac{R_{\parallel,i}^2 - 2\eta^2}{(R_{\parallel,i}^2 + \eta^2)^{5/2}}. \end{aligned} \tag{3.64}$$

In a similar way, in angular coordinates from the $\mathbf{R}_{\parallel,i}$ direction,

$$\begin{aligned} I_z(\eta, \mathbf{R}_{\parallel,i}) &= \int_0^\infty k_\parallel^2 e^{-k_\parallel \eta} dk_\parallel \int_{-\pi}^{\pi} e^{ik_\parallel R_{\parallel,i} \cos\theta_i} d\theta_i \\ &= 2\pi \int_0^\infty k_\parallel^2 e^{-k_\parallel \eta} J_0(k_\parallel R_{\parallel,i}) dk_\parallel = 2 I_x(\eta, \mathbf{R}_{\parallel,i}) \end{aligned} \tag{3.65}$$

By introducing equations 3.64-3.65 into equations 3.57 and taking the limit $\eta = 0; 2d$, one finds the depolarization field at the origin:

$$\begin{aligned} \mathbf{E}_{1,d,x}^x(\mathbf{r} = 0) &= \frac{p_x}{8\pi\epsilon_1} \left[\frac{\epsilon_1 - \epsilon_2}{\epsilon_1 + \epsilon_2} \sum_i \frac{R_{\parallel,i}^2 - 8d^2}{(R_{\parallel,i}^2 + 4d^2)^{5/2}} + \sum_i \frac{1}{R_{\parallel,i}^3} \right] \\ \mathbf{E}_{1,d,z}^z(\mathbf{r} = 0) &= \frac{p_z}{4\pi\epsilon_1} \left[\frac{\epsilon_1 - \epsilon_2}{\epsilon_1 + \epsilon_2} \sum_i \frac{R_{\parallel,i}^2 - 8d^2}{(R_{\parallel,i}^2 + 4d^2)^{5/2}} - \sum_i \frac{1}{R_{\parallel,i}^3} \right]. \end{aligned} \tag{3.66}$$

As in the previously treated cases, the polarizabilities corrected from the inter-particle interactions are therefore given by:

$$\alpha_x^c = \frac{\alpha_x}{1 + \mathcal{I}_+ \alpha_x}; \alpha_z^c = \frac{\alpha_z}{1 - 2\mathcal{I}_- \alpha_x}. \tag{3.67}$$

with the interaction constant:

$$\mathcal{I}_\pm = -\frac{1}{8\pi\epsilon_1} \left\{ \sum_i \frac{1}{R_{\parallel,i}^3} \pm \frac{\epsilon_1 - \epsilon_2}{\epsilon_1 + \epsilon_2} \sum_i \frac{R_{\parallel,i}^2 - 8d^2}{(R_{\parallel,i}^2 + 4d^2)^{5/2}} \right\}. \tag{3.68}$$

Straightforward geometry on figure 3.22-d where appears the image point $\mathbf{R}_{i,r}$ of point i shows that:

$$\begin{aligned} \frac{R_{\parallel,i}^2 - 8d^2}{(R_{\parallel,i}^2 + 4d^2)^{5/2}} &= \frac{1}{R_{i,r}^3} \left[\cos^2\left(\frac{\pi}{2} - \theta_i^r\right) - 2\sin^2\left(\frac{\pi}{2} - \theta_i^r\right) \right] \\ &= -\frac{1}{R_{i,r}^3} (3\cos^2(\theta_i^r) - 1) = -4\sqrt{\frac{\pi}{5}} Y_2^0(\theta, \Psi)|_{\mathbf{r}=\mathbf{R}_i^r}, \end{aligned} \tag{3.69}$$

and that:

$$\frac{1}{R_i^3} = -\frac{4}{R_i^3} \sqrt{\frac{\pi}{5}} Y_2^0(\theta, \Psi)|_{\mathbf{r}=\mathbf{R}_i}, \tag{3.70}$$

since the involved spherical harmonics is defined as: $Y_2^0(\theta, \Psi) = \frac{1}{4}\sqrt{\frac{5}{\pi}}(3\cos^2\theta - 1)$. Therefore, the interaction term can be rewritten as:

$$\mathcal{I}_\pm = \frac{1}{4\pi\epsilon_1} \frac{1}{L^3} \left[S_{20} \pm \frac{\epsilon_1 - \epsilon_2}{\epsilon_1 + \epsilon_2} S_{20}^r \right] \sqrt{\frac{4\pi}{5}} \tag{3.71}$$

where have been introduced the lattice sums defined in reference [Bedeaux and Vlieger, 2001]:

$$
\begin{aligned}
S_{20} &= \sum_{i \neq 0} \left(\frac{L}{r}\right)^3 Y_2^0(\theta, \Psi)|_{\mathbf{r}=\mathbf{R}_i} \\
S_{20}^r &= \sum_{i} \left(\frac{L}{r}\right)^3 Y_2^0(\theta, \Psi)|_{\mathbf{r}=\mathbf{R}_i^r}.
\end{aligned}
\tag{3.72}
$$

with L the lattice spacing of the regular array of dipoles.

3.7.4.2 Substrate covered by a layer

The solution in the case of a lattice of dipoles in front of a substrate of dielectric function ϵ_3 covered by a layer of dielectric function ϵ_2 and thickness t relies on the expression of the image term A_1 in Fourier space (equation 3.45). The electric field at the origin amounts to:

$$
\begin{aligned}
\mathbf{E}_{1,d,x}^{x}(\mathbf{r}=0) &= \frac{1}{(2\pi)^2}\frac{p_x}{2\epsilon_1}\left[\sum_i \int \frac{k_x^2}{k_\parallel}\frac{\mathcal{A}_{12}+\mathcal{A}_{23}e^{-2k_\parallel t}}{1+\mathcal{A}_{23}\mathcal{A}_{12}e^{-2k_\parallel t}} e^{-2k_\parallel d} e^{i\mathbf{k}_\parallel . \mathbf{R}_{\parallel,i}} d^2\mathbf{k}_\parallel \right. \\
&\quad \left. - \sum_{i\neq 0} \int \frac{k_x^2}{k_\parallel} e^{i\mathbf{k}_\parallel . \mathbf{R}_{\parallel,i}} e^{-k_\parallel \eta} d^2\mathbf{k}_\parallel \right] \\
E_{1,d,z}^{z}(\mathbf{r}=0) &= \frac{1}{(2\pi)^2}\frac{p_z}{2\epsilon_1}\left[\sum_i \int k_\parallel \frac{\mathcal{A}_{12}+\mathcal{A}_{23}e^{-2k_\parallel t}}{1+\mathcal{A}_{23}\mathcal{A}_{12}e^{-2k_\parallel t}} e^{-2k_\parallel d} e^{i\mathbf{k}_\parallel . \mathbf{R}_{\parallel,i}} d^2\mathbf{k}_\parallel \right. \\
&\quad \left. + \sum_{i\neq 0} \int k_\parallel e^{i\mathbf{k}_\parallel . \mathbf{R}_{\parallel,i}} e^{-k_\parallel \epsilon_z} d^2\mathbf{k}_\parallel \right].
\end{aligned}
\tag{3.73}
$$

where $\eta > 0$ is a convergence factor. While the direct term is, of course, the same as in the case of a semi-infinite substrate, the angular part of the integral involved in the image term is also the same:

$$
\begin{aligned}
I_x(2d, \mathbf{R}_{\parallel,i}) &= \int \frac{k_x^2}{k_\parallel}\frac{\mathcal{A}_{12}+\mathcal{A}_{23}e^{-2k_\parallel t}}{1+\mathcal{A}_{23}\mathcal{A}_{12}e^{-2k_\parallel t}} e^{-2k_\parallel d} e^{i\mathbf{k}_\parallel . \mathbf{R}_{\parallel,i}} d^2\mathbf{k}_\parallel \\
&= \pi \int_0^\infty k_\parallel^2 \frac{\mathcal{A}_{12}+\mathcal{A}_{23}e^{-2k_\parallel t}}{1+\mathcal{A}_{23}\mathcal{A}_{12}e^{-2k_\parallel t}} e^{-2k_\parallel d} J_0(k_\parallel R_{\parallel,i}) dk_\parallel
\end{aligned}
\tag{3.74}
$$

within again the hypothesis of symmetric lattice for which $\langle \cos^2 \tau_i \rangle = \frac{1}{2}$ (see above). In the same way as in the previous section, the integral for dipoles perpendicular to the surface is:

$$
\begin{aligned}
I_z(2d, \mathbf{R}_{\parallel,i}) &= \int k_\parallel \frac{\mathcal{A}_{12}+\mathcal{A}_{23}e^{-2k_\parallel t}}{1+\mathcal{A}_{23}\mathcal{A}_{12}e^{-2k_\parallel t}} e^{-2k_\parallel d} e^{i\mathbf{k}_\parallel . \mathbf{R}_{\parallel,i}} d^2\mathbf{k}_\parallel \\
&= 2I_x(2d, \mathbf{R}_{\parallel,i})
\end{aligned}
\tag{3.75}
$$

Thus the results in terms of polarizabilities corrected from dipole-dipole interactions on a regular lattice of parameter L is again given by:

$$
\alpha_x^c = \frac{\alpha_x}{1+\mathcal{I}_+\alpha_x}; \alpha_z^c = \frac{\alpha_z}{1-2\mathcal{I}_-\alpha_x}. \tag{3.76}
$$

but with the interaction term:

$$\mathcal{I}_{\pm} = -\frac{1}{8\pi\epsilon_1 L^3}\left\{\sum_{i\neq 0}\left(\frac{L}{R_{\parallel,i}}\right)^3 \pm \sum_i \mathbb{I}\left(\frac{R_{\parallel,i}}{L},\frac{d}{L},\frac{t}{L}\right)\right\} \tag{3.77}$$

where:

$$\mathbb{I}(\widetilde{R},\widetilde{d},\widetilde{t}) = \int_0^\infty u^2 \frac{\mathcal{A}_{12}+\mathcal{A}_{23}e^{-2ut}}{1+\mathcal{A}_{23}\mathcal{A}_{12}e^{-2ut}} e^{-2u\widetilde{d}} J_0(u\widetilde{R})du. \tag{3.78}$$

$\mathbb{I}(\widetilde{R},\widetilde{d},\widetilde{t})$ appears as an Hankel's transform and gives the same results as a semi-infinite substrate at the limit $\epsilon_2 = \epsilon_3$ or $t = 0$.
In the case of a regular lattice, the sum of image terms $\mathbb{I}$ in equation 3.77 can be considerably simplified by considering the reciprocal lattice [Bedeaux and Vlieger, 2001] and Ewald summation. One may use the identity valid for any function $f(\mathbf{R}_\parallel)$:

$$\sum_i f(\mathbf{R}_{\parallel,i}) = \frac{1}{S}\sum_G \int d^2\mathbf{R}_\parallel e^{-i\mathbf{G}.\mathbf{R}_\parallel} f(\mathbf{R}_\parallel) \tag{3.79}$$

where S is the area of the Bravais lattice considered and $\mathbf{G}$ a reciprocal lattice vector. For a function that depends only of the modulus $R_\parallel$, the double integral reverts to an Hankel's transform:

$$\sum_i f(R_{\parallel,i}) = \frac{2\pi}{S}\sum_G \int_0^\infty f(\mathbf{R}_\parallel) J_0(G.R_\parallel) R_\parallel dR_\parallel \tag{3.80}$$

Since $\mathbb{I}(R,d,t)$ is already an Hankel's transform which is know to be equivalent to its inverse, the sum of image terms in equation 3.77 can be recasted into:

$$\begin{aligned}\mathcal{S}_{\mathbb{I}}(d,t,L) &= \sum_i \mathbb{I}(R_{\parallel,i},d,t,L)\\ &= \frac{2\pi}{S}\sum_G G\frac{\mathcal{A}_{12}+\mathcal{A}_{23}e^{-2Gt}}{1+\mathcal{A}_{23}\mathcal{A}_{12}e^{-2Gt}} e^{-2Gd}\end{aligned} \tag{3.81}$$

For a square lattice, $S = L^2$ and $G_{mn} = \frac{2\pi}{L}\sqrt{n^2+m^2}$ while for an hexagonal one $S = \frac{\sqrt{3}}{2}L^2$ and $G_{mn} = \frac{4\pi}{\sqrt{3}L}\sqrt{n^2+m^2+mn}$ where n, m are two integers. In the form of equation 3.81, the integration disappeared; the fast convergence over reciprocal space nodes is insured by the decaying exponential terms. Of course, the summation can take benefit from the lattice symmetry; for instance, only one eight of space have to be considered for a square reciprocal lattice. As for the direct lattice sum, a trick to speed up the convergence of the sum of $\sum_i 1/R_{\parallel,i}^3$ of direct terms is given in reference [Bedeaux and Vlieger, 2001].

3.7.4.3 Example: a metal layer on a dielectric substrate

The case of a Cr layer on Al_2O_3 the dielectric constants of which appear in figure 3.21 has been used as an example. The modulus of the sum $|\mathcal{S}_{\mathbb{I}}(d,t,L,\epsilon_1,\epsilon_2,\epsilon_3)|$ has been plotted in figure 3.23 for a square Bravais lattice after different normalizations: (i) to $|\mathcal{S}_{\mathbb{I}}(d,t,L,\epsilon_1,\epsilon_1,\epsilon_3)| = |\mathcal{S}_{\mathbb{I}}(d+t,0,L,\epsilon_1,\epsilon_2,\epsilon_3)|$ which reverts to replace the layer by vacuum, (ii) to $|\mathcal{S}_{\mathbb{I}}(d,t,L,\epsilon_1,\epsilon_2,\epsilon_2)|$ which reverts to replace the substrate by the layer material or (iii) to $|\mathcal{S}_{\mathbb{I}}(d,t,L,\epsilon_1,\epsilon_3,\epsilon_3)|$ which reverts to replace the layer material by the substrate. Results are shown in figure 3.23 for three different values of $t/d = 0.1; 1; 5$ as function of photon energy and d/L. The simulations

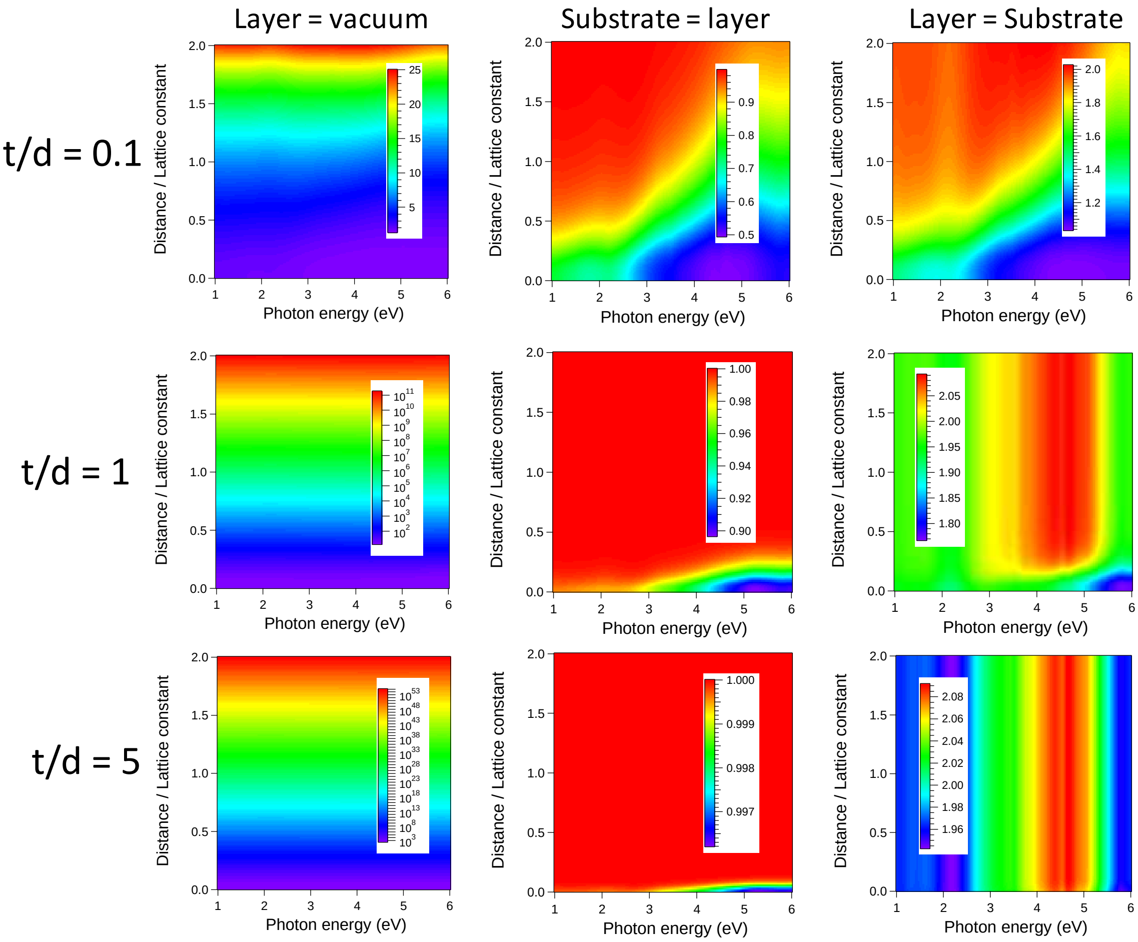

Figure 3.23: Image interaction sum $|\mathcal{S}_{\mathbb{I}}(d, t, L, \epsilon_1, \epsilon_2, \epsilon_3)|$ (see text) for a square lattice of dipoles in front of Cr layer on Al_2O_3 for $t/d = 0.1; 1; 5$ (lines). Values are normalized to fictitious situations (column) in which (i) the layer is replaced by vacuum, (ii) the substrate material is replaced by the layer one and (iii) the layer material is replaced by the substrate one.

demonstrate that ignoring the layer in terms of image interaction is catastrophic (case (i); left column in figure 3.23) while better results are obtained by extending the substrate to the $z = t$ surface (case (iii); right column in figure 3.23); this latter case leads to errors that are acceptable only if t/d and d/L are small. On the contrary, as soon as the thickness of the film is not too small (cases $t/d = 1; 5$), nearly similar results are given by extending the layer to infinity (case (ii); middle column in figure 3.23). The phase term follows exactly the same trend (not shown). This numerical finding can be easily rationalized from equation 3.81. Since

$$\mathcal{S}_{\mathbb{I}}(d, t, L) = \frac{2\pi}{S} \sum_G G \mathcal{A}_{12} e^{-2Gd} \frac{1 + \mathcal{A}_{23}/\mathcal{A}_{12} e^{-2Gt}}{1 + \mathcal{A}_{23}\mathcal{A}_{12} e^{-2Gt}}, \tag{3.82}$$

a fictitious semi-infinite substrate of dielectric function ϵ_2 which contribution is $\frac{2\pi}{S} \sum_G G \mathcal{A}_{12} e^{-2Gd}$ will account for the image dipole-dipole interaction over a lattice if the remaining fraction in equation 3.82 is close to one for all G. A straightforward algebra gives a minimal G value of:

$$G = \frac{1}{2t} \ln\left(\eta\,|\chi|\right) \quad \text{with} \quad \chi = \frac{4\epsilon_1\epsilon_2}{\epsilon_2^2 - \epsilon_1^2} \frac{\epsilon_3 - \epsilon_2}{\epsilon_2 + \epsilon_3} \tag{3.83}$$

required to reach an accuracy $\eta \ll 1$. Since for the dielectric constants of the Cr/Al$_2$O$_3$ system $|\chi| \simeq 0.5$ in the plotted spectral range, for a reasonable $\eta = 0.01$ value, the summation should goes up to $n_{max} \simeq 0.31L/t$. Therefore, since as soon as $t/L \gtrsim 1/3$, $n_{max} = 1$, the image term is equivalent to that obtained with a semi-infinite substrate with a dielectric function equal to the layer one. This can be understood quite qualitatively: as soon as the layer is not too thin compared to the dipole spacing $t/L \gtrsim 1/3$ and $t/d \gtrsim 0.1$, the projected path in the layer for lines of electric field of the image dipole of a given neighbor is long enough to forget the influence of the underlying substrate.

3.7.5 Polarizable dipole in front of a multilayer

Let's consider a point charge q in front of a stack of N layers of dielectric function ϵ_{n+1} and of thickness t_n located between z_n and z_{n+1} ($n = 1, \ldots, N$) on a substrate of dielectric function ϵ_{N+2} (figure 3.24). The charge is at distance $z_1 = d$ from the surface of the first layer. By using Fourier transform parallel to the surface, one can treat the case of a point charge in front of a multilayer in a similar way to the case of the single layer (see section 3.7.3.1). The Fourier components of the potential for $n = 2, \ldots, N+1$ read:

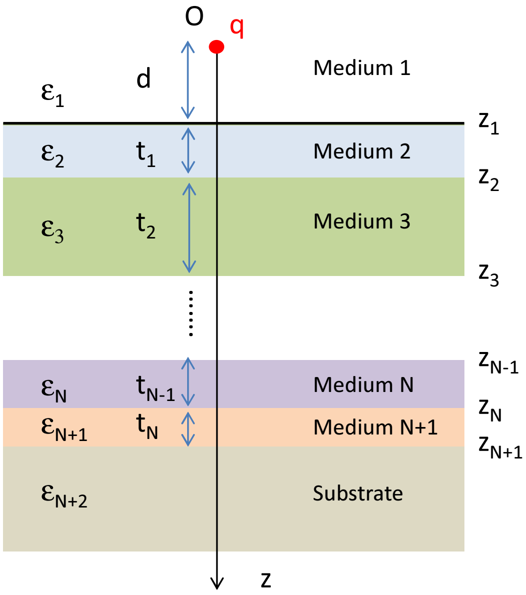

Figure 3.24: Point charge in front a stack of layer of dielectric function ϵ_{n+1}, of thickness t_n between z_n and z_{n+1}.

$$\begin{aligned}
\widetilde{\Psi}_1(\mathbf{k}_\parallel, z) &= A_1 e^{k_\parallel z} + \frac{q}{2\epsilon_1}\frac{e^{-k_\parallel |z|}}{k_\parallel} \\
\widetilde{\Psi}_n(\mathbf{k}_\parallel, z) &= A_n e^{k_\parallel z} + B_n e^{-k_\parallel z} + \frac{q}{2\epsilon_1}\frac{e^{-k_\parallel z}}{k_\parallel} \\
\widetilde{\Psi}_{N+2}(\mathbf{k}_\parallel, z) &= B_{N+2} e^{-k_\parallel z} + \frac{q}{2\epsilon_1}\frac{e^{-k_\parallel z}}{k_\parallel},
\end{aligned} \qquad (3.84)$$

and fulfill the continuity of potential and of the normal derivative of the displacement field at each interface z_n $(n = 1, \ldots, N+1)$, namely:

$$\begin{aligned} \widetilde{\Psi}_n(\mathbf{k}_\parallel, z_n) &= \widetilde{\Psi}_{n+1}(\mathbf{k}_\parallel, z_n) \\ \epsilon_n \frac{\partial \widetilde{\Psi}_n}{\partial z}(\mathbf{k}_\parallel, z_n) &= \epsilon_{n+1} \frac{\partial \widetilde{\Psi}_{n+1}}{\partial z}(\mathbf{k}_\parallel, z_n). \end{aligned} \tag{3.85}$$

This leads to a set of linear equations $(n = 2, \ldots, N)$:

$$A_1 e^{2k_\parallel z_1} = A_2 e^{2k_\parallel z_1} + B_2 \tag{3.86}$$

$$\epsilon_1 A_1 e^{2k_\parallel z_1} = \epsilon_2 A_2 e^{2k_\parallel z_1} - \epsilon_2 B_2 + \frac{q}{2k_\parallel \epsilon_1}(\epsilon_1 - \epsilon_2) \tag{3.87}$$

$$A_n e^{2k_\parallel z_n} + B_n = A_{n+1} e^{2k_\parallel z_n} + B_{n+1} \tag{3.88}$$

$$\epsilon_n A_n e^{2k_\parallel z_n} - \epsilon_n B_n = \epsilon_{n+1} A_{n+1} e^{2k_\parallel z_n} - \epsilon_{n+1} B_{n+1} + \frac{q}{2k_\parallel \epsilon_1}(\epsilon_n - \epsilon_{n+1}) \tag{3.89}$$

$$A_{N+1} e^{2k_\parallel z_{N+1}} + B_{N+1} = B_{N+2} \tag{3.90}$$

$$\epsilon_{N+1} A_{N+1} e^{2k_\parallel z_{N+1}} - \epsilon_{N+1} B_{N+1} = -\epsilon_{N+2} B_{N+2} + \frac{q}{2k_\parallel \epsilon_1}(\epsilon_{N+1} - \epsilon_{N+2}). \tag{3.91}$$

A suitable linear combination of equations 3.90-3.91 gives:

$$B_{N+1} = -\mathcal{A}^{-1}_{N+1,N+2} A_{N+1} e^{2k_\parallel z_{N+1}} - \frac{q}{2k_\parallel \epsilon_1}, \tag{3.92}$$

where $\mathcal{A}_{N+1,N+2} = \frac{\epsilon_{N+2} - \epsilon_{N+1}}{\epsilon_{N+1} + \epsilon_{N+2}}$. By introducing equation 3.92 into equations 3.88-3.89 and by using a linear combination to remove the A_n terms, it is possible to demonstrate recursively that :

$$B_n = -A_n e^{2k_\parallel z_n} \frac{1 + \mathcal{A}_{n,n+1} \widehat{\mathcal{A}}_{n+1,n+2} e^{-2k_\parallel t_n}}{\mathcal{A}_{n,n+1} + \widehat{\mathcal{A}}_{n+1,n+2} e^{-2k_\parallel t_n}} - \frac{q}{2k_\parallel \epsilon_1}, \tag{3.93}$$

for $n = N+1, \ldots, 2$ with the generalized dielectric contrast:

$$\widehat{\mathcal{A}}_{i,i+1} = \frac{\mathcal{A}_{i,i+1} + \widehat{\mathcal{A}}_{i+1,i+2} e^{-2k_\parallel t_i}}{1 + \mathcal{A}_{i,i+1} \widehat{\mathcal{A}}_{i+1,i+2} e^{-2k_\parallel t_i}}, \tag{3.94}$$

where:

$$\begin{aligned} \mathcal{A}_{i,j} &= \frac{\epsilon_j - \epsilon_i}{\epsilon_i + \epsilon_j}, \\ \widehat{\mathcal{A}}_{N+1,N+2} &= \mathcal{A}_{N+1,N+2}. \end{aligned} \tag{3.95}$$

The boundary conditions over the first interface given by equations 3.86-3.87 gives the image field term in vacuum:

$$A_1 = -\frac{q}{2k_\parallel \epsilon_1} e^{-2k_\parallel d} \frac{\mathcal{A}_{12} + \widehat{\mathcal{A}}_{23} e^{-2k_\parallel t_1}}{1 + \widehat{\mathcal{A}}_{23} \mathcal{A}_{12} e^{-2k_\parallel t_1}}. \tag{3.96}$$

Using the generic expression for the image dipole electric field at origin (equations 3.49), the corrections of polarizabilities are still given by equations 3.38, 3.41 where the fraction in the integral of equation 3.53 is replaced by the continuous fraction equations 3.96, 3.94. The same replacement holds true in the case of an array of dipoles in equation 3.81.

3.7.6 And beyond ?

The above-described polarizability correction at dipolar level shed light on the importance of screening of the image dipole induced by a continuous film on a substrate. Besides the relative dielectric functions of the film and of the substrate, the key parameter turned out to be the ratio d/t between the distance of the dipole to the film d and the film thickness itself t. The larger d/t the lower the screening induced by the film.

However, since surface susceptibilities of thin films are additive (section 3.7.1), handling accurately the case of a truncated particle on a film to compare to experimental data would require the exact calculation of its polarizability through an extension of this dipole approach to higher orders. The above sections give the track to follow. Indeed, using naively the effective film/substrate dielectric function of equation 3.56 to account for the substrate in the configurations of figure 3.1-b,c would face the arbitrariness of the d-parameter *i.e.* of the location of the potential expansion point. Moreover, due to a shorter range, quadrupole, octopole and so-on are expected to behave in different way than dipole. Sticking to the Yamaguchi's model [Yamaguchi et al., 1973, Yamaguchi et al., 1974] *i.e.* a full spheroid put on the film in dipolar interaction is a first approach but, unfortunately, this modelling is already known for not being accurate enough even on a semi-infinite substrate from a quantitative point of view, even in terms of aspect ratio [Bedeaux and Vlieger, 2001, Lazzari and Jupille, 2011].

3.8 Conclusion

This chapter gave an introduction to the plasmonics of supported particles in the framework of excess fields and interfacial susceptibilities by stressing on the link between optical response and morphology. In particular, it has been shown that a direct integration of the differential reflectivity signal could be a reliable indicator of the evolution of the particle aspect ratio and of the different stages of film evolution in the case of a Volmer-Weber growth. Despite intense interband transitions in Zn and Cr at the opposite to Ag, simulations of SDRS of Zn/Cr particles showed a non-negligible sensitivity to particle aspect ratio that can be used to monitor wetting at metal/alumina interface. Inversion of experimental Cr/Al_2O_3 optical spectra pointed at a strong anisotropy of the optical response between parallel and perpendicular directions assigned to the growth of flat particles. However, due to strong mixing, the theoretical decomposition in eigenmodes of polarization excited on intra or interband transitions turned to be difficult for Cr and Zn particles. Nevertheless, their optical response is dominated by a strongly damped dipole-like absorption mode. Finally, a first analytic approach of the electrostatic screening of a particle by a continuous film has been developed for an isolated dipole or a lattice of dipoles. Image corrections have been scrutinized in the case of a metal film on a dielectric substrate and vice-versa; an effective dielectric function was also proposed to account for the film induced screening at dipole level. This approach could be the basis of a more accurate calculation of the actual polarizability tensor of a film-supported particle.

CHAPTER 4

CHEMISTRY, ADSORPTION SITE AND GROWTH MODE OF CHROMIUM ON ALUMINA

The present chapter aims at exploring the chemistry at the chromium-alumina interface and the geometry of the adsorption site of the metal in connection with the hydroxylation state of the alumina. To do so, photoemission from the Cr, Al and O core levels, which is expected to be quite relevant to determine the oxidation states, is combined with extended x-ray absorption fine structure (EXAFS) at the Cr K-edge and *ab initio* calculations by density functional approach (DFT). In addition, the impact on the chromium particle morphology and growth mode is studied through optical spectroscopy (SDRS). Finally, LEED and RHEED are used to explore the crystallinity of the chromium deposit at the surface. The obtained results reveal to be helpful in understanding the chromium buffer effect on the growth of zinc.

4.1 Chemistry at the Cr/Al_2O_3 interface

4.1.1 The α-Al_2O_3(0001) (1×1) surface

4.1.1.1 Annealed surface

A series of Cr deposition experiments were performed on (1×1) surfaces of $Al_2O_3(0001)$; one-side epipolished $(9 \times 9 \times 0.5)$ mm^3 single cristals (provided by MaTecK [Mateck,]) were prepared according to the procedure explained in section 1.2.1. Shortly, it consists of an annealing of the as-loaded substrate at $\sim$ 1200 K (as measured with a pyrometer focused on the sample backplate) during 10 min in front of a gas doser with an O_2 background pressure of $\simeq 6 \times 10^{-7}$ mbar; with such a set-up, an enhancement of the local pressure on the surface by a factor of the order of ten is expected [Campbell and Valone, 1985]. The surface crystallinity and lack of reconstruction were checked by LEED after annealing, and carbon contamination levels were systematically verified through the C 1s core level and found lower than the detection threshold of about 1% of a monolayer; the monolayer (ML) is defined herein as the oxygen layer of the corundum alumina structure *i.e.* 1.5×10^{15} atom/cm^2. However, the unavoidable calcium segregation coming from bulk impurities rising up to 0.1 ± 0.1 ML on average was observed in photoemission. This finding is comparable with the transmission electron microscopy observation of 0.25 ML of Ca at the annealed Al/α-Al_2O_3 interface [Kaplan et al., 1995]. The Ca is spread over four cation layers resulting in a interface phase with a nominal composition of CaO.6Al_2O_3. However, the absence of any variation in the chemical state of Ca upon Cr deposition [1] led us to consider that its presence, on the surface or within the top atomic layers as seen from the enhancement of its contribution at grazing emission, does not affect our study from a chemical point of view. No other contaminants were found at the sensitivity of photoemission.

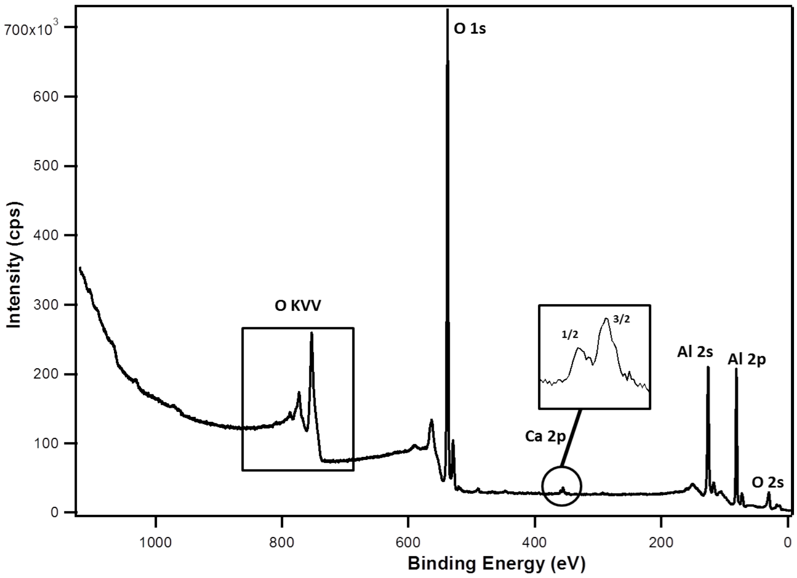

Figure 4.1: XPS widescan of a clean (1 × 1) surface of Al_2O_3(0001), recorded using a Mg-Kα anode, after annealing at 1200 K under oxygen ($p \simeq 6 \times 10^{-7}$ mbar). The main core levels and Auger transitions are labeled.

A typical widescan of a annealed (1×1) surface of alumina, recorded using a Mg-Kα source, is shown in figure 4.1. O 1s and Al 2s peaks were systematically recorded after annealing with a special care to avoid any spurious contribution coming from the molybdenum plate and/or the tantalum clips especially at grazing collection angles. This is particularly important in the frame of the O 1s peak analysis. In fact, the O 1s peaks, recorded from all (1 × 1) surfaces annealed following the above-mentioned procedure, exhibited a conspicuous asymmetry at high binding energy side. They could be decomposed into two components, the bulk one and a shoulder shifted by $\sim 1.8 \pm 0.2$ eV with respect to the former, using Voigt functions on a Shirley background. Figure 4.2 shows such a decomposition of an O 1s peak recorded using an Mg-Kα anode at normal incidence. An area ratio equal to 5% is found between the shoulder and the bulk components. Their full-width at half-maximum (FWHM) of the Lorentzian contribution was fixed at the x-ray emission linewidth (0.7 and 0.85 eV for spectra recorded using Mg-Kα and Al-Kα respectively). The remaining gaussian FWHM remained almost constant around 1.8 ± 0.06 eV for the bulk component while it varied from sample to sample, along with the relative intensity, for the shoulder peak due to slight discrepancies, mainly in the temperature of annealing for different samples (see figure 4.3).

The systematic increase of the relative area of the shoulder when switching from normal to grazing emission, as exemplified in figures 4.4, points at a surface species. But, by subtracting the NE spectra to the GE one (figure 4.4-right), another signature rather shifted to lower binding energies with respect to the main bulk component arises occasionally. In the absence of

---

[1] The Ca 2p core level does not evolve at all during Cr deposition; a chemical shift of ∼ 1 eV is expected between Ca and CaO [NIST, 2000]

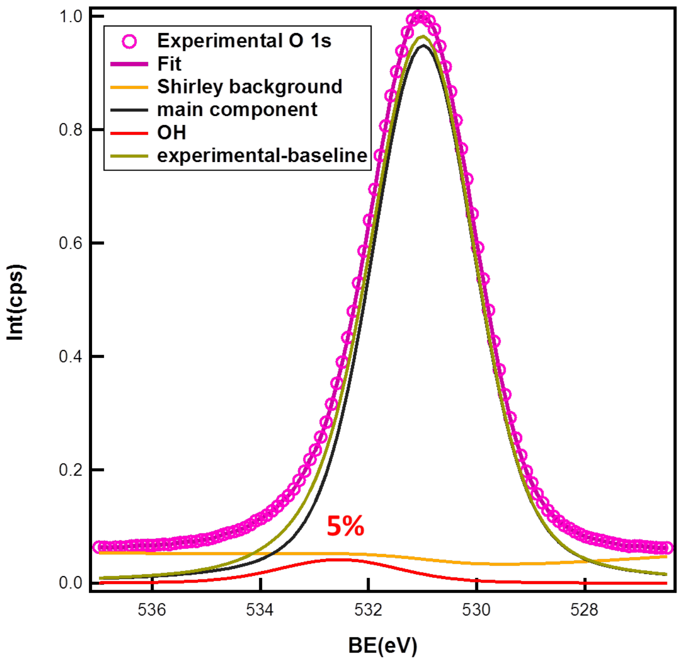

Figure 4.2: Decomposition of O 1s peak recorded at normal incidence after annealing an alumina sample under oxygen. Two components are necessary to fit the experimental spectra on a Shirley background: the bulk component at 531 eV and a shoulder at 532.55 eV.

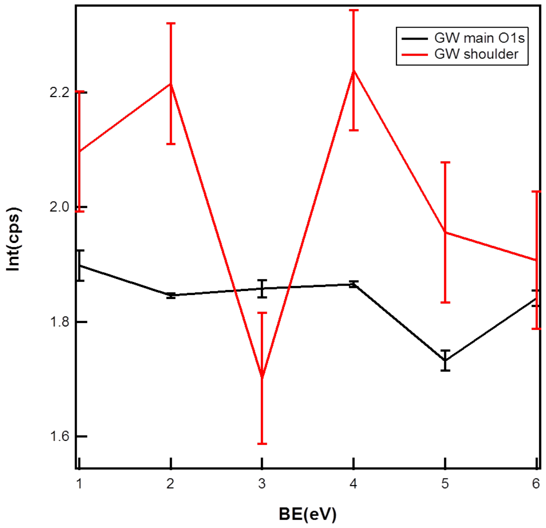

Figure 4.3: Values of FWHM of the gaussian component used in the decomposition of the O 1s peak for a series of (1×1) Al_2O_3 surfaces annealed at $\simeq$ 1200 K under oxygen $p =\sim 6 \times 10^{-7}$ mbar. Error bars come from uncertainties in the fit.

any change on the Al 2s peak at grazing emission (see figure 4.5), we assume that it corresponds to a surface contribution from the alumina sample, maybe related to Ca segregation, which implies the account of a third component in order to fit the O 1s peak for some of the alumina samples that we studied.

Based on the similarities with the literature, the high binding energy shoulder component is assigned to residual surface hydroxyl groups. Indeed, as we already pointed out in section 2.1.4, alumina surfaces manifest high reactivity towards water which leads to its dissociative adsorption as evidenced by Coustet and Jupille [Coustet and Jupille, 1997] through HREELS, Ahn and Rabalais [Ahn and Rabalais, 1997] through TOF-SARS, and Nelson and Elam et *al.* [Nelson et al., 1998,Elam et al., 1998] using TPD. Its total removal upon annealing

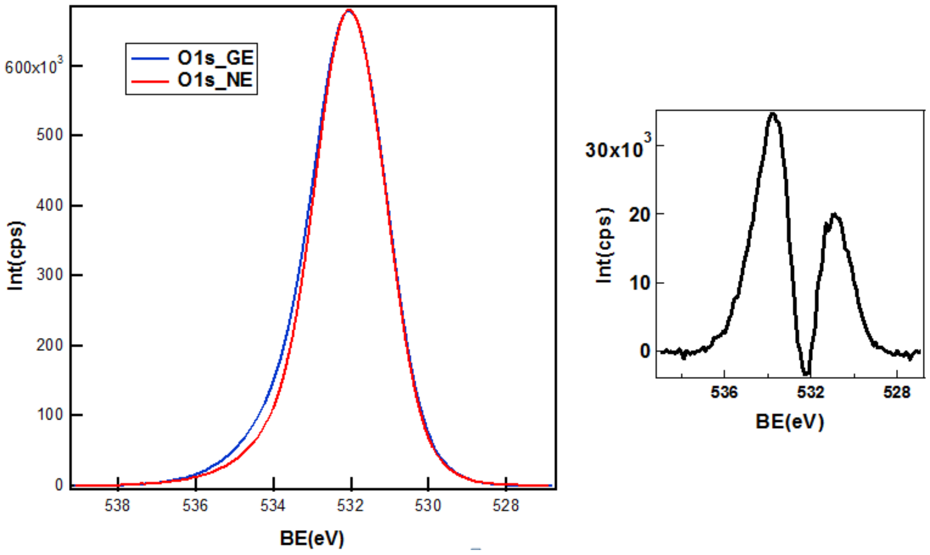

Figure 4.4: (Left) Superposition of raw O 1s XPS core levels collected at $\theta = 0°$ and 60° emission after background subtraction and normalization to maximum. (Right) Difference between the two normalized spectra.

before oxygen-deficient reconstruction appearance remained controversial, until being rebutted by Ahn and Rabalais [Ahn and Rabalais, 1997] and Lazzari and Jupille [Lazzari and Jupille, 2002, Lazzari and Jupille, 2005] who perceived remnants of hydroxyl groups, equivalent to ~ 0.2 ML $(3 \pm 1.5 \times 10^{14}\ OH/cm^2)$ for the last authors. This interpretation is fully supported by an increase of this component relative area when the surface is purposely exposed to water (see section 4.1.1.2). Using an inelastic mean free path of 16 Å in alumina [Tougaard,], the systematic analysis of the area ratio between shoulder and bulk component for our annealed surfaces under oxygen yielded to estimated values of residual hydroxyl coverage ranging between 0.14 and 0.37 ML (from 2.1×10^{14} to $5.6 \times 10^{14}\ OH/cm^2$). One should keep in mind that a relative error of the order of 20 % coming from the uncertainty on the mean free path applies also on this value. Residual OH groups on alumina surface annealed in UHV have often been observed [Ahn and Rabalais, 1997, Niu et al., 2000, Lazzari and Jupille, 2002, Lazzari and Jupille, 2005]. The above range of coverage corresponds rather well to values determined by recoiling spectroscopy [Ahn and Rabalais, 1997] $1.7 \times 10^{14}\ OH/cm^2$ and by photoemission $(3 \pm 1.5) \times 10^{14}\ OH/cm^2$ [Lazzari and Jupille, 2002] and $7 \times 10^{14}\ OH/cm^2$ (0.47 ML found by [Niu et al., 2000] with the definition of ML used herein since that definition is not given by Niu et al.). In what follows, the values measured for the residual OH coverage are indicated in all cases where it is involved. The role of these residual hydroxyl groups that remain up to the high temperature reconstruction of the surface and their interaction with chromium will be discussed in section 4.1.3.

4.1.1.2 Hydroxylated surface

The facts discussed in the previous section together with the knowledge of the important role played by hydroxyl groups in the interaction with supported metals [Libuda et al., 1997, Niu et al., 2000, Kelber et al., 2000, Chambers et al., 2002, Lazzari and Jupille, 2002, Lazzari and Jupille, 2005] prompted an investigation of purposely hydroxylated alumina surfaces. The

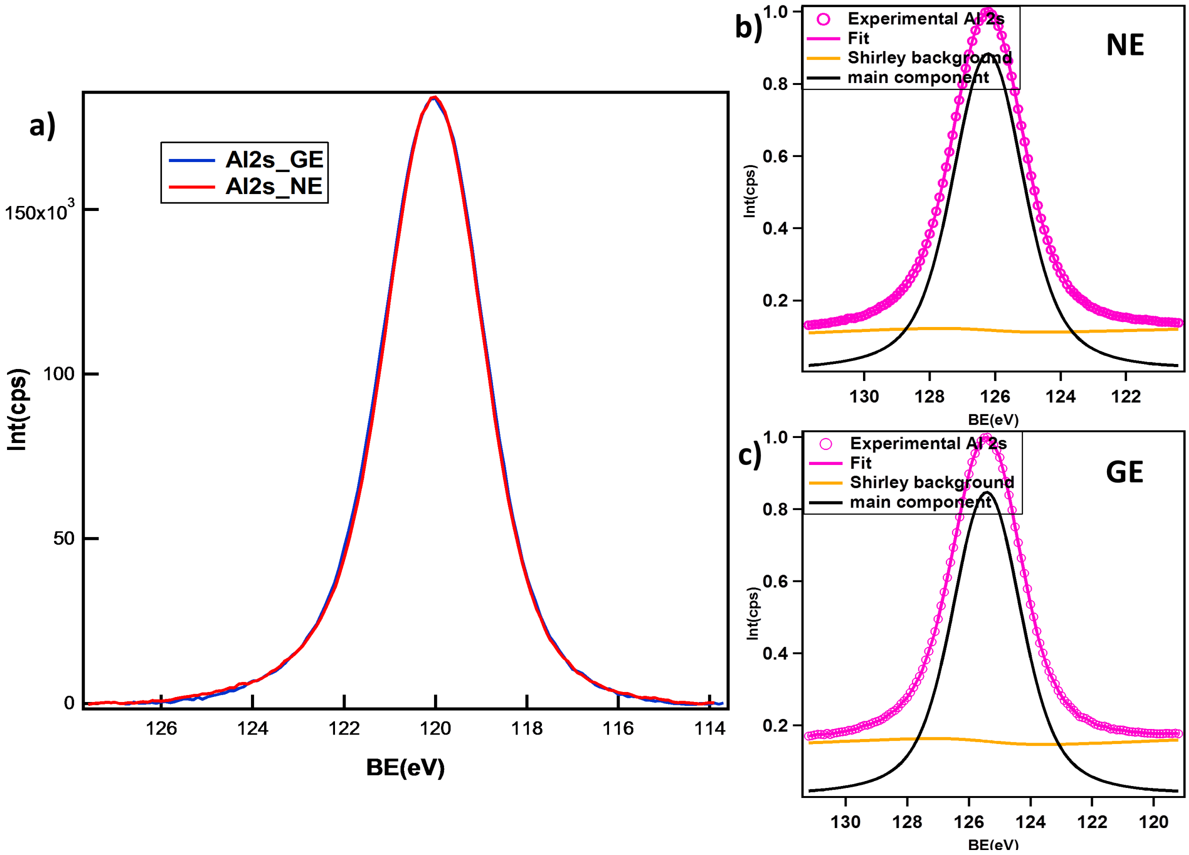

Figure 4.5: a) Superposition of raw Al 2s core level peaks collected at $\theta = 0°$ and $60°$ emission after background subtraction and normalization. b) c) Fits of the Al 2s peak with only one Voigt component on a Shirley background at normal and grazing incidence respectively. The fitting parameters are exactly the same.

hydroxylation was performed in the load-lock chamber after a careful bake out, where clean annealed alumina surfaces were exposed to a pressure of pure water vapor $\simeq 1 - 20$ mbar for one minute obtained by performing several cycles of freeze/pump on deionized water in an ancillary gas pipe system. Applying this method suggested a saturation coverage of 0.66 ML of hydroxyl groups according to Elam *et al.* [Elam et al., 1998], while 0.6 ML were found by Lazzari and Jupille [Lazzari and Jupille, 2005], and 0.3-0.5 ML were declared by Coustet and Jupille after ice desorption [Coustet and Jupille, 1997].
A simple superposition of the O 1s peaks after annealing and after hydroxylation collected at grazing incidence highlights a clear increase in the OH shoulder intensity (see figure 4.6). A decomposition of the O 1s peaks allowed a quantification of the hydroxyl coverage and yielded 0.6 ± 0.05 ML after exposure to 1 mbar of water vapor. This process resulted in an addition of 0.5 ML of hydroxyl groups to 0.14 ± 0.01 ML that already existed on the bare surface after annealing. We note that the additional component at low binding energies assigned to either a surface contribution or calcium oxide segregation accounts for 14% of the main bulk component and was kept constant before and after hydroxylation (figure 4.7). This percentage would correspond to an equivalent Ca thickness of ~ 1 Å which is exactly the value calculated based on the area ratio between Ca 2p and Al 2s peaks. However, the uncertainty concerning

the nature of this component leads to an error up to 8-20% on the quantification of OH groups. In addition, despite caution, this high-pressure hydroxylation procedure generally gives rise to some carbonaceous contaminants. These are assumed not to bias the calculated OH coverage.

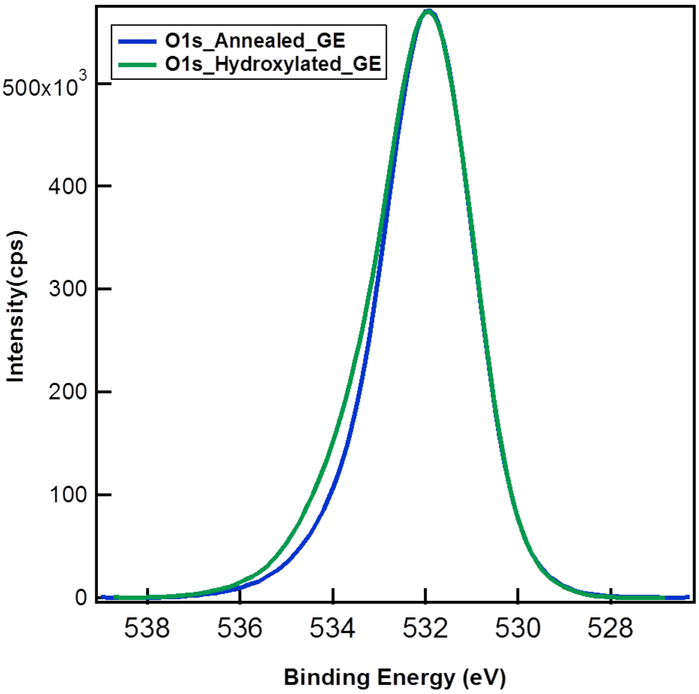

Figure 4.6: Superposition of O 1s peaks collected at grazing incidence ($\theta = 60°$) after annealing under oxygen and after hydroxylation in the load-lock chamber. The shoulder is clearly visible in the last case and signs the increase in hydroxyl group coverage.

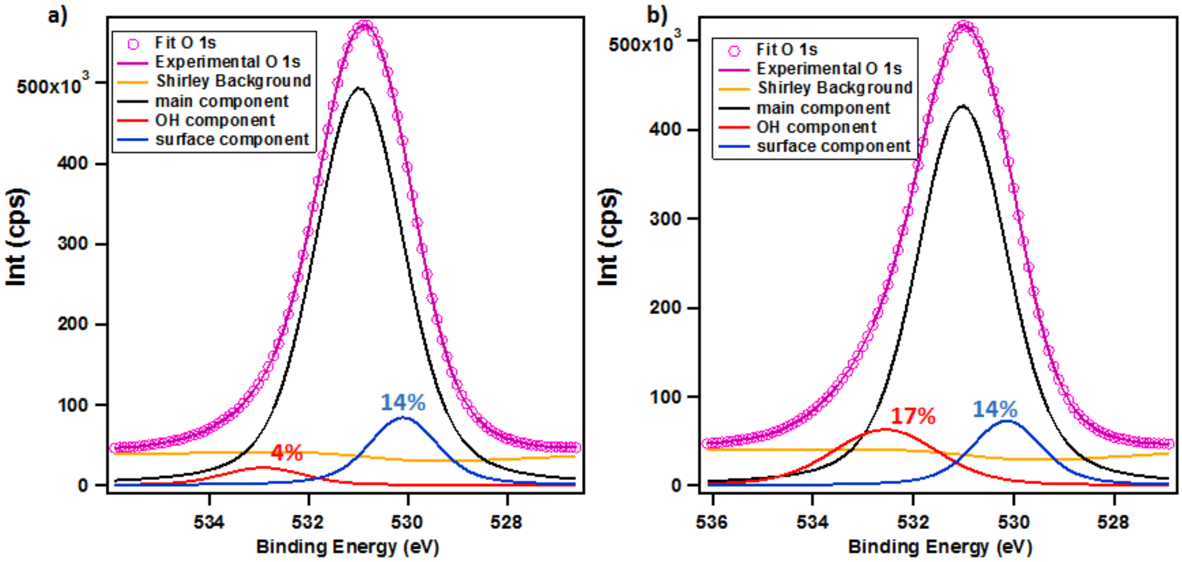

Figure 4.7: Fit of O 1s peaks collected at grazing incidence ($\theta = 60°$) a) after annealing under oxygen and b) after hydroxylation in the load-lock chamber. Three components : bulk, OH and surface/or CaO were necessary to fit the experimental spectra. The area ratio between the bulk and surface/CaO components was kept constant before and after hydroxylation.

4.1.2 Adsorption of Cr on Al_2O_3: quantitative photoemission analysis

The evaporation of Cr on annealed alumina surfaces was performed at room-temperature under high vacuum ($P \simeq 8 \times 10^{-10} - 5 \times 10^{-9}$ mbar) from a 99.5 % pure metallic rod heated at high temperature by electron bombardment in a EFM3 Focus OMICRON evaporation cell. The evaporation rate was calibrated by a quartz microbalance and cross-checked with photoemission. It ranged from 0.5 to 1 Å/min depending on the final sought thickness (a fraction of Å or 4-16 Å respectively). A typical XPS widescan of a Cr deposit on a clean (1×1) surface of α-Al_2O_3 is shown in figure 4.8. It features all the peaks characteristic of alumina and chromium accessible in the binding energy range going from 0 to 1200 eV. Despite its absence on the bare surface and a careful outgassing of the cell prior to deposition, a C 1s contamination shows up on the widescan spectrum. This unavoidable carbon coverage increased with deposition time and not really with exposure to residual vacuum, suggesting that this contamination comes from the evaporant itself. For instance, the quantification of carbon through an analysis of the C 1s and Al 2s areas yields $\sim 0.6 - 3$ Å for thick Cr deposits ($\sim$ 15 Å and above) compared to $\sim 0.05 - 0.3$ Å for the lowest thicknesses of metal.
Moreover, one can notice from the widescan that the O KVV and Cr LMM, LMV, and LVV Auger transitions are all superimposed, which precludes the retrieval of any useful chemical information on chromium from the Auger lines. Consequently, the analysis of the chemical state of Cr was scrutinized through the shift of the Cr 2p peak relative to the position of the Al 2s core level and on the spin-orbit splitting of Cr 2p (see more in section 4.1.3).

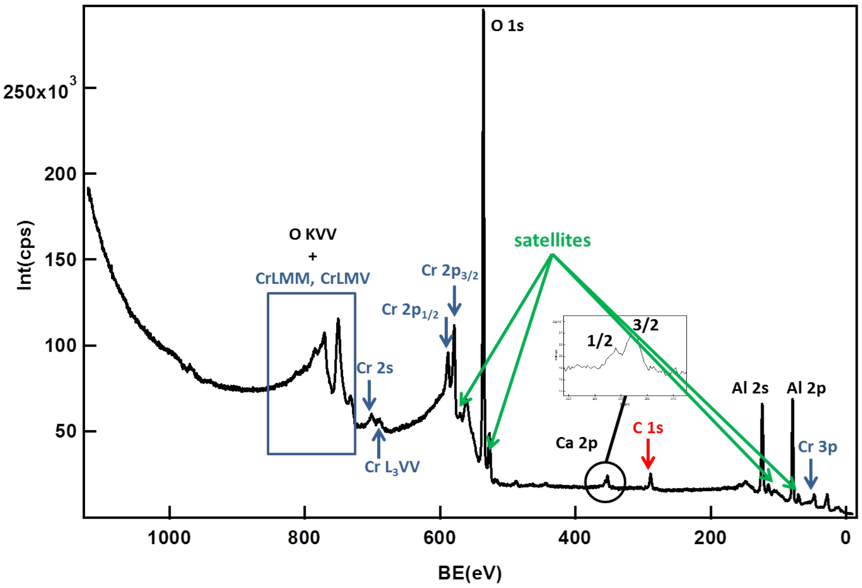

Figure 4.8: XPS widescan of a clean (1×1) surface of $Al_2O_3(0001)$ with a chromium deposit of 0.8 Å, recorded using an Mg-Kα anode at grazing incidence ($\theta = 60°$).

The understanding of the Cr/Al_2O_3 system required a special focus on the quantification of deposited chromium after each evaporation. For that purpose, the Cr 2p and Al 2s core levels were systematically considered, albeit the choice of Cr 3p and Al 2p would seem more relevant due to closer kinetic energies and analyzer transmission functions. However, for thick deposits, the superimposition of Cr 3p and Al 2p peaks requires a careful decomposition of the profile. Equivalent thicknesses were obtained based on a continuous film model as explained in section 1.3.7. As a matter of fact, since some differences in absolute thickness values appear upon the choice of peaks for quantification, we remind that our ascertainments are made based on a trend behavior. Consistently, we notice, from the plot of Cr thicknesses as a function of those calibrated on a quartz balance (see figure 4.9), that an agreement between both values only occurs for thick deposits. On the contrary, a lack of consensus is obvious at low thicknesses. This disagreement roots into the hypothesis of the continuous film model at the early stage of growth. This conclusion however gives an early accurate insight on the wetting behavior of Cr particles which will be proved rather correct in section 4.4.

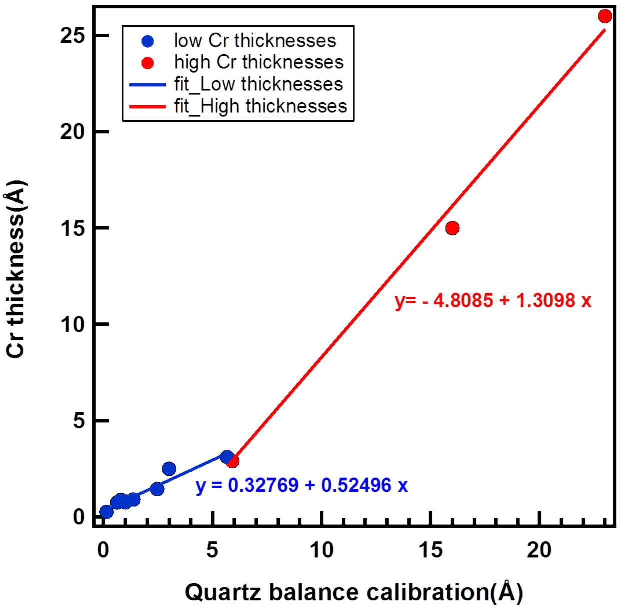

Figure 4.9: Plot of chromium thickness calculated from Cr 2p/Al 2s area ratio using a continuous film model versus the values as calibrated on a quartz balance. Linear fitting reveals an agreement between the quantification and the calibration for high thicknesses while a disagreement shows up at low thicknesses.

4.1.3 Deposition of Cr/Al_2O_3 : from chromium oxide to metal

The chemical state of the deposit constitutes a major topic to tackle. Chromium atom has a high spin electronic configuration $[Ar]3d^5 4s^1$ and exhibits a wide range of oxidation states from 0 to 6+ among which the most common and stable is 3+. Normally, it is rather easy to identify its oxidation state based on the chemical shift and on the Cr 2p doublet spin-orbit splitting. According to databases [NIST, 2000, Naumkin et al., 2012] [2], the binding energies of Cr $2p_{3/2}$ are 574.2 ± 0.25 eV for Cr metal (Cr^0), 577.2 ± 0.2 eV for $Cr(OH)_3$ (Cr^{3+}), 576.63 ± 1.3 eV for Cr_2O_3 (Cr^{3+}), 575.85 ± 0.6 eV for CrO_2 (Cr^{4+}), 579.3 ± 0.6 eV for CrO_3 (Cr^{6+}). The spin orbit splitting of the Cr 2p doublet are 9.25 ± 0.08 eV for Cr metal (Cr^0), 9.72 ± 0.2 eV for Cr_2O_3 eV (Cr^{3+}), 9.6 ± 0.14 eV for CrO_2 (Cr^{4+}). However, the analysis of absolute binding energies in our case would lead to erroneous conclusions because of important charge effects on the insulating alumina substrate. To overcome this issue, we relied on the analysis of relative binding energy shifts using the Al 2s peak position as an internal reference. Indeed, for one of the thickest Cr deposit (15 Å), the charge effects were almost completely eliminated leading to a Cr 2p binding energy in agreement with tabulated metallic chromium [NIST, 2000, Naumkin et al., 2012]; the metallization of the surface is a proof of the formation of a percolated metallic

---

[2] Error bars stems from the number of references in the database.

Cr film connected to the metallic clips as demonstrated later on by SDRS (section 4.4.1). The obtained Al 2s binding energy could therefore be used as an "absolute" value to determine the amount of charge effect. Moreover, the lack of change of Al 2s lineshape (see below) rules out any direct reduction of alumina by chromium. Figure 4.10 displays the Cr 2p peaks recorded for different thicknesses and shifted with respect to the Al 2s reference peak. Spectra are bounded by that of the 15 Å thick Cr metallic film, and that of a fully oxidized 15.4 Å Cr film prepared by heating the sample at ∼ 1500 K under oxygen $p = 2 \times 10^{-6}$ mbar. Their 3/2 binding energies peaks are at 574.3 eV and 577.7 eV after the charge effect correction, compared to 574.1 and 576.63 eV found on average over all values reported in the NIST XPS database [NIST, 2000, Naumkin et al., 2012] for metallic Cr and Cr_2O_3 respectively. These values prove in a first place that our choice of metallic reference was correct; however, the chromium oxide chemical shift seems to be overestimated by 0.5 eV maybe because of a complex band alignment at the oxide/oxide interface, a residual charge effect in the chromium oxide film or a different stoichiometry. Concerning the chemical state of Cr as a function of thickness, the position of all Cr 2p peaks is intermediate as highlighted in figure 4.11, suggesting a partial oxidation of chromium tending towards a metallic behavior as the film thickens. However, a final state effect due to partial screening of the positive photo-hole in small particles could also explain the observed increase in binding energy at small thicknesses. As observed for silver or gold clusters [Wertheim et al., 1983, Wertheim et al., 1986, Hövel et al., 1998, Howard et al., 2002, Ozawa et al., 2005, Chernysheva et al., 2018], this electrostatic

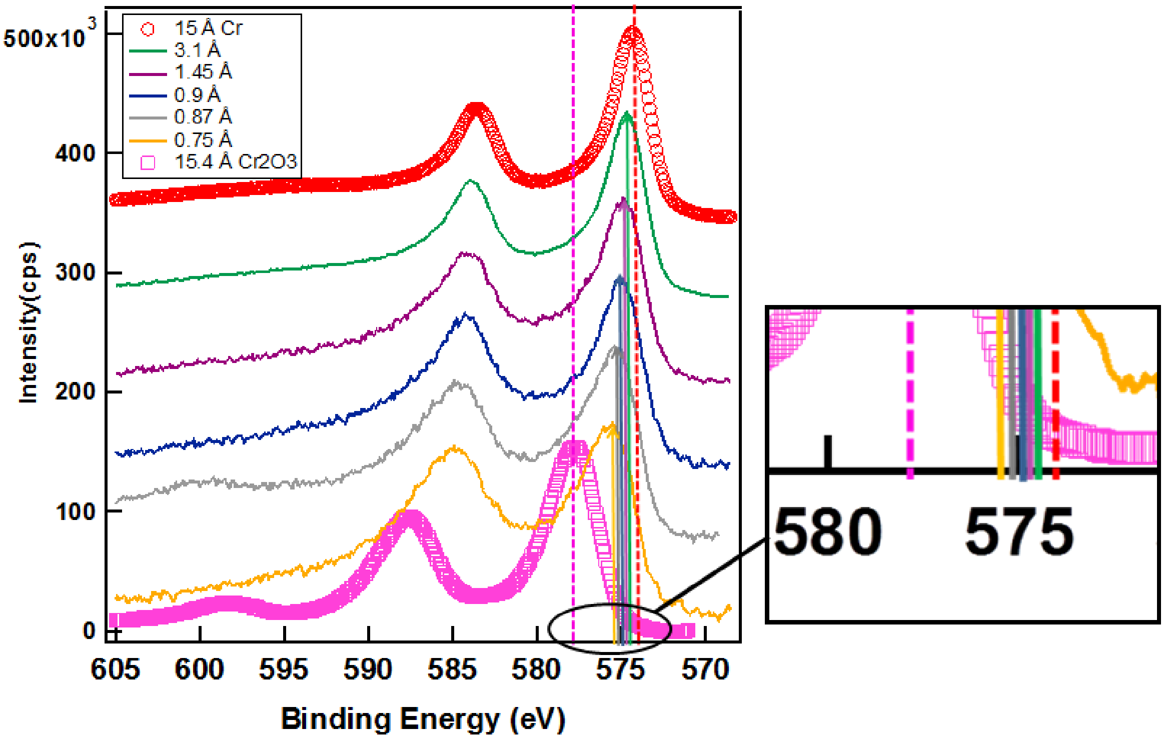

Figure 4.10: Series of Cr 2p peaks recorded for different Cr deposit thicknesses on α-Al_2O_3 (1×1) surfaces all shifted with reference to the Al 2s recorded for the thickest Cr deposit (15 Å: red spectra). A progressive displacement (see inset) is observed between the chromium oxide reference and the thick metallic Cr film as the coverage increases.

effect is strongly influenced by the coupling between the substrate and the particle. To a first approximation, the reference level of the clusters shifts by $E_{F,m} = \alpha e^2/4\pi\epsilon_0 R$, where R is the particle radius, ϵ_0 the vacuum permittivity and α a constant value around 0.5 [Hövel et al., 1998, Howard et al., 2002]. The observed shift of ~ 1 eV would correspond to cluster of around 1.5 nm.

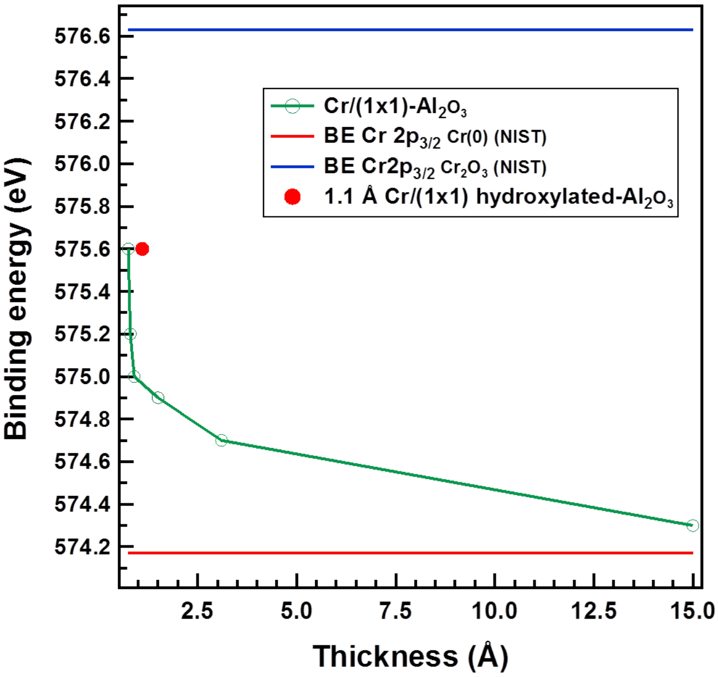

Figure 4.11: Plot of Cr $2p_{3/2}$ binding energy shift, after charge effect correction, for deposits of different thicknesses on a $Al_2O_3(0001)$-(1×1) compared to reference values of energy for metallic and fully oxidized (Cr_2O_3) chromium deduced from the NIST database [NIST, 2000, Naumkin et al., 2012]. The red disk pinpoints the binding energy of a 1.1 Å Cr deposit on a surface of alumina previously hydroxylated in the load-lock.

Therefore, the above findings are not sufficient to conclude on the exact chemical state of the chromium. In fact, a spin-orbit splitting of 9.2 and 9.8 eV very close to the values of the literature 9.3 and 9.7 eV [NIST, 2000, Naumkin et al., 2012] are found for the metallic and fully oxidized deposits respectively. Since the splitting averaged over the series is equal to 9.23 ± 0.09 eV, this factor could be indicative of the metallic chemical state for the rest of deposits. A lineshape decomposition would help resolving this riddle but accurately fitting a Cr 2p peak faces the problem of interplay between lineshape symmetry, satellite peaks, plasmon peak and background. This failure has been proven many times in the literature [Kirby et al., 1987, Salvi et al., 1995, Sainio et al., 2005, Aronniemi et al., 2005, Todeschini et al., 2017]. Although we never obtained a consistent fit, an agreement over the presence of different chemical states under the same Cr 2p peak was obviously common (not shown). Indeed, the lineshape of the Cr 2p exhibits a clear shoulder at high binding energies, the contribution of which decays as the growth proceeds (see figure 4.12); Cr is likely partially oxidized with a mixed valency compound at the interface with alumina. This finding is not surprising since a reaction of chromium, up to a limited thickness, with residual surface hydroxyl groups is expected as observed for other metals in the literature [Libuda et al., 1997, Niu et al., 2000, Kelber et al., 2000, Chambers et al., 2002, Lazzari and Jupille, 2002, Lazzari and Jupille, 2005, Todeschini et al., 2017] (see section 2.2.1). However, the possibility of chromium oxidation through an interaction with oxygen atoms of the alumina substrate has to be excluded. As a matter of fact, the superposition of Al 2s peak recorded before and after Cr deposits in addition to

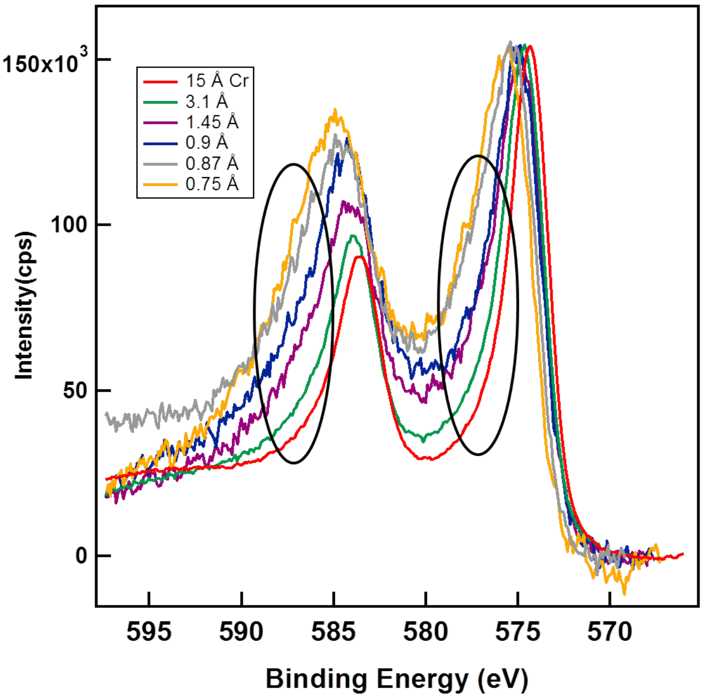

Figure 4.12: Series of Cr deposits with different thicknesses normalized in intensity. A shoulder feature circled in black shows up at the high binding energies side of Cr 2p. It is more intense for low thicknesses and fades away progressively as the coverage increases and a metallic film forms.

the identical fitting performed with a unique component (figure 4.13) discards any alumina reduction upon deposition of chromium on the surface at any coverage. The expected tabulated chemical shift of more than 1 eV between Al^{3+} and Al(0) reinforces this conclusion [NIST, 2000].

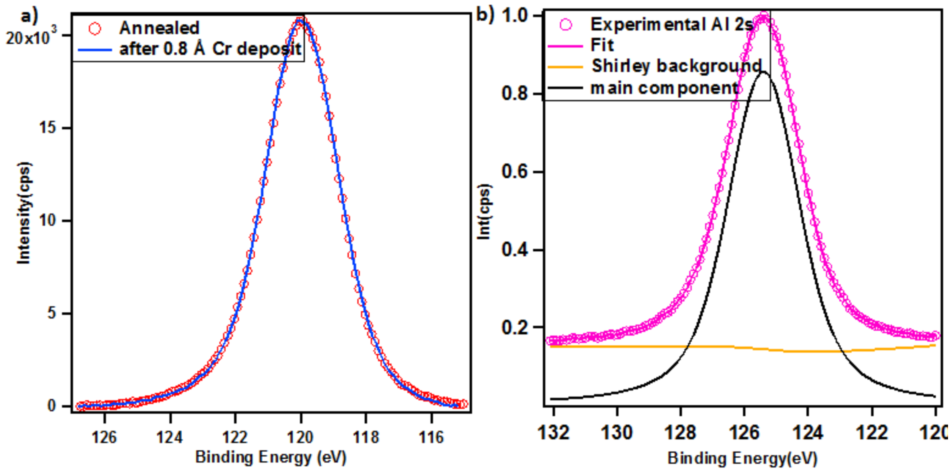

Figure 4.13: a) Superposition of Al 2s recorded at grazing incidence ($\theta = 60°$) before and after a deposit of 0.8 Å of Cr showing no change. b) An example of fit for the Al 2s peak with only one component, identical before and after Cr deposit.

At this stage, the O 1s peak will be scrutinized to elucidate the oxidation process of chromium at the beginning of growth. Starting with the superposition of O 1s peaks recorded at normal incidence before and after Cr deposit for different thicknesses, figure 4.14 shows that the shoulder seen at high binding energies on the bare surface and assigned to OH groups shrinks when another appear at low energies. Moreover, this shrinkage-popping out process is more pronounced for the 1.45 Å and 3.1 Å deposits than for the 0.75 Å, most probably because of an increased surface coverage. Consequently, in order to pinpoint more clearly this phenomenon at low thickness, XPS measurements at a grazing angle have been performed for an evaporation of 0.8 Å of Cr as shown in figure 4.15. Furthermore, in order to confirm again that chromium oxidation originates from a reaction with residual surface hydroxyl groups, we performed a 1.1 Å chromium deposit on a purposely hydroxylated surface. A superposition of the O 1s after hydroxylation and after the evaporation turned out to be assertive of our

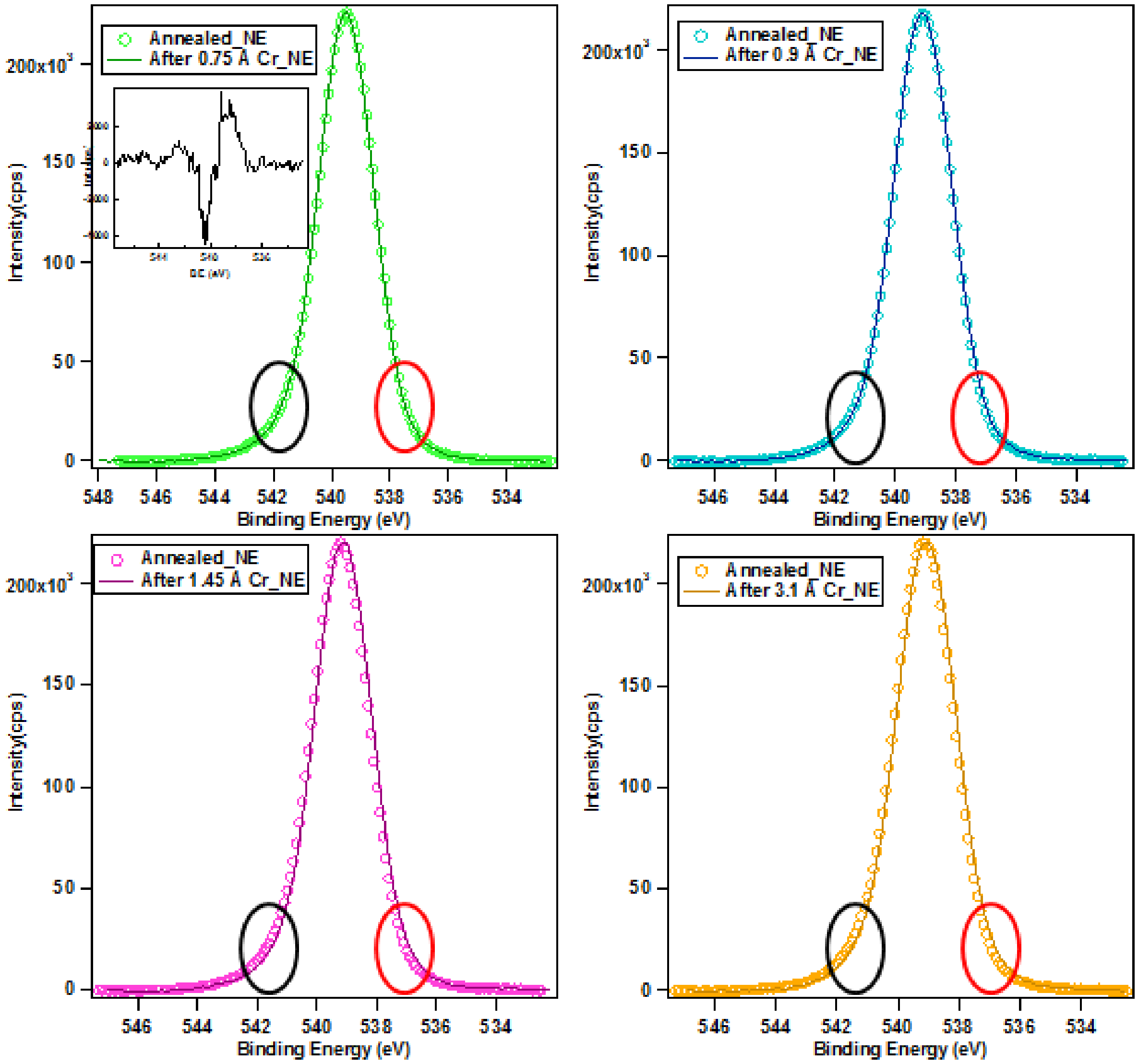

Figure 4.14: Superposition of O 1s core level peaks recorded at normal incidence before and after Cr deposition for different thicknesses showing a decrease of the hydroxyl shoulder at high binding energies (circled in black) and the appearance of a feature at low energies (circled in red). The inset in the first left top panel (0.75 Å) corresponds to a difference applied between the normalized peak after Cr deposit.

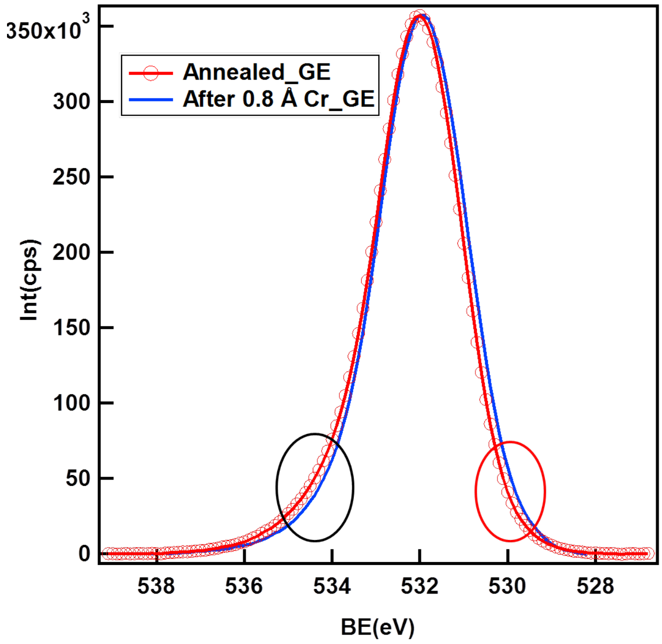

Figure 4.15: Superposition of O 1s recorded at grazing incidence before and after a 0.8 Å Cr deposit showing clearly the decrease of the OH shoulder at high binding energies (circled in black) and the appearance of a feature at low energies (circled in red).

hypothesis (see figure 4.16). The observed apparent chemical shift of Cr 2p is identical to that on annealed surfaces (red circle in figure 4.11).

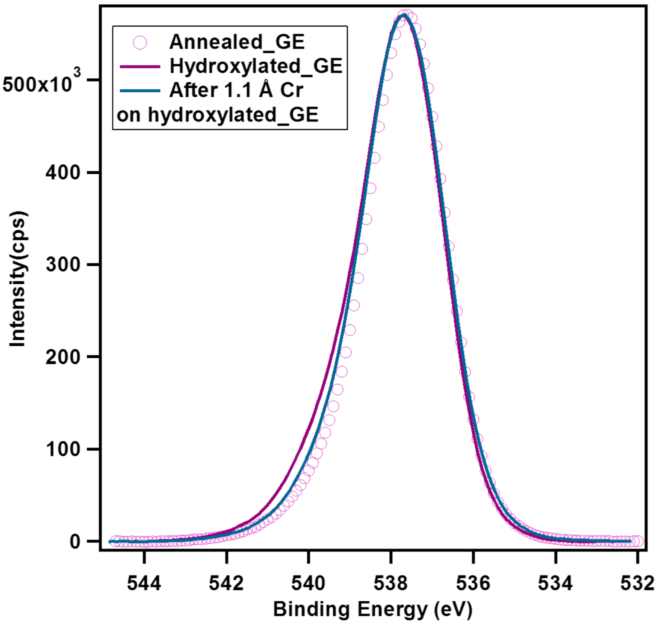

Figure 4.16: Superposition of O 1s recorded at grazing incidence before and after a 1.1 Å Cr deposit on a purposely hydroxylated surface compared to the surface before hydroxylation, highlighting the reaction of Cr with OH groups though the decrease of the OH shoulder at high binding energies and the appearance of a feature at low energies assigned to an oxidized chromium species.

Although many qualitative elements confirmed the reaction of Cr with residual OH groups, the access to quantitative information demanded further investigation through the decomposition of the O 1s peak. Figure 4.17 shows the fit of O 1s peaks recorded at normal incidence before and after a 3.1 Å Cr deposit on a $Al_2O_3(0001)$-(1×1) surface. A low binding energy

Cr_xO_y component was incorporated in the fitting after deposition. The area ratio relative to the main component of the OH feature decreased from 5 to 2 %, while the Cr_xO_y peak accounted for only 1.2 %. The quantification of these species based on inelastic mean free path revealed 0.37 ML of OH present at the surface after annealing which decreased to 0.14 ML after the Cr deposit along with the formation of 0.1 ML of Cr_xO_y. In fact, 0.23 ML of OH groups consumed during a reaction with chromium would lead, in a first approximation, to the formation of 0.077 ML of Cr_2O_3 (and/or CrO_3) or to 0.12 ML of CrO_2. Therefore, the values deduced from the decomposition are not totally absurd and prove that the quantity of OH that disappeared was actually involved in a reaction with Cr. Likewise, the consumption of residual hydroxyl groups after the deposition of Cr was also made explicit in the plot of the evolution of OH area ratio to that of the total peak as a function of the Cr thickness (figure 4.18). This graph points out at a systematic decrease of this ratio after each evaporation process. In parallel with each decrease of the OH component percentage, an increase of the Cr_xO_y species ratio appears.

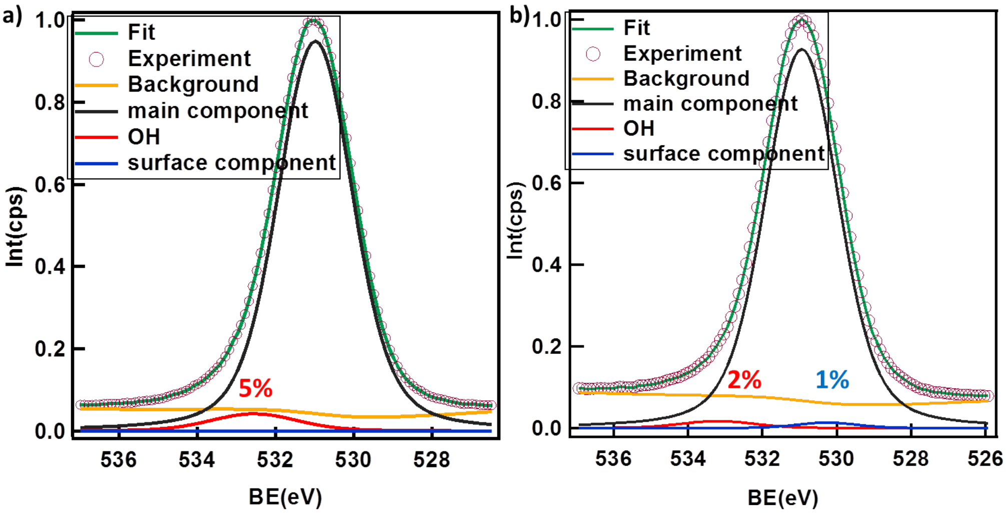

Figure 4.17: Fit of O 1s peak recorded at normal incidence before a) and after b) a 3.1 Å Cr deposit on a $Al_2O_3(0001)$-(1×1) surface. One bulk and an OH component (black and red respectively) were used to fit the peak before deposit, an additional component relative to Cr_xO_y was needed to fit the peak after deposition. Relative peak areas in reference to the main component are indicated on the figure.

To conclude, XPS measurements demonstrated that chromium probably grows following a Volmer-Weber mode, where clusters appear at the first stages of growth until forming a percolated continuous metallic film. The oxidation of Cr at the interface with alumina occurs through a reaction with residual surface hydroxyl groups and not with the bulk of alumina. Although the oxidation state of Cr was not totally clarified, a hypothesis of mixed valency is likely. Further clarification of this point is brought by the results of EXAFS experiments and DFT calculations.

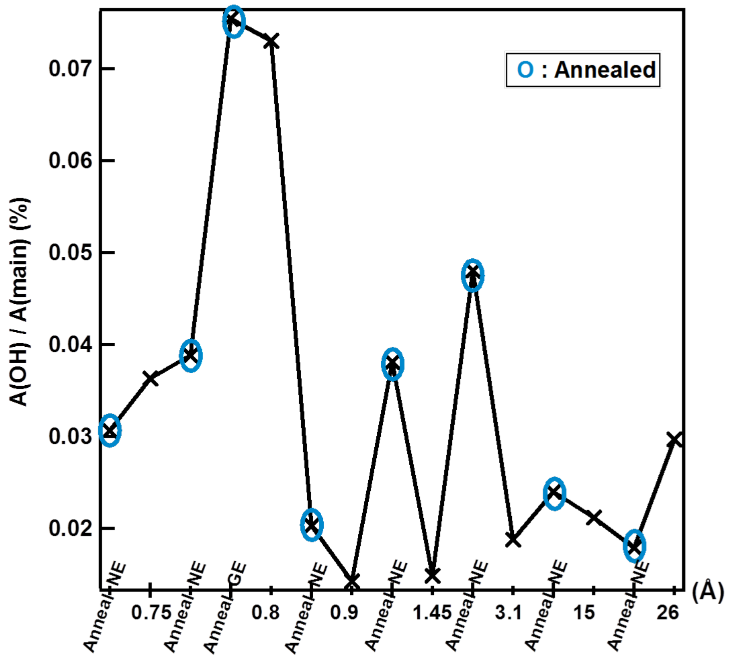

Figure 4.18: Plot of the OH component area ratio to that of the total peak as a function of the Cr thickness. Each point corresponds to a different sample. Blue circles indicate the annealed surfaces before any deposition. The angle of incidence is indicated on the X-axis. A systematic decrease is observed after deposition except for 2 samples (0.75 and 26 Å) where the amount of OH increased unexpectedly maybe because of a wrong decomposition.

4.2 Determination of the Cr/Al_2O_3 local environment by EXAFS

The need of knowledge of the Cr/alumina adsorption site, which is central in understanding the interface, has motivated extended x-ray absorption fine structure (EXAFS) experiments. These were performed at the LUCIA beamline of synchrotron SOLEIL (St Aubin, France) in the ultra-high vacuum apparatus described in section 1.6.2. In addition to the Cr local environment determination, two questions arise about the interface chemistry: (i) the possible reduction of alumina by chromium which was ruled out by XPS and (ii) the potential role of surface hydroxyl groups that was investigated by XPS.

4.2.1 Experimental

Besides α-Al_2O_3(0001) single crystals, an other type of sample (from Arcelor-Mittal Maizières Research) was additionally studied by EXAFS, a Fe-15%Al plate which was subjected to the same recrystallization treatment as industrial alloyed steel sheets, an annealing conducted at 800 °C in a reducing N_2-5%H_2 gas atmosphere containing only traces of water (approximately ~ -40°C dew point). Following this treatment, a pure alumina film of thickness around 60 Å has been observed by Auger spectroscopy (not shown) [Cavallotti, 2014a]. Once detached from the alloy substrate by appropriate dissolution treatment, such a polycrystaline alumina layer could be analyzed by transmission electron microscopy. It presented a structure of γ-alumina type with a lattice parameter ranging between 7.9 and 8.1 Å (figure 4.19). As already shown in the thesis of R. Cavallotti [Cavallotti, 2014a], the crystalline character of the γ-alumina adlayer formed on the model system which represents Al-alloyed steel grades is quite relevant for the comparison with α-Al_2O_3(0001).

All the alumina samples were O_2-annealed at $\sim$ 1200 K according to the same procedure

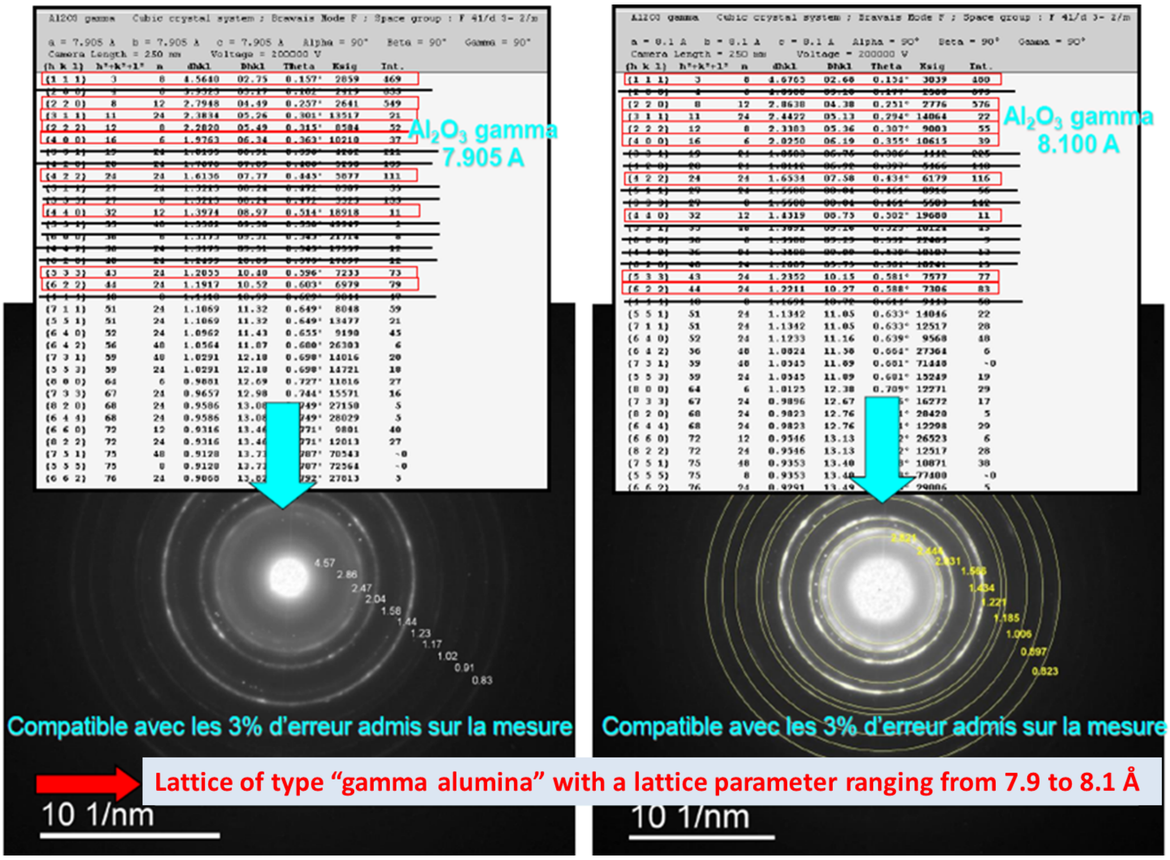

Figure 4.19: TEM diffraction pattern from an alumina layer grown on the Fe-15%Al alloy by annealing at 800°C in a reducing N_2+5%H_2 gas atmosphere containing only traces of water. According to atomic structure database, the positions of the diffraction rings of the polycristalline film agree the γ-alumina structure.

employed in the laboratory under a gas doser. The cleanliness of the surface was systematically controlled by LEED and Auger electron spectroscopy (AES) in the main chamber. Then Cr was deposited in the preparation chamber, the Cr flux being calibrated on a quartz balance and thicknesses checked later through AES and the EXAFS edge jump. Finally, the Cr-covered crystal was transferred in the main chamber, where it could be analyzed by x-ray absorption in total yield mode at the Cr K-edge around 6 keV , *i.e.* through the ratio between the drain current of the sample and the drain current of a thin metallic foil measuring the incoming flux. The x-ray beam was normal to the surface. Five Cr deposits on α-Al_2O_3(0001) were analyzed (0.5, 1.0, 1.5, 2.5 and 15 Å) and one on the γ-Al_2O_3 film (2 Å). The deposited thicknesses, as measured by the quartz balance, qualitatively agree with the height of the edge jumps (table 4.1). High quality EXAFS spectra have been recorded even at submonolayer coverage by averaging several scans with a 0.3 eV energy step close to the edge and 1 eV beyond with a dwell time of one second (figures 4.20-4.22). Absorption spectra of two reference compounds were also recorded, namely that of metallic α-Cr and of α-Cr_2O_3. Cr metal exhibits a cubic centered atomic structure with a lattice parameter of a = 2.91 Å with 8 first neighbors at 2.52 Å. Cr_2O_3 shares the same corindon structure as Al_2O_3 (a = 4.957 Å, c = 13.592 Å) with an octahedral configuration for Cr with 3 O neighbors at 1.96 Å and 3 O at 2.01 Å and 1 Cr second neighbors at 2.65 and 3 Cr at 2.89 Å.

4.2.2 Quantitative analysis of the Cr environment

EXAFS oscillations of the absorption coefficient $\chi(k)$ have been extracted and analyzed with ATHENA softwares [Rehr and Albers, 2000, Ravel and Newville, 2005]. To derive $\chi(R)$, the Fourier transform has been applied to $k^3\chi(k)$ raw data with a Kaiser-Bessel apodisation limited to 8.5 Å^{-1} due to diffraction peaks coming from the substrate. As explained in section 1.6.1, then $\chi(R)$ has been modeled with the ARTEMIS software [Ravel and Newville, 2005], the phase function coming from FEFF9 calculation [Rehr et al., 2009] applied to Cr metal and Cr oxide. Only O and Cr atoms were assumed to be in the local environment of Cr because of the striking similitude with the Cr_2O_3 compound at low thickness both on EXAFS oscillations (figure 4.20-a) and in the near edge structure (figure 4.22). The presence of Al atoms in the close environment of Cr definitively worsen the fit agreement (not shown). This will be confirmed by the comparison to *ab initio* calculations in terms of distance. A typical agreement between modeling and experiment is shown in figure 4.20-b for a 1 Å thick film on α-Al_2O_3. All others deposits gave similar results. The obtained coordination number N and the distance to neighbors R are gathered in table 4.1.

Sample	$t_{Cr-quartz}$ (Å)	$\Delta I/I$	$t_{Cr-EXAFS}$ (Å)	Cr local order (N, R)
$Al_2O_3(0001)$	0.5	0.02	0.18	(3.6 O, 1.92)
$Al_2O_3(0001)$	1	0.124	1.1	(4 O, 1.92) + (1 Cr, 2.88)
$Al_2O_3(0001)$	1.5	0.16	1.5	(3.1 O, 1.92)+ (1 Cr, 2.94)
$Al_2O_3(0001)$	2.5	0.24	2.2	(2.3 O, 1.90) + (1 Cr, 2.87)
$Al_2O_3(0001)$	15	1.63	15	(1.3 O, 1.94) + (5.5 Cr, 2.6) + (5.5 Cr, 2.92)
Fe-15%Al	2	0.2	1.8	(3 O, 1.92) + (1 Cr, 2.94)
Cr_2O_3	-	-	-	(6 O, 1.94) + (4 Cr, 2.96) (2-shell fit)
Cr-metal	-	-	-	(8 Cr, 2.52) + (6 Cr, 2.91)

Table 4.1: Results of the quantitative EXAFS analysis of data recorded at the Cr K-edge involving the edge jump $\Delta I/I$, the Cr thickness t_{Cr} as determined by the quartz balance and the environment of the Cr atoms. $t_{Cr-EXAFS}$ is obtained from $\Delta I/I$ by assuming a perfect agreement on the 15 Å deposit with quartz-balance calibration. The coordination number N, the nature (Cr/O) and the distance R to neighbors in the local environment of Cr are given with an accuracy of $(N \pm 0.3, R \pm 0.02$ Å) and $(N \pm 0.5, R \pm 0.04$ Å) for Cr-O and Cr-Cr. As a reminder, metallic Cr is body-centered and Cr_2O_3 adopts the corindon structure similar to α-Al_2O_3.

At this point, in order to be more specific on the description of the adsorption site, a more detailed description of the meaning of the coordination numbers N obtained by the fitting procedure is required. The polarization at normal incidence with a linearly polarized x-ray beam has to be considered. Assuming (as in figure 4.21) that the Cr atom is linked to 3 O surface atoms, the apparent coordination number as seen by EXAFS will be $\sum 3\cos(2\theta)$ where θ is the angle between the photon electric field and the Cr-O bond. Hence the contribution of these 3 surface atoms amounts roughly 3.3. Accordingly, the values returned by the fitting procedure lead the existence of an extra oxygen not belonging to the pure alumina surface, since the oxygen coordination (measured by EXAFS) is renormalized by the number of Cr atoms, some of which not being linked to oxygen but only to Cr. The same structure and chemical environment are found on the γ-alumina surface which compares very well (table 4.1 and figure 4.20-a) with the deposit of about the same thickness on α-$Al_2O_3(0001)$.

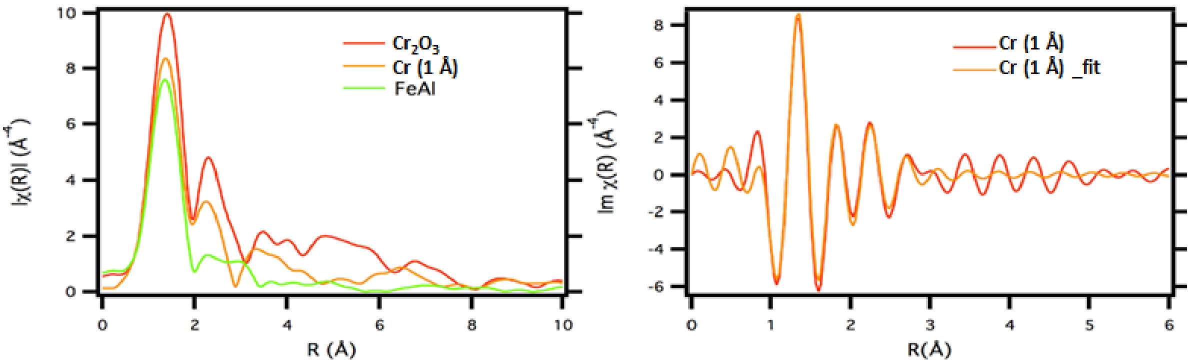

Figure 4.20: Fourier transforms $\chi(R)$ of the EXAFS signal collected at the Cr-edge: a) Modulus of $\chi(R)$ for Cr_2O_3 (red line), a 1 Å thick Cr film deposited on α-Al_2O_3(0001) (orange line) and a 2 Å thick Cr film deposited on a γ-Al_2O_3(0001) adlayer grown at the surface of a FeAl plate (green line). b) Imaginary parts of $\chi(R)$ of the 1 Å deposit of Cr on alumina : experimental data (red) and theoretical fit (orange).

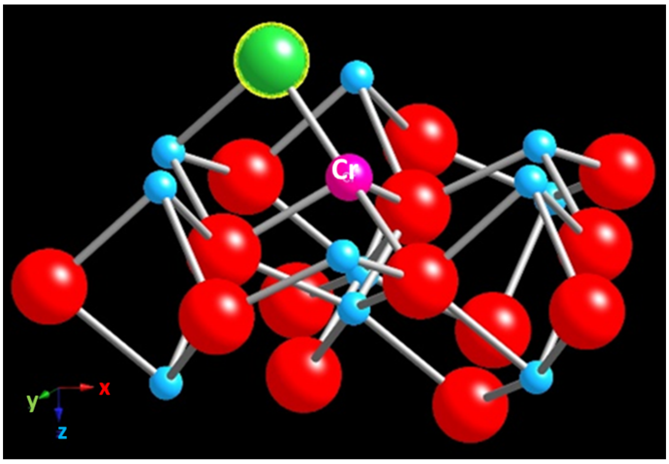

Figure 4.21: Local environment of the Cr atom (purple) on the alumina surface. The Al and O atoms of the alumina substrate are small blue and large red spheres, respectively. The extra oxygen atom of the Cr environment that is required by the EXAFS analysis - is represented by the green sphere.

4.2.3 Comparison of the measured geometry with reference compounds

As a first approximation, the Fourier transform $\chi(R)$ of the EXAFS signal of the films with the lowest thicknesses show a marked similarity with that of Cr_2O_3 (figure 4.22) with, however, different chemical environments that are presented in table 4.1. At least, they are clearly different from metallic chromium. The local environment of Cr evolves with the surface coverage in line with an expected reaction with surface OH-groups of alumina (table 4.1). For film thicknesses ranging between 0.5 and 2.5 Å, the chemical environment of Cr appears quite stable. Very similar interatomic distances are found both for α-Al_2O_3(0001) and for the FeAl-supported γ-Al_2O_3 film. Values of the interatomic Cr-O distances are 1.92-1.94 Å and Cr-Cr bonds appear for 1.0-2.5 Å thick films at a distance ranging between 2.88 and 2.94 Å. However, there is a decrease of the O-coordination number; four, three and two oxygen are found in near neighbor position around Cr at coverages of 0.5, 1.0-1.5 and 2.5 Å, respectively. The distances are in agreement with those found in the reference Cr_2O_3 compound. In the 1.0 Å thick Cr/alumina film, there are close to four oxygen atoms at 1.92 Å and a Cr atom at 2.94 Å. In Cr_2O_3, around each Cr atom, there are 6 oxygen atoms in near neighbor position at

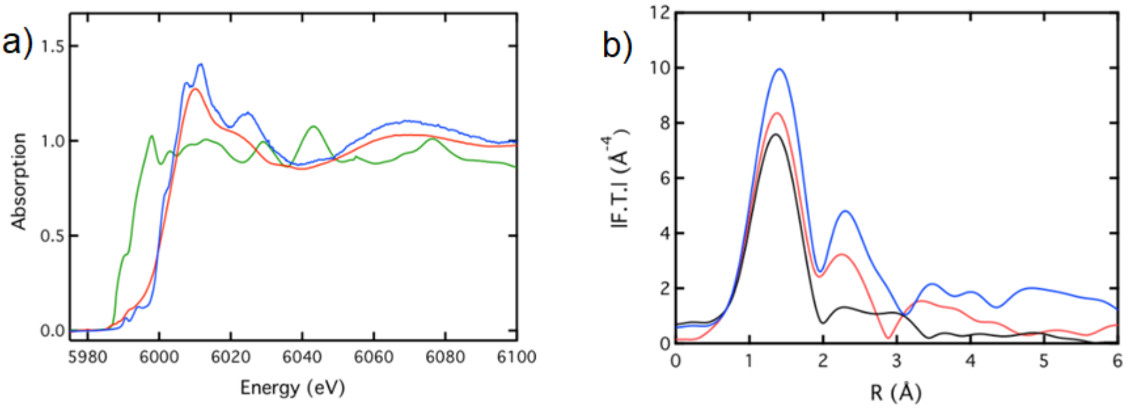

Figure 4.22: Experimental EXAFS spectra: a) XANES spectra of Cr_2O_3 (blue), Cr metal (green) and 1 Å Cr/α-Al_2O_3(0001) film (red). b) Modulus of the Fourier Transforms $\chi(R)$ at the Cr K edge of EXAFS collected on the 1 Å Cr/α-Al_2O_3(0001) film (red), on 2 Å of Cr on γ-Al_2O_3 (black) as well as on a bulk Cr_2O_3 sample (blue).

1.94 Å and four Cr atom at 2.96 Å. In the 2.5 Å thick Cr film, the average coordination with oxygen decreases while that with Cr increases as expected from film thickening and increase of the number of metal-metal bonds. At 15 Å, Cr-Cr distances characteristic of the metallic environment (2.52 Å in body centered metallic Cr) are observed.

4.3 Experimental measurements versus *ab initio* approaches

4.3.1 DFT insights into Cr adsorption on alumina

Density functional theory (DFT) calculations were realized to support the previous findings. The discussion is organized on the basis of calculations which were performed by Jacek Goniakoswki (INSP) and are presented in what follows.

4.3.1.1 Computational methods and settings

All calculations are performed within the DFT implemented in VASP (Vienna *ab initio* simulation package) [Kresse and Furthmüller, 1996, Kresse and Furhmuller, 1993]. The interaction of valence electrons with ionic cores is described within the projector augmented wave (PAW) method [Blöchl, 1994, Kresse and Joubert, 1999]. The Kohn-Sham orbitals are developed on a plane-wave basis set with a cutoff energy of 400 eV and the self-consistent iterative solution of the electronic Hamiltonian is pursued until energy differences become less than 10^{-6} eV. The dispersion-corrected generalized gradient approximation (GGA) of the exchange-correlation functional (optB86-vdW) [Dion et al., 2004, Klimeš et al., 2009, Klimeš et al., 2011] is used to improve the description of adsorption and adhesion characteristics. Moreover, selected configurations are also reconsidered within the DFT+U approximation proposed by Dudarev [Anisimov et al., 1997, Dudarev et al., 1998] (U_{Cr}-J_{Cr} = 3.0 eV) as to asses the effect of localization of the Cr 3d electrons. All calculations are spin-polarized and the relative stability of ferro- (FM) and anti-ferromagnetic (AF) is systematically tested. Atomic charges are estimated with the partition scheme proposed by Bader [Bader, 1991, Henkelman et al., 2006] and magnetic moments are obtained by integration of the spin density within Bader's volumes. Atomic configurations are plotted with VESTA [Momma and Izumi, 2011].

The $Al_2O_3(0001)$ surface is modeled with symmetric alumina slabs, terminated by a single layer of Al (non polar, stoichiometric termination) separated by at least 10 Å of vacuum. Dipole corrections are used to further reduce the effect of periodic boundary conditions in the direction normal to the slab surfaces. Cr adatoms and Cr deposits as well as various H_nO_m surface hydroxylation layers are added on one slab side only. Atomic coordinates of all atoms are relaxed until forces become smaller than 0.01 eV $Å^{-1}$. The Brillouin zone of the (1×1)-$Al_2O_3(0001)$ surface unit cell is sampled on a Γ-centered (8×8×1) Monkhorst-Pack grid.

4.3.1.2 Cr adatoms on bare alumina

Table 4.2 and figure 4.23 summarize the adsorption characteristics of Cr adatoms on a bare $Al_2O_3(0001)$ surface. Adsorption in surface hollow sites (B), which is the prolongation of the corundum lattice, is systematically favored. The increase of the adsorption energy as a function of coverage reveals an attractive interaction between the co-adsorbates and suggests a formation of compact (3D) Cr deposits. We note that such increase occurs both at low coverage (between 1/4 and 1 ML) where no direct Cr-Cr bonds are formed and at higher coverage (between 1 and 2 ML) where Cr-Cr bonds are formed in addition to the adsorbate surface interaction.

Cr adatoms become positively charged upon adsorption; the loss of electron contributes to the reduction of the magnetic moment with respect to this in the unsupported atom (6 μ_B). The transferred electrons are localized at the top-most surface Al atoms, where they induce a non-vanishing spin polarization. The effect is particularly well pronounced for the 1 ML coverage, where it results in a substantial charge reduction at surface Al cations.

Coverage	E_{ads}	Q_{Cr}	μ_{Cr}
1/4 ML (A)	1.21	0.5	5.0
1/4 ML (B)	1.67	0.6	4.9
1 ML (A)	1.62	0.8	4.1
1 ML (B)	2.15	0.8	4.1
2 ML (B)	2.58	0.2, 0.4	4.3, -3.8

Table 4.2: Cr adsorption characteristics: adsorption energy E_{ads} (eV/Cr), Bader charge Q_{Cr} (e), and magnetic moment μ_{Cr} (μ_B) as a function of Cr coverage: 1/4, 1, and 2 ML. 1 ML corresponds to a single Cr adatom per $Al_2O_3(0001)$-(1×1) unit cell. Labels (A) and (B) refer to the two hollow surface sites. (B) corresponds to the prolongation of the corundum lattice.

4.3.1.3 Cr adatoms on the hydroxylated alumina

Table 4.3 and figure 4.24 summarize the adsorption characteristics of 1 ML of Cr adatoms on a hydroxylated $Al_2O_3(0001)$ surface. Several alternative compositions of the hydroxylation layer H_nO_m have been purposely considered as to induce different oxidation states of the adsorbed Cr adatom.

While O atoms in the hydroxylation layer systematically preserve their 2− oxidation state, hydrogen atoms may become either positively or negatively charged depending on the layer composition and the atomic configuration. This is the case of OH composition of the hydroxylation layer, where the configuration (A) corresponds to the formation of usual $O^{2-}H^{+}$

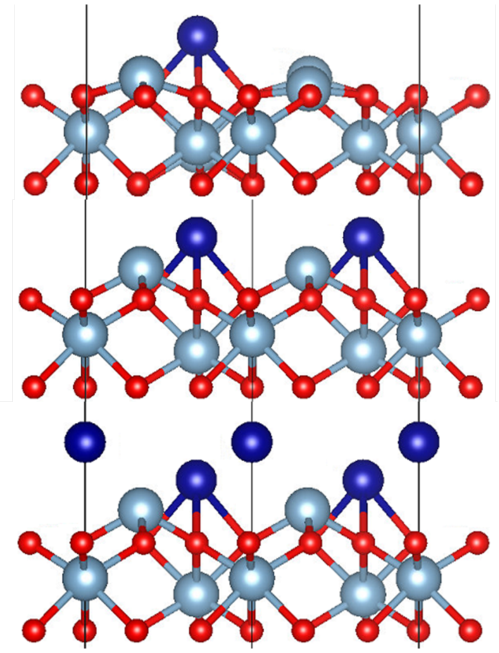

Figure 4.23: Cr adsorption configurations at 1/4 ML (B) (top), 1 ML (B) (middle), and 2 ML (bottom) coverage. Al and Cr atoms are represented with large light and dark blue balls and O atoms with small red ones. The (B) configuration corresponds to absorption in the surface hollow site *i.e.* to the prolongation of the corundum lattice.

hydroxyl group, while in the more stable configuration (B) an H^- is formed at the surface. This confers to the adsorbed Cr atom a 1+ and 3+ oxidation states, respectively. Similarly, an H^+ is formed in case of HO_2 layer, leading to a Cr^{3+} state for the adsorbate. Finally, in the H_2O case, the H^+ and H^- coexist; the first is tightly bound to an O anion and forms a usual OH^- group, the second is electrostatically trapped at the surface, with no short chemical bonds to the neighboring Cr and Al cations.

We note a systematically good correlation between the calculated Bader charges of Cr adatoms Q_{Cr}, their magnetic moments μ_{Cr}, and their formal oxidation state. As a reference, calculated μ_{Cr} are equal to 3.3, 2.6, and 2.1 μ_B in bulk CrO, Cr_2O_3, and CrO_2, respectively. Unsurprisingly, the vdW+DFT+U approximation systematically enhances the calculated moments $\mu_{Cr} = 3.7$, 2.9, and 2.3 μ_B, respectively.

The present results suggest that a partial oxidation of low coverage of Cr adatoms takes place upon adsorption at the hydroxylated surface (table 4.3).

H_nO_m	Q_{Cr}	μ_{Cr}	Cr oxidation state
H_2O	1.2	3.7	Cr^{2+}
HO_2	1.6	2.7	Cr^{3+}
OH (A)	0.8	4.6	Cr^{1+}
OH (B)	1.5	2.8	Cr^{3+}

Table 4.3: Cr adsorption characteristics: Bader charge Q_{Cr} (e), magnetic moment μ_{Cr} (μ_B), and formal Cr oxidation state for alternative compositions and configurations of the surface hydroxylation layer (see figure 4.24).

4.3.1.4 Cr oxides on alumina

Table 4.4 and figure 4.25 summarize the adsorption characteristics of a low coverage of Cr adatoms in presence of oxygen excess or resulting from a dehydrogenation of the alternative surface hydroxylation layers, such that various chromium oxide species form on the

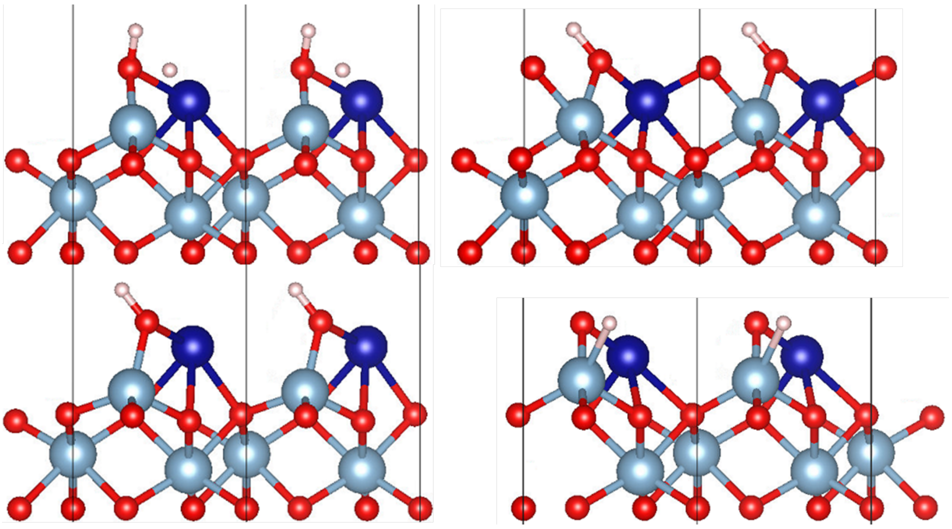

Figure 4.24: Adsorption of 1 ML of Cr on alumina in presence of a surface hydroxylation layer. Top: H_2O (left) and HO_2 (right) per unit cell. Bottom: alternative (A and B) configurations with a single OH/cell. Al and Cr atoms are represented with large light and dark blue balls. O and H atoms are plotted as small red and white balls.

$Al_2O_3(0001)$ surface. Three alternative stoichiometries of the resulting surface oxide species CrO_x have been purposely considered: $x = 1$, 1.5, and 2.

CrO_x	Q_{Cr}	μ_{Cr}	Cr oxidation state
CrO	1.3	3.8	Cr^{2+}
Cr_2O_3	1.5, 1.7	3.0, 2.6	Cr^{3+}
CrO_2	1.7	1.9	Cr^{4+}

Table 4.4: Cr characteristics in surface oxide species: Bader charge Q_{Cr} (e), magnetic moment μ_{Cr} (μ_B), and formal Cr oxidation states, figure 4.25.

Again, a systematic good correlation between the calculated Bader charges of Cr adatoms Q_{Cr}, their magnetic moments μ_{Cr}, and their formal oxidation states is found. In particular, the magnetic moments seem to be good indicators of the Cr oxidation state.

4.3.1.5 Cr-O bond lengths

Table 4.5 summarizes lengths of Cr-O bonds obtained for the various alternative Cr adsorption configurations considered at bare, hydroxylated, and oxygen-rich alumina surfaces. Moreover, corresponding results obtained within the vdW-DFT+U approximation are given. As a reference, average vdW-DFT (vdW-DFT+U) Cr-O bond lengths are equal to 2.16 (2.22), 2.00 (2.02), and 1.92 (1.93) Å in bulk CrO, Cr_2O_3, and CrO_2, respectively.

4.3.2 Geometry and chemistry of Cr/Al_2O_3

4.3.2.1 Oxidation of Cr at the contact with alumina

The theoretical models associated to Cr adatoms deposited on a bare α-$Al_2O_3(0001)$ surfaces are shown in figure 4.23. They have been established for 1/4 ML, 1 ML and 2 ML (where 1 ML

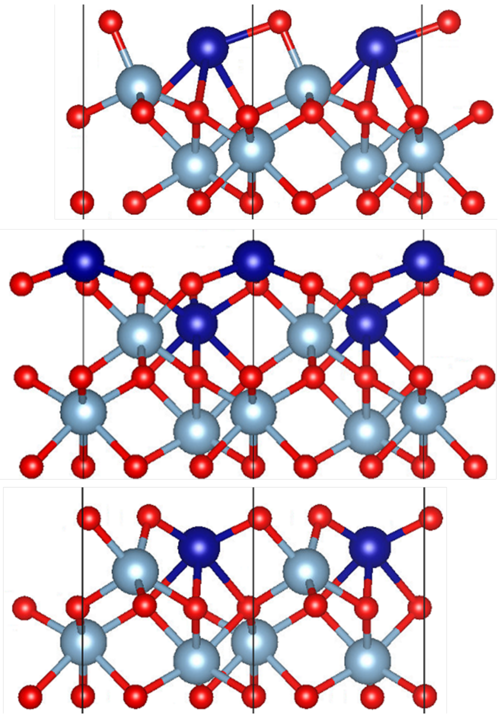

Figure 4.25: Cr oxide species on the alumina surface: CrO (top), Cr_2O_3 (middle), and CrO_2 (bottom) per surface unit cell. Al and Cr atoms are represented with large light and dark blue balls. O atoms are plotted as small red ones.

config.	Cr^{n+}	d_{Cr-O} (vdW-DFT) within Cr layer ; with alumina	d_{Cr-O} (vdW-DFT+U) within Cr layer ; with alumina
1 ML (A)	0-1	; 2.24, 2.24, 2.24	; 2.37, 2.37, 2.37
1 ML (B)	0-1	; 2.15, 2.15, 2.15	; 2.24, 2.24, 2.24
OH (A)	1	2.09 ; 2.18, 2.26, 2.35	2.14 ; 2.25, 2.30, 2.39
H_2O	2	2.00 ; 2.05, 2.08, 2.16	2.05 ; 2.10, 2.10, 2.20
CrO	2	1.88 ; 2.03, 2.29, 2.39	1.96 ; 2.08, 2.32, 2.38
OH (B)	3	1.77 ; 1.94, 2.12, 2.19	1.81 ; 1.96, 2.13, 2.19
Cr_2O_3	3	3×1.80 ;	3×1.80 ;
		3×1.90 ; 2.00, 2.00, 2.00	3×1.92 ; 2.00, 2.00, 2.00
HO_2	3	1.76, 1.88 ; 1.96, 2.02, 2.17	1.79, 1.89 ; 1.97, 2.04, 2.17
CrO_2	4	1.69, 1.69 ; 1.93, 2.16, 2.18	1.71, 1.71 ; 1.94, 2.16, 2.18

Table 4.5: Cr-O bond lengths d_{Cr-O} (Å) obtained for Cr adsorption at the bare (table 4.2), hydroxylated (table 4.3), and oxygen-rich (table 4.4) alumina surfaces. Both vdW-DFT and vdW-DFT+U results are given. For clarity, lengths of Cr-O bond formed within the adsorbate layer and those with alumina surface oxygen atoms are separated by ";".

involves a single Cr atom per (1×1) unit cell), which corresponds roughly to 0.5 Å, 1.0-1.5 Å and 2.0-2.5 Å thick Cr films, respectively. Those models are therefore representative of the Cr coverages that have been examined in the experiments. On bare alumina, the Cr atoms are predicted by DFT calculations to undergo a charge transfer of up to one electron at the contact of alumina (table 4.2). As a result of the localization of the transferred electrons at the top-most Al atoms of the alumina substrate, an Al core-level shift should be observed, but none was found by photoemission (section 4.1.3). As regards to the predicted charge transfer, the Al core-level shift might indeed remain modest, so that the absence of experimental observation of such shift does not prove or discard the model. The feature that unambiguously leads to a firm conclusion is the value of the Cr-O distances. For Cr on bare alumina, the calculated Cr-O distances that range between 2.15 and 2.37 Å (table 4.5), strongly differ from the experimental values of 1.92-1.94 Å (table 4.1). This difference is well-beyond any type of error bars. Therefore, the experimental values of Cr-O call for more oxidized Cr atoms than in the case of Cr on bare alumina. This points at a possible reaction of Cr with the residual surface hydroxyl groups.

4.3.2.2 Cr site on alumina

Theoretical models of the interaction of Cr adatoms with hydroxylated alumina surfaces are shown in figure 4.24. A series corresponding to one Cr atom per (1×1) unit cell was calculated. Each unit cell also involved an additional moiety, either OH, or H_2O, or HO_2. Depending on the proton configuration (either H^+, or H^- or the combination of both), the degree of oxidation of Cr varies from Cr^+ to Cr^{3+} (table 4.3). Values of the Cr-O distance are 2.09-2.35 or 2.14-2.39 Å for Cr^+, which is clearly at odd with experiment (table 4.1). The same can be said about the Cr-O distances of 2.00-2.16 or 2.05-2.20 Å that are determined for Cr^{2+} in the presence of H_2O (table 4.5). However, the Cr^{3+} ion created via the reaction of a Cr adatom with a unique surface OH group deserves attention. Two Cr-O distances of the model (1.77 and 1.88 Å or 1.81 and 1.96 Å, for vdW-DFT or vdW-DFT+U, respectively, see table 4.5) are consistent with the experimental distance of 1.92-1.94 Å. Indeed, this reaction has a good probability of being realized since, as above mentioned, the OH groups which participate in it are the most stable surface OH configurations. These are those which involve a H^-. Such process allows the formation of highly ionized Cr by reaction with very low OH coverage, which is indeed observed in experiments, as described in Section 4.1.3. Most importantly, the combination of DFT approach with the EXAFS findings of more than three neighboring oxygen atoms at distances of ∼1.92 Å to the chromium atoms, unambiguously demonstrates the presence of OH groups on the alumina surface even after annealing at high temperature in UHV. Unlike core-level shifts observed in photoemission (Section 4.1.3), whose origin can be complex (surface core-level shift or impurities), the EXAFS gives for the first time a direct proof of the existence of these OH groups.

Short Cr-O distances are determined for Cr oxides deposited on the alumina surface. Among the model corresponding to CrO, Cr_2O_3 and CrO_2 layer (figure 4.25), it is the second which better corresponds to the EXAFS experiment. It exhibits three Cr-O distances of 1.8 Å and three other of 1.90 Å (or 1.92 Å) (table 4.5) in good agreement with the three to four Cr-O distances of 1.92 Å that are derived from the EXAFS after deposition of 0.5 to 1.5 Å thick Cr film (table 4.1). Similar distances are found at higher Cr coverage but, then, the number of neighboring O atoms decreases as that of metallic neighbors increases (table 4.1). Those findings are consistent with the striking similarity of the experimental EXAFS spectra of the Cr films with that of the bulk Cr_2O_3 (figures 4.20-4.22). Finally all simulated configuration validate the lack of Al atoms in the first shell of Cr as obtained by EXAFS;d_{Cr-Al} is typical for cation-cation distance in an oxide and is above 2.6 Å in the explored configuration.

4.3.2.3 A summary

To sum up, photoemission results through the analysis of the Cr 2p lineshape and the energy shift pointed at a possible oxidation of chromium at the first stages of deposit. An unambiguous determination of the Cr oxidation state turned out to be difficult using only XPS. However,

O 1s core level peak revealed the presence of 0.25 ML of residual OH groups that increased up to ~ 0.6 ML upon water exposure. Its evolution demonstrated the reaction of these species with chromium. Indeed, the consumption of OH was paralleled by the appearance of an CrO_x oxidized species following the chromium deposition. EXAFS pointed at an excess of O in the neighborhood of Cr compared to expectations on bare alumina. Even if a charge transfer is predicted between the Cr adatom and the Al atom of the bare substrate, it is not high enough to lead to appropriate Cr-O distances. The comparison between DFT calculations of several H_nO_m alumina surface configurations and experiments on such a parameter unambiguously favors a reaction with hydroxyl groups to form a species with an oxidation state and an environment similar to Cr_2O_3.
In the same context, the chemistry of surface hydroxyl groups with the metal was previously examined, at Cu/Al_2O_3 and Ti/Al_2O_3 interfaces [Kelber et al., 2000,Lazzari and Jupille, 2005]. It was proven that the initial Cu adlayer is oxidized to Cu^+ with a maximum surface coverage of 0.35 ML through a reaction with hydroxyl groups on a hydroxylated alumina sample. The oxidation of Ti at the contact with the annealed Al_2O_3 surface was likewise straightforwardly explained by Ti-OH reaction. However, the puzzling issue was the formation of highly ionized Ti by interaction with a poorly hydroxylated alumina surface ($\sim 3.5 \times 10^{14}$ OH/cm^2 ~ 0.23 ML), *i.e.* that didn't undergo any exposure to water vapor, which supports our observation of Cr oxidation on bare alumina. A mix of Ti^{2+} and Ti^{4+} valencies was pointed out up to 2 Å of thickness above which metallic Ti starts to appear. These oxidation states equally suggested that the considered reaction took place with $OH^{(-)}$ groups, similar to the preferred hydroxyl configuration that is found for Cr/Al_2O_3 based on DFT calculations.
These results provide a very strong argument in the old debate [Ahn and Rabalais, 1997,Lazzari and Jupille, 2005, Fu et al., 2006] about the persistence of hydroxyl groups at the α-Al_2O_3(0001) surface even after annealing at temperatures that are just below reconstructions (see section 2.1.4).

4.3.2.4 Cr on γ-Al_2O_3

Quite importantly with respect to the objective of the thesis, Cr adatom are shown to be bonded to oxygen in a similar way (which compares to Cr_2O_3) on both α-Al_2O_3(0001) and γ-alumina. Indeed, the γ-alumina surface involves more than 60 % of octahedral sites similar to those found at the α-Al_2O_3(0001) surface. Therefore, the α-Al_2O_3(0001) surface appears as a model of relevance for the γ-alumina surfaces that are often encountered in applications. In addition, the similarity of the behavior of the two interfaces with Cr suggests that the as-prepared γ-Al_2O_3 film is also hydroxylated.

4.4 Growth mode and structure of Cr/Al_2O_3(0001)

4.4.1 Quantitative analysis of SDRS spectra

The growth at room temperature of Cr on an Al_2O_3(0001)-(1 × 1) surface was followed by differential reflectivity. Spectra and their inversion to obtain the surface susceptibilities have been presented in figure 3.10 and commented in section 3.6 in terms of polarization modes. In order to get more insight into the morphology, spectra have been fitted by χ^2-minimization with the *GranFilm* software [Lazzari and Simonsen, 2002, Granfilm,] (with constant error bars of 5.10^{-3}) using a model of truncated spheroid in the framework of surface susceptibilities formalism as detailed in chapter 3. Only s-polarization has been considered, since as demonstrated in sections 3.5-3.6, the responses for the two states of polarization poorly differ for flat particles. To limit the number of fitted parameters, only parallel radius $R_\parallel$, perpendicular radius $R_\perp$ and interparticle spacing L (hexagonal network) were fitted (see figure 3.1-c) while keeping an hemispheroidal shape (truncation $t_r = 0$). An *ad hoc* broadening (equation 3.7) of $\sigma_\parallel \sim 1$ eV had to be introduced to obtain the agreement shown in figure 4.26.

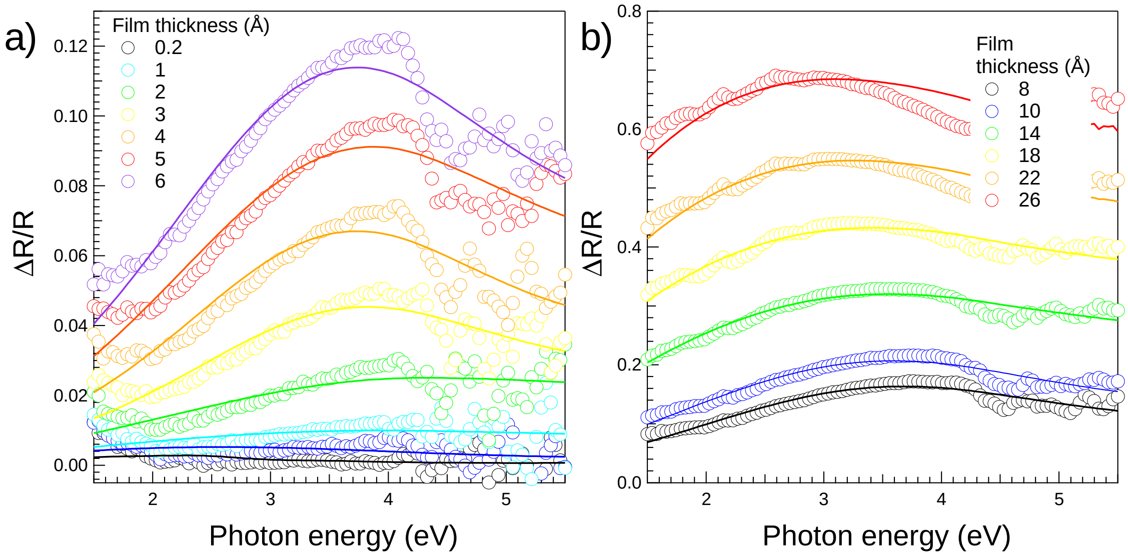

Figure 4.26: Fits (lines) of the s-polarization SDRS spectra (points) during growth of Cr on $Al_2O_3(0001)$ for polarization (a) p and (b) s. Average film thickness obtained from photoemission calibration are given in the figure. A similar agreement is obtained in p-polarization. All surface susceptibilities have been accounted for. $M = 24$ multipoles have been used in the simulation as well as a quadrupolar particle-particle interaction on an hexagonal lattice.

Unfortunately, it turned out the error bars on the fitted parameters ($a_1 = R_\parallel, a_2 = R_\perp, a_3 = L$) were important due to correlations close to 100 % as seen in the covariance matrix $V^a_{ij} = [C^a_{ij}]^{-1}$ which is the inverse of the curvature matrix $C^a_{ij} = \frac{\partial\chi^2}{\partial a_i a_j}$ of χ^2 at minimum. Sizes and particle spacing are ill-defined. Since fitting in the *GranFilm* software is technically limited to those parameters, C^a_{ij} was transformed into a more physical set of parameters ($b_1 = t \propto R_\parallel^2 R_\perp / L^2, b_2 = A_r \propto R_\parallel / R_\perp, b_3 = \Theta \propto R_\parallel^2 / L^2$), namely thickness t, aspect ratio A_r and surface coverage Θ . Their choice rely on the intrinsic sensitivity of SDRS to the amount of substance and the particle flattening (see figure 3.5 and equations 3.4). Using the obvious relations between their logarithmic differential:

$$\begin{pmatrix} \frac{\delta t}{t} \\ \frac{\delta A_r}{A_r} \\ \frac{\delta\Theta}{\Theta} \end{pmatrix} = \begin{bmatrix} 1 & 1 & -2 \\ 1 & -1 & 0 \\ 2 & 0 & -2 \end{bmatrix} \begin{pmatrix} \frac{\delta R_\parallel}{R_\parallel} \\ \frac{\delta R_\perp}{R_\perp} \\ \frac{\delta L}{L} \end{pmatrix} ; \begin{pmatrix} \frac{\delta R_\parallel}{R_\parallel} \\ \frac{\delta R_\perp}{R_\perp} \\ \frac{\delta L}{L} \end{pmatrix} = \begin{bmatrix} 1 & 1 & -1 \\ 1 & 0 & -1 \\ 1 & 1 & -\frac{3}{2} \end{bmatrix} \begin{pmatrix} \frac{\delta t}{t} \\ \frac{\delta A_r}{A_r} \\ \frac{\delta\Theta}{\Theta} \end{pmatrix} \tag{4.1}$$

and the transformation between curvature matrices:

$$C^b_{kl} = \sum_{i,j} \frac{\partial a_i}{\partial b_k} \frac{\partial\chi^2}{\partial a_i a_j} \frac{\partial a_j}{\partial b_l} \tag{4.2}$$

the new covariance matrix $V^b_{kl} = [C^b_{ij}]^{-1} = \left[\frac{\partial \chi^2}{\partial b_k b_l}\right]^{-1}$ was straightforwardly derived. As expected on the physics point of view, C^b_{kl} yielded much lower correlation coefficients except between Θ and t. The fitted parameters and the associated error bars as defined as the square-root of the diagonal elements of the covariance matrix are presented in figure 4.27.

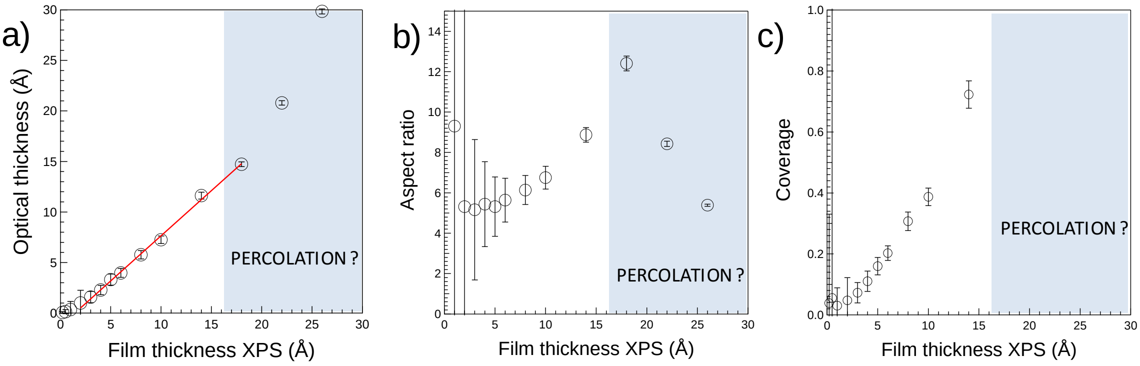

Figure 4.27: Evolution as function of the deposited thickness of the fitted morphology of a Cr deposit on $Al_2O_3(0001)$: a) Optical thickness t, b) particle aspect ratio $\mathcal{A}_r$ and c) surface coverage Θ. Shaded regions correspond to breakdown of the modeling with truncated particles.

A nearly one to one correlation (figure 4.27, slope 0.9) between the thickness t derived from SDRS and that derived from photoemission and evaporation time shows the consistency of those determinations. But an offset in thickness of 1.5 Å does exist before the appearance of the plasmonic behavior in the nanoparticles; it can be partly assigned to the above discussed reaction of Cr with surface hydroxyls groups. Since the onset of growth, particle with very large aspect ratio above 5 are observed. In parallel to the uptake in mass of the film, the particles cover more and more the surface and thicken at constant aspect ratio up to an average thickness of 10 Å. Above, they start to coalesce as the aspect ratio rises up. However, above a thickness of 15 Å (shaded regions in figure 4.27), the analysis breaks down in terms of shape and interparticle coupling, probably because of film percolation as seen through the disappearance of charge effect in photoemission. To conclude, optics reveals the growth of an early percolating film that covers a sizable fraction of the surface even after 10-15 Å of thickness. Below, a partial coverage and Volmer-Weber growth is observed in line with photoemission conclusions.

Beyond the information gained on morphology by direct fitting, SDRS proves its interest in distinguishing the different regimes of growth otherwise difficult to unveil with microscopy techniques, through the approach of signal integration explained in section 3.3.3. The integral $\mathcal{A}_s$ of the reflectivity signal (equation 3.11) is driven by the oscillator strength of polarizability resonances which makes it sensitive to the aspect ratio variations and consequently to the sequence of different steps in the growth process. Figure 4.28 presents the result of signal integration for different deposits. The general trend is reproducible and is characteristic of a Volmer-Weber growth mode. A U-shape accounts for the sequence of the nucleation, growth and coalescence/percolation phases, where the first is linked to depolarization of isolated dipoles related to an increase of particle density, the second takes place at constant aspect ratio, and the last occurs when particles start to flatten and aspect ratio increases.

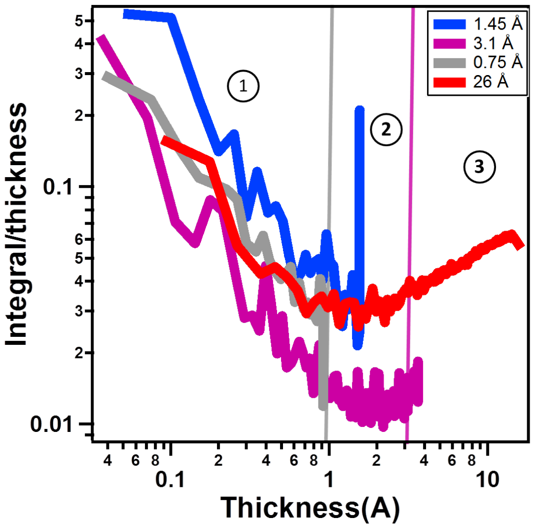

Figure 4.28: Integral of the SDRS signal in polarization s for different Cr deposits on α-$Al_2O_3(0001)$ showing the different steps of growth: 1-nucleation, 2-growth, 3-coalescence. The grey and purple lines limit the nucleation and growth phases.

Nucleation occurs up to ~ 1 Å while the onset of coalescence (around 3 Å) is much earlier than non reactive metal on alumina as shown in figure 3.3-a.

Occasionally, samples were imaged *ex situ* by atomic force microscopy (AFM); despite a possible influence of oxidation by the atmosphere, all the AFM observations were in favor of SDRS findings. Indeed, figure 4.29 displays AFM images recorded on a Al_2O_3-(1×1) surface with ~ 6 Å of chromium on top that confirm the Volmer-Weber growth mode, where particles start to form 3D clusters and grow until they coalesce and form a continuous film. The film is close to percolation and covers a large fraction of the surface. Islands have large aspect ratio since their average height is around ~ 8 Å.

The chemical reaction between residual hydroxyl groups could play a role in the wetting of chromium on alumina as testified by the rapid percolation and the growth of particles with large aspect ratio. As underlined in section 2.2.1, in the case of $Co/Al_2O_3(0001)$ [Chambers et al., 2002], OH groups were shown by RHEED to lead to a laminar growth of the metal by acting as anchors. Le *et al.* [Le et al., 2017b] underlined by thermal desorption and *ab initio* calculations the key role of interfacial undercoordinated anions, remnants of the hydroxylation layer in the enhancement of adhesion at $Zn/Al_2O_3(0001)$, leading to a cohesive cleavage rather than an interfacial one. As seen by SDRS [Lazzari and Jupille, 2005], the growth of Ti and Al proceeds also through high aspect ratio particles while an interfacial reaction with hydroxyl groups takes place at the first stage of growth. However, like for Ti [Lazzari and Jupille, 2005, Lazzari, 2000], Cr is a metal with a low vapor pressure and a low mobility. Therefore, the supersaturation effect (see section 2.2.4.2) may change the trend of wetting predicted by surface/interface energies. In other words, kinetic rather than thermodynamic may be at work in the observed morphology.

4.4.2 Diffraction analysis

LEED patterns of chromium deposits on alumina suffer from charge effects and from the lack of any diffraction spots. Those effects are likely related to the growth of a non-epitaxial layer and/or to nanoparticles. To circumvent this problem, the crystallography of the Cr film

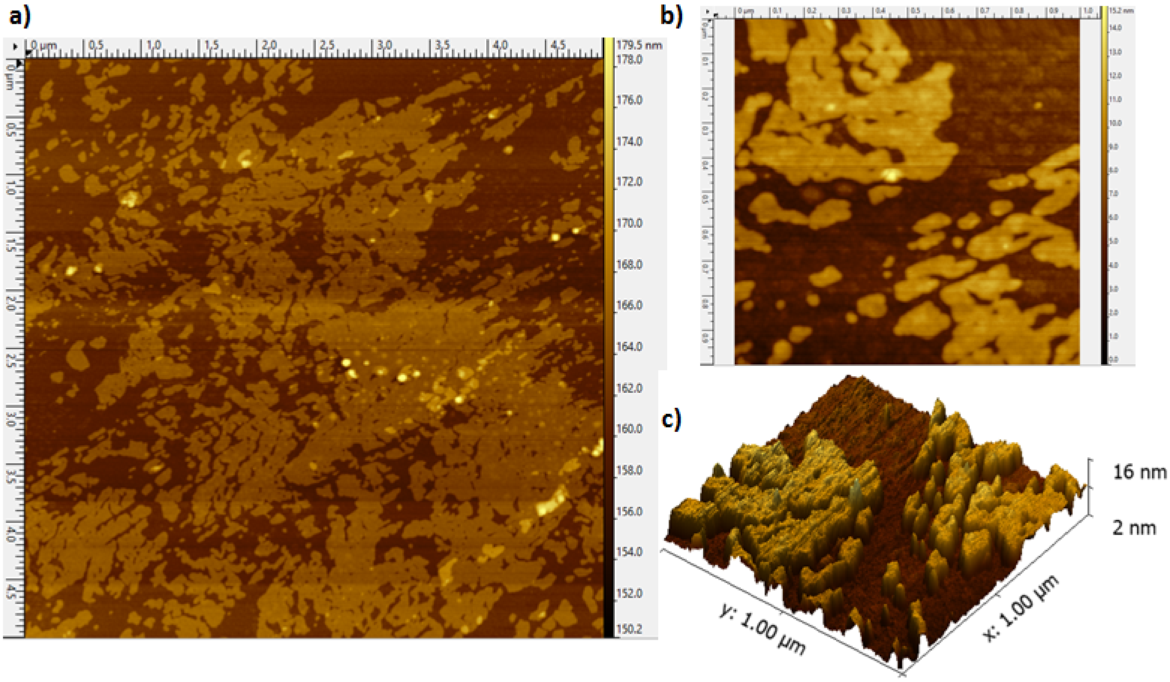

Figure 4.29: *Ex situ* AFM images of 6 Å of Cr on Al_2O_3-(1×1): a) 5×5 µm scale showing a percolating film. b)c) 1×1 µm scale showing a region representative of the surface topography with a maximum peak to valley height of 8 nm. Film thickness is calibrated by a quartz microbalance.

on a $Al_2O_3(0001)$-(1×1) surface was analyzed by reflection high energy electron diffraction (RHEED). Figure 4.30-a shows a set of diffraction patterns at different deposited thicknesses for an electron beam aligned along the $[10\bar{1}0]$ direction of $Al_2O_3(0001)$. As seen directly from the pattern (figure 4.30-a), the profiles of intensity (figure 4.30-b) or the integrated intensity compared to background (figure 4.30-c), diffraction rods that are characteristic of the surface rapidly vanish to reach a nearly uniform background level after 5 Å of equivalent thickness. Only for thick films, a low contrast ring shape pattern typical for a poorly crystallized or amorphous layer is recovered (pink line in figure 4.30). This ring is isotropic as it is independent of the azimuth. The comparison of its radius to the reference on the bare alumina gives a distance of $d = 2.57 \pm 0.05$ Å.

This lack of growth of an epitaxial film is in line with the initial reaction of Cr with the residual hydroxyl groups of the surface that leads to a disordered interfacial oxidized Cr layer on which a ill-cristallized Cr film grows. On a structural point, *per se*, the growth of a poorly crystallized layer is not a surprise for chromium. The expected hexagon/hexagon epitaxy of bulk body-centered cubic (bcc) α-Cr on $Al_2O_3(0001)$ (figure 4.31-a) would lead to the atomically rough and open (111) surface [Madey et al., 2008]. The more compact and lower energy (110) orientation would give rise by symmetry to three variants on alumina (2-fold symmetry on a 3-fold symmetry). But beyond these basic considerations, chromium is a metal known to display a phase transition upon size reduction [Nishida et al., 1972, Durbin et al., 1988, Saraf et al., 2003, Lovrinčić and Pucci, 2009, Kimoto and Nishida, 1973, Nishida and Kimoto, 1974, Chu et al., 1997, Hayashi et al., 1977]. Apart from bulk bcc $\alpha-$Cr and a report about a possible epitaxial face-centered cubic (fcc) Cr on Au(100) [Durbin et al., 1988], chromium at the nansocale (either in the form of free [Nishida and Kimoto, 1974] or of sup-

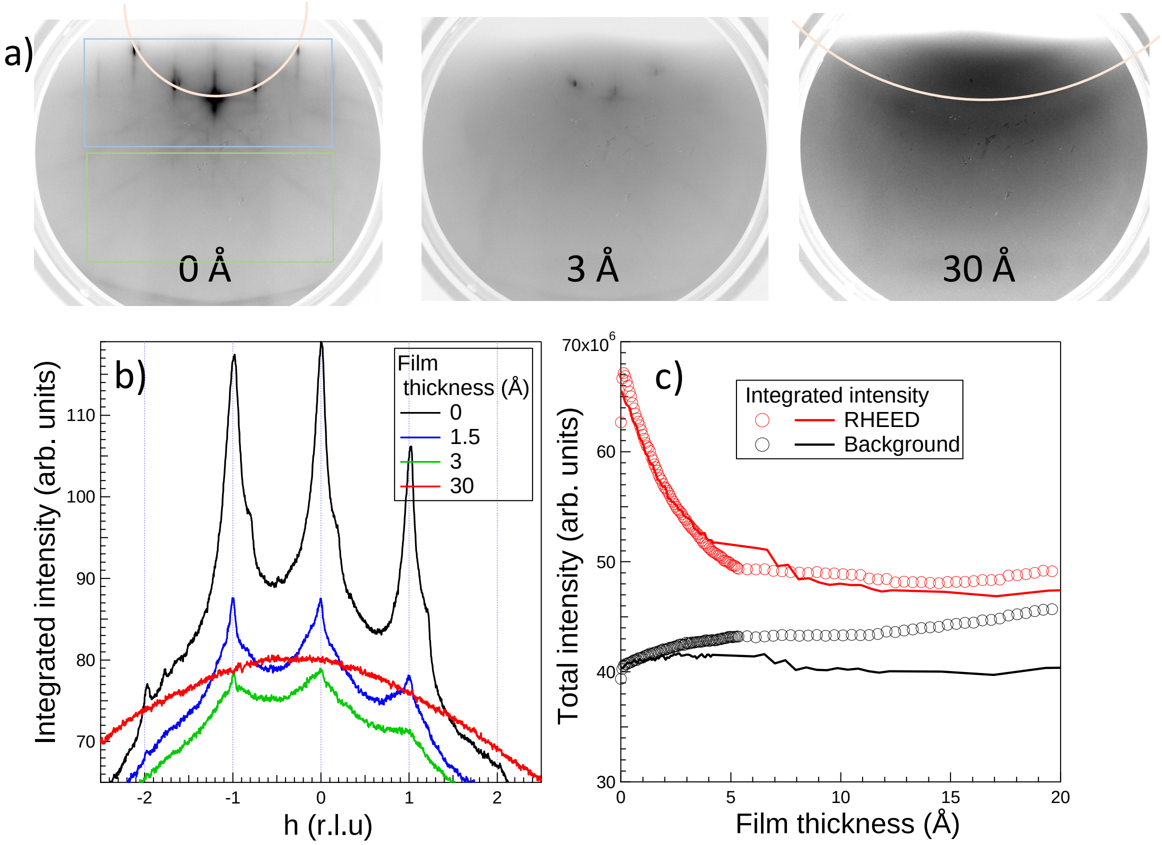

Figure 4.30: a) Evolution of the RHEED diffraction pattern (beam energy of 9.5 keV) along the $[10\bar{1}0]$ direction of $Al_2O_3(0001)$ upon Cr deposition at room temperature. Film thickness calibrated by XPS is given in figure. Pink circle at the end of the deposit points at a polycristalline layer. b) Cross section of intensity (integrated over the blue box of figure a) in reciprocal lattice unit (r.l.u.) along the $[10\bar{1}0]$ direction. c) Integrated signal over the blue box and background over the green box of figure-a versus film thickness. The evaporation rate was in the range of 0.4 Å.min^{-1}.

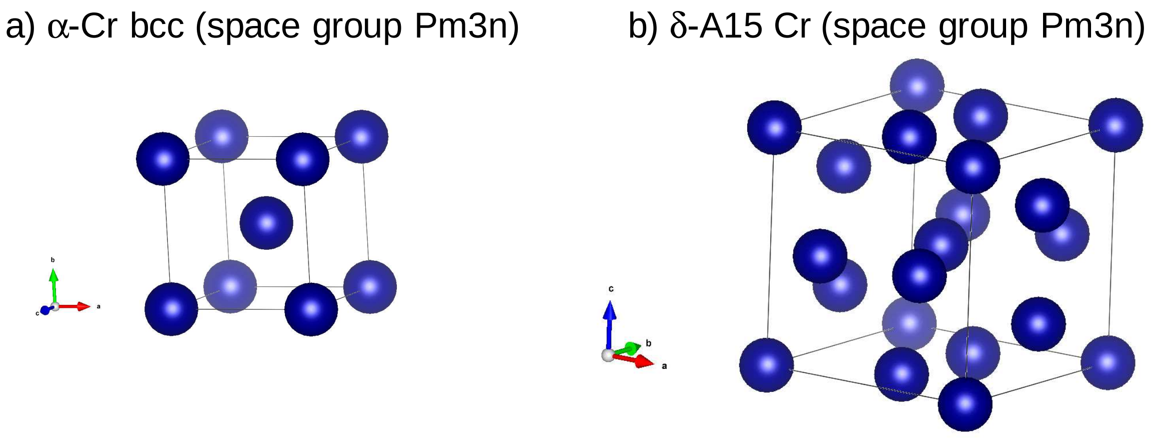
a) α-Cr bcc (space group Pm3n)

b) δ-A15 Cr (space group Pm3n)

Figure 4.31: Ball models of a) bcc α-Cr (a = 2.91 Å) and b) A15 δ-Cr (a = 4.59 Å) structures. The first neighbor distance is 2.52 Å in bcc and 2.29, 2.56 Å in A15 δ-Cr.

ported [Kimoto and Nishida, 1973] particles or of continuous films [Nishida et al., 1972, Saraf et al., 2003, Chu et al., 1997]) exists in a cubic A15 δ type structure (figure 4.31-b, lattice parameter 4.59 Å). This phase is stable up to 450°C at which phase transformation to bcc occurs through grain growth [Kimoto and Nishida, 1973, Chu et al., 1997]. A transition from A15 δ to bcc was also observed as function of the film thickness depending on the angle of incidence during growth [Nishida et al., 1972, Lovrinčić and Pucci, 2009] and assigned to a phase transition due to heating during sputtering deposition [Chu et al., 1998]. Free Cr particles of size lower than 10 nm adopt the A15 δ structure [Kimoto and Nishida, 1973]. In spite of a debate about the possible role of spurious oxidation [Gasgnier and Névot, 1981, Chu et al., 1997], it is now admitted that A15 δ is a metastable allotrope phase of Cr with a first order transition to bcc [Chu et al., 1997, Chu et al., 1998, Gasgnier and Névot, 1981]. It has also been found for other bcc metals such as W, Mo, Nb [Chu et al., 1997] and is thought to be the vestiges of icosahedral configurations present in initial nuclei [Kimoto and Nishida, 1973]. It was even suggested to be related to an amorphous glassy icosahedral short range arrangment [Brjega and Popescu-Pogrion, 1989].

The distances $d = 2.57 \pm 0.03$ Å found by RHEED and $d = 2.6 \pm 0.03$ Å found by EXAFS for Cr-Cr metal are in close agreement with the Cr-Cr distance in bulk bcc α-Cr (2.52 Å) but matches also with the A15 one. However, the short Cr-Cr distance of 2.3 Å in A15 phase is not present in EXAFS (table 4.1) but could be blurred by the overwhelming distance of 2.56 Å with an icosahedral coordination (12 neighbors); moreover, the value found by RHEED is much larger than that expected from the lowest angle (110) bcc reflection ($d = 2.07$ Å) or (200) A15 reflection ($d = 2.30$ Å). Therefore, the metallic part of the Cr deposit is likely to be more disordered than expected in these ideal structures.

4.5 Conclusion

Core-level photoemission, x-ray absorption, *ab initio* calculations and optical reflectivity have been combined to tackle the question of chemical state, absorption site and morphology of Cr deposits on $Al_2O_3(0001)$-(1×1) surface. The analysis of the evolution of Cr 2p and O 1s core level lineshapes upon Cr deposition showed that Cr is oxidized at the interface with the annealed alumina surface. Reduction of alumina was ruled-out by scrutinizing the Al 2s core level but the comparison with intentionally hydroxylated surface pointed at a chemical reaction with residual hydroxyl groups that amount to 0.25 ± 0.08 ML on average. The resulting intermediate oxidized chromium species is confined to the interface.

At the monolayer thickness range, an excess of oxygen in the near-neighbor environment of Cr was demonstrated by the striking similarity of EXAFS spectra with Cr_2O_3 compound and by an analysis of the coordination number. The key argument came from the comparison between *ab initio* calculations and EXAFS measurements in terms of Cr-O distance. Going from bare alumina to H_mO_n and oxygen-rich surfaces, the agreement focused only on Cr^{3+} formed upon a reaction with OH^-. This set of results serves as a strong proof of the long-debated existence of residual OH groups at the surface of annealed alumina. The same environment was observed for Cr deposited on γ-Al_2O_3 film grown on the FeAl alloy.

Quantification in photoemission led to a Cr sticking coefficient close to one especially at high thicknesses. Optics and AFM confirmed a Volmer-Weber growth of flat particles that percolate rapidly around 10-15 Å. This good wetting can not be safely assigned to the interfacial reaction as kinetic aspects of growth maybe at work due to low mobility and vapor pressure of chromium. Finally, the lack of growth of an epitaxial Cr film was pointed out by RHEED and is in line with the initial formation of oxidized chromium layer. Those results will serve as a firm basis to understand the Cr buffer effect on Zn growth on alumina.

CHAPTER 5

CHROMIUM BUFFER EFFECT AT THE ZINC/ALUMINA INTERFACE: WETTING AND DESORPTION

In line with the industrial background of this thesis, this chapter focuses on the chromium buffer effect on the growth mode, chemistry and thermal stability of zinc deposits on α-$Al_2O_3(0001)$ surface. Results were compared to the case of bare alumina surfaces studied in R. Cavallotti thesis [Cavallotti, 2014a]. XPS and SDRS were combined to investigate the wetting of alumina surfaces by zinc. The former technique was particularly used to analyze the chemistry of zinc and quantify the dependence of the zinc sticking coefficient on the chromium thickness. The latter served as a powerful tool to follow the evolution of zinc particle morphology through their plasmonic response. AFM experiments under air were occasionally carried out to verify. These tools were supplemented by thermal desorption measurements (TPD) to scrutinize the influence of the Cr buffer on the desorption energy which, in a first approximation, is related to the heat of adsorption.

5.1 Photoemission analysis of $Zn/Cr/Al_2O_3$

5.1.1 Photoelectron peak characteristic of zinc

A typical XPS widescan recorded for a 9.4 Å thick Zn deposit atop 3.1 Å of Cr on a α-$Al_2O_3(0001)$-(1×1) surface is shown in figure 5.1. It features all core level peaks and Auger transitions characteristic of Zn, Cr, Al and O accessible in the binding energy range from 0 to 1200 eV. The isolated Zn 2p and Al 2s peaks are mainly used for quantification of zinc deposits; owing to the high photo-ionization cross section of the former with respect to the latter ($\sigma_{Zn\ 2p}/\sigma_{Al\ 2s} \simeq 40$ [Yeh and Lindau, 1985]) zinc is easily detectable even at submonolayer levels. As discussed hereafter, the chemical analysis of zinc mainly relied on the investigation of the Zn $L_3M_{45}M_{45}$ lineshape together with the Auger parameter to overcome charge effect. The Mg-Kα X-ray source was systematically chosen to study Zn deposits on Cr/Al_2O_3 because it allows the separation of the Zn $L_3M_{45}M_{45}$ and the Cr 2p peaks otherwise overlapping with a Al-Kα anode.

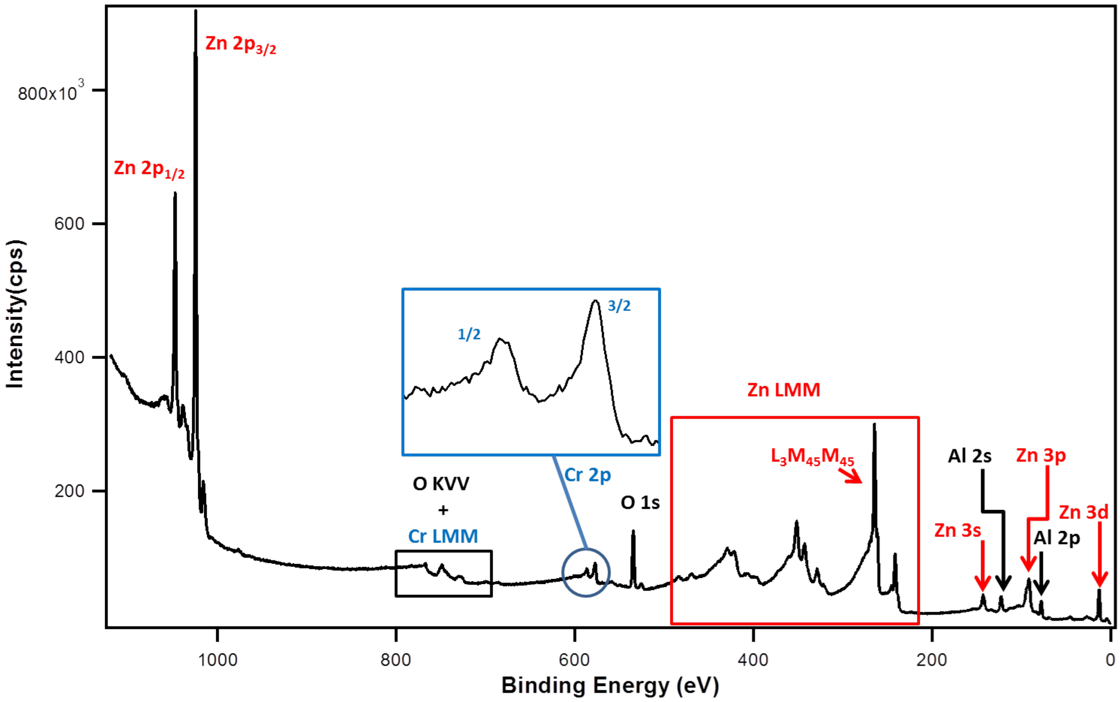

Figure 5.1: A widescan photoemission spectrum collected with a Mg-Kα anode on a Zn(9.4 Å)/Cr(3.1 Å)/α-Al_2O_3(0001) sample.

5.1.2 Photoemission analysis of the sticking coefficient of zinc on Cr/Al_2O_3

Let's first underline that the sticking coefficient of zinc on a bare alumina surface is negligible at room temperature [Rodriguez et al., 1996, Cavallotti, 2014a]. For this reason, a sizeable condensation on (1 × 1) (dry and hydroxylated) and $(\sqrt{31} \times \sqrt{31})R \pm 9°$ alumina surfaces could only be achieved in the work of R. Cavallotti [Cavallotti, 2014a, Le et al., 2017b] by cooling down to 100 K; by using identical exposure times (8, 13 and 25 mins), he evidenced a hierarchical decrease of the sticking coefficient of Zn on the different surfaces as follows: (1 × 1) ¿ hydroxylated (1 × 1) ¿ $(\sqrt{31} \times \sqrt{31})R \pm 9°$. Values are summed up in table 5.2 where the fluence is measured following a calibration on a quartz balance.

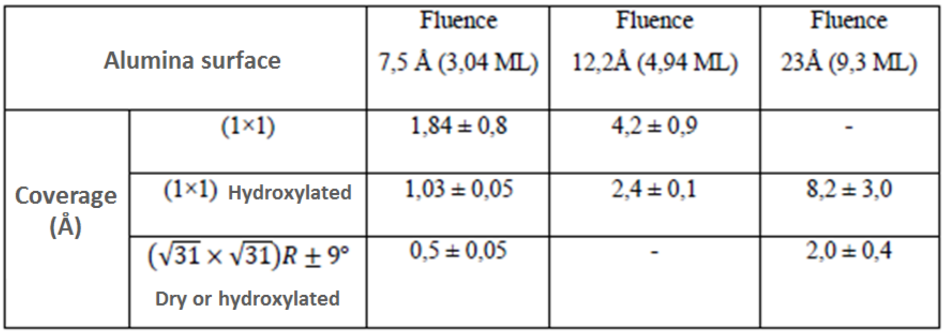

Alumina surface		Fluence 7,5 Å (3,04 ML)	Fluence 12,2Å (4,94 ML)	Fluence 23Å (9,3 ML)
Coverage (Å)	(1×1)	1,84 ± 0,8	4,2 ± 0,9	-
	(1×1) Hydroxylated	1,03 ± 0,05	2,4 ± 0,1	8,2 ± 3,0
	$(\sqrt{31} \times \sqrt{31})R \pm 9°$ Dry or hydroxylated	0,5 ± 0,05	-	2,0 ± 0,4

Figure 5.2: Values of zinc coverage on (1×1), hydroxylated (1×1), and $(\sqrt{31}\times\sqrt{31})R\pm 9°$ alumina. The values are averaged over different measurements, and uncertainties correspond to standard deviation. From [Cavallotti, 2014a].

To determine the effect of the Cr buffer on the sticking coefficient of zinc, alumina substrates were pre-covered by various amounts of Cr; then, surfaces were exposed to a given fluence of 14.7-16.8 Å of Zn obtained by evaporating the metal during 14-16 mins at a rate of 1.1 Å/min as calibrated on the quartz microbalance. The Zn amounts, as determined by XPS, are displayed in figure 5.3 as a function of the Cr pre-coverage. The quantification was done through an analysis of ratios between areas under Zn 2p (Cr 2p) and Al 2s peaks for Zn (Cr) thicknesses in the frame of a continuous film stack model by taking into account signal damping in all films (see section 1.3.7). Notice that the values given for oxidized chromium were calculated using the mean free path of Cr 2p and Al 2s electrons in Cr_2O_3. At Cr coverages lower than 0.7 Å, the sticking of Zn on the surface is negligible. Above that value, the amount of Zn increases steeply, much more rapidly than the Cr coverage. However, it is only for a Cr coverage of 26 Å, at which the alumina surface is likely fully covered by Cr, that the thickness of the deposited Zn corresponds to the evaporated amount (14 Å compared to 14.7 Å as calibrated on the quartz balance). On that surface, the sticking probability of Zn at 300 K is ~ 1, in stark contrast with the bare alumina on which the condensation of Zn requires a substrate temperature lower than 220 K [Rodriguez et al., 1996,Cavallotti et al., 2016]. For Cr coverage lower than 0.7 Å, the absence of Zn on the surface is likely explained by the oxidation of the deposited Cr. As it was proved in the previous chapter, in this coverage range, Cr is oxidized via a reaction with the surface hydroxyl groups in the same way as Ti [Lazzari and Jupille, 2002,Lazzari and Jupille, 2005], Cu [Niu et al., 2000], Co [Chambers et al., 2002] and Rh [Libuda et al., 1997,Sterrer and Freund, 2013]. Indeed, the poor sticking on the chromium oxide formed by reaction with surface OH parallels the observation made on a purposely oxidized Cr films obtained by annealing Cr at 1575 K under an oxygen partial pressure of 2 $\times 10^{-6}$ mbar during 10 mins (red dots in figure 5.3). However, on one of these deposits (2.6 Å) synthetized at a lower temperature (1150 K), 3.75 Å of Zn were found. These two results are consistent with DFT calculations of separation energy at a Zn/M interface compared to

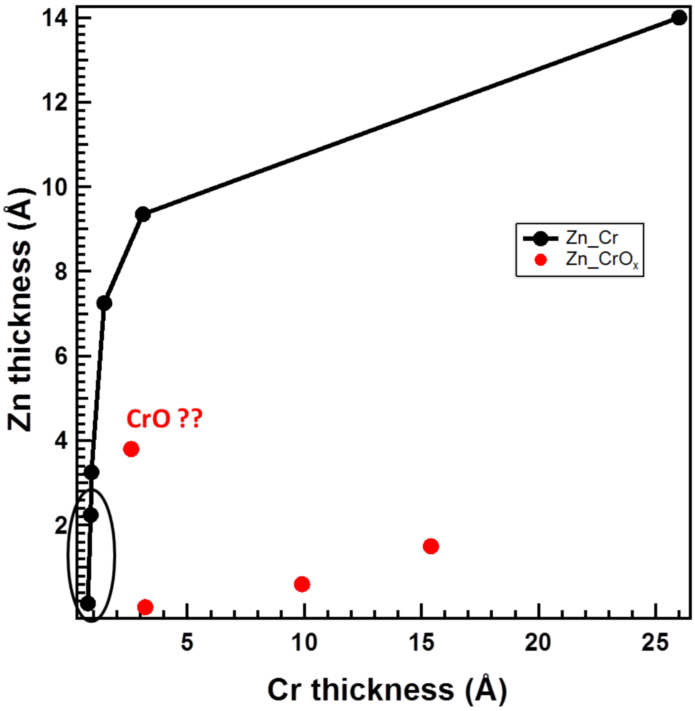

Figure 5.3: Correlation between the amount of zinc found on the surface after an exposure of the substrate to a constant fluence of zinc (16 Å) and the quantity of Cr pre-deposited, all depositions being performed at 300 K. The region of low thicknesses in which chromium is partially oxidized through reaction with hydroxyl groups is circled. The amount of zinc found on purposely oxidized Cr films (red symbols) demonstrates the poor sticking of zinc on chromium oxide at 300 K except for the 2.6 Å CrO_x formed by annealing at 1150 K on which 3.75 Å of Zn were found.

that at Zn/MO_x (M for metal and MO_x for its metal oxide) [Le et al., 2016] which showed that buffer oxidation generally tends to reduce the number of metal/buffer strong bonds. In the case of chromium oxide, the adhesion of zinc is particularly sensitive to the buffer stoichiometry and ranges from very strong for CrO to especially weak for Cr_2O_3 (E_{sep} = 4 vs 1.01 J/m^2), which suggests that the thin chromium oxide buffer is understoichiometric at the opposite to the thicker one. Beyond a Cr coverage of ∼0.7 Å, as the surface hydroxyl groups have presumably totally reacted with Cr, Zn is seen to stick better and better (figure 5.3) as the metallic component of Cr dominates. However, the increase of Zn sticking is not only related to the chemical state of Cr underneath but, likely, to the actual coverage, morphology and growth mode of Cr particles as it will be discussed in details in the following sections dealing with SDRS observations. Indeed as already underlined in section 4.4.1 (figure 4.27), the surface covered by the Cr particles increases steadily up to 15 Å.
One should finally note that the absolute values of calculated thicknesses with the approximation of continuous films are only indicative of a trend since both Cr and Zn follow a 3D growth in the low thickness regime (see section 4.4.1 for Cr and below for Zn). The use of an alternative model with hemispheroids partially covering the surface would be the only recourse for a more accurate quantification but would require extra-information on the coverage or XPS angular measurements.

5.1.3 The chemical state of zinc from the Zn $L_3M_{45}M45$ Auger peak

The determination of the Zn chemical state at Zn/Cr interface relied on the analysis of the Zn $L_3M_{45}M_{45}$ Auger lineshape, energy shift and the corresponding Auger parameter. In fact, the litterature has shown that for some metals, including zinc, ionized atoms are more sensitive to the chemical environment than those in a ground state [Schön, 1973a, Schön, 1973b]. Indeed, the Auger energy shift between Zn and ZnO is ~ 4.3 eV whereas the direct chemical shift of the most intense core level Zn 2p is only $\sim 0.2 - 0.5$ eV which makes difficult to accurately retrieve useful information on the chemical state of Zn from this latter.

Figure 5.4 represents the shifted binding energy of Zn $2p_{3/2}$ for different Zn deposits over varying Cr thicknesses. As done for Cr 2p peak in section 4.1.3, all binding energies values were referenced to the Al 2s peak of the thickest deposit (Zn(14 Å)/Cr(26 Å) since these films are expected to be purely metallic and to totally cover the surface thus reducing at best the charge effects due to substrate insulating character. In passing, the corresponding absolute binding energies of Cr 2p and Zn 2p do correspond to tabulated metallic compounds. Two of the points of figure 5.4 (represented in red) correspond to Zn evaporated on oxidized Cr. The oxidation of the buffer was achieved by annealing under O_2 gas doser (chamber pressure of $p = 2 \times 10^{-6}$ mbar) for 10 mins at a temperature ranging between 1150 and 1500 K. Beyond a possible final state effect in small particles like for Cr 2p (see section 4.1.3), Zn 2p binding energy fluctuates by 0.5 eV around 1021.04 eV in most cases. As a consequence, this method is not reliable enough to really comment on the chemical state of Zn.

The Zn $L_3M_{45}M_{45}$ kinetic energy shift of can be used as an alternative. As represented in figure 5.5, this kinetic energy is almost stable for all samples around an average value of 992.7 eV very close to the kinetic energy of the thickest Zn deposit (992.1 eV), supposedly purely metallic and to 992.5 eV found in the literature for metallic zinc [Schön, 1973a]. On the other hand, for 1.5 Å of Zn deposited on 15.4 Å of oxidized chromium, the Zn $L_3M_{45}M_{45}$ transition appears at 988.7 eV, in close agreement with 988.2 eV found for ZnO in the lit-

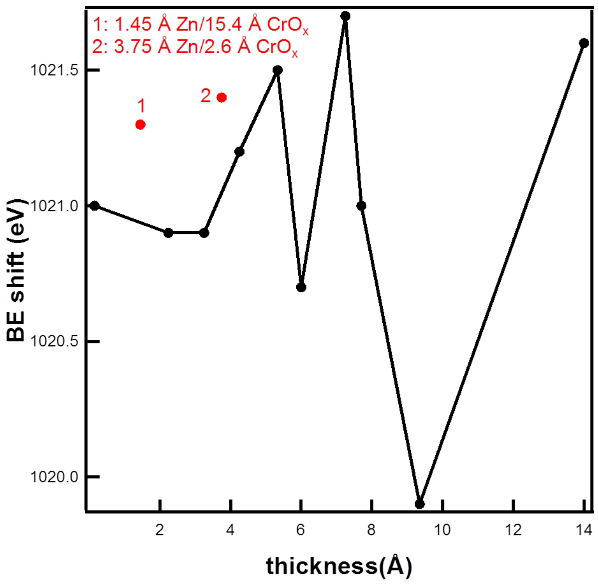

Figure 5.4: Zn $2p_{3/2}$ core level binding energy shift versus Zn thickness for several Zn deposits above various thicknesses of Cr on Al_2O_3(0001)-(1 × 1). Red points correspond to deposits over oxidized chromium.

erature [Schön, 1973a]. A shift of 3.4 eV compared to the metallic thick film indicates an oxidation of Zn at the contact of a thick chromium oxide buffer. However, this conclusion does not apply for Zn (3.75 Å) on the thin oxidized Cr deposit (2.6 Å). This could lie in the stoichiometry of the so-formed chromium oxide. Indeed, according to DFT calculations [Le et al., 2016], the number of Zn-Cr bonds is preserved compared to the metallic Cr one for a CrO buffer and no Zn-O bonds are found, contrary to the case of Cr_2O_3.

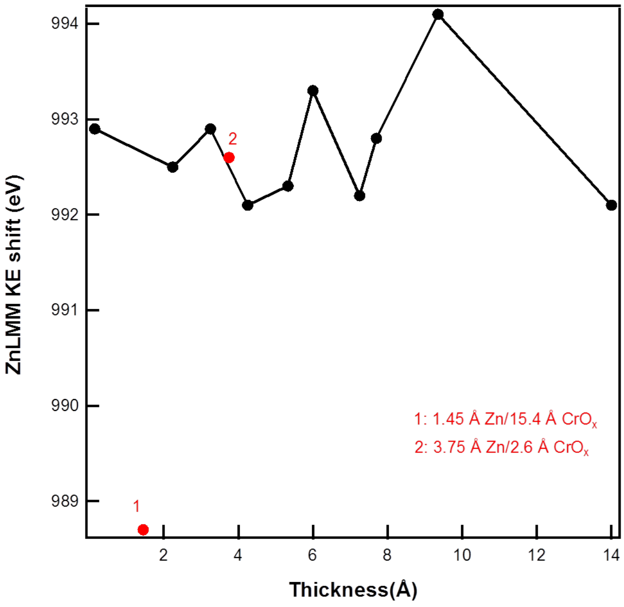

Figure 5.5: Kinetic energy shift of Zn $L_3M_{45}M_{45}$ Auger transition versus Zn thickness for several Zn deposits above various thicknesses of Cr on Al_2O_3(0001) (1 × 1). Red marks correspond to deposits over oxidized chromium.

An other approach used to tackle the question of the Zn chemical state totally free from charge effects is the analysis of the Auger parameter given by:

$$\alpha_{Zn} = \mathrm{BE}(\mathrm{Zn}\ 2\mathrm{p}_{3/2}) + \mathrm{KE}(\mathrm{Zn}\ \mathrm{L}_3\mathrm{M}_{45}\mathrm{M}_{45}). \tag{5.1}$$

The Auger parameter evaluated over the same population of samples yielded an average value of 2013.9 ± 0.11 eV (figure 5.6) characteristic of metallic zinc as found in the literature [Schön, 1973a, Antonides et al., 1977a] for all deposits on metallic Cr or thin chromium oxide (2.6 and 3.2 Å). On the other hand, a value of 2010 eV typical of ZnO was found for the deposit done on a 15.4 Å of voluntarily oxidized Cr. These results confirm the conclusions based on the kinetic energy shift of Zn $L_3M_{45}M_{45}$ peak. Accordingly, zinc exhibits a metallic state on all the Cr deposits, except on the oxidized thick film where an oxidation of Zn takes place.

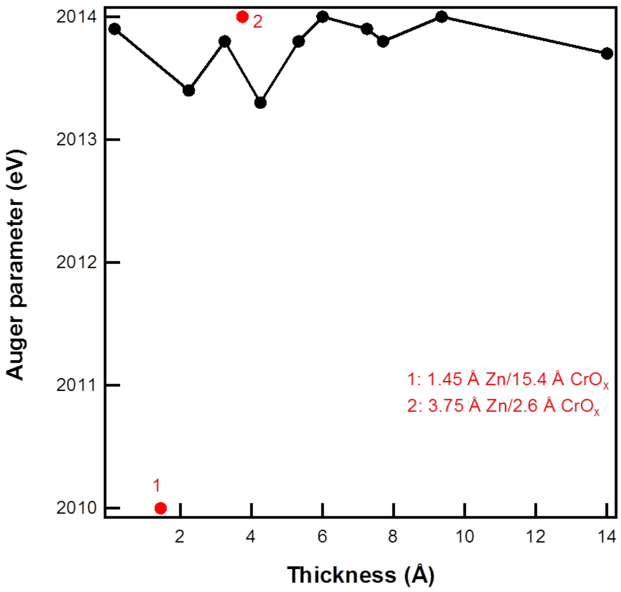

Figure 5.6: Auger parameter of zinc versus deposit thickness for several Zn deposits above various thicknesses of Cr on Al_2O_3 (1 × 1). Red marks correspond to deposits over oxidized chromium.

One last method used for the determination of the chemical state of zinc was the investigation of the Zn $L_3M_{45}M_{45}$ lineshape. The scan of the considered region for the Zn(14 Å)/Cr(26 Å) sample is shown in figure 5.7. The general profile reproduces all the fine structures, accounting for multiplet splitting in the d^8 final state, reported in the litterature for metallic zinc [Schön, 1973a, Kowalczyk et al., 1973a, Ley et al., 1973, Yin et al., 1974, Fox et al., 1977, Antonides et al., 1977a, Antonides et al., 1977b]. Based on calculations of transition probabilities, Antonides *et al.* [Antonides et al., 1977a] made a clear assignment of the peaks where the prominent feature is attributed to the ^1G state. The binding energy shifts referenced to the ^1G component deduced from our experiments for the ^1S and ^3F states are compared to values found in the literature in table 5.1. The low binding energy side is slightly broadened by the unresolved ^3P and ^1D lines. A broad feature shifted by ~ 9.2 eV to higher binding energies (lower kinetic energies) with respect to ^1G is assigned to plasmon losses in agreement with [Fox et al., 1977]. However, the identification of the satellite structure at high binding energies indexed with a red arrow in figure 5.7 demanded careful examination in the past literature. Experiments and calculations proved that this feature is a direct result of the $L_2L_3M_{45}$ Coster-Kronig transition preceeding the $L_3M_{45}M_{45}$ Auger process [Antonides et al., 1977b]. When this process occurs, an initial L_2 hole converts to an L_3 hole thereby ejecting an M_{45} electron. The L_3 hole then decays through the normal $L_3M_{45}M_{45}$ Auger process ending up in a final state with three M_{45} holes, the system being left with an M_{45} hole after the Coster-Kronig process. Consequently, a shift to lower kinetic energies (higher BE) takes place as a result of Coulomb interaction between the Auger electrons and the additional M_{45} hole [Antonides et al., 1977b].

Over the series of samples studied in this chapter, all Zn $L_3M_{45}M_{45}$ peaks exhibited the same prfofile corresponding to metallic zinc including the deposits on thin oxidized chromium

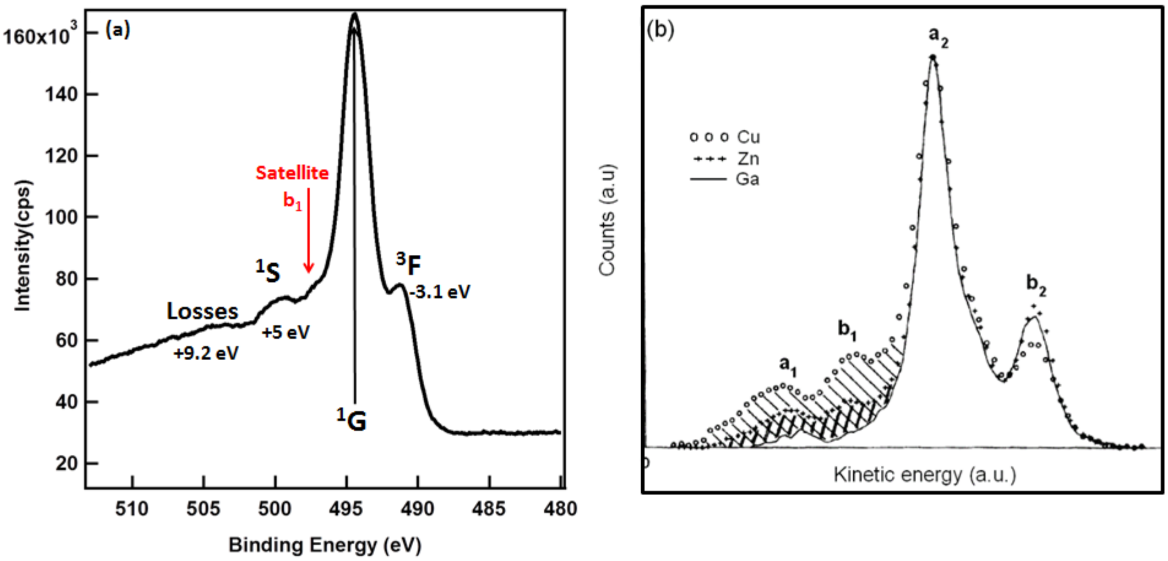

Figure 5.7: a) Zn $L_3M_{45}M_{45}$ Auger peak of a 14 Å Zn film deposited on 26 Å metallic Cr film recorded using an Al Kα anode. The multiplet structures are assigned according to [Antonides et al., 1977a] and are compared to b) the $L_3M_{45}M_{45}$ for Zn, Ga, and Cu from [Antonides et al., 1977b]. b_1 structure in figure-b corresponds to the satellite in figure-a.

buffers, except for the 1.4 Å deposit on 15.4 Å of Cr oxide. Despite a spurious signal coming from the supporting plate, the obvious line broadening of ~ 2.3 eV in agreement with the value found upon oxidation by Fox *et al.* suggested the oxidation of this particular zinc deposit on oxidized chromium [Schön, 1973a, Fox et al., 1977].

5.2 Wetting at the Zn/Cr/Al_2O_3 interface as seen by differential reflectivity

Despite the existence of interband transitions that broaden the optical resonance of Zn particles, the differential reflectivity technique (see section 1.7 for the description of SDRS setup) remains quite sensitive to the evolution of the particle aspect ratio and therefore to wetting at the nanoscale (see section 3.5). Therefore, the influence of the Cr buffer on the growth mode and the wetting of Zn has been analyzed *in situ* and in real time by SDRS during the exposure of $Al_2O_3(0001)$-(1×1) surfaces precovered by various thicknesses of Cr to a constant fluence of Zn equal to ~ 16.8 Å as calibrated on the quartz balance. The following Zn SDRS spectra were systematically normalized to the bare alumina signal before Cr growth. Film thicknesses will be given accordingly to the photoemission calibration.

5.2.1 Morphology of Zn particles on different Cr thicknesses

The SDRS spectra recorded in p- and s-polarizations associated to the final achieved Zn thickness are displayed in figure 5.8. Spectra are impacted by the form and intensity of the chromium pre-deposit, but they all exhibit an asymmetric (to the red wavelength side) broad band typical for the plasmonic response in Zn nanoparticles (figure 3.7). Of course, the feature is dramatically broadened by interband transitions and the intensity is enhanced in p-polarization compared to s-one as expected from a lower alumina absolute reflection coeffi-

Reference	^1S	^3F
[Aksela et al., 1974]	4.68	-3.22 - -3.75
zinc vapor		
[Kowalczyk et al., 1973b]	5.2	-3.4
[Yin et al., 1974]	4.6	-3.4
[Yin et al., 1972]	5.1	-3.4
[Fox et al., 1977]	4.8	-3.4
[Antonides et al., 1977a]	4.8	-3.3
[Cavallotti, 2014a]	5.2	-3.4
present work	5	-3.1

Table 5.1: Energy shifts calculated with reference to ^{1}G for ^{1}S and ^{3}F states compared to values found in the literature.

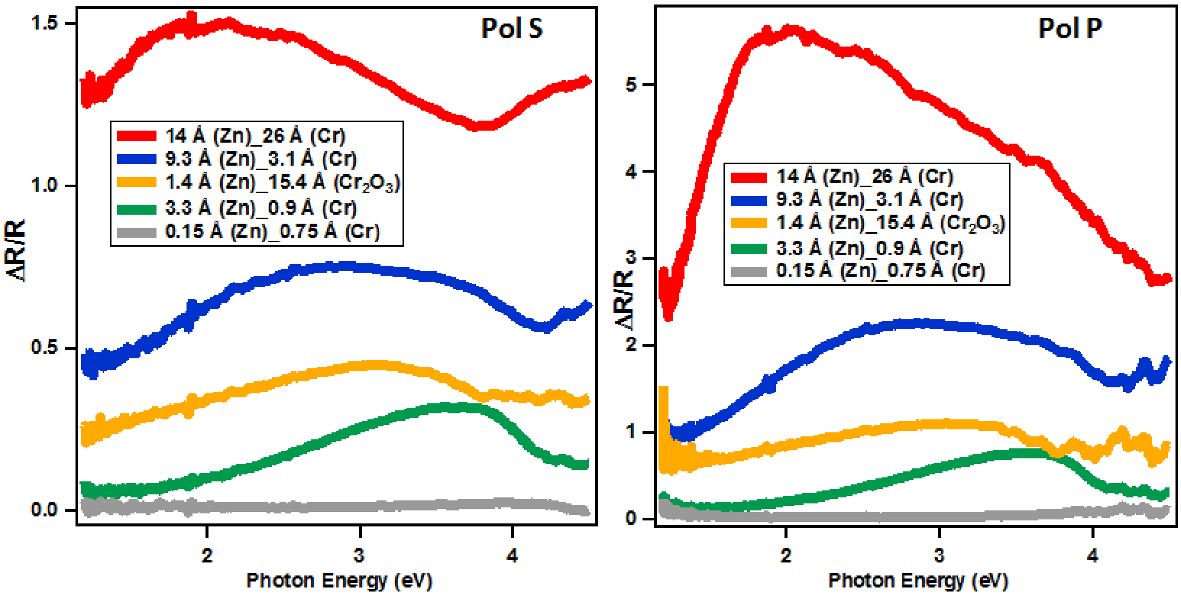

Figure 5.8: SDRS spectra recorded in s- (left) and p- (right) polarization after an exposure of Cr-covered Al_2O_3 (0001)-(1 × 1) surfaces to a constant fluence of Zn. All spectra are referenced to the bare alumina substrate.

cient (figure 3.5). Since spectra are quite similar in s- and p-polarization and poorly differ for flat particles (see section 3.5), the following discussion will be focused on the s-polarization spectra which depend only on the parallel susceptibility $\gamma(\omega)$, while the former combines both parallel $\gamma(\omega)$ and perpendicular $\beta(\omega)$ contributions.

By considering at first the samples with a metallic Cr deposit (not purposely oxidized), one can note a progressive shift in energy of the band from 4.2 to 2.1 eV as the Zn film thickens from 0.15 to 14 Å. This redshift is clearly indicative of particles flattening upon Cr coverage increase and suggests beforehand a Volmer-Weber growth mode. To qualitatively estimate the aspect ratio of the Zn particles involved in the deposit, experiments were compared to first-order susceptibilities dielectric simulations as detailed in section 3.5 (figure 5.9). Shortly, particles were modeled by truncated hemispheroid or truncated sphere of different aspect ratios (diameter/height $A_r = D_{\parallel}/H$) without accounting for particle-particle interaction and size/shape broadening but by keeping the amount of Zn (film thickness) constant. Particles are supposed to lie on an alumina substrate so that the main pitfall of such a comparison is the lack of account of the screening induced by the Cr layer on the image field in the substrate. A first account of this phenomenon at the dipolar level was developed in section 3.7 in the simple case of a continuous Cr film. Calculations showed that, ignoring the Cr film is valid for Zn particle size larger than the Cr film thickness (see section 3.7.4.3). However, the actual experimental situation is more complex that this basic model since Zn growth happens on Cr nanoparticles. Nevertheless, the comparison to the simulations of figure 5.9 is expected to be indicative of the actual trend of wetting but values should be taken cautiously.

Values of aspect ratio < 2, 2 and > 16 are assigned to 3.3, 9.3, and 14 Å thick Zn deposits,

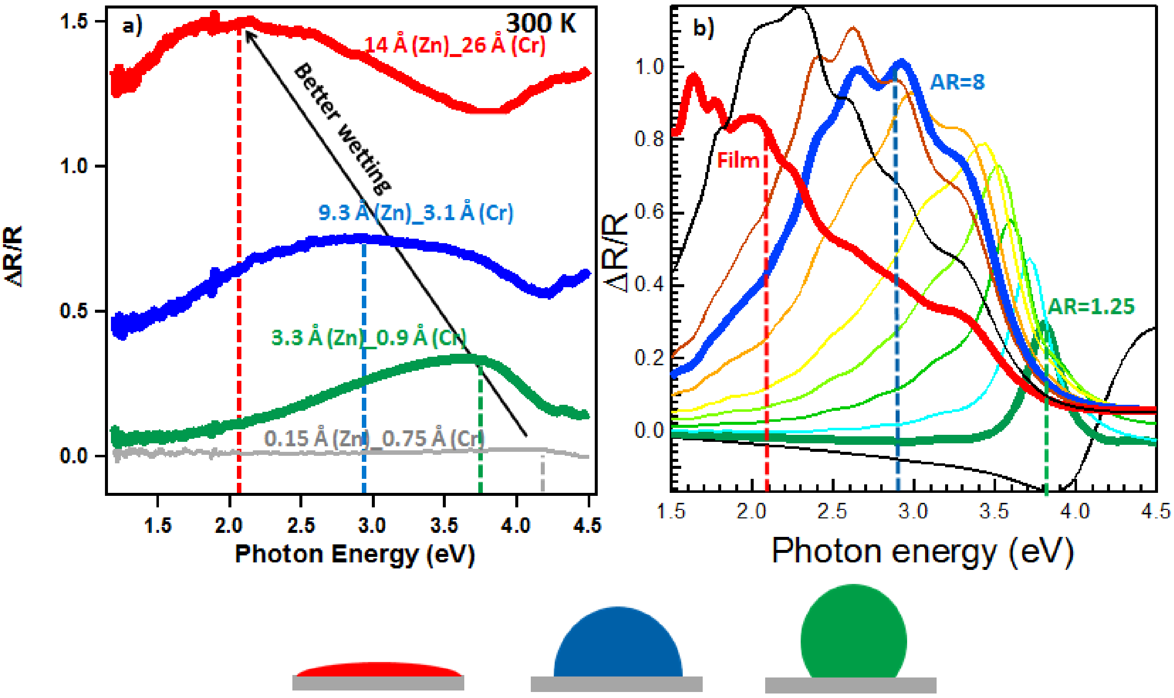

Figure 5.9: Comparison between final experimental (figure-a; same exposure time to Zn flux) SDRS spectra for Zn on various Cr deposits to dielectric simulations (figure-b) for different particle aspect ratios A_r (see text). Comparison is made for s-polarization.

respectively. The sensitivity of the resonance position to the particle morphology allowed therefore the distinction between the non-wetting behavior at low Cr thicknesses and the good wetting obtained at 14 Å where a nearly continuous film is formed. The variation of the Zn particle aspect ratio with the chromium thickness underneath underlines a close dependence between the wetting behavior of both deposits. As a reminder (see figure 4.27), above 1.5 Å, chromium grows as high aspect ratio particles ($A_r \sim 5$) that cover progressively the surface before percolating above 15 Å. Consistently, Zn particles start flattening over 3.3 Å of Cr and flatten even further as the buffer percolates. This observation emphasizes the dictation of Zn particles wetting by the Cr beneath. For the thickest films, the good quantitative agreement between experiment and the exact dielectric simulations performed for a stack of two continuous films on alumina (see section 3.7.1) does confirm this hypothesis. However, at intermediate Cr thicknesses, the fitting of Zn SDRS spectra turned out to be unsatisfactory

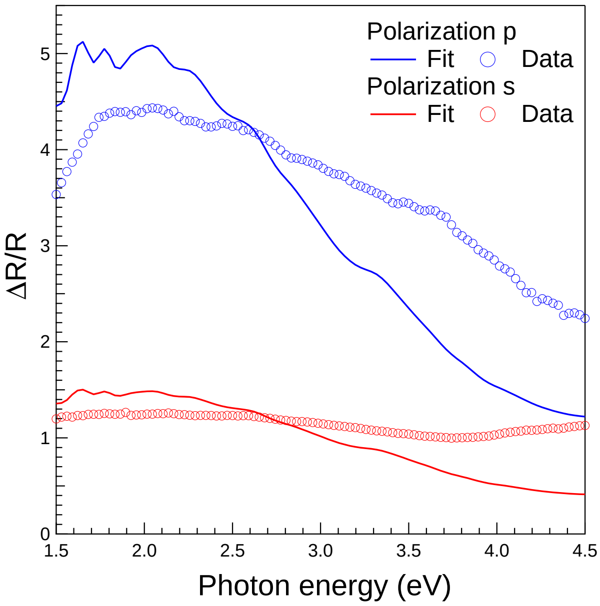

Figure 5.10: Comparison between exact SDRS simulations of a stack of two continuous films Zn(14 Å)/Cr(26 Å)/Al_2O_3 and the corresponding experimental spectra. Polarization are indicated in the figure.

(not shown) in terms of intensity owing to the simplified assumption on the particle morphology (Zn particles on bulk alumina or on effective medium with a dielectric constant as defined in section 3.7 in equation 3.56). Encapsulation of Cr particles by Zn or even interdiffusion as reported for Au on a Cr adhesion layer [Todeschini et al., 2017] could be likely explanation for this failure.

In order to highlight the enhanced wetting of the surface by zinc promoted by the chromium buffer layer, the present SDRS results on Cr/Al_2O_3 at 300 K are compared to those obtained on bare alumina at 100 K in figure 5.11. The low temperature allowed an enhanced sticking but also favored an enhanced wetting [Cavallotti, 2014a]. According to the optical absorption energy position, zinc likely forms a percolated continuous layer over Cr at 300 K, while hemispherical particles poorly wet the surface of bare alumina at 100 K. This is not surprising as the use of wetting layers has likewise proven their efficiency for the growth of silver and gold [Anders et al., 2006, Fukuda et al., 2008, Logeeswaran et al., 2008, Formica et al., 2013, Todeschini et al., 2017], where the buffer material works as seed sites for the nucleation of the top-metal leading to its earlier coalescence.

To further support SDRS conclusions, AFM imaging was occasionally performed *ex situ* using an atomic force microscope in a non-contact tapping mode at ambient conditions. Despite possible evolution of film morphology in air, in the example of a 7.25 Å Zn deposit on 1.45 Å Cr layer, the representative image of figure 5.12-a,b shows that Zn seems to cover the surface with an average root mean square roughness of 1.04 nm. In comparison, Logeeswaran *et al* [Logeeswaran et al., 2008] found a drastic reduction (by at least a factor of ten) of the rms roughness of Ag deposited on SiO_2/Si when a Ge buffer layer of at least 5 Å is added.

At last, it is interesting at this point to consider the 1.4 Å deposit of zinc on 15.4 Å of purposely oxidized chromium shown in figure 5.8 (orange spectra). The absorption peak for this sample appears at ~ 3.2 eV compared to ~ 3.4 eV on bare alumina at 100 K. Although chromium oxide favors the sticking of zinc, this comparison points at a similar wetting. As

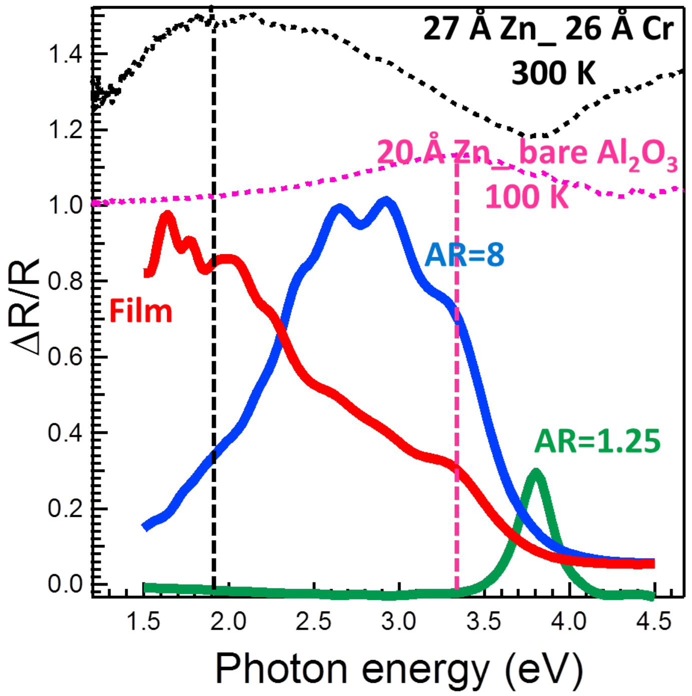

Figure 5.11: Comparison between the experimental SDRS of Zn(14 Å)/Cr(26 Å)/Al_2O_3, that of Zn(20 Å)/Al_2O_3 20 Å grown at 100 K and dielectric simulations using truncated spheroid models of various aspect ratios.

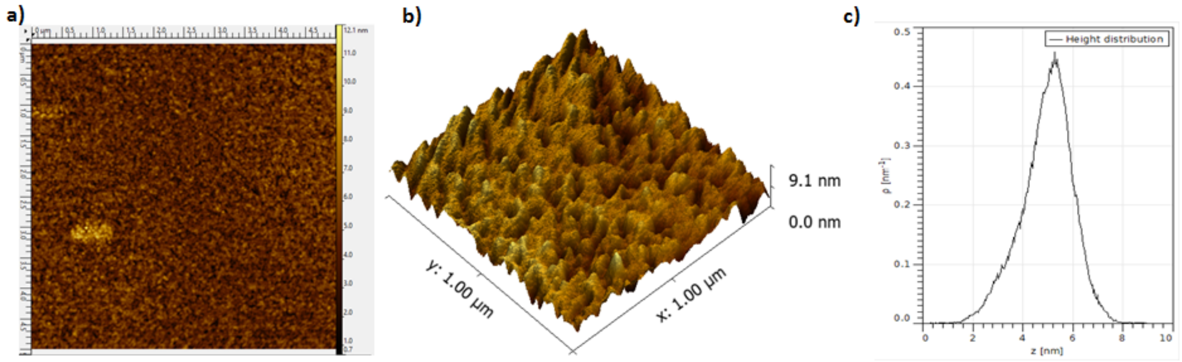

Figure 5.12: AFM images for Zn(7.25 Å)/Cr(1.45 Å)/Al_2O_3. a) 5×5 µm scale showing a homogeneous total coverage of the surface. b) 1×1 µm scale tilted representative image of the surface topography with a maximum peak to valley height of 9 nm. c) Histogram of the height distribution.

expected, oxidation of the buffer is therefore detrimental to zinc wetting.

5.2.2 Dynamics of Zn growth on Cr buffer

5.2.2.1 Spectra evolution: thick versus thin Cr deposits

An interesting aspect of the SDRS is the real time capability which allows to follow the evolution of particle morphology as the film grows. Figure 5.13 compares the temporal evolution of the spectra of the above described deposits. A global redshift of the resonance characteristic of particles flattening is observed for Zn(3.3 Å)/Cr(0.9 Å)/Al_2O_3 and for Zn(9.3 Å)/Cr(3.1 Å)/Al_2O_3. However, the position appears nearly constant over 2.7-3.3 Å and 1.7-4.3 Å for each sample (see arrows in figure) in line with a constant aspect ratio during the growth regime as demonstrated in the next section by signal integration. On the other hand, a puzzling phenomenon occurs for the 14 Å thick zinc film grown on 26 Å of Cr. The spectrum is nearly homothetical above 0.3 Å with a maximum at a constant energy position, indicating a constant aspect ratio all from the earliest stages of growth. This could be explained by a nearly "layer-by-layer" growth of zinc on flat-top, high-aspect ratio and large Cr particles (see figure 4.27).

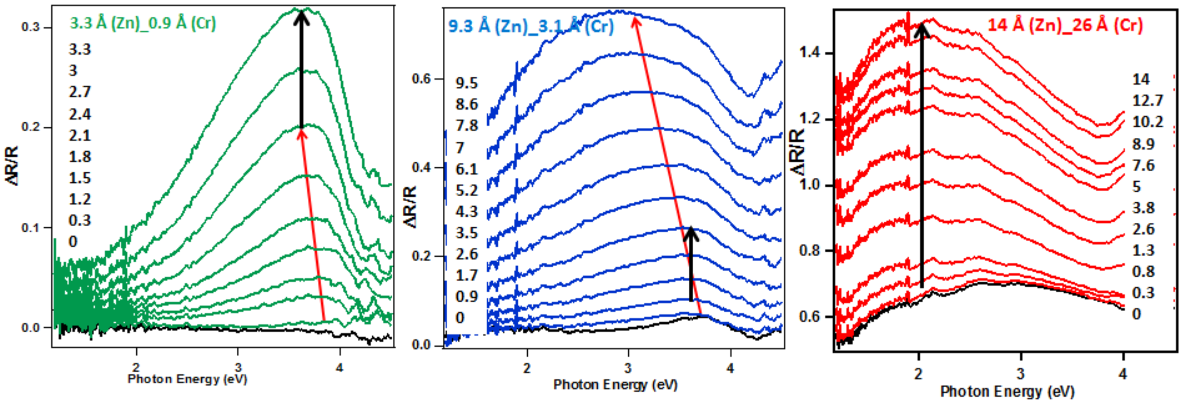

Figure 5.13: Evolution of SDRS spectra (polarization s) during the growth of 3.3, 9.3 and 14 Å of zinc on 0.9, 3.1 and 26 Å of chromium, respectively. Red and black arrows point at a redshift and a constant energy position respectively as the film thickens.

5.2.2.2 Following the growth phases: integration

As developed in section 3.3.3 and applied to the case of chromium alone on alumina (section 4.4.1), further insights about the growth process can be gained by the integrated SDRS signal in s-polarization $\mathcal{A}_s$ (equation 3.11). For a standard metal growth on alumina (see figure 3.3), this quantity is sensitive to the different onsets of growth regimes (nucleation, growth, coalescence) through changes of aspect ratio. However, as highlighted above, the Zn sticking coefficient and morphology are dictated by that of the Cr buffer layer. Therefore, as seen figure 5.14, Zn growth stops at the nucleation phase for the Zn(0.15 Å)/Cr(0.75 Å)/Al_2O_3 because the chemical reaction with hydroxyl groups, the metallic Cr particle density and/or surface coverage do not allow Zn particles to really grow and reach coalescence. At the opposite, a U-shape of the $\mathcal{A}_s$ curve typical for a Volmer-Weber 3D growth is observed for Zn(3.3 Å)/Cr(0.9 Å)/Al_2O_3 and Zn(9.3 Å)/Cr(3.1 Å)/Al_2O_3; but a higher $\mathcal{A}_s$ value is found for the larger Cr thickness in agreement with the formation of particles with larger aspect ratios. At last, the behavior of $\mathcal{A}_s$ for the thickest Cr buffer Zn(14 Å)/Cr(26 Å)/Al_2O_3; red curve in figure 5.14) is drastically different and typical of a continuous rough layer that smoothens while growing. Indeed, the parallel surface susceptibility of such a film of average thickness t is given by [Bedeaux and Vlieger, 2001]:

$$\gamma = (\epsilon_l - \epsilon_s)t - \sqrt{\pi}\frac{\epsilon_s + 1}{8\epsilon_s}(\epsilon_l - 1)^2\frac{h^2}{\xi} \tag{5.2}$$

where ϵ_s, ϵ_l are the dielectric functions of the layer and the substrate, h the layer roughness and ξ its height-height correlation length in a model of Gaussian height-height correlation function. Putting aside the surface susceptibility of the underlying Cr layer that acts only as an offset due to susceptibility additivity for thin film stack (see section 3.7.1), the quantity:

$$\mathcal{A}_s \propto \frac{1}{t} \int \frac{1}{\omega} \mathrm{Im}[\gamma(\omega)] d\omega \tag{5.3}$$

for such a film will follow the evolution of $h^2/t\xi$ and decay continuously towards a constant value (given by the first term in equation 5.2) if the film smoothens (*i.e.* if its roughness correlation length ξ increases and its roughness h decreases). In passing, all curves of figure 5.14 seem indeed to converge towards a common value, that given by the dielectric function of zinc. Finally, the comparison of the evolution of $\mathcal{A}_s$ for Cr/Al_2O_3 to that of Zn/Cr/Al_2O_3 (figure 5.15) demonstrates, that despite the lack of intense coalescence between Cr particles, Zn particles that grow on top enter the coalescence regime. This finding is in agreement with a much larger Zn average thickness than that of Cr (figure 5.3 and 5.15). Cr particles act as seeds for Zn particle growth, that most likely, flatten and encapsulate them as soon as enough metallic Cr is present.

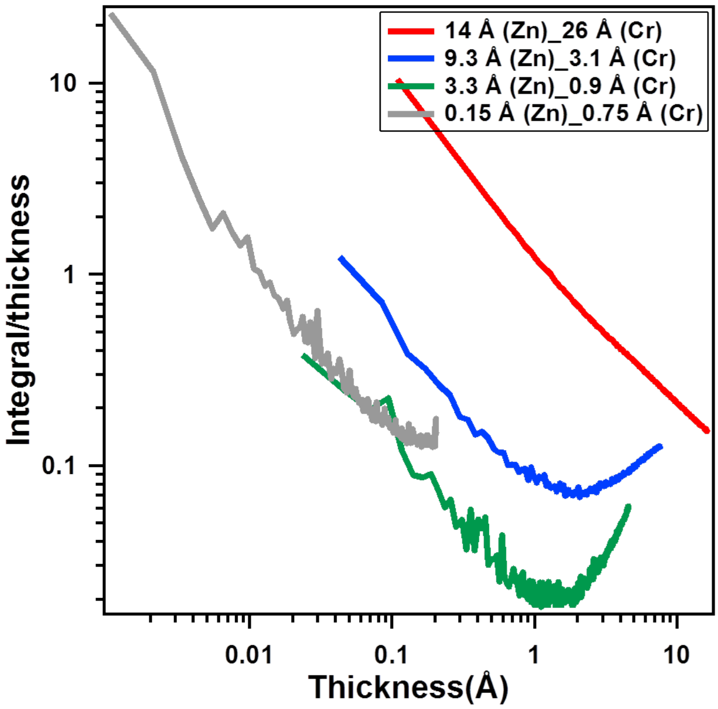

Figure 5.14: Evolution of the integrated SDRS signals $\mathcal{A}_s$ (s-polarization) for various Zn deposits on different Cr thicknesses as a function of thickness (log scale). $\mathcal{A}_s$ is normalized to thickness.

To conclude, figure 5.16 sums up schematically all the XPS and SDRS conclusions on the impact of the Cr buffer chemistry and morphology on the wetting of Zn.

5.3 Thermal stability of zinc films and chromium enhancement of desorption energy

Temperature Programmed Desorption (TPD) from 300 to 750 K at fixed heating rate of $\alpha = 0.33$ K.s^{-1} (see section 1.5.1 for experimental details) was used to explore the thermal stability of Zn films and the influence of a Cr buffer layer on the Zn desorption energy compared to previous results on bare alumina [Cavallotti, 2014a, Le et al., 2017b].

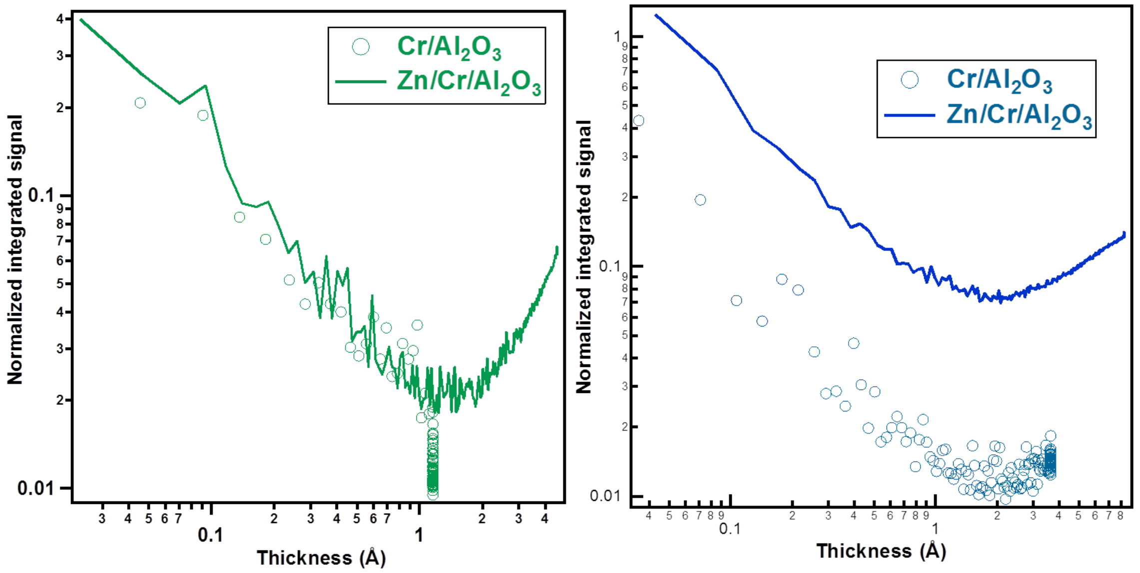

Figure 5.15: Comparison between the integrated signal for Zn/Cr/Al$_2$O$_3$ to that of Cr/Al$_2$O$_3$ for two final thicknesses of Cr: 0.9 Å (left) and 3.1 Å (right). The horizontal scale corresponds to Cr or Zn film thickness.

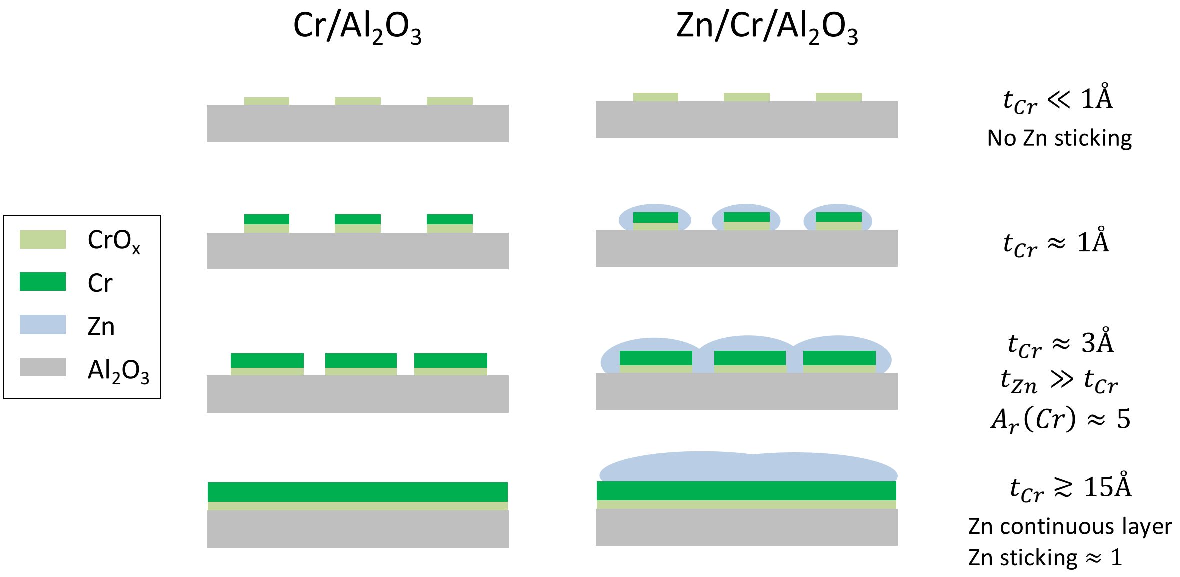

Figure 5.16: Schematic evolution of the Zn layer morphology as a function of Cr thickness.

5.3.1 The leading edge analysis of TPD lineshape

The straighforward analysis of TPD lineshape through the Polanyi-Wigner anszat of desorption rate r_d based on a quasi-equilibrium between adsorption and desorption [King, 1975,Ibach, 2006], namely:

$$r_d = -\frac{d\Theta}{dt} = \nu(\Theta)\Theta^{n(\Theta)} \exp\left[-\frac{E_a(\Theta)}{k_B T}\right], \tag{5.4}$$

is hampered by the dependence of the frequency prefactor $\nu(\Theta)$, the desorption order $n(\Theta)$ and the activation energy $E_a(\Theta)$ on coverage Θ of the desorbing species (or more generally on film thickness and morphology) that evolves during heating. However, at the onset of desorption, the coverage does not have yet changed significantly to impact drastically those factors. With a linear heating ramp of slope α and a suitable differential pumping of the mass spectrometer, the variation of the coverage is proportional to the detector ion current i_d corresponding to the mass of interest: $-\frac{d\Theta}{dT} \propto P \propto i_d$ (see section 1.5.2). Therefore, assuming constant ν, n and E_a values in the leading edge of desorption [Redhead, 1962, King, 1975, Falconer and Schwarz, 1983, de Jong and Niemantsverdriet, 1990, Franz et al., 1999], equation 5.4 can be recasted into:

$$i_d(T) \propto \left(\int_T^{\infty} i_d(T')dT' \right)^n \times \exp\left[-\frac{E_a}{k_B T} \right]. \tag{5.5}$$

By taking the logarithm of the previous equation, *i.e.*

$$\mathcal{I}_d(n,T) = \ln[i_d(T)] - n \ln \left[\int_T^{\infty} i_d(T')dT' \right] = \kappa - \frac{E_a}{k_B T}, \tag{5.6}$$

the quantity $\mathcal{I}_d(n,T)$ appears as a linear function of $1/T$ in an Arrhenius graph the slope of which is the activation energy E_a. The intercept is a complex function of n, ν, α and of the exact link between pressure and ion current. Therefore, a set of curves of $\mathcal{I}_d(n,T)$ drawn for different n values allows to see if it is possible to linearize the measured signal at best in the threshold of desorption.

5.3.2 TPD results and an example of data analysis

A series of desorption experiments have been performed on zinc films deposited on (1×1) and $(\sqrt{31} \times \sqrt{31}) \pm 9°$ alumina surfaces precovered by a chromium film. All thicknesses have been thoroughly determined by photoemission using the continuous film stack model by taking into account the damping of the substrate signal in the overlayers (see section 1.3.7). For each surface, Cr films of submonolayer (~ 0.8 Å), monolayer ($\sim 2-3$Å) and multilayer (> 12 Å) thickness have been deposited and the exposure to zinc flux was limited to reach a thickness of the order of one or two monolayers [1] to better see the actual impact of Cr on the Zn desorption energy and to avoid being dominated by desorption from "bulk" Zn. Thick Cr deposits were thoroughly oxidized by O_2 under the gas doser at a partial pressure of 2×10^{-6} mbar to form an oxide layer; the obtained films were exposed to a flux of Zn during more than 45 mins to reach a very low amount of condensed zinc (0.1-1 Å) thus confirming the very poor zinc condensation coefficient on an oxide surface as in the case of bare alumina [Cavallotti, 2014a, Le et al., 2017b].

Figure 5.17-a shows a series of TPD spectra of mass $m/e = 64$ characteristic of Zn^+; double ionization (Zn^{2+}) leads to the same lineshape at $m/e = 32$, therefore excluding any O_2 desorption. For all deposits, the desorption signal peaks between 470 and 570 K. The signals from all the other main isotopes of zinc ($m/e = 64, 66, 68$) have the same lineshape and their intensities follow the expected natural isotopic ratio (not shown). Neither noticeable ZnO ($m/e = 80$) nor Cr desorption ($m/e = 52$) were observed in all experiments showing the thermal stability of the Cr film as expected from its very low vapor pressure at such temperatures at the opposite to Zn ($p_{Zn} \sim 10^{-1}$ mbar, $p_{Cr} \ll 10^{-11}$ mbar at 700 K). This stability is

---

[1] Its is difficult to control precisely the amount of condensed zinc since its sticking coefficient (see section 5.1.2) strongly depends on the chromium coverage and changes from 0 on bare alumina to nearly 100 % on a continuous chromium film.

confirmed by any substantial change of the amount of Cr measured by XPS; the lack of change of the Cr 2p core level lineshape before and after desorption rules out any reaction between the substrate and the metal after heating. After desorption, substrates were completely free of Zn at the XPS sensitivity despite a sizeable photo-ionization cross section of the Zn 2p core level ($\frac{\sigma_{Zn\ 2p}}{\sigma_{C\ 1s}} \simeq 30$ [Yeh and Lindau, 1985]). Whatever the alumina surface, the desorption peak

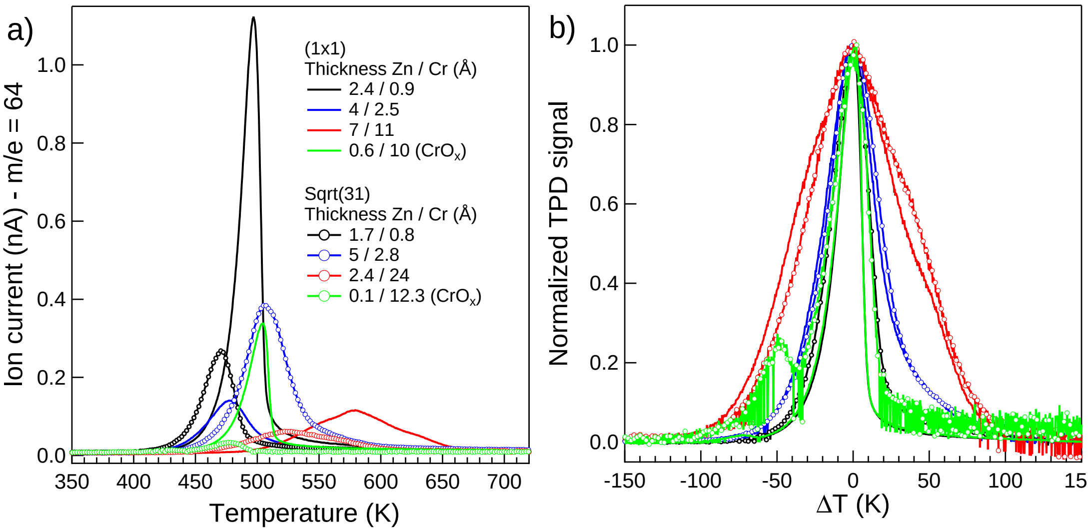

Figure 5.17: a) Raw desorption spectra of Zn ($m/e = 64$) from Cr covered (1×1) and $(\sqrt{31} \times \sqrt{31}) \pm 9°$ alumina surfaces. Film thicknesses are given in the figure. The heating rate is $\alpha = 0.33$ K.s^{-1}. b) Same spectra normalized to peak maximum and position.

(figure 5.17-a) broadens and shifts upwards in temperature upon increasing the Cr coverage. Strikingly, once normalized to maximum and position, desorption peaks from reconstructed and (1×1) surfaces overlap for a similar film thickness, thus demonstrating a similar Cr effect on all surfaces. For submonolayer Cr deposit, the lineshape closely resembles that on bare alumina (not shown). The greater the amount of Cr the broader and the more asymmetric the lineshape. For the largest Cr thickness (red curves in figure 5.17-b), multi-peak desorption is quite clear. The oxidized chromium films (green lines in figure 5.17-a) give rise to two desorption features; owing to the very small involved amount of Zn, the analysis was restricted to the most intense peak.

Prior to lineshape analysis, a background similar to the Shirley one commonly used in photoemission [Shirley, 1972] was subtracted to compensate from residual pressure increase in the quartz tube and to zero the tails of spectra at temperatures T_1 (before the peak) and T_2 (after the peak). In other words, the background signal $i_b(T)$ is assumed to be proportional to the integral of the signal up to a given temperature T; it reads:

$$i_b(T) = i_d(T_1) + [i_d(T_2) - i_d(T_1)] \frac{\int_{T_1}^{T} i_d(T')dT'}{\int_{T_1}^{T_2} i_d(T')dT'}. \tag{5.7}$$

An example of background subtraction is shown in figure 5.18. Then data have been quantitatively analyzed to obtain the apparent activation energy of desorption either through (i) the Redhead approach using the position of the maximum of the desorption peak and assuming an order of $n = 1$ or through (ii) the leading edge fit as explained above [Redhead, 1962, King,

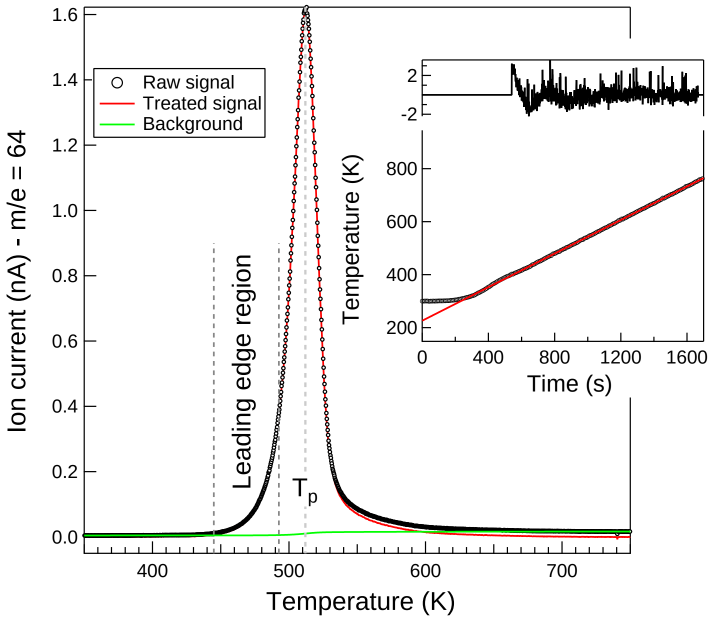

Figure 5.18: Example of TPD spectrum analysis. Data correspond to 15 Å of Zn on 3 Å of Cr on a (1×1) alumina surface. Raw (circles) and background subtracted (red line) spectra are compared. Vertical dotted lines pinpoint the leading edge region and the peak position T_p used in data analysis. As shown in the inset, the linear fit of the measured temperature allows to get rid of the electronic noise on temperature reading.

1975, Falconer and Schwarz, 1983, de Jong and Niemantsverdriet, 1990, Franz et al., 1999]. A series of plots of $\mathcal{I}_d(n,T)$ for various values of desorption order n (figure 5.19) show that the signal cannot be linearized over the whole range of temperature as expected from coverage dependent desorption parameters. However, it allows to identify the leading edge range where it is linear at best. It corresponds to a variation of the zinc coverage between -1 % and -30 %; below the signal is limited by noise, while above the values of the parameters of equation 5.4 can no longer be assumed to be constant (see figure 5.19).

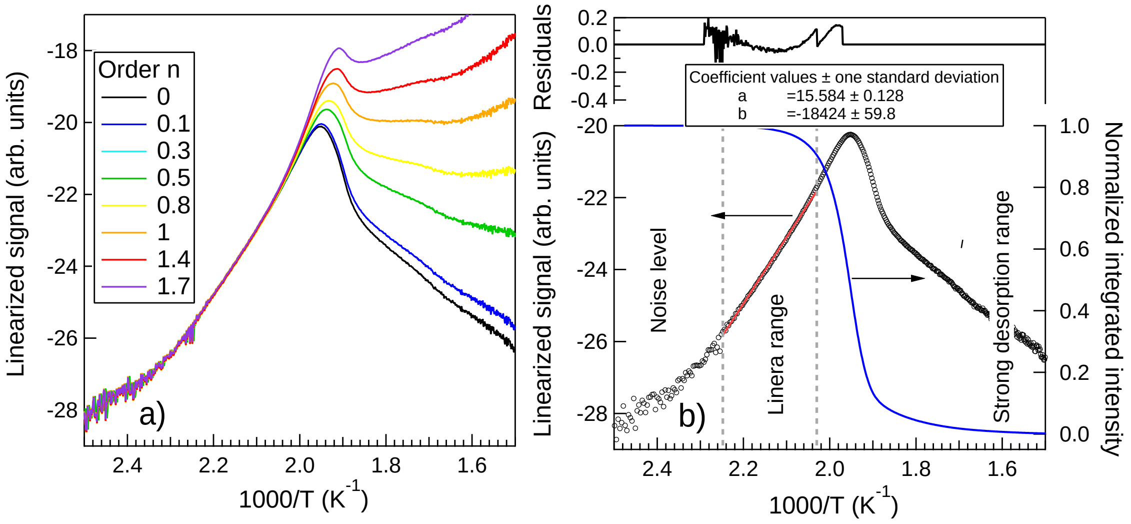

Figure 5.19: a) Linearized desorption spectra $\mathcal{I}_d(n,T)$ for desorption orders n indicated in figure. b) Linear fit (red line) of $\mathcal{I}_d(0,T)$ in the leading edge region in an Arrhenius graph (left scale). The evolution of the integrated signal is plotted on the right scale (blue line). The spectrum corresponds to that of figure 5.18 where the fit region is indicated by dotted lines.

5.3.3 Effect of Cr on the activation energy and the order of desorption

Activation energies deduced by both methods are plotted in figure 5.20 and figure 5.21 as function of Cr and Zn film thickness respectively. Data are compared to the results of the thesis of R. Cavallotti [Cavallotti, 2014a,Le et al., 2017b] obtained on (1×1) and reconstructed surfaces after zinc condensation at 100 K. Including the measurement noise, the actual signal linearity and the reliability of the thermal contact between the insulating alumina and the heated back plate ($\Delta T \sim 50$ K) , the error bar in the determination of E_a remains always well below 1 %. The main fluctuation on data points comes from the reproducibility of initial coverages and morphologies.

The results of figures. 5.20-5.21 call for different comments:

- the Redhead method overestimates the activation energy of desorption on bare substrate (red points) which, in a picture of quasi-equilibrium between adsorption and desorption, should not be greater than the bulk cohesive energy of zinc $E_{coh}(Zn) = 1.35$ eV.atom^{-1} [webelements,]. Indeed, at the opposite of the underlying $n = 1$ Redhead hypothesis, the desorption order obtained is closer to zero for all deposits, except for the thickest Cr deposits for which n is closer to 2 and the desorption lineshape is much broader and multi-peaked (red curves in figure 5.17).

- focusing only on the leading edge results (figures. 5.20-a,5.21-a), the chromium buffer layer increases noticeably the desorption energy well above that of uncovered surfaces, up to values larger than $E_{coh}(Zn)$. Since desorption happens from undercoordinated sites, an estimate of the desorption energy in the simple picture of broken bonds are given by $9/12E_{coh}(Zn)$ for a Zn atom in a (0001) plane, $7/12E_{coh}(Zn)$ for a Zn atom in a $[10\bar{1}0]$ step on a (0001) surface and $4/12E_{coh}(Zn)$ for a kink atom; indeed, the coordination 12 of hexagonal compact Zn is reduced to 9,7 and 4 for surface, step and kink configurations. If experimental values of E_a are close to $7/12 - 9/12E_{coh}(Zn)$ on bare surfaces, larger values are found on Cr pre-covered surfaces showing the important role of Zn-Cr bonds in the enhancement of E_a.

- while the presence of hydroxyl groups were found to increase the desorption energy through an activated reaction process on bare surfaces [Cavallotti, 2014a, Le et al., 2017b] (open vs filled red symbols in figure 5.20-a), chromium buffer seems to erase the difference between reconstructed-dry and (1×1) surfaces and even to reverse the hierarchy in particular for the lowest amount of chromium; the explanation could lie in the consumption of metallic chromium by residual hydroxyl groups on the (1×1) surface to produce oxidized chromium at the opposite to the dry reconstructed surface.

- the observed change of desorption order and lineshape by increasing the Cr thickness points at different desorption mechanism when enough metallic chromium is present. Alloying is a likely explanation. Indeed, Zn-rich Zn_xCr_y compounds are present in the bulk phase diagram below 700 K (figure 5.22-left). Similar conclusions were reached during desorption from Zn deposits on Ag, Cu, Ni, Rh, Rh, Pt, Pd single crystals [Kourouklis and Nix, 1994,Rodriguez et al., 1996,Rodriguez, 1996,Jeroro et al., 2007,Ho et al., 2013]; high temperature peaks were usually assigned to Zn interacting with the metallic substrate. The desorption temperature of Zn and the strength of the interaction with the metal was found to be correlated to the fraction of empty states in electronic structure of the metallic substrate (figure 5.22).

- the results on chromium oxide films seem counter-intuitive (green symbols in figure 5.20). While the sticking coefficient is very low on such surfaces, E_a is sizeable, probably because of a strong interaction with defects in the oxide films. A similar behavior was also observed with ZnO films on alumina [Cavallotti, 2014a].

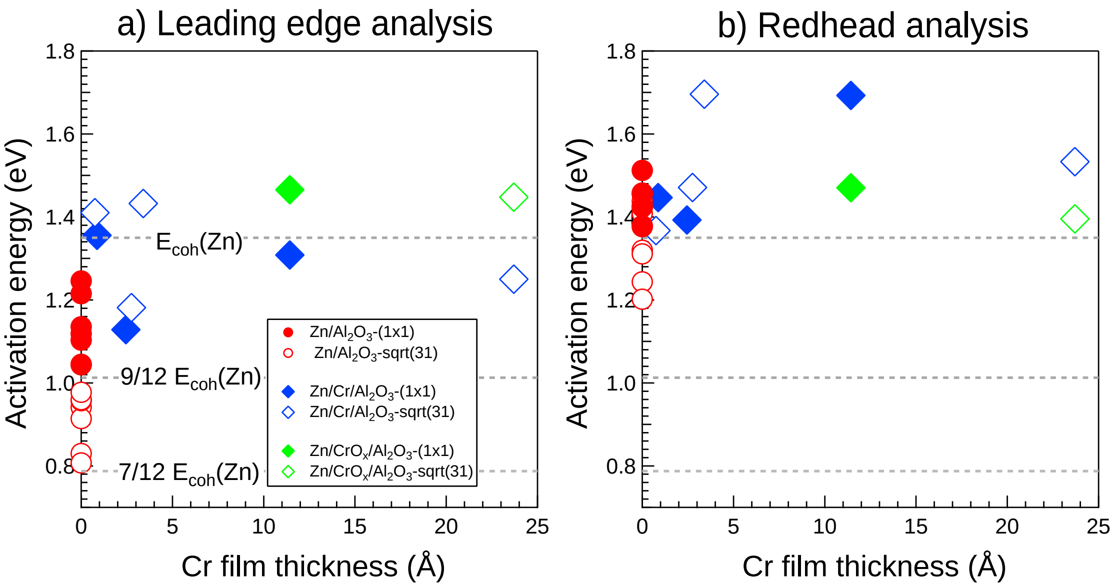

Figure 5.20: Plot of the activation energy of desorption as deduced from a) the leading edge analysis and b) the Redhead method of maximum position for different chromium film thicknesses and substrates as indicated in the figure. Data are compared to the bare surface [Cavallotti, 2014a, Le et al., 2017b] and the cohesive energy of zinc (dotted lines; see text).

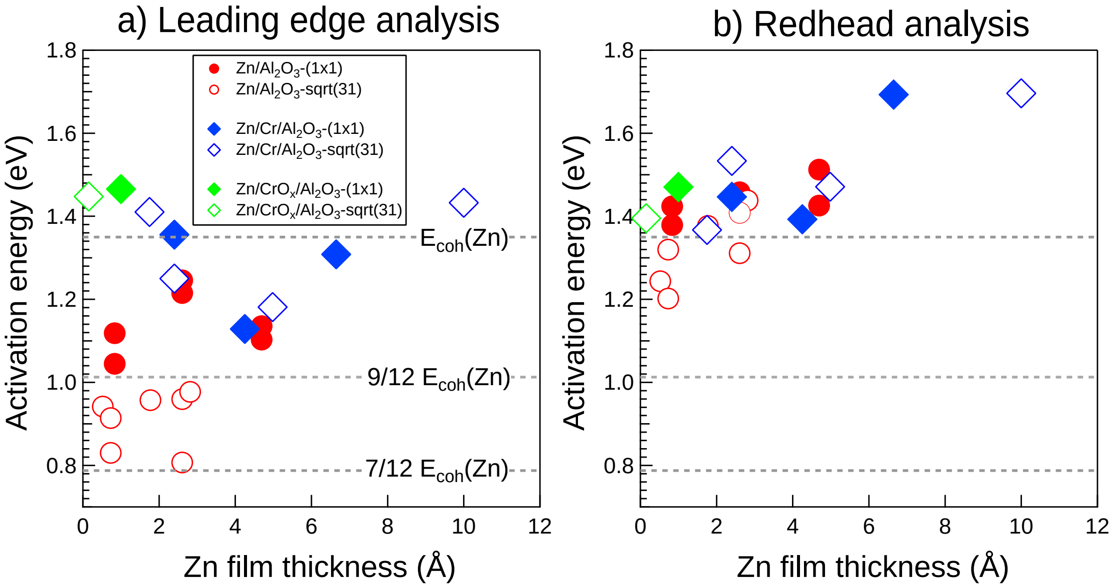

Figure 5.21: Same as figure 5.20 but as a function of zinc film thickness.

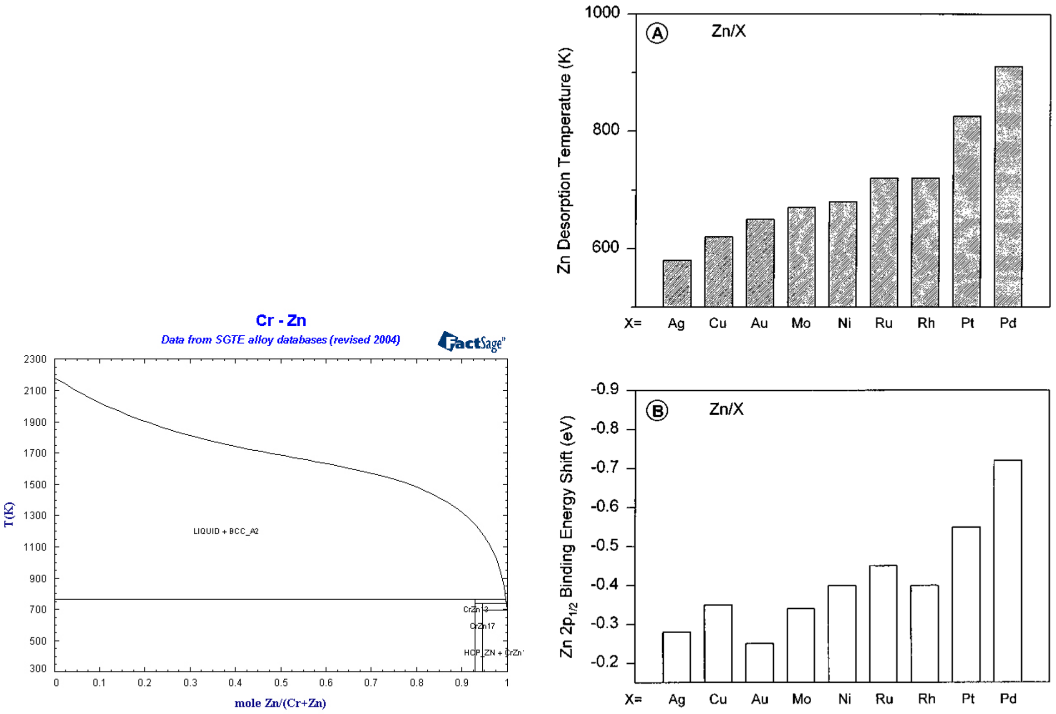

Figure 5.22: (Left) Bulk phase diagram of Zn-Cr system from the chemical thermodynamics FactSage database [factsageweb,]. (Right) Zn desorption temperatures for a monolayer of Zn supported on several metal substrates and difference in Zn $2p_{1/2}$ binding energy between 1 ML of supported Zn and the bulk atoms of metallic Zn as a function of metal substrate [Rodriguez et al., 1996].

5.4 Conclusion

Chromium intermediate buffer layer dramatically modifies the behavior of zinc/alumina interface in terms of sticking, morphology and thermal stability. While condensation could be achieved only at low temperatures on bare alumina [Cavallotti, 2014a], the sticking coefficient of Zn at room temperature increases non-linearly with the thickness of Cr underneath until reaching a value close to one on a percolated thick Cr film. Sticking remains poor on chromium oxidized on purpose or through hydroxyl groups. From photoemission fingerprints, zinc exhibits a metallic character at all Cr coverages, except for the thick Cr_2O_3 film (15.4 Å) where partially oxidized Zn is evidenced. Plasmonics (figure 5.16) shows a close dependence between the wetting behavior of Zn and the underlying Cr. Earlier coalescence of Zn particles, due probably to Cr particle encapsulation by Zn, is promoted by the Cr particle flattening; on thick buffers, the growth of a continuous rough film that smoothens with thickness is observed. In addition, desorption experiments on monolayer deposits pinpointed a noticeable increase of Zn desorption energy due to the Cr layer, well above that of the uncovered surface and of the value expected from Zn cohesion energy. No sizable difference between reconstructed and (1×1) surfaces was observed as the enhancement of the desorption energy is related to strong metallic Zn-Cr bonds. The consumption of OH groups by oxidation of Cr prevents thus any subsequent activated reaction between Zn and hydroxyl groups as observed on the bare surface. The multi-peak desorption on thick metallic Cr films suggests the formation of an alloy during heating as already pointed out in the literature for other metals. Beyond a very low sticking coefficient and in agreement with Zn oxidation, very high desorption energies found on oxidized chromium buffers in a similar way to Zn/ZnO/Al_2O_3 point at a strong interaction with defect sites.

CONCLUSION AND PERSPECTIVES

This thesis falls in the industrial context of galvanization of highly-alloyed new generations of steel grades. Despite the reductive atmosphere of the used furnaces, the recrystallization annealing of steel strips induces the detrimental segregation of oxides of the alloying elements at the steel surface that impedes the adhesion of the anti-corrosive zinc coating. A potential way to overcome this issue is based on the use of metallic buffer layers at the zinc/oxide interface, in particular in the framework of the development of factories based on jet-vapor deposition of zinc under vacuum. The understanding of their role is at the heart of this thesis. But instead of tackling the question on the "material science" side on complex steel samples, a more model "surface science" approach was developed during this work. Owing to the importance of aluminum-based steel, our choice focused on alumina as a model oxide in the form of single crystals of corumdum type. Despite the favored formation of γ-alumina at the steel surface, previous works based on electrostatic arguments and *ab initio* calculations [Cavallotti, 2014a, Cavallotti et al., 2014, Cavallotti et al., 2016, Le et al., 2017b] pointed at the relevance of α-Al_2O_3(0001) surface as a model system to mimic the industrial layers. Regarding the buffer, chromium was selected as simulations demonstrated the positive influence of this transition metal on the adhesion of zinc at the surface of alumina; in fact among the candidates, Cr and Ti were found as the best ones [Le et al., 2016, Le et al., 2017a] due to both strong metal-alumina and metal-zinc bonds.

The present study was split into two parts, the first dealing with Cr/Al_2O_3 interface and the second one with the actual buffer effect in the case of Zn/Cr/Al_2O_3. As a matter of fact, the investigation of the buffer/alumina interface was essential for understanding the latter. Complementary experimental techniques were combined to examine the chemistry, the growth mode, the wetting, the structure and the thermal stability of those interfaces. The chemistry of the films was mainly studied by X-ray photoemission spectroscopy which turned out to be also a key technique in terms of quantification. Additional chemical but also structural information was brought by extended X-ray absorption fine structure spectroscopy supported by density functional calculations, essentially for the determination of the Cr adatom adsorption site. On an other side, the growth and morphology evolution of particles were followed during deposition using surface differential reflectivity spectroscopy supplemented by dielectric simulations to access information about growth process and wetting. Finally, the enhancement of zinc adsorption energy induced by chromium was highlighted by thermal desorption.

In a first part, photoemission from O 1s, Cr 2p and Al 2s core levels suggested the early stage oxidation of chromium at contact with the bare alumina surface. Starting by excluding any reduction of alumina and then by making a comparison with chromium deposits on deliberately hydroxylated surfaces, the origin of this oxidation was assigned to a reaction with residual hydroxyl groups that are still present at the alumina surface despite high temperature annealing. This findings was further confirmed thanks to EXAFS measurements at the Cr K-edge that showed an excess of oxygen in the chromium environment in the monolayer thickness range and a puzzling similarity with Cr_2O_3. The Cr-O distance was screened by DFT calculations for different Cr/Al_2O_3 interface configurations leading to different chromium oxidation states. Going from bare alumina to various H_mO_n and oxygen-rich configurations, the theoretical distance that agreed the best with the experimental findings corresponded to Cr oxidized to a 3+ state upon a reaction with OH^- groups. Above this oxidized interface, as seen by SDRS and AFM, chromium grows with a sticking coefficient close to one through a Volmer-Weber growth mode, but in the form of high aspect ratio metallic particles that percolate quickly to form a continuous film. This good wetting is likely to be of kinetic type due to the low vapor pressure and mobility of chromium. Finally, a non-epitaxial growth was evidenced by RHEED and assigned to the presence of an disordered oxidized interface.

In a second part, the effect of the chromium buffer on growth and wetting behavior of zinc was proved to be positive. Beyond the striking enhancement of the sticking coefficient of zinc on alumina at ambient temperature, a non-linear increase as a function of chromium coverage was evidenced with an overall metallic zinc fingerprint. Compared to the non-sticking zinc on bare alumina and on intentionally oxidized chromium layer, the introduction of a buffer even at the submonolyaer range solves the first problem of sticking provided that it is metallic. Concerning wetting, SDRS results showed a close relationship between the behavior of zinc and that of the underlying chromium. For intermediate coverages, a much earlier percolation of zinc with respect to chromium particles underneath was evidenced in line with a likely encapsulation of the latter by the former. On top of thicker multilayer buffer, zinc forms a continuous rough film that smoothens as the thickness increases. The importance of the strong Zn-Cr metallic bonds was further evidenced by thermal desorption experiments showing an enhanced desorption energy compared to uncovered alumina and a strong similarity between (1×1) and OH-free reconstructed surfaces. Owing to the presence of multiple desorption peaks, an alloy likely forms during heating of thick chromium buffers. In the case of oxidized chromium, in parallel to a very low sticking coefficient, very high desorption energies were measured indicating a strong interaction of oxidized zinc with defect sites in a similar manner to ZnO/Al_2O_3.

Aside from the results on $Zn/Cr/Al_2O_3$, an attempt to understand the optical response of Cr and Zn nanoparticles was carried out. The theoretical decomposition of reflectivity spectra on the basis of polarization eigenmodes, although complicated, led to the conclusion that the response is dominated by a strongly damped dipole-like absorption mode with a strong impact of interband transitions. In addition, a first analytic approach of the electrostatic screening of a dipole by a continuous film has been developed. Image corrections have been scrutinized for an isolated dipole and a lattice of dipoles in the case of a metal film on a dielectric substrate and vice-versa; an effective dielectric function was also proposed to account for the film induced screening at dipolar level. This approach is a first step towards the calculation of the actual polarizability of a film-supported nanoparticle which is the key quantity in its optical response.

Although this study clarified some aspects of buffer effect on metallic layer wetting at the alumina surface, some questions remain open and could lead to interesting directions of research:

- on a fundamental point of view, what is the nature of those residual hydroxyl groups? If the reaction with transition metals prooves their existence, their exact configuration remains unknown. Does other transition metals like titanium occupy the same adsorption site as chromium ? In line with that, what is the behavior of chromium at the reconstructed surface that is assumed to be dry ?
- are the above findings on α-Al_2O_3(0001) really relevant for γ-alumina film ? At least, the local environment seen by EXAFS seems the same for the first step of chromium adsorption.
- is the apparent good wetting of chromium on alumina due to kinetics ? Is there any role played by the interfacial oxidized layer as already suggested in the litterature [Chambers et al., 2002] ? Growth experiments in temperature could be quite indicative in this respect.
- what is the actual growth mode of Zn on top of Cr particles ? Can more real space imaging help revealing the suspected encapsulation process ?
- what is the weak interface in terms of adhesion energy ? Does chromium allow really to switch from interfacial to cohesive cleavage ? Mechanical tests could give an hint on this question.
- what is the impact of the atmosphere on the buffer effect ?

BIBLIOGRAPHY

[Ahn and Rabalais, 1997] Ahn, J. and Rabalais, J. (1997). Composition and structure of the Al_2O_3 {0001}-(1× 1) surface. *Surface Science*, 388(1-3):121–131.

[Aksela et al., 1974] Aksela, S., Väyrynen, J., and Aksela, H. (1974). High-resolution $L_{2,3}M_{4,5}M_{4,5}$ auger spectrum of free zinc atoms. *Physical Review Letters*, 33:999–1002.

[Albella et al., 2011] Albella, P., Garcia-Cueto, B., Gonzalez, F., Moreno, F., Wu, P. C., Kim, T. H., Brown, A., Yang, Y., Everitt, H. O., and Videen, G. (2011). Shape matters: plasmonic nanoparticle shape enhances interaction with dielectric substrate. *Nano Letters*, 11:3531–3537.

[Alemany et al., 1993] Alemany, P., Boorse, R. S., Burlitch, J. M., and Hoffmann, R. (1993). Metal-ceramic adhesion: quantum mechanical modeling of transition metal-alumina interfaces. *Journal of Physical Chemistry*, 97(32):8464–8475.

[Anders et al., 2006] Anders, A., Byon, E., Kim, D.-H., Fukuda, K., and Lim, S. H. (2006). Smoothing of ultrathin silver films by transition metal seeding. *Solid State Communications*, 140(5):225–229.

[Anisimov et al., 1997] Anisimov, V. I., Aryasetiawan, F., and Lichtenstein, A. (1997). First-principles calculations of the electronic structure and spectra of strongly correlated systems: the LDA+U method. *Journal of Physics: Condensed Matter*, 9(4):767.

[Antonides et al., 1977a] Antonides, E., Janse, E., and Sawatzky, G. (1977a). LMM Auger spectra of Cu, Zn, Ga, and Ge. I. Transition probabilities, term splittings, and effective Coulomb interaction. *Physical Review B*, 15(4):1669.

[Antonides et al., 1977b] Antonides, E., Janse, E., and Sawatzky, G. (1977b). LMM Auger spectra of Cu, Zn, Ga, and Ge, II. Relationship with the L_{23} photoelectron spectra via the $L_2L_3M_{45}$ Coster-Kronig process. *Physical Review B*, 15:4596.

[Aronniemi et al., 2005] Aronniemi, M., Sainio, J., and Lahtinen, J. (2005). Chemical state quantification of iron and chromium oxides using XPS: the effect of the background subtraction method. *Surface Science*, 578(1-3):108–123.

[Aubry et al., 2011] Aubry, A., Lei, D. Y., Maier, S. A., and Pendry, J. B. (2011). Plasmonic hybridization between nanowires and a metallic surface: a transformation optics approach. *ACS Nano*, 5:3293–3308.

[Bader, 1991] Bader, R. F. (1991). A quantum theory of molecular structure and its applications. *Chemical Reviews*, 91(5):893–928.

[Barrera and Duke, 1976] Barrera, R. and Duke, C. (1976). Dielectric continuum theory of the electronic structure of interfaces. *Physical Review B*, 13(10):4477.

[Barth and Reichling, 2001] Barth, C. and Reichling, M. (2001). Imaging the atomic arrangements on the high-temperature reconstructed α-Al_2O_3(0001) surface. *Nature*, 414(6859):54.

[Batyrev et al., 1999] Batyrev, I., Alavi, A., and Finnis, M. W. (1999). *Ab initio* calculations on the Al_2O_3(0001) surface. *Faraday Discussions*, 114:33–43.

[Batyrev and Kleinman, 2001] Batyrev, I. G. and Kleinman, L. (2001). In-plane relaxation of Cu(111) and Al(111)/α- Al_2O_3(0001) interfaces. *Physical Review B*, 64(3):033410.

[Bauer, 1958] Bauer, E. (1958). Phenomenological theory of crystal deposition on surfaces. *Journal of Crystallographic Crystalline Materials*, 110(1-6):395–431.

[Bedeaux and Vlieger, 1973] Bedeaux, D. and Vlieger, J. (1973). A phenomenological theory of the dielectric properties of thin films. *Physica*, 67(1):55–73.

[Bedeaux and Vlieger, 1974] Bedeaux, D. and Vlieger, J. (1974). A statistical theory of the dielectric properties of thin island films: I. The surface material coefficients. *Physica*, 73(2):287–311.

[Bedeaux and Vlieger, 1983] Bedeaux, D. and Vlieger, J. (1983). A statistical theory for the dielectric properties of thin island films: application and comparison with experimental results. *Thin Solid Films*, 102(3):265–281.

[Bedeaux and Vlieger, 2001] Bedeaux, D. and Vlieger, J. (2001). *Optical Properties of Surfaces.* Imperial College Press, London.

[Beitia et al., 1999] Beitia, C., Borensztein, Y., Lazzari, R., Nieto, J., and Barrera, R. (1999). Substrate-induced multipolar resonances in supported free-electron metal spheres. *Physical Review B*, 60(8):6018.

[Bernath et al., 1998] Bernath, S., Wagner, T., Hofmann, S., and Rühle, M. (1998). Interface formation between ultrathin films of titanium and (0001) sapphire substrates. *Surface Science*, 400(1-3):335–344.

[Biesinger et al., 2004] Biesinger, M., Brown, C., Mycroft, J., Davidson, R., and McIntyre, N. (2004). X-ray photoelectron spectroscopy studies of chromium compounds. *Surface and Interface Analysis*, 36(12):1550–1563.

[Blöchl, 1994] Blöchl, P. E. (1994). Projector augmented-wave method. *Physical Review B*, 50(24):17953.

[Bogicevic and Jennison, 1999] Bogicevic, A. and Jennison, D. R. (1999). Role of surface vacancies and water products in metal nucleation: Pt/MgO(100). *Surface Science*, 437(1-2):L741–L747.

[Bohren and Huffman, 1983] Bohren, C. F. and Huffman, D. R. (1983). *Absorption and Scattering of Light by Small Particles.* John Wiley & Sons, New York.

[Bos and Lynch, 1970] Bos, L. W. and Lynch, D. W. (1970). Optical properties of antiferromagnetic chromium and dilute Cr-Mn and Cr-Re alloys. *Physical Review B*, 2:4567–4577.

[Brandes and Brook, 1983] Brandes, E. A. and Brook, G. (1983). *Smithells metals reference book*. Elsevier.

[Briggs and Seah, 1983] Briggs, D. and Seah, M. P. (1983). *Practical surface analysis by Auger and X-ray Photoelectron Spectroscopy*. John Wiley & Sons, New York.

[Brjega and Popescu-Pogrion, 1989] Brjega, M. I. and Popescu-Pogrion, N. (1989). On the relations between the δ-Cr and α-Cr phases. *Thin Solid Films*, 171:33–41.

[Bruggeman, 1935] Bruggeman, D. (1935). Berechnung verschiedener physikalischer konstanten von heterogenen substanzen. i. dielektrizittskonstanten und leitfhigkeiten der mischkrper aus isotropen substanzen. *Ann.der. Phys.*, 24:636–664.

[Campbell and Valone, 1985] Campbell, C. and Valone, S. (1985). Design consideration for simple gas dosers in surface science application. *J. Vac. Sci. Technol. A*, 3:408–411.

[Campbell, 1997] Campbell, C. T. (1997). Ultrathin metal films and particles on oxide surfaces: structural, electronic and chemisorptive properties. *Surface Science Reports*, 27(1-3):1–111.

[Cappus et al., 1993] Cappus, D., Xu, C., Ehrlich, D., Dillmann, B., Ventrice Jr, C., Al Shamery, K., Kuhlenbeck, H., and Freund, H.-J. (1993). Hydroxyl groups on oxide surfaces: NiO(100), NiO(111) and Cr_2O_3(111). *Chemical Physics*, 177(2):533–546.

[CasaXPS,] CasaXPS. `http://www.casaxps.com/help_manual/manual_updates/peak_fitting_in_xps.pdf`.

[Causa et al., 1989] Causa, M., Dovesi, R., Pisani, C., and Roetti, C. (1989). *Ab initio* characterization of the (0001) and (1010) crystal faces of α-alumina. *Surface Science*, 215(1-2):259–271.

[Cavallotti, 2014a] Cavallotti, R. (2014a). *Effets de la Terminaison de l'α-Alumine (0001) sur le Comportement au Mouillage du Zinc*. PhD thesis, Ph. D. thesis, Universiteé Pierre et Marie Curie (UPMC), Paris, France.

[Cavallotti, 2014b] Cavallotti, R. (2014b). *Effets de la terminaison de lα-alumine sur le comportement au mouillage du zinc*. PhD thesis, Université Pierre et Marie Curie-Paris VI.

[Cavallotti et al., 2014] Cavallotti, R., Goniakowski, J., Lazzari, R., Jupille, J., Koltsov, A., and Loison, D. (2014). Role of surface hydroxyl groups on zinc adsorption characteristics on α-Al_2O_3(0001) surfaces: First-principles study. *The Journal of Physical Chemistry C*, 118(25):13578–13589.

[Cavallotti et al., 2016] Cavallotti, R., Le, H.-L. T., Goniakowski, J., Lazzari, R., Jupille, J., Koltsov, A., and Loison, D. (2016). New routes for improving adhesion at the metal/α-Al_2O_3(0001) interface. *Physical Chemistry Chemical Physics*, 18(4):3032–3039.

[Chambers et al., 2002] Chambers, S. A., Droubay, T., Jennison, D. R., and Mattsson, T. (2002). Laminar growth of ultrathin metal films on metal oxides: Co on hydroxylated α-Al_2O_3(0001). *Science*, 297(5582):827–831.

[Chang, 1971] Chang, C. C. (1971). Auger electron spectroscopy. *Surface Science*, 25(1):53–79.

[Chatain et al., 1988] Chatain, D., Coudurier, L., and Eustathopoulos, N. (1988). Wetting and interfacial bonding in ionocovalent oxide-liquid metal systems. *Revue De Physique Appliquee*, 23(6):1055–1064.

[Chen et al., 2011] Chen, H., Shao, L., Ming, T., Woo, K. T., Man, Y. C., Wang, J., and Lin, H. Q. (2011). Observation of the Fano resonance in gold nanorods supported on high-dielectric-constant substrates. *ACS Nano*, 5:6754–6763.

[Chernysheva et al., 2018] Chernysheva, E., Srour, W., Philippe, B., Baris, B., Chenot, S., Duarte, R. F., Gorgoi, M., Cruguel, H., Rensmo, H., Montigaud, H., Jupille, J., Cabailh, G., Grachev, S., and Lazzari, R. (2018). Band alignment at Ag/ZnO(0001) interfaces: a combined soft and hard X-ray photoemission study. *Physical Review B*, 97:235430.

[Chu et al., 1997] Chu, J. P., Chang, J. W., and Lee, P. Y. (1997). Phase transformation of A15 crystal structure chromium thin films grown by the sputter deposition. *Materials Chemistry and Physics*, 50(1):31 – 36.

[Chu et al., 1998] Chu, J. P., Chang, J. W., Lee, P. Y., Wu, J. K., and Wang, J. Y. (1998). On the formation of nonequilibrium A15 crystal structure chromium thin films by sputter deposition. *Thin Solid Films*, 312(1):78 – 85.

[Coustet and Jupille, 1997] Coustet, V. and Jupille, J. (1997). Hydroxyl groups on oxide surfaces. *Il Nuovo Cimento D*, 19(11):1657–1664.

[Cuccureddu et al., 2010] Cuccureddu, F., Murphy, S., Shvets, I., Porcu, M., Zandbergen, H., Sidorov, N., and Bozhko, S. (2010). Surface morphology of c-plane sapphire (α-alumina) produced by high temperature anneal. *Surface Science*, 604(15-16):1294–1299.

[de Jong and Niemantsverdriet, 1990] de Jong, A. M. and Niemantsverdriet, J. W. (1990). Themal desorption analysis: comparative test of ten commonly applied procedures. *Surface Science*, 233:355–365.

[Dehm et al., 1997] Dehm, G., Scheu, C., Möbus, G., Brydson, R., and Rühle, M. (1997). Synthesis of analytical and high-resolution transmission electron microscopy to determine the interface structure of Cu/Al_2O_3. *Ultramicroscopy*, 67(1-4):207–217.

[Dehm et al., 1998] Dehm, G., Scheu, C., Rühle, M., and Raj, R. (1998). Growth and structure of internal Cu/Al_2O_3 and Cu/Ti/Al_2O_3 interfaces. *Acta Materialia*, 46(3):759–772.

[Di Castro and Polzonetti, 1987] Di Castro, V. and Polzonetti, G. (1987). A photoemission study of the Cu/MnO interface. *Chemical Physics Letters*, 139(2):215–218.

[Di Castro et al., 1985] Di Castro, V., Polzonetti, G., and Zanoni, R. (1985). Photoemission study of two model catalysts using synchrotron radiation. *Surface Science*, 162(1-3):348–353.

[Di Felice and Northrup, 1999] Di Felice, R. and Northrup, J. E. (1999). Theory of the clean and hydrogenated $Al_2O_3(0001)$-(1×1) surfaces. *Physical Review B*, 60(24):R16287.

[Didier and Jupille, 1994] Didier, F. and Jupille, J. (1994). The van der Waals contribution to the adhesion energy at metal-oxide interfaces. *Surface Science*, 314(3):378–384.

[Didier and Jupille, 1996] Didier, F. and Jupille, J. (1996). Contribution of the van der Waals forces to the work of adhesion at metal/oxide interfaces. *Journal of Adhesion Science and Technology*, 10(4):373–382.

[Digne et al., 2006] Digne, M., Raybaud, P., Sautet, P., Rebours, B., and Toulhoat, H. (2006). Comment on examination of spinel and nonspinel structural models for γ-Al_2O_3 by dft and rietveld refinement simulations. *The Journal of Physical Chemistry B*, 110(41):20719–20720.

[Digne et al., 2004] Digne, M., Sautet, P., Raybaud, P., Euzen, P., and Toulhoat, H. (2004). Use of DFT to achieve a rational understanding of acid-basic properties of γ-alumina surfaces. *Journal of Catalysis*, 226(1):54–68.

[Dion et al., 2004] Dion, M., Rydberg, H., Schröder, E., Langreth, D. C., and Lundqvist, B. I. (2004). Van der Waals density functional for general geometries. *Physical Review Letters*, 92(24):246401.

[Dmitriev et al., 2008] Dmitriev, A., Hägglund, C., Chen, S., Fredriksson, H., Pakizeh, T., Käll, M., and Sutherland, D. (2008). Enhanced nanoplasmonic optical sensors with reduced substrate effect. *Nano Letters*, 8:13893–3898.

[Doniach and Sunjic, 1970] Doniach, S. and Sunjic, M. (1970). Many-electron singularity in X-ray photoemission and X-ray line spectra from metals. *Journal of Physics C: Solid State Physics*, 3(2):285.

[Drillet et al., 2004] Drillet, P., Zermout, Z., Bouleau, D., Mataigne, J., and Claessens, S. (2004). Selective oxidation of high Si, Mn and Al steel grades during recrystallization annealing and steel/Zn reactivity. *Revue de Métallurgie–International Journal of Metallurgy*, 101(10):831–837.

[Dudarev et al., 1998] Dudarev, S., Botton, G., Savrasov, S., Humphreys, C., and Sutton, A. (1998). Electron-energy-loss spectra and the structural stability of nickel oxide: a LSDA+U study. *Physical Review B*, 57(3):1505.

[Durbin et al., 1988] Durbin, S. M., Berman, L. E., Batterman, B. W., Brodsky, M. B., and Hamaker, H. C. (1988). Epitaxial growth of fcc Cr on Au(100). *Physical Review B*, 37:6672–6675.

[Ehrlich, 1961] Ehrlich, G. (1961). Kinetic and experimental basis of flash desorption. *Journal of Applied Physics*, 32(1):4–15.

[Einstein, 1965] Einstein, A. (1965). Concerning an heuristic point of view toward the emission and transformation of light. *American Journal of Physics*, 33(5):367.

[Elam et al., 1998] Elam, J., Nelson, C., Cameron, M., Tolbert, M., and George, S. (1998). Adsorption of H_2O on a single-crystal α-Al_2O_3(0001) surface. *The Journal of Physical Chemistry B*, 102(36):7008–7015.

[Eng et al., 2000] Eng, P. J., Trainor, T. P., Brown Jr, G. E., Waychunas, G. A., Newville, M., Sutton, S. R., and Rivers, M. L. (2000). Structure of the hydrated α-Al_2O_3(0001) surface. *Science*, 288(5468):1029–1033.

[Ertl and Freund, 1999] Ertl, G. and Freund, H.-J. (1999). Catalysis and surface science. *Physics Today*, 52(1):32–38.

[Etchegoin et al., 2006] Etchegoin, P. G., Le Ru, E. C., and Meyer, M. (2006). An analytic model for the optical properties of gold. *Journal of Chemical Physics*, 125:164705.

[factsageweb,] factsageweb. FactSage chemical thermodynamics database : http://www.factsage.com/.

[Fadley and Shirley, 1970] Fadley, C. and Shirley, D. (1970). Electronic densities of states from X-ray photoemission spectroscopy. *JOURNAL OF RESEARCH of the Natianal Bureau of Standards - A. Physics and Chemistry*, 74A:543–558.

[Falconer and Schwarz, 1983] Falconer, J. L. and Schwarz, K. (1983). Temperature-programmed desorption and reaction: applications to supported catalysts. *Catal. Rev. Sci. Eng.*, 25:141–227.

[Falke et al., 1977] Falke, W. L., Schwaneke, A. E., and Nash, R. W. (1977). Surface tension of zinc: The positive temperature coefficient. *Metallurgical Transactions B*, 8(1):301–303.

[Flank et al., 2006] Flank, A.-M., Cauchon, G., Lagarde, P., Bac, S., Janousch, M., Wetter, R., Dubuisson, J.-M., Langlois, F., Idir, M., Moreno, T., and Vantelon, D. (2006). LUCIA, a microfocus soft XAS beamline. *Nuclear Instruments and Methods B*, 246:269–274.

[Formica et al., 2013] Formica, N., Ghosh, D. S., Carrilero, A., Chen, T. L., Simpson, R. E., and Pruneri, V. (2013). Ultrastable and atomically smooth ultrathin silver films grown on a copper seed layer. *ACS Applied Materials and Interfaces*, 5(8):3048–3053.

[Fox et al., 1977] Fox, J., Nuttall, J., and Gallon, T. (1977). Solid state effects in the Auger spectrum of zinc and oxidised zinc. *Surface Science*, 63:390–402.

[Franz et al., 1999] Franz, A. J., Ranney, J. T., Jackson, W. B., and Gland, J. L. (1999). Using fractional desorption spectroscopy to determine kinetic parameters for surface processes. *The Journal of Physical Chemistry B*, 103(21):4457–4465.

[French, 1990] French, R. H. (1990). Electronic band structure of Al_2O_3, with comparison to Al on and AIN. *Journal of the American Ceramic Society*, 73(3):477–489.

[French and Somorjai, 1970] French, T. and Somorjai, G. A. (1970). Composition and surface structure of the (0001) face of. alpha-alumina by low-energy electron diffraction. *The Journal of Physical Chemistry*, 74(12):2489–2495.

[Fu et al., 2006] Fu, Q., Wagner, T., and Rühle, M. (2006). Hydroxylated α-Al_2O_3 (0001) surfaces and metal/α-Al_2O_3 (0 0 0 1) interfaces. *Surface Science*, 600(21):4870–4877.

[Fukuda et al., 2008] Fukuda, K., Lim, S. H., and Anders, A. (2008). Coalescence of magnetron-sputtered silver islands affected by transition metal seeding (Ni, Cr, Nb, Zr, Mo, W, Ta) and other parameters. *Thin Solid Films*, 516(14):4546–4552.

[Gasgnier and Névot, 1981] Gasgnier, M. and Névot, L. (1981). Analysis and crystallographic structures of chromium thin films. *Physica Status solidi a*, 66(2):525–540.

[Gautier et al., 1991a] Gautier, M., Duraud, J., and Van, L. P. (1991a). Influence of the $Al_2O_3(0001)$ surface reconstruction on the Cu/Al_2O_3 interface. *Surface Science*, 249(1-3):L327–L332.

[Gautier et al., 1991b] Gautier, M., Duraud, J., Van, L. P., and Guittet, M. (1991b). Modifications of α-$Al_2O_3(0001)$ surfaces induced by thermal treatments or ion bombardment. *Surface Science*, 250(1-3):71–80.

[Gautier et al., 1994] Gautier, M., Fenaud, G., Pham Van, L., Villette, B., Pollak, M., Thromat, N., Jollet, F., and Duraud, J.-P. (1994). α-$Al_2O_3(0001)$ surfaces: Atomic and electronic structure. *Journal of the American Ceramic Society*, 77(2):323–334.

[Gautier et al., 1992] Gautier, M., Van, L. P., and Duraud, J. (1992). Copper clusters formation on Al_2O_3 surfaces: an XPS and SEXAFS study. *Europhysics Letters*, 18(2):175.

[Gautier-Soyer et al., 1996] Gautier-Soyer, M., Gota, S., Douillard, L., Duraud, J., and Le Fevre, P. (1996). Submonolayer scaling due to coalescence of subnanometric copper clusters on alumina. *Physical Review B*, 54(15):10366.

[Giorgi et al., 2012] Giorgi, M.-L., Diawara, J., Chen, S., Koltsov, A., and Mataigne, J.-M. (2012). Influence of annealing treatment on wetting of steels by zinc alloys. *Journal of Materials Science*, 47(24):8483–8495.

[Gloege et al., 1999] Gloege, T., Meyerheim, H. L., Moritz, W., and Wolf, D. (1999). X-ray structure analysis of the $Cr_2O_3(0001)$-(1× 1) surface: evidence for Cr interstitial. *Surface Science*, 441(2-3):L917–L923.

[Gomes et al., 2002] Gomes, J., Illas, F., Hernández, N. C., Sanz, J. F., Wander, A., and Harrison, N. (2002). Surface model and exchange-correlation functional effects on the description of Pd/α-$Al_2O_3(0001)$. *Journal of Chemical Physics*, 116(4):1684–1691.

[Goniakowski, 1999] Goniakowski, J. (1999). Transition metals on the MgO(100) surface: Evolution of adsorption characteristics along the 4d series. *Physical Review B*, 59(16):11047.

[Goniakowski et al., 2007] Goniakowski, J., Finocchi, F., and Noguera, C. (2007). Polarity of oxide surfaces and nanostructures. *Reports on Progress in Physics*, 71(1):016501.

[Gota et al., 1995] Gota, S., Gautier, M., Douillard, L., Thromat, N., Duraud, J., and Le Fevre, P. (1995). Influence of the substrate oxidation state in the growth of copper clusters on $Al_2O_3(0001)$ surface: a XANES and EXAFS study. *Surface Science*, 323(1-2):163–174.

[Gota et al., 1996] Gota, S., Gautier-Soyer, M., Douillard, L., Duraud, J., and Le Fevre, P. (1996). The initial stages of the growth of copper on a (1× 1) and a $(\sqrt{31} \times \sqrt{31})$ r±9° α-$Al_2O_3(0001)$ surface. *Surface Science*, 352:1016–1021.

[Granfilm,] Granfilm. `GranFilm` can be downloaded with a user guide from: http://www.insp.jussieu.fr/-Logiciels-.html.

[Guénard et al., 1998] Guénard, P., Renaud, G., Barbier, A., and Gautier-Soyer, M. (1998). Determination of the α-$Al_2O_3(0001)$ surface relaxation and termination by measurements of crystal truncation rods. *Surface Review Letters*, 5(321).

[Haarmans and Bedeaux, 1995] Haarmans, M. and Bedeaux, D. (1995). Optical properties of thin films up to second order in the thickness. *Thin Solid Films*, 258(1-2):213–223.

[Haarmans and Bedeaux, 1993] Haarmans, M. T. and Bedeaux, D. (1993). The polarizability and the optical properties of lattices and random distributions of small metal spheres on a substrate. *Thin Solid Films*, 224:117–131.

[Harrison et al., 1999] Harrison, N., Wang, X.-G., Muscat, J., and Scheffler, M. (1999). The influence of soft vibrational modes on our understanding of oxide surface structure. *Faraday Discussions*, 114:305–312.

[Hass et al., 1998] Hass, K. C., Schneider, W. F., Curioni, A., and Andreoni, W. (1998). The chemistry of water on alumina surfaces: Reaction dynamics from first principles. *Science*, 282(5387):265–268.

[Hayashi et al., 1977] Hayashi, T., Ohno, T., Yatsuya, S., and Uyeda, R. (1977). Formation of ultrafine metal particles by gas-evaporation technique. IV. Crystal habits of iron and fcc metals, Al, Co, Ni, Cu, Pd, Ag, In, Au and Pb. *Japanese Journal of Applied Physics*, 16(5):705.

[Heemeier et al., 2000] Heemeier, M., Frank, M., Libuda, J., Wolter, K., Kuhlenbeck, H., Bäumer, M., and Freund, H.-J. (2000). The influence of OH groups on the growth of rhodium on alumina: a model study. *Catalysis Letters*, 68(1-2):19–24.

[Henke et al., 1993] Henke, B. L., Gullikson, E. M., and Davis, J. C. (1993). X-ray interactions: photoabsorption, scattering, transmission, and reflection at $e = 50 - 30000$ eV, $z = 1 - 92$. *Atomic Data and Nuclear Data Tables*, 54(2):181–342.

[Henkelman et al., 2006] Henkelman, G., Arnaldsson, A., and Jónsson, H. (2006). A fast and robust algorithm for Bader decomposition of charge density. *Computational Materials Science*, 36(3):354–360.

[Henry, 1998] Henry, C. R. (1998). Surface studies of supported model catalysts. *Surface Science Reports*, 31(7-8):231–325.

[Hilger et al., 2001] Hilger, A., Tenfelde, M., and Kreibig, U. (2001). Silver nanoparticles deposited on dielectric surfaces. *Appl. Phys. B: Laser Opt.*, 73:361–372.

[Ho et al., 2013] Ho, C. S., Martono, E., Banerjee, S., Roszell, J., Vohs, J., and Koel, B. E. (2013). Alloy formation and chemisorption at Zn/Pt(111) bimetallic surfaces using alkali ISS, XPD, and TPD. *The Journal of Physical Chemistry A*, 117:11684–11694.

[Hoffman, 2013] Hoffman, S. (2013). Auger and X-ray photoelectron spectroscopy in material science.

[Hövel et al., 1998] Hövel, H., Grimm, B., Pollmann, M., and Reihl, B. (1998). Cluster-substrate interaction on a femtosecond time scale revealed by a high-resolution photoemission study of the Fermi-level onset. *Physical Review Letters*, 81:4608–4611.

[Howard et al., 2002] Howard, A., Clark, D. N. S., Mitchell, C. E. J., Egdell, R. G., and Dhanak, V. R. (2002). Initial and final state effects in photoemission from Au nanoclusters on TiO_2(110). *Surface Science*, 518:210–224.

[Hüfner, 1995] Hüfner, S. (1995). *Photoelectron spectroscopy: principles and applications.* Springer.

[Ibach, 2006] Ibach, H. (2006). *Physics of Surfaces and Interfaces*, volume 10. Springer-Verlag Berlin Heidelberg.

[Jackson, 1975] Jackson, J. D. (1975). *Classical Electrodynamics.* Wiley & Sons, New York.

[Jeroro et al., 2007] Jeroro, E., Lebarbier, V., Datye, A., Wang, Y., and Vohs, J. M. (2007). Interaction of CO with surface PdZn alloys. *Surface Science*, 601:5546 – 5554.

[Johnson and Pepper, 1982] Johnson, K. and Pepper, S. (1982). Molecular-orbital model for metal-sapphire interfacial strength. *Journal of Applied Physics*, 53(10):6634–6637.

[Johnson and Christy, 1972] Johnson, P. and Christy, R. (1972). Optical constant of noble metals. *Physical Review B*, 6:4370–4379.

[Johnson and Christy, 1974] Johnson, P. B. and Christy, R. W. (1974). Optical constants of transition metals: Ti, V, Cr, Mn, Fe, Co, Ni, and Pd. *Physical Review B*, 9:5056–5070.

[Jupille and Lazzari, 2006] Jupille, J. and Lazzari, R. (2006). Improving the wetting of oxides by metals. *Journal of Optoelectronics and Advanced Materials*, 8(3):901.

[Kaplan et al., 1995] Kaplan, W. D., Mxillejans, H., Rühle, M., Rödel, J., and Claussen, N. (1995). Ca segregation to basal surfaces in α-alumina. *Journal of the American Ceramic Society*, 78(10):2841–2844.

[Kelber et al., 2000] Kelber, J., Niu, C., Shepherd, K., Jennison, D., and Bogicevic, A. (2000). Copper wetting of α-Al_2O_3(0001): Theory and experiment. *Surface Science*, 446(1-2):76–88.

[Kelber, 2007] Kelber, J. A. (2007). Alumina surfaces and interfaces under non-ultrahigh vacuum conditions. *Surface Science Reports*, 62(7):271–303.

[Kimoto and Nishida, 1973] Kimoto, K. and Nishida, I. (1973). Crystal structure of very small particles of chromium and iron. *Thin Solid Films*, 17(1):49–58.

[King, 1975] King, D. A. (1975). Thermal desorption from metal surfaces: a review. *Surf. Sci.*, 47:384–402.

[Kirby et al., 1987] Kirby, R., Garwin, E., King, F., and Nyaiesh, A. (1987). Surface properties of Cr_2O_3. *Journal of Applied Physics*, 62(4):1400–1405.

[Klimeš et al., 2009] Klimeš, J., Bowler, D. R., and Michaelides, A. (2009). Chemical accuracy for the van der Waals density functional. *Journal of Physics: Condensed Matter*, 22(2):022201.

[Klimeš et al., 2011] Klimeš, J., Bowler, D. R., and Michaelides, A. (2011). Van der Waals density functionals applied to solids. *Physical Review B*, 83(19):195131.

[Knight et al., 2009] Knight, M. W., Wu, Y., Lassiter, J. B., Nordlander, P., and Halas, N. J. (2009). Substrates matter: influence of an adjacent dielectric on an individual plasmonic nanoparticle. *Nano Letters*, 9:2188–2192.

[Kourouklis and Nix, 1994] Kourouklis, H. and Nix, R. (1994). The uptake and characterisation of zinc on low index silver and copper surfaces. *Surface Science*, 314:201 – 211.

[Kowalczyk et al., 1973a] Kowalczyk, S., Pollak, R., McFeely, F., Ley, L., and Shirley, D. (1973a). $L_{2,3}M_{45}M_{45}$ Auger spectra of metallic copper and zinc: theory and experiment. *Physical Review B*, 8(6):2387.

[Kowalczyk et al., 1973b] Kowalczyk, S., Pollak, R., McFeely, F., Ley, L., and Shirley, D. (1973b). $L_{2,3}M_{45}M_{45}$ Auger spectra of metallic copper and zinc: theory and experiment. *Physical Review B*, 8(6):2387.

[Kreibig, 1977] Kreibig, U. (1977). Anomalous frequency and temperature dependence of the optical absorption of small gold particles. *Le Journal de Physique Colloques*, 38(C2):C2–97.

[Kreibig, 2008] Kreibig, U. (2008). Interface-induced dephasing of mie plasmon polaritons. *Appl. Phys. B: Laser Opt.*, 93:79–89.

[Kreibig and Fragstein, 1969] Kreibig, U. and Fragstein, C. (1969). The limitation of electron mean free path in small silver particles. *Z. Phys.*, 224:307–323.

[Kreibig and Vollmer, 1995] Kreibig, U. and Vollmer, M. (1995). *Optical Properties of Metal Clusters*, volume 25. Springer Series in Material Science, Springer Verlag, Berlin, Germany.

[Kresse and Furhmuller, 1993] Kresse, G. and Furhmuller, J. (1993). Software VASP, Vienna (1999); Kresse G. and Hafner J. *Physical Review B*, 47:R558.

[Kresse and Furthmüller, 1996] Kresse, G. and Furthmüller, J. (1996). Computer code VASP, Vienna, Austria, 1999. *Comput. Mater. Sci*, 6:15.

[Kresse and Joubert, 1999] Kresse, G. and Joubert, D. (1999). From ultrasoft pseudopotentials to the projector augmented-wave method. *Physical Review B*, 59(3):1758.

[Krokidis et al., 2001] Krokidis, X., Raybaud, P., Gobichon, A.-E., Rebours, B., Euzen, P., and Toulhoat, H. (2001). Theoretical study of the dehydration process of boehmite to γ-alumina. *The Journal of Physical Chemistry B*, 105(22):5121–5130.

[Lai et al., 1998] Lai, X., Clair, T. S., Valden, M., and Goodman, D. (1998). Scanning tunneling microscopy studies of metal clusters supported on TiO_2 (110): Morphology and electronic structure. *Progress in Surface Science*, 59(1-4):25–52.

[Lazzari, 2000] Lazzari, R. (2000). *Vers la maitrise de la croissance de couches minces: une etude par spectroscopie optique et d'electrons.* PhD thesis, PARIS 11, ORSAY.

[Lazzari et al., 2016] Lazzari, R., Goniakowski, J., Cabailh, G., Cavallotti, R., Trcera, N., Lagarde, P., and Jupille, J. (2016). Surface and epitaxial stresses on supported metal clusters. *Nano Letters*, 16(4):2574–2579.

[Lazzari and Jupille, 2001] Lazzari, R. and Jupille, J. (2001). Silver layers on oxide surfaces: morphology and optical properties. *Surface Science*, 482:823–828.

[Lazzari and Jupille, 2002] Lazzari, R. and Jupille, J. (2002). Chemical reaction via hydroxyl groups at the titanium/α-Al_2O_3 (0 0 0 1) interface. *Surface Science*, 507:683–687.

[Lazzari and Jupille, 2005] Lazzari, R. and Jupille, J. (2005). Wetting and interfacial chemistry of metallic films on the hydroxylated α- $Al_2O_3(0001)$ surface. *Physical Review B*, 71(4):045409.

[Lazzari and Jupille, 2011] Lazzari, R. and Jupille, J. (2011). Quantitative analysis of nanoparticle growth through plasmonics. *Nanotechnology*, 22(44):445703.

[Lazzari and Jupille, 2012] Lazzari, R. and Jupille, J. (2012). Growth kinetics and size-dependent wetting of ag/α-$Al_2O_3(0001)$ nanoparticles studied via the plasmonic response. *Nanotechnology*, 23(13):135707.

[Lazzari et al., 2014a] Lazzari, R., Jupille, J., Cavallotti, R., and Simonsen, I. (2014a). Model-free unraveling of supported nanoparticles plasmon resonance modes. *The Journal of Physical Chemistry C*, 118(13):7032–7048.

[Lazzari et al., 2003a] Lazzari, R., Layet, J. M., and Jupille, J. (2003a). Electron-energy-loss channels and plasmon confinement in supported silver particles. *Physical Review B*, 68:045428.

[Lazzari et al., 2009] Lazzari, R., Renaud, G., Revenant, C., Jupille, J., and Borensztein, Y. (2009). Adhesion of growing nanoparticles at a glance: Surface differential reflectivity spectroscopy and grazing incidence small angle X-ray scattering. *Physical Review B*, 79:125428.

[Lazzari et al., 2002] Lazzari, R., Roux, S., Simonsen, I., Jupille, J., Bedeaux, D., and Vlieger, J. (2002). Multipolar plasmon resonances in supported silver particles: The case of ag/α-$Al_2O_3(0001)$. *Physical Review B*, 65(23):235424.

[Lazzari and Simonsen, 2002] Lazzari, R. and Simonsen, I. (2002). GRANFILM: a software for calculating thin-layer dielectric properties and fresnel coefficients. *Thin Solid Films*, 419(1-2):124–136.

[Lazzari et al., 2001] Lazzari, R., Simonsen, I., Bedeaux, D., Vlieger, J., and Jupille, J. (2001). Polarizability of truncated spheroidal particles supported by a substrate: model and applications. *The European Physical Journal B-Condensed Matter and Complex Systems*, 24(2):267–284.

[Lazzari et al., 2003b] Lazzari, R., Simonsen, I., and Jupille, J. (2003b). Onset of charge localisation on coupling multipolar absorption modes in supported metal particles. *EPL (Europhysics Letters)*, 61(4):541.

[Lazzari et al., 2014b] Lazzari, R., Simonsen, I., and Jupille, J. (2014b). Interfacial susceptibilities in nanoplasmonics via inversion of Fresnel coefficients. *Plasmonics*, 9(2):261–272.

[Le et al., 2016] Le, H.-L. T., Goniakowski, J., Noguera, C., Koltsov, A., and Mataigne, J.-M. (2016). First-principles study on the effect of pure and oxidized transition-metal buffers on adhesion at the alumina/zinc interface. *The Journal of Physical Chemistry C*, 120(18):9836–9844.

[Le et al., 2017a] Le, H.-L. T., Goniakowski, J., Noguera, C., Koltsov, A., and Mataigne, J.-M. (2017a). Improving adhesion at the alumina/zinc interface by stainless steel buffers. *The Journal of Physical Chemistry C*, 121(45):25143–25151.

[Le et al., 2017b] Le, H.-L. T., Lazzari, R., Goniakowski, J., Cavallotti, R., Chenot, S., Noguera, C., Jupille, J., Koltsov, A., and Mataigne, J.-M. (2017b). Tuning adhesion at metal/oxide interfaces by surface hydroxylation. *The Journal of Physical Chemistry C*, 121(21):11464–11471.

[Lenham and Treherne, 1964] Lenham, A. and Treherne, D. (1964). The optical constants of single crystals of cadmium and zinc. *Proceedings of the Physical Society*, 83(6):1059.

[Lermé et al., 2013] Lermé, J., Bonnet, C., Broyer, M., Cottancin, E., Manchon, D., and Pellarin, M. (2013). Optical properties of a particle above a dielectric interface: cross sections, benchmark calculations, and analysis of the intrinsic substrate effects. *Journal of Physical Chemistry C*, 117:6383–6398.

[Letnes et al., 2011] Letnes, P., Simonsen, I., and Mills, D. (2011). Substrate influence on the plasmonic response of clusters of spherical nanoparticles. *Physical Review B*, 83:075426.

[Levin and Brandon, 1998] Levin, I. and Brandon, D. (1998). Metastable alumina polymorphs: crystal structures and transition sequences. *Journal of the American Ceramic Society*, 81(8):1995–2012.

[Ley et al., 1973] Ley, L., Kowalczyk, S., McFeely, F., Pollak, R., and Shirley, D. (1973). X-ray photoemission from zinc: evidence for extra-atomic relaxation via semilocalized excitons. *Physical Review B*, 8(6):2392.

[Libuda et al., 1997] Libuda, J., Frank, M., Sandell, A., Andersson, S., Brühwiler, P., Bäumer, M., Mårtensson, N., and Freund, H.-J. (1997). Interaction of rhodium with hydroxylated alumina model substrates. *Surface Science*, 384(1-3):106–119.

[Liebsch, 1993] Liebsch, A. (1993). Surface-plasmon dispersion and size dependence of Mie resonance : Silver versus simple metals. *Physical Review B*, 48(15):11317–11328.

[Liu et al., 1998] Liu, P., Kendelewicz, T., Brown Jr, G. E., Nelson, E. J., and Chambers, S. A. (1998). Reaction of water vapor with α-Al_2O_3(0001) and α-Fe_2O_3(0001) surfaces: synchrotron X-ray photoemission studies and thermodynamic calculations. *Surface Science*, 417(1):53–65.

[Łodziana et al., 2003] Łodziana, Z., Nørskov, J., and Stoltze, P. (2003). The stability of the hydroxylated (0001) surface of α-Al_2O_3. *Journal of Chemical Physics*, 118(24):11179–11188.

[Logeeswaran et al., 2008] Logeeswaran, V., Kobayashi, N. P., Islam, M. S., Wu, W., Chaturvedi, P., Fang, N. X., Wang, S. Y., and Williams, R. S. (2008). Ultrasmooth silver thin films deposited with a germanium nucleation layer. *Nano Letters*, 9(1):178–182.

[Lovrinčić and Pucci, 2009] Lovrinčić, R. and Pucci, A.-M. (2009). Infrared optical properties of chromium nanoscale films with a phase transition. *Physical Review B*, 80:205404.

[Lüth, 2001] Lüth, H. (2001). *Solid surfaces, interfaces and thin films*, volume 4. Springer.

[Madey et al., 2008] Madey, T. E., Chen, W., Wang, Kaghazchi, P., and Jacob, T. (2008). Nanoscale surface chemistry over faceted substrates: structure, reactivity and nanotemplate. *Chemical Society Reviews*, 37:2310–2327.

[Manassidis et al., 1993] Manassidis, I., De Vita, A., and Gillan, M. (1993). Structure of the (0001) surface of α-Al_2O_3 from first principles calculations. *Surface Science Letters*, 285(3):L517–L521.

[Markov and Kaischew, 1976] Markov, I. and Kaischew, R. (1976). Influence of supersaturation on the mode of crystallization on crystalline substrates. *Thin Solid Films*, 32(1):163–167.

[Markov and Kishishev, 1976] Markov, I. and Kishishev, R. (1976). Influence of substrate inhomogeneity on the kinetics of heterogeneous nucleation. *Krist. Tech.*, 11:685–692.

[Mateck,] Mateck. https://mateck.com/.

[Maxwell Garnett, 1904] Maxwell Garnett, J. C. (1904). Colours in metal glasses and in metallic films. *Phil. Trans. Roy. Soc. London*, 203(230A):385–420.

[McIntyre and Aspnes, 1971] McIntyre, J. and Aspnes, D. (1971). Differential reflection spectroscopy of very thin surface films. *Surface Science*, 24:417–434.

[Mie, 1908] Mie, G. (1908). Beitrage zur optik trüber medien speziell kolloidaler metallösungen. *Ann. Phys.*, 25:377–445.

[Mock et al., 2008] Mock, J. J., Hill, R. T., Degiron, A., Zauscher, S., Chilkoti, A., and Smith, D. R. (2008). Distance-dependent plasmon resonant coupling between a gold nanoparticle and gold film. *Nano Letters*, 8:2245–2252.

[Momma and Izumi, 2011] Momma, K. and Izumi, F. (2011). VESTA 3 for three-dimensional visualization of crystal, volumetric and morphology data. *Journal of Applied Crystallography*, 44(6):1272–1276.

[Mosteller Jr and Wooten, 1968] Mosteller Jr, L. and Wooten, F. (1968). Optical properties of Zn. *Physical Review*, 171(3):743.

[Myroshnychenko et al., 2008] Myroshnychenko, V., Rodríguez-Fernández, J., Pastoriza-Santos, I., Funston, A. M., Novo, C., Mulvaney, P., Liz-Marzán, L. M., and García de Abajo, F. J. (2008). Modelling the optical response of gold nanoparticles. *Chemical Society Reviews*, 37:1792–1805.

[Naidich, 1981] Naidich, J. V. (1981). The wettability of solids by liquid metals. In *Progress in surface and membrane science*, volume 14, pages 353–484. Elsevier.

[Nash and Sambles, 1998] Nash, D. and Sambles, J. (1998). Surface plasmon-polariton study of the optical dielectric function of zinc. *Journal of Modern Optics*, 45(12):2585–2596.

[Naumkin et al., 2012] Naumkin, A., Kraut-Vass, A., and Gaarenstroom, S. (2012). Nist X-ray photoelectron spectroscopy database. *Ref. Database 20, Version*, 4.

[Nelson et al., 1998] Nelson, C., Elam, J., Cameron, M., Tolbert, M., and George, S. (1998). Desorption of H_2O from a hydroxylated single-crystal α-Al_2O_3(0001) surface. *Surface Science*, 416(3):341–353.

[Nishida and Kimoto, 1974] Nishida, I. and Kimoto, K. (1974). Crystal habit and crystal structure of fine chromium particles: An electron microscope and electron diffraction study of fine metallic particles prepared by evaporation in argon at low pressures (III). *Thin Solid Films*, 23:179–189.

[Nishida et al., 1972] Nishida, I., Sahashi, T., and Kimoto, K. (1972). Oblique incidence effect on the crystal structure of thin vacuum-deposited chromium films. *Thin Solid Films*, 10(2):265 – 272.

[NIST, 2000] NIST (2000). https://srdata.nist.gov/xps/selEnergyType.aspx.

[Niu et al., 2000] Niu, C., Shepherd, K., Martini, D., Tong, J., Kelber, J., Jennison, D., and Bogicevic, A. (2000). Cu interactions with α-Al_2O_3(0001): effects of surface hydroxyl groups versus dehydroxylation by Ar-ion sputtering. *Surface Science*, 465(1-2):163–176.

[Noguez, 2007] Noguez, C. (2007). Surface plasmons on metal nanoparticles: The influence of shape and physical environment. *Journal of Physical Chemistry C*, 111:3806–3819.

[Nordlander and Prodan, 2004] Nordlander, P. and Prodan, E. (2004). Plasmon hybridization in nanoparticles near metallic surfaces. *Nano Letters*, 11:2209–2213.

[Nygren et al., 1997] Nygren, M. A., Gay, D. H., Richard, C., and Catlow, A. (1997). Hydroxylation of the surface of the corundum basal plane. *Surface Science*, 380(1):113–123.

[O'Connor et al., 2013] O'Connor, D. J., Sexton, B. A., and Smart, R. S. (2013). *Surface analysis methods in materials science*, volume 23. Springer Science & Business Media.

[Ollivier-Leduc et al., 2010] Ollivier-Leduc, A., Giorgi, M.-L., Balloy, D., and Guillot, J.-B. (2010). Nucleation and growth of selective oxide particles on ferritic steel. *Corrosion Science*, 52(7):2498–2504.

[Oura et al., 2013] Oura, K., Lifshits, V., Saranin, A., Zotov, A., and Katayama, M. (2013). *Surface science: an introduction*. Springer Science & Business Media.

[Ozawa et al., 2005] Ozawa, K., Sato, T., Kato, M., Edamoto, K., and Aiura, Y. (2005). Angle-resolved photoemission spectroscopy study of adsorption process and electronic structure of silver on ZnO($10\bar{1}0$). *Journal of Physical Chemistry B*, 109:14619–14626.

[Paglia et al., 2005] Paglia, G., Rohl, A. L., Buckley, C. E., and Gale, J. D. (2005). Determination of the structure of γ-alumina from interatomic potential and first-principles calculations: The requirement of significant numbers of nonspinel positions to achieve an accurate structural model. *Physical Review B*, 71(22):224115.

[Pakizeh et al., 2009] Pakizeh, T., Langhammer, C., Zorić, I., Apell, P., and Käll, M. (2009). Intrinsic Fanointerference of localized plasmons in Pd nanoparticles. *Nano Letters*, 9:882–886.

[Palik, 1985] Palik, E. D. (1985). *Handbook of Optical Constants of Solids*, volume 1-3. Academic Press.

[Pang et al., 2000] Pang, C., Raza, H., Haycock, S., and Thornton, G. (2000). Growth of copper and palladium on α-Al_2O_3(0001). *Surface Science*, 460(1-3):L510–L514.

[Pashley, 1985] Pashley, D. (1985). The growth and structure of epitaxial layers. In *Mat. Res. Soc. Symp. Proc.*, volume 37, pages 67–76.

[Persson et al., 2001] Persson, P., Lunell, S., Szöke, A., Ziaja, B., and Hajdu, J. (2001). Shake-up and shake-off excitations with associated electron losses in X-ray studies of proteins. *Protein Science*, 10(12):2480–2484.

[Pinchuk et al., 2004] Pinchuk, A., Hilger, A., von Plessen, G., and Kreibig, U. (2004). Substrate effect on the optical response of silver nanoparticles. *Nanotechnology*, 15:18901896.

[Puchin et al., 1997] Puchin, V., Gale, J., Shluger, A., Kotomin, E., Günster, J., Brause, M., and Kempter, V. (1997). Atomic and electronic structure of the corundum (0001) surface: comparison with surface spectroscopies. *Surface Science*, 370(2-3):190–200.

[Rakić et al., 1998] Rakić, A. D., Djurišić, A. B., Elazar, J. M., and Majewski, M. L. (1998). Optical properties of metallic films for vertical-cavity optoelectronic devices. *Applied Optics*, 37(22):5271–5283.

[Rana et al., 2014] Rana, R., Lahaye, C., and Ray, R. K. (2014). Overview of lightweight ferrous materials: Strategies and promises. *Jom*, 66(9):1734–1746.

[Ravel and Newville, 2005] Ravel, B. and Newville, M. (2005). ATHENA, ARTEMIS, HEPHAESTUS: data analysis for X-ray absorption spectroscopy using IFEFFIT. *Journal of Synchrotron Radiation*, 12:537–541.

[Redhead, 1962] Redhead, P. A. (1962). Thermal desorption of gases. *Vacuum*, 12:203–211.

[Rehr and Albers, 2000] Rehr, J. J. and Albers, R. C. (2000). Theoretical approaches to X-ray absorption fine structure. *Reviews of Modern Physics*, 72(3):621.

[Rehr et al., 2009] Rehr, J. J., Kas, J. J., Prange, M. P., Sorini, A. P., Takimoto, Y., and Vila, F. (2009). *Ab initio* theory and calculations of X-ray spectra. *Comptes Rendus Physique*, 10(6):548–559.

[Renaud, 1998] Renaud, G. (1998). Oxide surfaces and metal/oxide interfaces studied by grazing incidence X-ray scattering. *Surface Science Reports*, 32(1-2):5–90.

[Renaud et al., 1994] Renaud, G., Villette, B., Vilfan, I., and Bourret, A. (1994). Atomic structure of the α- $Al_2O_3(0001)(31\times\ 31)$ r±9° reconstruction. *Physical Review Letters*, 73(13):1825.

[Rodriguez, 1996] Rodriguez, J. A. (1996). Physical and chemical properties of bimetallic surfaces. *Surface Science Reports*, 24:223 – 287.

[Rodriguez et al., 1996] Rodriguez, J. A., Kuhn, M., and Hrbek, J. (1996). Interaction of silver, cesium, and zinc with alumina surfaces: Thermal desorption and photoemission studies. *The Journal of Physical Chemistry*, 100(46):18240–18248.

[Román-Velázquez et al., 2000] Román-Velázquez, C. E., Noguez, C., and Barrera, R. G. (2000). Substrate effects on the optical properties of spheroidal nanoparticles. *Physical Review B*, 61(15):10427–10436.

[Rubloff, 1971] Rubloff, G. (1971). Normal-incidence reflectance, optical properties, and electronic structure of Zn. *Physical Review B*, 3(2):285.

[Ruffieux et al., 2000] Ruffieux, P., Schwaller, P., Gröning, O., Schlapbach, L., Gröning, P., Herd, Q., Funnemann, D., and Westermann, J. (2000). Experimental determination of the transmission factor for the Omicron EA125 electron analyzer. *Review of Scientific Instruments*, 71(10):3634–3639.

[Rycenga et al., 2011] Rycenga, M., Cobley, C. M., Zeng, J., Li, W., Moran, C. H., Zhang, Q., Qin, D., and Xia, Y. (2011). Controlling the synthesis and assembly of silver nanostructures for plasmonic applications. *Chemical Reviews*, 111:3669–3712.

[Sainio et al., 2005] Sainio, J., Aronniemi, M., Pakarinen, O., Kauraala, K., Airaksinen, S., Krause, O., and Lahtinen, J. (2005). An XPS study of CrO_x on a thin alumina film and in alumina supported catalysts. *Applied Surface Science*, 252(4):1076–1083.

[Salvi et al., 1995] Salvi, A. M., Castle, J. E., Watts, J. F., and Desimoni, E. (1995). Peak fitting of the chromium 2p XPS spectrum. *Applied Surface Science*, 90(3):333–341.

[Saraf et al., 2003] Saraf, L., Wang, C., Engelhard, M. H., and Baer, D. R. (2003). Temperature-induced phase separation in chromium films. *Applied Physics Letters*, 82:2230–2232.

[Scheu et al., 1996] Scheu, C., Dehm, G., Müllejans, H., and Rühle, M. (1996). Electron energy-loss spectroscopy at cu/Al_2O_3 and ti/Al_2O_3 interfaces. In *Materials Science Forum*, volume 207, pages 181–184. Trans Tech Publ.

[Schön, 1973a] Schön, G. (1973a). Auger and direct electron spectra in X-ray photoelectron studies of zinc, zinc oxide, gallium and gallium oxide. *Journal of Electron Spectroscopy and Related Phenomena*, 2(1):75–86.

[Schön, 1973b] Schön, G. (1973b). Esca studies of Cu, Cu_2O and CuO. *Surface Science*, 35:96–108.

[Schroeder and Gottfried, 2002] Schroeder, S. L. and Gottfried, M. (2002). *Notes: Temperature-Programmed Desorption (TPD) Thermal Desorption Spectroscopy (TDS).*

[Shinotsuka et al., 2015] Shinotsuka, H., Tanuma, S., Powell, C., and Penn, D. (2015). Calculations of electron inelastic mean free paths. X. Data for 41 elemental solids over the 50 eV to 200 keV range with the relativistic full Penn algorithm. *Surface and Interface Analysis*, 47(9):871–888.

[Shirley, 1972] Shirley, D. A. (1972). High-resolution X-ray photoemission spectrum of the valence bands of gold. *Physical Review B*, 5(12):4709.

[Siegbahn, 1970] Siegbahn, K. (1970). A discussion on photoelectron spectroscopy-electron spectroscopy for chemical analysis (ESCA). *Phil. Trans. R. Soc. Lond. A*, 268(1184):33–57.

[Siegel et al., 2002] Siegel, D. J., Hector Jr, L. G., and Adams, J. B. (2002). Adhesion, atomic structure, and bonding at the Al(111)/α- Al_2O_3(0001) interface: A first principles study. *Physical Review B*, 65(8):085415.

[Simonsen et al., 2000] Simonsen, I., Lazzari, R., Jupille, J., and Roux, S. (2000). Numerical modeling of the optical response of supported metallic particles. *Physical Review B*, 61(11):7722.

[Smith, 1985] Smith, D. (1985). *Handbook of Optical Constants of Solids*, volume 1, chapter Dispersion theory, sum rules and their applications in the analysis of optical data, pages 35–64. Academic Press.

[Soares et al., 2002] Soares, E., Van Hove, M., Walters, C., and McCarty, K. (2002). Structure of the α- $Al_2O_3(0001)$ surface from low-energy electron diffraction: Al termination and evidence for anomalously large thermal vibrations. *Physical Review B*, 65(19):195405.

[Søndergård et al., 2003] Søndergård, E., Kerjan, O., Abriou, D., and Jupille, J. (2003). Buffer effects of titanium in the case of silver/α-$Al_2O_3(0001)$. *The European Physical Journal D-Atomic, Molecular, Optical and Plasma Physics*, 24(1):343–345.

[Søndergård et al., 2004] Søndergård, E., Kerjan, O., Barreteau, C., and Jupille, J. (2004). Structure and growth of titanium buffer layers on Al_2O_3 (0 0 0 1). *Surface Science*, 559(2-3):131–140.

[Stahrenberg et al., 2001] Stahrenberg, K., Herrmann, T., Wilmers, K., Esser, N., Richter, W., and Lee, M. (2001). Optical properties of copper and silver in the energy range 2.5–9.0 eV. *Physical Review B*, 64(11):115111.

[Stern, 1974] Stern, E. A. (1974). Theory of the extended X-ray-absorption fine structure. *Physical Review B*, 10(8):3027.

[Sterrer and Freund, 2013] Sterrer, M. and Freund, H.-J. (2013). Towards realistic surface science models of heterogeneous catalysts: influence of support hydroxylation and catalyst preparation method. *Catalysis Letters*, 143(5):375–385.

[Stoneham and Tasker, 1985] Stoneham, A. and Tasker, P. (1985). Metal-non-metal and other interfaces: the role of image interactions. *Journal of Physics C: Solid State Physics*, 18(19):L543.

[Sun et al., 2006] Sun, M., Nelson, A. E., and Adjaye, J. (2006). Examination of spinel and nonspinel structural models for γ-Al_2O_3 by DFT and Rietveld refinement simulations. *The Journal of Physical Chemistry B*, 110(5):2310–2317.

[Suzuki et al., 1999] Suzuki, T., Hishita, S., Oyoshi, K., and Souda, R. (1999). Structure of α-$Al_2O_3(0001)$ surface and Ti deposited on α-$Al_2O_3(0001)$ substrate: CAICISS and RHEED study. *Surface Science*, 437(3):289–298.

[Swanglap et al., 2011] Swanglap, P., Slaughter, L. S., Chang, W.-S., Willingham, B., Khanal, B. P., Zubarev, E. R., and Link, S. (2011). Seeing double: coupling between substrate image charges and collective plasmon modes in self-assembled nanoparticle superstructures. *ACS Nano*, 5:4892–4901.

[Tanuma et al., 2005] Tanuma, S., Powell, C., and Penn, D. (2005). Calculations of electron inelastic mean free paths. *Surface and Interface Analysis*, 37(1):1–14.

[Tanuma et al., 1988] Tanuma, S., Powell, C. J., and Penn, D. R. (1988). Calculations of electron inelastic mean free paths for 31 materials. *Surface and Interface Analysis*, 11(11):577–589.

[Tanuma et al., 1991a] Tanuma, S., Powell, C. J., and Penn, D. R. (1991a). Calculations of electorn inelastic mean free paths. II. Data for 27 elements over the 50-2000 eV range. *Surface and Interface Analysis*, 17(13):911–926.

[Tanuma et al., 1991b] Tanuma, S., Powell, C. J., and Penn, D. R. (1991b). Calculations of electron inelastic mean free paths. III. Data for 15 inorganic compounds over the 50-2000 eV range. *Surface and Interface Analysis*, 17(13):927–939.

[Tanuma et al., 1993] Tanuma, S., Powell, C. J., and Penn, D. R. (1993). Calculations of electron inelastic mean free paths (IMFPS). IV. Evaluation of calculated IMFPs and of the predictive IMFP formula TPP-2 for electron energies between 50 and 2000 eV. *Surface and interface analysis*, 20(1):77–89.

[Tanuma et al., 1994] Tanuma, S., Powell, C. J., and Penn, D. R. (1994). Calculations of electron inelastic mean free paths. V. Data for 14 organic compounds over the 50-2000 eV range. *Surface and Interface Analysis*, 21(3):165–176.

[Tanuma et al., 1997] Tanuma, S., Powell, C. J., and Penn, D. R. (1997). Calculations of electron inelastic mean free paths (IMFPs) VI. Analysis of the Gries inelastic scattering model and predictive IMFP equation. *Surface and interface analysis*, 25(1):25–35.

[Tanuma et al., 2003] Tanuma, S., Powell, C. J., and Penn, D. R. (2003). Calculation of electron inelastic mean free paths (IMFPs) VII. Reliability of the TPP-2M IMFP predictive equation. *Surface and interface analysis*, 35(3):268–275.

[Tepesch and Quong, 2000] Tepesch, P. and Quong, A. (2000). First-principles calculations of α-alumina (0001) surfaces energies with and without hydrogen. *Physica Status Solidi (b)*, 217(1):377–387.

[Todeschini et al., 2017] Todeschini, M., Bastos da Silva Fanta, A., Jensen, F., Wagner, J. B., and Han, A. (2017). Influence of Ti and Cr adhesion layers on ultrathin Au films. *ACS Applied Materials & Interfaces*, 9(42):37374–37385.

[Toofan and Watson, 1998] Toofan, J. and Watson, P. (1998). The termination of the α-Al_2O_3(0001) surface: a LEED crystallography determination. *Surface Science*, 401(2):162–172.

[Tougaard,] Tougaard, S. Quases-imfp-tpp2m software.

[Udagawa, 1996] Udagawa, Y. (1996). *X-ray absorption fine structure for catalysts and surfaces*, volume 2.

[Verdozzi et al., 1999] Verdozzi, C., Jennison, D., Schultz, P., and Sears, M. (1999). Sapphire (0001) surface, clean and with d-metal overlayers. *Physical Review Letters*, 82(4):799.

[Vernon et al., 2010] Vernon, K. C., Funston, A. M., Novo, C., Gómez, D. E., Mulvaney, P., and Davis, T. J. (2010). Influence of particle-substrate interaction on localized plasmon resonances. *Nano Letters*, 10:2080–2086.

[Vij, 2006] Vij, D. (2006). *Handbook of Applied Solid State Spectroscopy*. Springer.

[Vilfan et al., 1997] Vilfan, I., Villain, J., et al. (1997). Rotational reconstruction of sapphire (0001). *Surface Science*, 392(1-3):62–68.

[Vlieger and Bedeaux, 1980] Vlieger, J. and Bedeaux, D. (1980). A statistical theory for the dielectric properties of thin island films. *Thin Solid Films*, 69(1):107–130.

[Wagner, 1979] Wagner, C. D. (1979). *Handbook of X-ray photoelectron spectroscopy: a reference book of standard data for use in X-ray photoelectron spectroscopy*. Perkin-Elmer.

[Wang et al., 2000] Wang, X.-G., Chaka, A., and Scheffler, M. (2000). Effect of the environment on α- $Al_2O_3(0001)$ surface structures. *Physical Review Letters*, 84(16):3650.

[Weaver et al., 1972] Weaver, J., Lynch, D. W., and Rosei, R. (1972). Optical properties of single-crystal zinc. *Physical Review B*, 5(8):2829.

[webelements,] webelements. http://www.webelements.com.

[Wertheim et al., 1986] Wertheim, G. K., DiCenzo, S. B., and Buchanan, D. N. E. (1986). Noble- and transition-metal clusters: The d bands of silver and palladium. *Physical Review B*, 33:5384–5390.

[Wertheim et al., 1983] Wertheim, G. K., DiCenzo, S. B., and Youngquist, S. E. (1983). Unit charge on supported gold clusters in photoemission final state. *Physical Review Letters*, 51:2310–2313.

[Wind et al., 1987a] Wind, M., Bobbert, P., Vlieger, J., and Bedeaux, D. (1987a). The polarizability of a truncated sphere on a substrate II. *Physica A: Statistical Mechanics and its Applications*, 143(1-2):164–182.

[Wind et al., 1987b] Wind, M., Vlieger, J., and Bedeaux, D. (1987b). The polarizability of a truncated sphere on a substrate I. *Physica A: Statistical Mechanics and its Applications*, 141(1):33–57.

[Woodruff, 2013] Woodruff, D. P. (2013). Quantitative structural studies of corundum and rocksalt oxide surfaces. *Chemical Reviews*, 113(6):3863–3886.

[Xu et al., 1997] Xu, C., Lai, X., Zajac, G., and Goodman, D. (1997). Scanning tunneling microscopy studies of the $TiO_2(110)$ surface: structure and the nucleation growth of Pd. *Physical Review B*, 56(20):13464.

[Yamaguchi et al., 1973] Yamaguchi, T., Yoshida, S., and Kinbara, A. (1973). Anomalous optical absorption of aggregated silver films. *Thin Solid Films*, 18:63–70.

[Yamaguchi et al., 1974] Yamaguchi, T., Yoshida, S., and Kinbara, A. (1974). Optical effect of the substrate on the anomalous absorption of aggregated silver films. *Thin Solid Films*, 21:173–187.

[Yang et al., 2010] Yang, D., Krasowska, M., Sedev, R., and Ralston, J. (2010). The unusual surface chemistry of α-$Al_2O_3(0001)$. *Physical Chemistry Chemical Physics*, 12(41):13724–13729.

[Yeh and Lindau, 1985] Yeh, J. and Lindau, I. (1985). Atomic subshell photoionization cross sections and asymmetry parameters: $1 \leq z \leq 103$. *Atomic Data and Nuclear Data Tables*, 32(1):1–155.

[Yin et al., 1972] Yin, L., Tsang, T., Adler, I., and Yellin, E. (1972). L-s coupling interpretation of high-resolution LMM Auger spectra of Cu and Zn. *Journal of Applied Physics*, 43(8):3464–3467.

[Yin et al., 1974] Yin, L. I., Adler, I., Tsang, T., Chen, M. H., Ringers, D. A., and Crasemann, B. (1974). Widths of atomic m-shell vacancy states and quasiatomic aspects of radiationless transitions in solids. *Physical Review A*, 9:1070–1080.

[Zhang and Smith, 2000a] Zhang, W. and Smith, J. (2000a). Nonstoichiometric interfaces and Al_2O_3 adhesion with Al and Ag. *Physical Review Letters*, 85(15):3225.

[Zhang and Smith, 2000b] Zhang, W. and Smith, J. (2000b). Stoichiometry and adhesion of Nb/Al_2O_3. *Physical Review B*, 61(24):16883.

[Zhao et al., 2008] Zhao, J., Pinchuk, A., Mc. Mahon, J. M., Li, S., Ausman, L. K., Atkinson, A. L., and Schatz, G. C. (2008). Methods for describing the electromagnetic properties of silver and gold nanoparticles. *Accounts of Chemical Research*, 41:1710–1720.

[Zhukovskii et al., 2002] Zhukovskii, Y., Kotomin, E., Herschend, B., Hermansson, K., and Jacobs, P. (2002). The adhesion properties of the $Ag/Al_2O_3(0001)$ interface: an *ab initio* study. *Surface Science*, 513:343–358.